

University of Kentucky

UKnowledge

---

Theses and Dissertations--Electrical and  
Computer Engineering

Electrical and Computer Engineering

---


2022

## Hourly Dispatching Wind-Solar Hybrid Power System with Battery-Supercapacitor Hybrid Energy Storage

Pranoy Kumar Singha Roy

*University of Kentucky*, pranoyroy@uky.edu

Author ORCID Identifier:

 <https://orcid.org/0000-0003-0073-1543>

Digital Object Identifier: <https://doi.org/10.13023/etd.2022.369>

[Right click to open a feedback form in a new tab to let us know how this document benefits you.](#)

### Recommended Citation

Roy, Pranoy Kumar Singha, "Hourly Dispatching Wind-Solar Hybrid Power System with Battery-Supercapacitor Hybrid Energy Storage" (2022). *Theses and Dissertations--Electrical and Computer Engineering*. 185.

[https://uknowledge.uky.edu/ece\\_etds/185](https://uknowledge.uky.edu/ece_etds/185)

This Doctoral Dissertation is brought to you for free and open access by the Electrical and Computer Engineering at UKnowledge. It has been accepted for inclusion in Theses and Dissertations--Electrical and Computer Engineering by an authorized administrator of UKnowledge. For more information, please contact [UKnowledge@lsv.uky.edu](mailto:UKnowledge@lsv.uky.edu).

## **STUDENT AGREEMENT:**

I represent that my thesis or dissertation and abstract are my original work. Proper attribution has been given to all outside sources. I understand that I am solely responsible for obtaining any needed copyright permissions. I have obtained needed written permission statement(s) from the owner(s) of each third-party copyrighted matter to be included in my work, allowing electronic distribution (if such use is not permitted by the fair use doctrine) which will be submitted to UKnowledge as Additional File.

I hereby grant to The University of Kentucky and its agents the irrevocable, non-exclusive, and royalty-free license to archive and make accessible my work in whole or in part in all forms of media, now or hereafter known. I agree that the document mentioned above may be made available immediately for worldwide access unless an embargo applies.

I retain all other ownership rights to the copyright of my work. I also retain the right to use in future works (such as articles or books) all or part of my work. I understand that I am free to register the copyright to my work.

## **REVIEW, APPROVAL AND ACCEPTANCE**

The document mentioned above has been reviewed and accepted by the student's advisor, on behalf of the advisory committee, and by the Director of Graduate Studies (DGS), on behalf of the program; we verify that this is the final, approved version of the student's thesis including all changes required by the advisory committee. The undersigned agree to abide by the statements above.

Pranoy Kumar Singha Roy, Student

Dr. JiangBiao He, Major Professor

Dr. Daniel Lau, Director of Graduate Studies

Hourly Dispatching Wind-Solar Hybrid Power System with Battery-Supercapacitor  
Hybrid Energy Storage

---

DISSERTATION

---

A dissertation submitted in partial fulfillment of the  
requirements for the degree of Doctor of Philosophy  
in Electrical Engineering in the College of  
Engineering at the University of Kentucky

By

Pranoy Roy

Lexington, Kentucky

Director: Dr. JiangBiao He

Department of Electrical and Computer Engineering

2022

Copyright© Pranoy Roy 2022

## ABSTRACT OF DISSERTATION

### Hourly Dispatching Wind-Solar Hybrid Power System with Battery-Supercapacitor Hybrid Energy Storage

This dissertation demonstrates a dispatching scheme of wind-solar hybrid power system (WSHPS) for a specific dispatching horizon for an entire day utilizing a hybrid energy storage system (HESS) configured by batteries and supercapacitors. Here, wind speed and solar irradiance are predicted one hour ahead of time using a multilayer perceptron Artificial Neural Network (ANN), which exhibits satisfactory performance with good convergence mapping between input and target output data. Furthermore, multiple state of charge (SOC) controllers as a function of energy storage system (ESS) SOC are developed to accurately estimate the grid reference power ( $P_{\text{Grid,ref}}$ ) for each dispatching period. A low pass filter (LPF) is employed to decouple the power between a battery and a supercapacitor (SC), and the cost optimization of the HESS is computed based on the time constant of the LPF through extensive simulations. Besides, the optimum value of depth of discharge for ESS considering both cycling and calendar expenses has been investigated to optimize the life cycle cost of the ESS, which is vital for minimizing the cost of a dispatchable wind-solar power scheme. Finally, the proposed ESS control algorithm is verified by conducting control hardware-in-the loop (CHIL) experiments in a real-time digital simulator (RTDS) platform.

**KEYWORDS:** Hybrid wind-solar power system, hybrid energy storage, hourly dispatching, particle swarm optimization, state of charge controller, cost analysis.

---

Pranoy Roy

---

October 8, 2022

Hourly Dispatching Wind-Solar Hybrid Power System with Battery-Supercapacitor  
Hybrid Energy Storage

By

Pranoy Roy

Dr. JiangBiao He

---

Director of Dissertation

Dr. Daniel Lau

---

Director of Graduate Studies

October 8, 2022

---

Date

## ACKNOWLEDGMENTS

First and foremost, I would like to express my sincere gratitude and appreciation to my Ph.D. supervisor, Professor JiangBiao He, whose advice, encouragement, and support have been crucial in both my academic and personal development. Under his invaluable guidance, I learned how to effectively execute a research project, make good presentations and write technical articles, as well as build up career goals. I am extremely lucky and grateful to have an advisor who helped me find a place to call home in the academic family of the AMPERE Lab, not only by expertly guiding my doctoral studies but also by recognizing my potential for professional growth. His door is always open whenever I have questions about my dissertation or advice on career development. He has never hesitated to introduce me to opportunities such as summer internships and industrial projects that have helped me gain valuable experience.

Meanwhile, I am very grateful for the advice and feedback that I received from my dissertation committee members, including: Professors Aaron Cramer, Yuan Liao, Joseph Sottile, and the external examiner, Professor Joseph Dvorak. I would also like to extend my sincere thanks to my mentors during my internship at Eaton Research Labs. I am deeply indebted to Professor Bora Karayaka as well for his caring mentorship. Additionally, the greatest appreciation goes to all my colleagues in the AMPERE Lab for their support and friendship.

Furthermore, I would like to acknowledge the support from two research projects, namely, the DOD Defense University Research Instrumentation Program (Award No. N00014-21-1-2972) and the Tennessee Valley Authority (TVA) project, which are led by Professor Yuan Liao. The established RTDS platform and the related research experience have played an important role in my dissertation work.

## TABLE OF CONTENTS

Acknowledgments . . . . .	iii
List of Tables . . . . .	vii
List of Figures . . . . .	viii
Chapter 1 Introduction . . . . .	6
1.1 Background . . . . .	6
1.2 Research Objectives and Contributions . . . . .	9
1.3 Dissertation Outline . . . . .	14
1.4 Related Publications . . . . .	18
Chapter 2 State of the Art on Wind-Solar Hybrid Renewable Energy Systems	20
2.1 System Structures of HRES . . . . .	27
2.1.1 Hybrid Renewable Energy Sources . . . . .	27
2.1.2 System Architectures of HRES . . . . .	29
2.1.3 Coupling Topologies of HRES . . . . .	31
2.2 Energy Storage System . . . . .	33
2.3 Modeling of HRES . . . . .	39
2.3.1 Modeling of PV System . . . . .	40
2.3.2 Modeling of WT system . . . . .	43
2.3.3 Maximum Power Point Tracking . . . . .	46
2.3.4 Degradation Model of ESS . . . . .	50
2.4 Power Converter Configurations for HRES . . . . .	53
2.4.1 AC Shunt Coupled HRES . . . . .	53
2.4.2 DC Shunt Coupled HRES . . . . .	54
2.4.3 Multi-input Coupled HRES . . . . .	55
2.4.4 Inverter Configurations for HRES . . . . .	56
2.4.5 Grid Coupled Inverter Controller . . . . .	64
2.4.6 Filter Topologies for HRES . . . . .	70
2.5 HRES Optimization . . . . .	72
2.6 Benefits and Challenges of HRES . . . . .	78
2.7 Future Trends of HRES . . . . .	80
2.8 Summary . . . . .	82
Chapter 3 Cost Optimization of Battery-Supercapacitor Hybrid Energy Storage for Hourly Dispatching Wind-Solar Hybrid Power System . . . . .	84
3.1 State-of-the-Art Review . . . . .	88
3.2 The Proposed Methodology . . . . .	91
3.2.1 WSHPS Framework . . . . .	91
3.2.2 Control of PVES . . . . .	92

3.2.3	Control of WES . . . . .	93
3.2.4	Modeling of ESS . . . . .	94
3.2.5	Determination of Dispatch Power Reference . . . . .	94
3.2.6	Control of HESS . . . . .	98
3.2.7	HESS Energy and Power Capacity . . . . .	100
3.2.8	DOD Optimization for HESS . . . . .	102
3.2.9	Cost Optimization for HESS . . . . .	103
3.2.10	Expected Lifetimes of the BESS and SESS . . . . .	104
3.2.11	Cost Calculation for HESS . . . . .	106
3.3	Simulation Results . . . . .	109
3.4	Summary . . . . .	123
Chapter 4	Cost, Reliability, and Power Converter Interface for Integrating PV into Utility with ESS . . . . .	124
4.1	Proposed Methodology . . . . .	129
4.1.1	System Structure for PV Farm . . . . .	129
4.1.2	Cost Optimization for HESS . . . . .	136
4.1.3	Techno-economic Optimization using HOMER Pro . . . . .	138
4.2	Isolated Multiport Power Converter Interface . . . . .	140
4.2.1	System Structure for PV Farm with TAB-NPC Converter . . . . .	140
4.2.2	TAB-NPC Converter Power Flow Control . . . . .	141
4.2.3	Decoupled TAB-NPC Topology Analysis . . . . .	143
4.2.4	BESS Power Controller . . . . .	144
4.2.5	TAB-NPC Converter Performance Analysis . . . . .	146
4.2.6	Multilevel Inverters . . . . .	147
4.3	Simulation Results . . . . .	149
4.3.1	Optimal Dispatch Scheduling . . . . .	149
4.3.2	ESS Cost Investigation using HOMER Pro . . . . .	155
4.3.3	TAB Power Converter Interface for the PV-BESS System . . . . .	159
4.4	Summary . . . . .	165
Chapter 5	Economic Dispatch Analysis of Wind Power Integration into Utility with Battery-Supercapacitor Hybrid Energy Storage System . . . . .	166
5.1	Proposed Methodology for WT Farm . . . . .	168
5.1.1	System Architecture of WES . . . . .	168
5.1.2	Wind Speed Forecasting . . . . .	168
5.1.3	Grid Reference Power Calculation . . . . .	171
5.1.4	Control and Sizing of HESS . . . . .	172
5.1.5	Cost Optimization for ESS . . . . .	173
5.1.6	Cost Calculation for ESS . . . . .	175
5.2	Simulation Results . . . . .	178
5.3	Comparative Study on ESS Cost . . . . .	186
5.4	Summary . . . . .	187



Chapter 6	Hardware-in-loop Experimental Verifications for Hourly Dispatching Wind-Solar Power with Battery Energy Storage . . . . .	189
6.1	RTDS-Based Testbed . . . . .	193
6.1.1	RTDS-Based Representative WSHPS Model . . . . .	193
6.1.2	PVES Model . . . . .	193
6.1.3	WES Model . . . . .	195
6.1.4	Battery Model . . . . .	196
6.1.5	BESS Controller . . . . .	197
6.2	Controller Hardware-in-the-loop for WSHPS . . . . .	198
6.3	Experimental Setup and Results . . . . .	202
6.4	Summary . . . . .	206
Chapter 7	Conclusions and Future Work . . . . .	207
	Bibliography . . . . .	211
	Vita . . . . .	229

## LIST OF TABLES

2.1	Recent HRES projects. . . . .	26
2.2	Battery and SC performance comparison. . . . .	35
2.3	Comparison of characteristics of various MPPT techniques. . . . .	50
2.4	Parameters of the Li-ion battery aging model. . . . .	52
2.5	Parameters of the SC aging model. . . . .	53
2.6	Types of power converter configurations implemented in wind-solar HRES. . . . .	58
2.7	Summarized advantages and disadvantages of classical topologies. . . . .	67
2.8	Optimization algorithms of “Wind+Solar” HRES. . . . .	74
2.9	Comparative comparison among the commonly used optimization techniques for HRES. . . . .	77
3.1	$P_{\text{Grid,ref}}$ calculation from adjusting $P_{\text{Grid,est}}$ with BESS SOC. . . . .	98
3.2	Battery and SC cost comparison . . . . .	109
3.3	Energy storage cost comparison at different LPF time constants . . . . .	115
4.1	ANN model specifications. . . . .	133
4.2	Summary of the PV system component specifications. . . . .	139
4.3	Semiconductor devices specifications . . . . .	147
4.4	ESS cost comparison at different DOD levels. . . . .	152
5.1	BESS and SESS cost information. . . . .	178
6.1	Coefficients for the WT model. . . . .	196

## LIST OF FIGURES

2.1	Renewable energy capacity and generation in the USA. . . . .	20
2.2	Annual PV and wind capacity additions in the USA. . . . .	21
2.3	Duck curve illustration: Load, solar, and wind profiles for California on March 29, 2013 in a scenario with 11% annual wind and 11% annual solar.	23
2.4	Global electricity generation by PV and WT. . . . .	24
2.5	PV and WT complementary profiles on a day-to-day basis. . . . .	24
2.6	PV and WT complementary profiles on a seasonal basis. . . . .	25
2.7	Classification of different types of HRES. . . . .	27
2.8	Hybrid PV-Wind-Battery system structure. . . . .	30
2.9	Hybrid PV-Wind-Diesel system structure. . . . .	30
2.10	DC-Bus connected HRES. . . . .	32
2.11	AC-Bus connected HRES. . . . .	32
2.12	Dual-Bus connected HRES (Type 1). . . . .	33
2.13	Dual-Bus connected HRES (Type 2). . . . .	34
2.14	Classification of the battery-supercapacitor HESS topologies. . . . .	36
2.15	Passive HESS topology. . . . .	37
2.16	Semi-active HESS topology. . . . .	38
2.17	Active HESS topology. . . . .	39
2.18	Power-Voltage characteristics of PV array at various temperatures. . . . .	41
2.19	Power-Voltage characteristics of PV array at various irradiance. . . . .	41
2.20	The $C_p$ - $\lambda$ characteristics of PMSG wind turbine. . . . .	45
2.21	WT power characteristics curve. . . . .	46
2.22	AC shunt coupled HRES. . . . .	54
2.23	DC shunt coupled HRES. . . . .	55
2.24	Non-isolated MIC coupled HRES. . . . .	57
2.25	Isolated MIC coupled HRES. . . . .	57
2.26	Semi-isolated MIC coupled HRES. . . . .	57
2.27	Grid-connected inverters. . . . .	61
2.28	Circuit topology of 3-level I-type NPC inverter. . . . .	63
2.29	Circuit topology of 3-level T-type NPC inverter. . . . .	64
2.30	Classic multilevel inverter topologies (with one phase shown). (a) Three level diode clamped. (b) Three level flying capacitor. (c) Five level cascade H-bridge. . . . .	65
2.31	The topology of a modular multilevel converter. . . . .	65
2.32	Multilevel inverter classification. . . . .	66
2.33	Control working principles: (a) Grid Following Inverter (Top), (b) Grid Forming Inverter (Bottom). . . . .	69
3.1	Structure of the wind-solar hybrid power system with HESS. . . . .	92
3.2	Block diagram of grid reference power calculation. . . . .	97
3.3	Linearization of step rules algorithm. . . . .	98

3.4	Output of the fuzzy inference. . . . .	99
3.5	HESS power control framework. . . . .	100
3.6	Rule-based algorithm for the BESS SOC control. . . . .	100
3.7	The relationship between DOD and cycle life. . . . .	103
3.8	PSO functional flowchart. . . . .	105
3.9	Dispatchable power reference case: Simulation results for one-hour dispatching for September 30 <sup>th</sup> , 2019. . . . .	110
3.10	Load following case: simulation results for one-hour dispatching for September 30 <sup>th</sup> , 2019. . . . .	111
3.11	One-hour simulation results considering all possible cases of the availability of sources. . . . .	111
3.12	Simulation results of the SOC with the battery and SC. . . . .	112
3.13	HESS cost comparison at different primary SOC control algorithms. . . . .	113
3.14	ESS cost (¢/kWh) at different DOD levels. . . . .	114
3.15	Simulation results using the optimization method. . . . .	115
3.16	Convergence rate of the PSO technique. . . . .	116
3.17	HESS cost (¢/kWh) at 62 s of the LPF time constants. . . . .	116
3.18	Annual HESS cost comparison at 62 s of the LPF time constants. . . . .	118
3.19	Cumulative probability density function of the BESS energy capacities. . . . .	118
3.20	Histogram of hourly dispatching error results. . . . .	119
3.21	Injected current into the grid. . . . .	120
3.22	Three-phase voltage waveforms of the grid. . . . .	120
3.23	Rainflow matrix histogram of the BESS. . . . .	121
3.24	Rainflow matrix histogram of the SESS. . . . .	121
3.25	Spectrogram of the BESS. . . . .	122
3.26	Spectrogram of the SESS. . . . .	122
3.27	Battery lifetime (in years) comparison. . . . .	123
4.1	Structure of the dispatching PV-ESS system. . . . .	130
4.2	Grid estimated power calculation on June 10, 2019. . . . .	131
4.3	Grid estimated power calculation on July 16, 2019. . . . .	132
4.4	Block diagram of the primary SOC controller with ANFIS. . . . .	134
4.5	ANFIS training data set as a function of ESS SOC. . . . .	134
4.6	ANFIS output for ESS (from 60% SOC to 100% SOC). . . . .	135
4.7	HESS power control framework for PV farm. . . . .	135
4.8	Modified secondary SOC control algorithm. . . . .	136
4.9	Hourly dispatching PV system with the TAB-NPC converter. . . . .	141
4.10	Voltage waveforms of the low voltage and high voltage side bridges. . . . .	143
4.11	(a) Equivalent circuit of decoupled TAB-NPC converter (b) Equivalent topology diagram of TAB-NPC converter with three vertexes and two edges. . . . .	144
4.12	BESS power flow controller in TAB framework. . . . .	145
4.13	Inverter controller block diagram. . . . .	148
4.14	Design flowchart of the LCL filter. . . . .	150
4.15	Simulation results with entire day dispatching horizon considered. . . . .	151

4.16	Simulation results with semi-hourly dispatching horizon considered. . . .	151
4.17	ESS cost (¢/kWh) at different DOD levels with a curve fitting approach. . . .	153
4.18	Entire day dispatching case: HESS cost as a function of DOD. . . . .	154
4.19	Semi-hourly dispatching case: HESS cost as a function of DOD. . . . .	154
4.20	Simulation results for 1-hour dispatching on July 16, 2019. . . . .	155
4.21	Solar irradiance forecasting result using ANN. . . . .	156
4.22	Simulation results of the ESS SOC on July 16, 2019. . . . .	157
4.23	Proposed primary SOC controller effectiveness on July 16, 2019. . . . .	157
4.24	Cost summary for the battery-only scheme. . . . .	158
4.25	Cost summary for the SC-only scheme. . . . .	158
4.26	Simulation results for 1-hour dispatching on June 30, 2019. . . . .	160
4.27	BESS charging-discharging zoomed view. . . . .	160
4.28	Power losses comparison at different PV irradiance levels. . . . .	161
4.29	Efficiency comparison at different PV irradiance levels. . . . .	162
4.30	Comparison of power losses between 3L-TNPCI and 3L-INPCI. . . . .	162
4.31	Power losses of 3L-TNPCI at different switching frequencies. . . . .	163
4.32	Power losses of 3L-INPCI at different switching frequencies. . . . .	164
4.33	Power losses breakdown in Phase-A leg of the 3L-TNPCI. . . . .	164
4.34	THD comparison of the inverters at different frequencies. . . . .	164
5.1	Hourly dispatching wind turbine framework. . . . .	169
5.2	HESS power control framework for WT farm. . . . .	172
5.3	Overall workflow of the proposed methodology. . . . .	179
5.4	WT farm 1-hour dispatching results on January 20, 2019. . . . .	180
5.5	Histogram error results on January 20, 2019. . . . .	180
5.6	The ESS SOC variation profile on January 20, 2019. . . . .	181
5.7	Proposed primary SOC controller effectiveness on January 20, 2019. . . .	181
5.8	BESS and SESS cost (¢/kWh) at different DOD levels with WT farm. . . .	182
5.9	Annual ESS cost (¢/kWh) comparison with WT farm. . . . .	183
5.10	HESS cost as a function of DOD utilization on January 20, 2019. . . . .	184
5.11	Battery service life (in years) comparison. . . . .	185
5.12	Hourly wind speed forecasting results using the ANN method. . . . .	185
6.1	Overview of the WSHPS framework. . . . .	194
6.2	Electrical equivalent circuit of Min/Rincon-Mora model. . . . .	196
6.3	BESS controller framework. . . . .	198
6.4	Typical CHIL setup. . . . .	199
6.5	Overall structure of the WSHPS with a CHIL setup. . . . .	201
6.6	RTDS Control-Hardware-in-Loop experimental setup. . . . .	203
6.7	Case 1: BESS discharging instance. . . . .	204
6.8	Case 2: BESS discharging instance. . . . .	204
6.9	Scenario 1: BESS charging mechanism. . . . .	205
6.10	Scenario 2: BESS charging mechanism. . . . .	206

## **Nomenclature**

<b>ANN</b>	Artificial Neural Network
<b>AI</b>	Artificial Intelligence
<b>ANFIS</b>	Adaptive Neuro-Fuzzy Inference System
<b>BESS</b>	Battery Energy Storage System
<b>CHIL</b>	Control hardware-in-the loop
<b>CHB</b>	Cascaded H-bridge
<b>CDF</b>	Cumulative Density Function
<b>CSI</b>	Current Source Inverter
<b>DAC</b>	Digital to Analog Converters
<b>DOD</b>	Depth of Discharge
<b>DSP</b>	Digital Signal Processor
<b>ESS</b>	Energy Storage System
<b>EIA</b>	Energy Information Administration
<b>ESC</b>	Extremum-seeking Control
<b>ESSs</b>	Energy Storage Systems
<b>EMT</b>	Electromagnetic Transient
<b>FC</b>	Flying Capacitor
<b>FIS</b>	Fuzzy Inference System

<b>GUI</b>	Graphical User Interface
<b>GTAO</b>	Gigabit Transceiver Analogue Output
<b>GTDI</b>	Gigabit Transceiver Digital Input
<b>GA</b>	Genetic Algorithm
<b>HIL</b>	Hardware-in-the-Loop
<b>HCS</b>	Hill Climb Search
<b>HESS</b>	Hybrid Energy Storage System
<b>HOMER Pro</b>	Hybrid Optimization of Multiple Energy Resources
<b>HRES</b>	Hybrid Renewable Energy System
<b>IEA</b>	International Energy Agency
<b>IncCond</b>	Incremental Conductance
<b>LCOE</b>	Levelized Cost of Energy
<b>LPF</b>	Low Pass Filter
<b>MPP</b>	Maximum Power Point
<b>MPPT</b>	Maximum Power Point Tracking
<b>MLI</b>	Multilevel Inverter
<b>MMC</b>	Modular Multilevel Converter
<b>MIC</b>	Multi-input Converter
<b>NPC</b>	Neutral Point Clamped

<b>NPCs</b>	Net Present Cost
<b>NREL</b>	National Renewable Energy Laboratory
<b>ORNL</b>	Oak Ridge National Laboratory
<b>OCV</b>	Open Circuit Voltage
<b>PV</b>	Photovoltaic
<b>PVES</b>	PV Energy System
<b>PHES</b>	Pumped Hydro Energy Storage
<b>PMSG</b>	Permanent Magnet Synchronous Generator
<b>PSC</b>	Partial Shading Conditions
<b>PSF</b>	Power-signal Feedback
<b>PSO</b>	Particle Swarm Optimization
<b>PWM</b>	Pulse Width Modulation
<b>PLL</b>	Phase Locked Loop
<b>PCC</b>	Point of Common Coupling
$P_{PVES}$	PV Output Power
<b>PI</b>	Proportional Integral
<b>PDF</b>	Probability Density Function
$P_{BESS,ref}$	BESS Reference Power
$P_{Grid,ref}$	Desired grid reference power



$P_{HESS,ref}$	HESS Reference Power
$P_{WSPHS}$	Hybrid WT-PV Output Power
$P_{Grid,est}$	Grid estimated power
$P_{SESS,ref}$	SESS Reference Power
$P_{WES}$	WT Output Power
<b>RE</b>	Renewable Energy
<b>RTDS</b>	Real Time Digital Simulator
<b>RMSE</b>	Root Mean Square Error
<b>SESS</b>	Supercapacitors Energy Storage System
<b>SC</b>	Supercapacitor
<b>SOC</b>	State of Charge
<b>SCC</b>	Short Circuit Current
<b>SiC</b>	Silicon Carbide
<b>THD</b>	Total Harmonic Distortion
<b>TAB</b>	Triple Active Bridge
<b>TSR</b>	Tip-speed Ratio Control
<b>TSO</b>	Transmission System Operator
<b>WIF</b>	Workstation Inter-Face
<b>WT</b>	Wind Turbine

**WSHPS**      Wind Solar Hybrid Power System

**WES**        Wind Energy System

## Chapter 1 Introduction

### 1.1 Background

The International Energy Agency (IEA) reported that the global average temperature is expected to increase by 2.8–4.5°C by 2100 compared to the temperature in 2013, if no countermeasures are taken to reduce the carbon emissions [1]. The present electrical grid represents the largest single source accounting for carbon emissions into the atmosphere. One response to reduce the carbon emissions for the electrical grid is to transform it to a low-carbon energy through increased integration of renewable energy sources. As a result, renewable energy (RE) resources have witnessed explosive growth globally over the past decade. For instance, California adopted a renewable portfolio standard of 33% by 2020, and it is expected to reach 50% by 2030 [1].

Renewable energy sources, particularly Photovoltaic (PV) and Wind Turbine (WT), have become attractive options for power generation globally, and the global penetration of the PV and WT energy in power systems have been increasing rapidly. From 2017 to 2018, the WT installed capacity has been increased from 540 GW to 591 GW, and the solar PV installed capacity has been increased from 405 GW to 505 GW [2]. As the output of the RE sources significantly depends on weather and meteorological conditions, i.e., clouds movement and wind speed, their output power possesses unstable characteristics. However, large penetration of such an intermittent RE sources into the utility grid are associated with serious technical challenges related to power quality, generation dispatch control and electric system reliability. Therefore, power generation using the PV or WT is often considered as non-dispatchable

without sufficient energy storage. It is even claimed that the PV or WT power will never be suited to contribute substantially toward utility-scale supply or provide base-load power [3].

Generally, energy production by the Wind-PV resources compensate each other on a seasonal or day-to-day basis. Thus, the hybrid utilization of the PV and WT deserves more attention because they have the advantages of complementary power profiles. Hybridization techniques can be used to solve the variable nature of solar and wind power. The wind solar hybrid power system (WSHPS) incorporates the WT and PV subsystems together to provide increased system efficiency, lower capacity of energy storage, and improved stability in power supply [4]. The WSHPS has the ability to suppress the rapid change of a single RE source, which is more advantageous than using a single wind or PV system. Also, the WSHPS helps to reduce the infrastructure costs especially for rural electrification projects through facilitating the point of generation and consumption being close to each other. Therefore, the WSHPS projects at a single location are emerging as a major trend in the global transition to renewable energy.

The uncertainty of RE resources can also be diminished by incorporating energy storage system (ESS) in the WSHPS architecture. Battery energy storage system (BESS) is most frequently utilized to solve such an issue among the several types of the ESS that are available in the market. However, when the WSHPS output is highly fluctuating, it is very difficult for the BESS to recover from drastic power ramps without its significant lifetime degradation. Consequently, the downtime cost associated with the BESS poses a severe challenge for market acceptance. A hybrid energy storage system (HESS) consisting of a BESS and a supercapacitors energy storage system (SESS) can be leveraged to develop a more economical ESS. The

HESS utilizes the high power density property of the supercapacitor (SC) (i.e., the capability of rapidly charging or discharging energy at lower energy levels) and the high energy density property of the battery (i.e., the capability of slowly charging or discharging energy at higher energy levels) [5]. In such a HESS scheme, the SC helps to mitigate the high-frequency power components passing through the battery that is beneficial for extending the battery's lifetime.

There are several challenges existing for the high penetration of intermittent RE into the utility, such as voltage and frequency regulation, mismatch between generated power and load demand, grid operation economics, and scheduling of generation units. For instance, the utility paid an additional 28.6% of price to the distributed generation operator for every kWh of smoothed energy delivered to the grid [6]. Hence, grid operators need to take additional actions to maintain system stability. For example, fossil-fueled generators must be turned on and off or adjust their outputs more periodically to accommodate the power variations due to the presence of additional solar and wind power into the grid. This type of cycling of fossil-fueled generators is responsible for increasing its wear and tear costs and decreasing its efficiency as well. The high penetrations of RE power lead to cycling costs of \$0.47/MWh to \$1.28/MWh per fossil-fueled generator, which was reported in [7]. Therefore, a constant power dispatch commitment at an acceptable interval is demanded from the RE framework to overcome the aforementioned economic challenges.

## 1.2 Research Objectives and Contributions

### Research Objectives

The main objective of this dissertation is to enhance the integration of RE that secures a desired dispatching of the RE power at specified horizon interval for an entire day to the power grid. It is important to mention that a dispatching scheme is developed in this dissertation rather than the traditional peak shaving or smoothing approach to provide the RE output power to the grid. The dispatching scheme enables the RE to be a reliable source of power for the utility, which can be regulated like any other conventional generator. Furthermore, the RE output power supplied to the grid using a dispatched scheme provides considerable flexibility to the utility, especially in the scheduling of generation units, grid operation economics, and grid ancillary services.

The WSHPS architecture is proposed here that consists of a wind energy system (WES) and a PV energy system (PVES). The WSHPS incorporates the PV and WT subsystems together to provide increased systematic efficiency, lower required capacity of energy storage, and improved stability in power supply. Since the BESS has a high energy density property and the SESS has a high power density property, the HESS is utilized to leverage the performance merits of the two energy storage apparatus. The HESS consisting of a battery and a SC can be employed to develop a cost-effective ESS, where the SC facilitates to alleviate the fast-changing power components passing through the battery, which is beneficial for increasing the battery's service life. The impact of the SC on battery longevity is also investigated to make the system more practical.

The output of the WSHPS mainly depends on the wind speed and solar insolation. Generators in the utility grid are typically scheduled several hours or days in advance.

In order to treat the WSHPS farm as a schedulable resource, it is necessary to predict the WSHPS power in advance and inform the grid operators of its power level. Here, a multilayer perceptron Artificial Neural Network (ANN) is used to predict the wind speed and solar insolation one hour ahead of time so that the grid operators can be informed beforehand about the WSHPS power level, which will provide more flexibility to the grid operators' scheduling of their generation units.

The cost optimization of the ESS is one of the important catalysts for the rapid growth of global RE generation. In this study, the low pass filter (LPF) is employed to assign the power reference for the BESS and SESS. Since SC is more expensive than a battery, a proper value of the filter time constant is needed to minimize the total expenditure (\$/kWh) of the HESS. Here, the particle swarm optimization (PSO) technique is deployed for determining the optimum LPF time constant. This research also presents an economic comparison to investigate the significance of using different types of ESS for dispatching the WSHPS power. Furthermore, based on the usage of state of charge (SOC), there is a trade-off between the service life and the minimum capacity required of the ESS. In this research, the optimum value of depth of discharge (DOD) has been investigated which exhibits the best competitive ESS cost for dispatching the RE power to the utility grid. In addition, after seeking the optimal value of DOD for the ESS, one secondary SOC control algorithm is also employed to regulate the ESS SOC in the optimal range.

Besides, several control algorithms based on the ESS SOC are developed to achieve accurate estimation of the grid reference power ( $P_{\text{Grid,ref}}$ ) for each dispatching period. The SOC control algorithms also ensure the ESS to complete each dispatching period with the same SOC as it started. This mechanism plays a significant role in regulating the battery SOC within a specified range which helps to minimize the energy storage

cost and ensures that the ESS has enough capacity available for next-day operation. An economic comparison is presented to investigate the impact of using different types of SOC control algorithms in the  $P_{\text{Grid,ref}}$  estimation.

The optimal scheduling for dispatchable utility-scale RE power with the HESS is also explored in this dissertation. The optimal capacity of the ESS is assessed based on its usage of DOD, which is critical for minimizing the cost of a dispatchable RE power scheme. The hybrid system can successfully dispatch the scheduled power at any dispatching horizon by leveraging the optimal ESS capacity. Both cycling and calendar expenses are taken into account during the cost optimization of the ESS to make it more practical. Here, the proposed ESS control framework is responsible for tracking the grid reference power for each intended dispatching period by supplying or absorbing the required power. The proposed ESS control algorithm is also verified employing control hardware-in-the loop (CHIL) testing in the real time digital simulator (RTDS) platform in the laboratory.

Multiport active bridge converter has attracted increasing attention due to its salient advantages, such as multiple power interface ports, high-power density, galvanic isolation, bidirectional power flow capability, and soft-switching capability. In this study, two three-level neutral point clamped (NPC) switching poles are used in the high-voltage side of the developed multiport converter configuration. Thus, a five-level line voltage waveform in the high-voltage bridge is produced, which leads to semiconductor switches being exposed to only half of the DC bus voltage, resulting in lower stress of  $dv/dt$  and ameliorating converter efficiency.

Multilevel inverters are employed in this work due to their superior attributes: high DC bus voltage withstanding capability, high efficiency, low total harmonic distortion (THD), and reduced common mode voltage. This research presents a



comparative power loss analysis between the multilevel I-type NPC and the T-type NPC inverter for dispatching the RE power at 1-hour increments for an entire day for a grid-connected RE system. This study also deals with the optimized design procedure of an LCL filter for a grid-connected RE system. Compared with other passive filters, the LCL filter has a better attenuation capacity for high-order harmonics and better dynamic characteristics. The switching of the power conversion devices causes high-frequency harmonics, which are one of the main factors causing problems to sensitive equipment or the connected loads. Therefore, the THD is an essential consideration in the system design phase. Here, an LCL filter is designed to satisfy the harmonic standard regulations stated in IEEE-1547.

### **Original Contributions**

The major contributions of the dissertation are summarized as follows:

- Conducting a comprehensive review of wind-solar HRES from the perspectives of power architectures, mathematical modeling, power electronic converter topologies, and design optimization algorithms.
- Developing a dispatching scheme to provide a pre-determined constant RE power to the utility grid from the intermittent RE framework. The proposed dispatching technique enables the RE architecture to be a reliable source of power for the utility that can be regulated in the same way as any other traditional generator, while also providing greater flexibility, particularly in grid operating economics, generation unit scheduling, and grid ancillary services.
- Predicting the wind speed and solar insolation one-hour ahead of time by using a relatively small set of historical hourly wind speed and solar insolation data as

well as a smaller number of input parameters for training the ANN model, which also significantly reduces the model complexity and computational burden.

- Proposing a primary state of charge controller as a function of both battery and supercapacitor SOC in the HESS framework to adjust the grid estimated power ( $P_{\text{Grid,est}}$ ) at the start of each dispatching period, which aids in achieving the desired  $P_{\text{Grid,ref}}$  for each dispatching period. This controller would also make sure that the energy storage system finishes each dispatching period with the same SOC it started with.
- Implementing the particle swarm optimization approach to seek the optimum value of the low-pass filter time constant that yields the most cost-effective HESS for hourly dispatching the RE power scheme.
- Optimizing the ESS life-cycle cost by employing the advanced optimization technique to determine the optimal depth of discharge usage. In addition, after seeking the optimal value of depth of discharge for the energy storage system, one secondary state of charge control algorithm is also employed to regulate the ESS state of charge in the optimal range.
- Investigating the annual ESS life-cycle cost, including the actual wind speed and solar insolation data of four different days, representing each season.
- Presenting a cost comparison analysis to assess the impact of dispatching horizon selection on ESS cost estimation. The optimal scheduling for dispatchable RE power is determined by the ESS depth of discharge utilization levels, which is critical for minimizing the cost of a dispatchable scheme.

- Developing an isolated multiport converter for interfacing the RE framework to the utility and present a comparative power loss analysis between the conventional triple active bridge (TAB) converter and the developed TAB-NPC converter for dispatching the RE power scheme.
- Verifying the proposed ESS control algorithm, employing control hardware-in-loop testing in the real time digital simulator platform.

### 1.3 Dissertation Outline

Following the Chapter 1 on the research background introduction, Chapter 2 presents the state of the art on Wind-Solar Hybrid Renewable Energy Systems. The objective of this chapter is to conduct a comprehensive review of wind-solar HRES from the perspectives of power architectures, mathematical modeling, power electronic converter topologies, and design optimization algorithms. Since the uncertainty of HRES can be reduced further by including the ESS, this study presents several HESS coupling technologies, highlighting their major advantages and disadvantages. Various HRES power converters and control strategies from the state-of-the-art have been discussed. Different types of energy source combinations, modeling, power converter architectures, sizing, and optimization techniques used in the existing HRES are reviewed, which intends to serve as a comprehensive reference for researchers, engineers, and policymakers in this field. This chapter also discusses the technical challenges associated with HRES as well as the scope of future advances and research on HRES.

Chapter 3 discusses on “Cost Optimization of Battery-Supercapacitor Hybrid Energy Storage for Hourly Dispatching Wind-Solar Hybrid Power System”. This chapter demonstrates a dispatching scheme of WSHPS for a one-hour dispatching period for

an entire day utilizing battery and supercapacitor hybrid energy storage subsystem. A frequency management approach is deployed to extend the longevity of the batteries through extensively utilizing the high energy density property of batteries and the high power density property of supercapacitors in the HESS framework. A LPF is employed to decouple the power between a battery and a supercapacitor. The cost optimization of the HESS is computed based on the time constant of the LPF through extensive simulations in MATLAB/SIMULINK platform. The curve fitting and PSO approaches are applied to seek the optimum value of the LPF time constant. Several control algorithms as a function of the battery SOC are developed to achieve accurate estimation of the grid reference power for each one-hour dispatching period. This estimation helps to minimize the ESS cost, in addition to ensuring that the ESS has sufficient capacity for next-day operation. The optimum value of DOD for HESS considering both cycling and calendar expenses has also been investigated for the best competitive ESS cost for hourly dispatching the power of the WSHPS. This chapter also presents an economic comparison to investigate the significance of using different types of ESS for hourly dispatching the WSHPS. The simulation results show that the presented HESS is superior to battery or SC-only operation.

Chapter 4 discusses on “Cost and Reliability for Interfacing PV to Utility with ESS”. The optimal scheduling for dispatchable utility-scale solar PV power with a HESS consisting of a battery and a SC is explored in this chapter. The optimal capacity of the ESS is assessed based on its usage of DOD, which is critical for minimizing the cost of a dispatchable PV power scheme. The hybrid system can successfully dispatch the scheduled power at any dispatching horizon by leveraging the optimal ESS capacity. Both cycling and calendar expenses are taken into account during the cost optimization of the ESS to make it more practical. A multilayer perceptron

ANN is utilized to predict PV irradiance one hour ahead of time, which performs well with good convergence mapping between input and target output data. Moreover, this chapter proposes a SOC control algorithm based on an adaptive neuro-fuzzy inference system (ANFIS) that can accurately estimate the grid reference power for each one-hour dispatching period, which is necessary for ensuring the ESS completes each dispatching period with its starting SOC and has sufficient capacity for next-day operation. Finally, an economic comparison is presented utilizing the Hybrid Optimization of Multiple Energy Resources (HOMER Pro) software to develop a cost-effective ESS for an hourly PV power dispatching scenario.

Chapter 4 also investigates a dispatching scheme of megawatt-scale solar PV power for a one-hour dispatching period for an entire day utilizing an isolated multiport converter configuration with battery energy storage system. A multilevel TAB DC-DC converter has been developed where a neutral-point-clamped H-bridge is employed in the high-voltage side, and the conventional two-level full-bridge is configured in the low-voltage side across the high-frequency transformer. The power losses between the developed TAB-NPC converter and conventional TAB converter are compared to identify the superior multiport converter topology for this application. The converter loss analysis is conducted using the parameter values of the switching devices in the MATLAB/SIMULINK environment, and the developed TAB-NPC converter is found to exhibit better performance than the conventional TAB for megawatt-scale grid-connected PV arrays.

Also, multilevel inverters, T-type and I-type neutral point clamped inverters, are investigated due to their superior attributes: high efficiency, low THD, and reduced common-mode voltage. The power losses between the three-level T-type and I-type NPC inverters are compared, to identify the superior grid inverter topology for this

application. The inverter loss analysis is conducted in the MATLAB/SIMULINK environment, and the T-type NPC inverter was found to exhibit better performance than the I-type NPC inverter for megawatt-scale grid connected PV arrays. Furthermore, an LCL filter has been designed for higher efficiency and better harmonic attenuation to interface the inverter with the utility grid.

Chapter 5 discusses on “Economic Dispatch Analysis of Wind Power Integration into Utility with Battery-Supercapacitor Hybrid Energy Storage System”. This chapter demonstrates an effective dispatching scheme of utility-scale wind power at one-hour increments for an entire day with a HESS consisting of a battery and a SC. Accurate forecasting of wind power is crucial for generation scheduling and economic operation. Here, wind speed is predicted by one hour ahead of time using a multilayer perceptron ANN, which exhibits satisfactory performance with good convergence mapping between input and target output data. Furthermore, the ANFIS is employed to devise a SOC controller to accurately estimate the  $P_{\text{Grid,ref}}$  for each one-hour dispatching period. This type of desired  $P_{\text{Grid,ref}}$  estimation is critical to ensure the ESS completes each dispatching period with its starting SOC and has adequate capacity available for next-day operation. Also, the PSO technique is implemented to optimize the life cycle cost of the ESS based on its DOD usage, which is vital for minimizing the cost of a dispatchable wind power scheme. The actual wind speed data of four different days as a representative of each season recorded at Oak Ridge National Laboratory (ORNL) are utilized in the simulations to provide a realistic economic assessment for dispatching the wind power.

Chapter 6 discusses on “Hardware-in-loop Experimental Verifications for Hourly Dispatching Wind-Solar Power with Battery Energy Storage”. The hardware in the loop (HIL) technique allows to reproduce the behavior of a dynamic system in real

time. This quality makes HIL a useful tool in the controller validation process and is widely used in multiple areas. This chapter presents a CHIL based test system for testing the proposed ESS controller for dispatching the WSHPS power. With the CHIL, the actual controller used in the real hardware system can be tested for its operation with a simulation based WSHPS. The CHIL has been used to validate the proposed ESS controller performance under various conditions of the ESS charging-discharging for maintaining the desired  $P_{\text{Grid,ref}}$ . For the CHIL, the WSHPS farm is modeled in the RTDS and the ESS controller is designed in the digital signal processor (DSP). Here, the power converter coupled to the ESS is controlled by the DSP, which is connected between the gigabit transceiver analogue output (GTAO) card and the gigabit transceiver digital input (GTDI) card in the RTDS interface boards.

Finally, conclusions and future work are provided in Chapter 7.

#### 1.4 Related Publications

The main elements of this dissertation have been peer-reviewed and published in the following journal papers:

- **P. Roy**, Y. Liao, and J. He, “Economic Dispatch for Grid-Connected Wind Power with Battery-Supercapacitor Hybrid Energy Storage System,” in *IEEE Transactions on Industry Applications*, pp. 1-11, 2022.
- **P. Roy**, J. He, T. Zhao, and Y. V. Singh, “Recent Advances of Wind-Solar Hybrid Renewable Energy Systems for Electrical Power Generation,” *IEEE Open Journal of the Industrial Electronics Society*, vol. 3, pp. 81-104, 2022.
- **P. Roy**, J. He and Y. Liao, “Cost Minimization of Battery-Supercapacitor Hybrid Energy Storage for Hourly Dispatching Wind-Solar Hybrid Power System,”

in *IEEE Access*, vol. 8, pp. 210099-210115, 2020.

Additional peer-reviewed papers have been published in multiple conference proceedings and are also listed as follows:

- **P. Roy**, Y. Liao, and J. He, “Energy Storage for Hourly Dispatching Utility-Scale Solar PV Power using HOMER Pro - A Cost Investigation,” 2022 *IEEE Energy Conversion Congress & Expo (ECCE)*, MI, USA, Oct. 2022.
- **P. Roy**, J. He, and Y. Liao “Optimal Scheduling for Dispatchable Utility-Scale Solar PV Power with Battery-Supercapacitor Hybrid Energy Storage System,” 2022 IEEE Power & Energy Society General Meeting, CO, USA, 2022.
- **P. Roy**, J. He and A. Cramer, “Three-Port Multilevel Converter for Hourly Dispatching Solar PV Power with Battery Energy Storage System,” *IEEE Energy Conversion Congress & Expo (ECCE) 2021*, Vancouver, Canada, Oct. 2021.
- **P. Roy**, and J. He, “Hourly Dispatching Utility-Scale Solar PV Power with Megawatt Multilevel Grid Inverter,” *2<sup>nd</sup> Annual Conference of the IEEE Kansas Power and Energy Conference (KPEC)*, Manhattan, KS, April 2021.
- **P. Roy**, J. He and Y. Liao, “Cost Optimization of Battery and Supercapacitor Hybrid Energy Storage System for Dispatching Solar PV Power,” *IEEE Energy Conversion Congress & Expo (ECCE) 2020*, Detroit, MI, Oct. 2020.



## Chapter 2 State of the Art on Wind-Solar Hybrid Renewable Energy Systems

An urgent need for alternative sources of energy becomes imminent due to the rapid depletion of fossil fuels, which have been extensively utilized to meet the load demand nowadays. The usage of fossil fuel is also responsible for global warming phenomena [8]. RE sources are the best candidate to provide green energy to overcome this global energy issue. Therefore, it is anticipated that the RE sources will play a pivotal role in the future power supply [9]. For instance, from 2017 to 2018, the cumulative global capacity of renewable electricity increased from 2,181 GW to 2,355 GW. In 2018, renewable electricity was 20.5% of cumulative electricity capacity and provided 17.6% of the total annual generation in the United States [10]. The United States' renewables capacity and generation from 2009 to 2018 are illustrated in Fig. 2.1 (Data obtained from [10]).

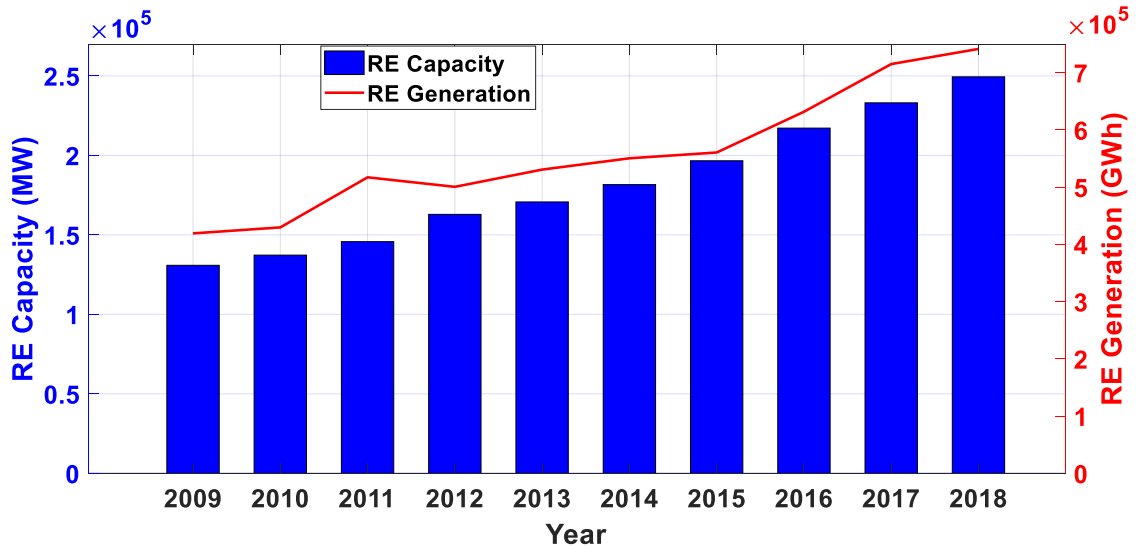


Figure 2.1: Renewable energy capacity and generation in the USA.

As reported in [11], RE was the only energy source which saw increased demand in 2020 despite the pandemic, while all other fuel consumption declined. Annual renewable capacity additions increased by 45 percent in 2020 to nearly 280 GW, the highest year-on-year increase since 1999. Specifically, solar PV capacity additions are predicted to reach 162 GW by 2022, representing a nearly 50% increase from the pre-pandemic level of 2019. In addition, global wind capacity additions grew by more than 90% in 2020 to 114 GW, a 50% increase from the 2017-2019 average [11]. The annual PV and wind capacity additions by the U.S. are also illustrated in Fig. 2.2 (Data obtained from [11]). The U.S. have also provided \$280 million in funding for solar power integration and research, and \$110 million in funding for wind power integration in the fiscal year 2021 budget [12].

According to the U.S. Energy Information Administration (EIA), about 39.7 GW of new electricity generating capacity will come online in 2021, with PV accounting for 39% of the new capacity and wind accounting for 31%. In 2021, 15.4 GW of utility-scale PV capacity is expected to be added to the grid, with four states accounting

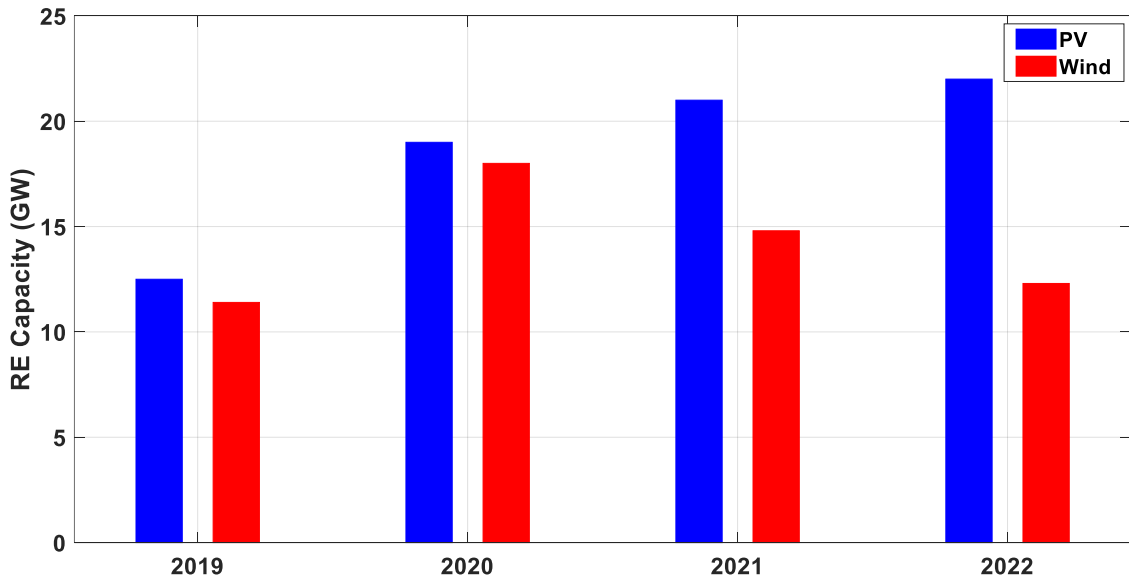


Figure 2.2: Annual PV and wind capacity additions in the USA.

for more than half of the new utility-scale solar capacity: Texas (28%), Nevada (9%), California (9%), and North Carolina (7%). Furthermore, it is anticipated that approximately 12.2 GW of utility-scale wind capacity is scheduled to come online in 2021, with Texas and Oklahoma states accounting for more than half of the 2021 wind capacity additions, including the 999-MW Traverse wind farm in Oklahoma, which is the largest wind project [13].

It is known that the output of the most RE sources such as PV and WT substantially depends on ambient environmental conditions. Subsequently, they are producing unstable output characteristics, which is the fundamental disadvantage of RE generations [14]. Thus, various power converters and control strategies are developed for controlling and monitoring active and reactive power, which encounters challenges due to the intermittent nature of RE sources. This kind of power fluctuation poses severe problems for power grid companies such as power quality, load leveling, generation dispatch control, and electric system reliability [3]. The duck curve shown in Fig. 2.3 can be used to illustrate the considerable challenge of accommodating solar and wind energy, and the potential for overgeneration and curtailment. Fig. 2.3, modified from [15], illustrates a graph of the total system load of the state of California, the wind and solar PV power feed-in, and the residual load on March 29, 2013. The scenario was considered here with the potential to meet 11% of the annual demand from wind and 11% of the annual demand from solar.

The hybrid utilization of the PV and WT are one of the most promising technologies among RE sources for satisfying the load demand because they have complementary energy generation profiles. Specifically, hybrid renewable energy systems (two or more generation units combined together) can be used to solve such power intermittent issue and enhance power system reliability [16]. Consequently, the pen-

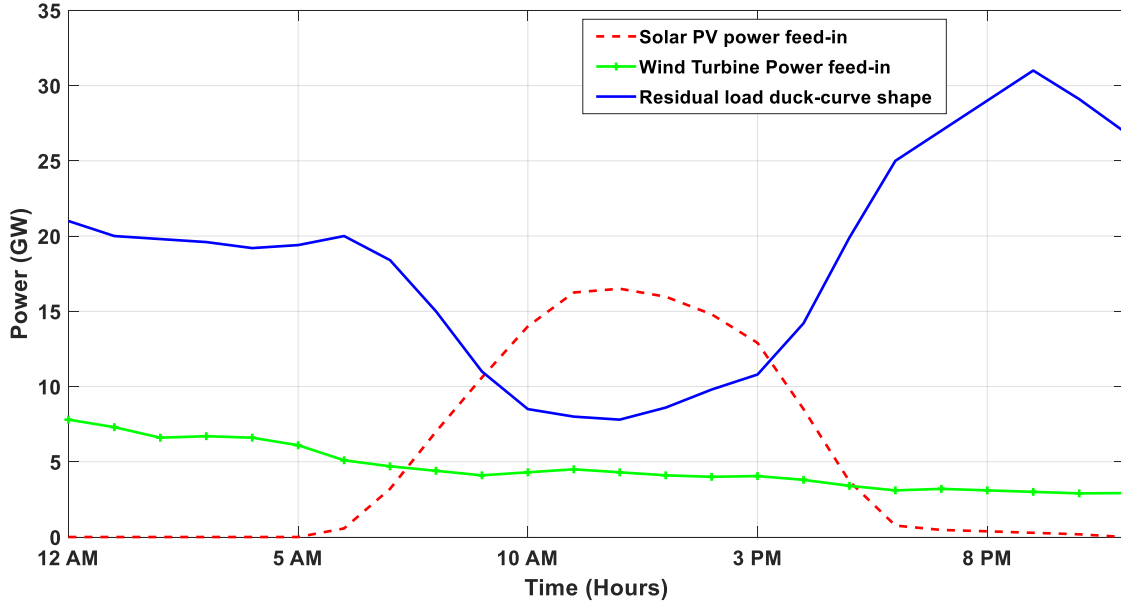


Figure 2.3: Duck curve illustration: Load, solar, and wind profiles for California on March 29, 2013 in a scenario with 11% annual wind and 11% annual solar.

etration of PV and WT energy in power systems has been continuously increasing globally, as is demonstrated in Fig. 2.4 [10]. Due to the weather and climate patterns, the energy production by Wind-PV resources offset each other on a seasonal or day-to-day basis. For instance, Fig. 2.5 shows the PV and WT complementary profiles on a day-to-day basis based on actual meteorological data recorded at the National Renewable Energy Laboratory (NREL) on June 10, 2020 [17]. Moreover, the monthly average solar irradiance and wind speed of the U.S. state of Colorado in 2019 are illustrated in Fig. 2.6 [17]. Note that MATLAB Tools “Basic Fitting” is utilized to increase the resolution of the data in Fig. 2.5 and Fig. 2.6.

The wind-solar hybrid renewable energy system (HRES) has the ability to suppress the change of single source output power to some extent. In addition, a properly designed hybrid wind-solar system shows satisfactory performance in handling transients compared to a single wind or PV generation for both grid-connected and stand-alone systems [18]. Moreover, the aim is to acquire more stable power output

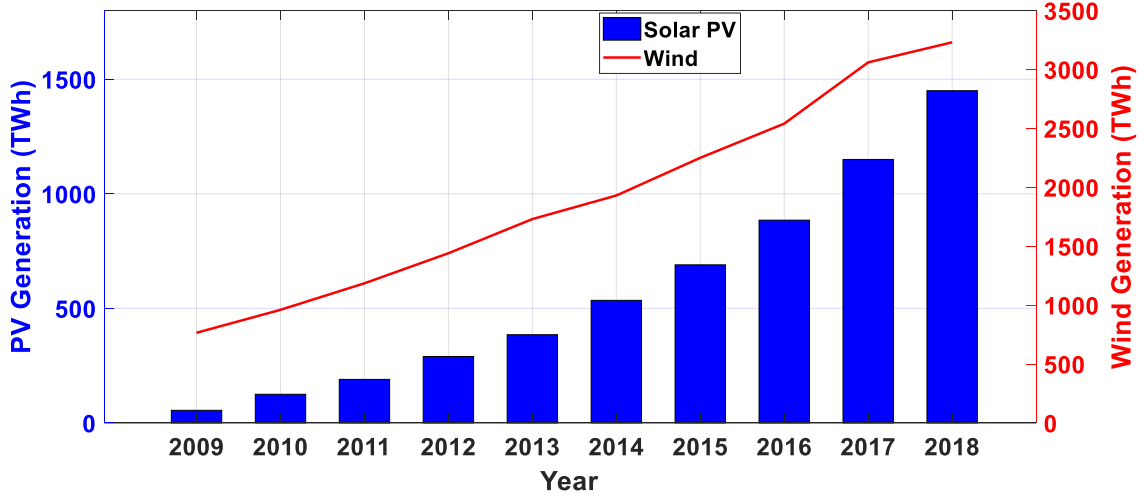


Figure 2.4: Global electricity generation by PV and WT.

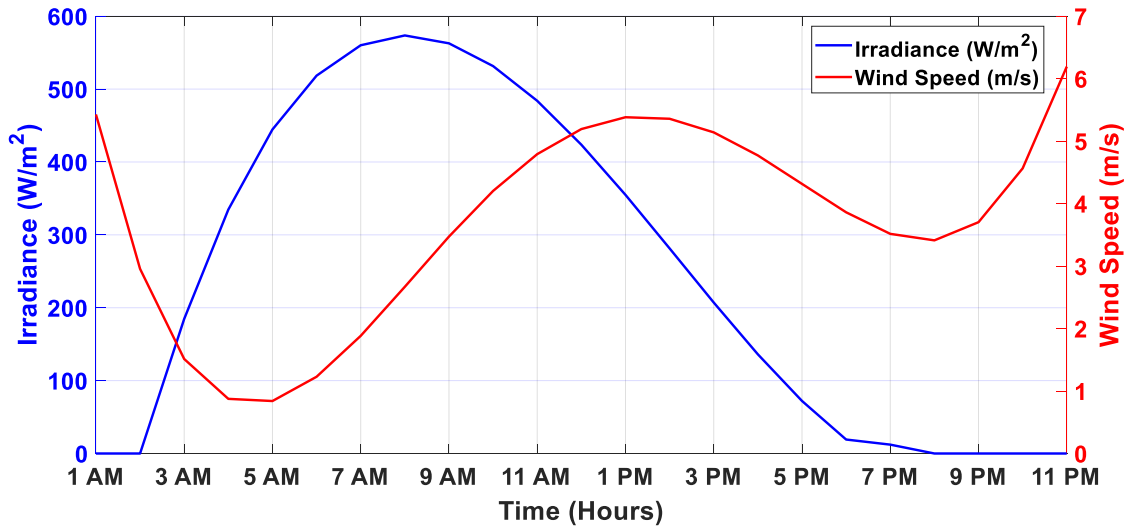


Figure 2.5: PV and WT complementary profiles on a day-to-day basis.

from RE sources, which can be connected with diesel generators, battery banks, ultra-capacitors, or hydrogen production systems. Pumped hydro energy storage (PHES) systems are also employed as a ESS, particularly for large-scale HRES deployment. As the PHES primarily depends on the site specifications, i.e., the height difference, source of water, and the type of land, there is no fixed initial cost or running cost for a PHES, which aids in minimizing the ESS expenditure in the HRES framework [19]. Undoubtedly, the HRES has the ability to improve the reliability and utilization fac-

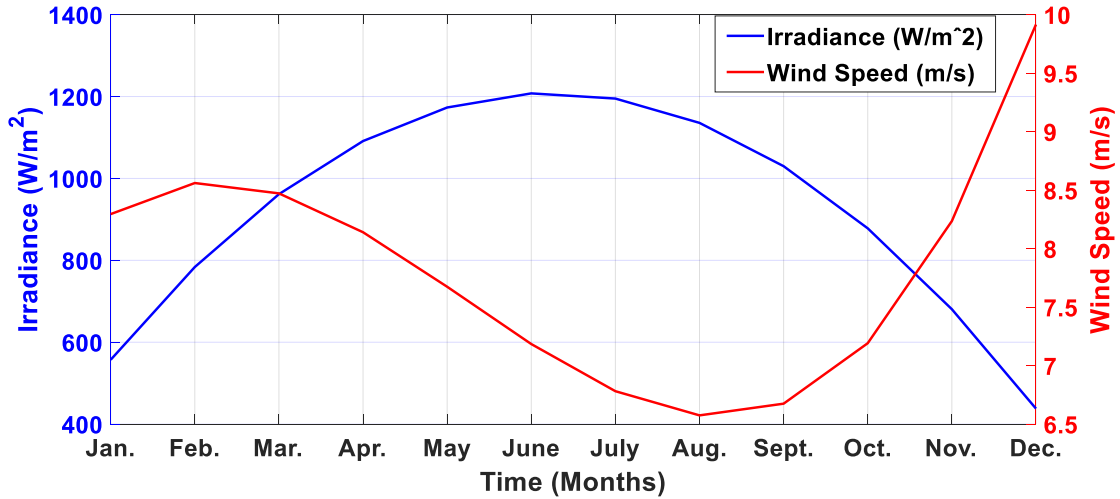


Figure 2.6: PV and WT complementary profiles on a seasonal basis.

tor of the system. Therefore, the HRES projects at a single location are emerging as a major trend in the global transition to renewable energy. Examples of some practical HRES projects are documented in Table 2.1 [20], [21], [22].

The objective of this chapter is to present a state-of-the-art review that concentrates on analyzing significant research issues about the HRES. The main contribution of this chapter can be summarized as follows:

- Different possible combinations and coupling technologies of the HRES have been documented.
- Mathematical modeling of the HRES and characteristics of different energy storage elements have been reported.
- Contemporary power converter configurations for the HRES have been explained.
- Summary of different types of optimization algorithms including the optimization constraints utilized in the HRES has been presented.

Table 2.1: Recent HRES projects.

Projects	Specifications	Location
Solar after Sunset	65 MW PV plus 50 MW battery	USA
Solar-storage solicitation	100 MW PV and 100 MW storage	USA
Wheatridge	300 MW of WT, 50 MW of PV and 30 MW of 4-hour duration battery storage	USA
GE Renewables'	2.3 MW WT with 500 kW of PV	USA
NextEra	250 MW WT, 250 MW PV and 200 MW Energy storage	USA
GE Renewables'	1.6 kW WT with 223 kW of PV	India
Le Plana	850 kW WT with 245 kW of PV	Spain
Enel's	497 MW High Lonesome WT project and 450 MW Roadrunner PV project	USA
Fjord	18.9 MW of solar capacity as part of its overall 44.1 MW	Denmark
Vestas	3.3 MW WT and PV hybrid demonstration project	Spain
Flinders Shire	43.2 MW of Vestas WT, 15 MW of PV and 2 MW, 4 MWh lithium-ion battery	Australia

The remainder of this chapter is structured as follows: the power architectures of the HRES are presented in Section 2.1. The characteristics of different energy storage elements is documented in Section 2.2. The mathematical modeling of the HRES is elaborated in Section 2.3. The power converter topologies utilized in the HRES are covered in Section 2.4. Commonly used algorithms in the literature for optimizing the HRES are analyzed and summarized in Section 2.5. The benefits and technical challenges associated with HRES and the scope of future advances and research on HRES are documented in Section 2.6 and Section 2.7, respectively. Finally, the summary of this review is drawn in Section 2.8.

## 2.1 System Structures of HRES

### 2.1.1 Hybrid Renewable Energy Sources

Hybridization techniques can be used to increase the efficiency and reliability of RE sources [4]. Fig. 2.7 shows different possible combinations of the HRES.

#### Hybrid Wind-Solar Energy System

The hybrid wind-solar energy system incorporates wind and solar energy technologies to produce electrical energy. Due to the complementary profile of wind and solar energy, the hybrid system offers several advantages over the solar or wind energy technology operates alone. It is also noticeable that the peak operating time for wind and solar systems occurs at different times of the day and the year. Therefore, the hybrid wind-solar energy system has the capability to produce more power than the wind or solar energy system operates individually [23].

#### Hybrid Wind-Solar-Diesel energy system

The hybrid wind-solar-diesel energy system is an attractive option, especially when a system is not directly connected to electrical distribution or power grid. The diesel generating system, which is powered with non-conventional fuels, is employed as a backup electricity supply source. Basically, a diesel generating system is deployed to ensure the continuity of the electricity supply in the HRES scheme. By adding

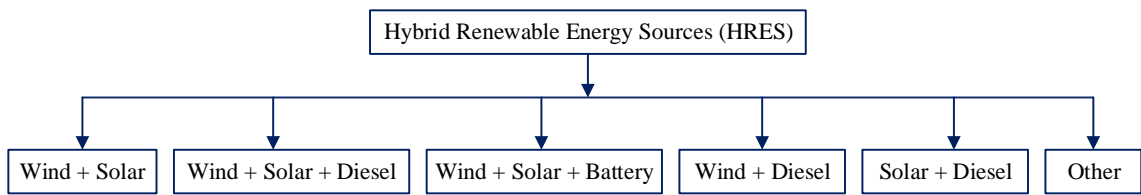


Figure 2.7: Classification of different types of HRES.



an engine generator in the HRES framework, the system becomes more complicated. However, modern controllers have the capability to operate these systems automatically. Moreover, the engine generator helps to reduce the size of the power electronic converter needed for the system [24].

### **Hybrid Wind-Solar-Battery energy system**

There are several disadvantages, i.e., expensive, bulky, non-environmentally friendly, incorporating a diesel engine in the HRES framework. A battery energy system can be utilized instead of using a diesel generator as a backup emergency option. When the power generated by the renewables is higher than the energy demand, the excess energy can be stored in the battery. Subsequently, it helps to reduce the hybrid system expenditure.

### **Hybrid Wind-Diesel energy system**

The hybrid wind-diesel energy system is an exciting alternative to meet the load demand, especially for remote locations. When the wind conditions are satisfactory, a wind-diesel hybrid system can provide enough electricity for such places. The amount of wind power is the deciding factor for designing the hybrid wind-diesel energy system. When the wind power production is always less than the load, other power plants constantly remain in line to control grid frequency and voltage.

### **Hybrid Solar-Diesel energy system**

Since the PV system hardly has any marginal cost, it is treated with priority on the grid. In this scheme, the diesel generating set is responsible for continuously fill the gap between the load and the actual power generated by the solar energy system. As

the generation capacity of diesel generators is limited to a specific range and the solar energy is fluctuating, it is always advisable to include the battery storage to optimize solar energy contribution to the generation of the hybrid system.

### **Other hybrid energy systems**

There are several determining factors, i.e, the cost of hybrid technology, and the availability of natural resources, which the operator needs to consider while designing a hybrid energy system. It is also possible to combine different types of systems and to work as a hybrid system. Wind-hydropower system, solar-hydropower system, solar-wind-geothermal system are some examples of this type of hybrid energy systems [25].

#### **2.1.2 System Architectures of HRES**

A hybrid wind-solar-battery energy storage system is a combination of a wind turbine, a photovoltaic array, and a battery energy storage system. A typical hybrid wind-solar-battery storage system scheme is shown in Fig. 2.8. Here, the WT, PV arrays, and battery energy storage are connected to a common DC bus through appropriate power converters for the purpose of power conditioning. Another typical hybrid wind-PV-diesel-battery storage system scheme is shown in Fig. 2.9. According to this scheme, the WT and PV array are charging the battery while supplying power to the load when the renewable energy is abundant. The purpose of using a dump load is to prevent overcharging of the battery. The controller is responsible for starting the diesel generator, which supplies the load when SOC of the battery hits the lower limit [26].

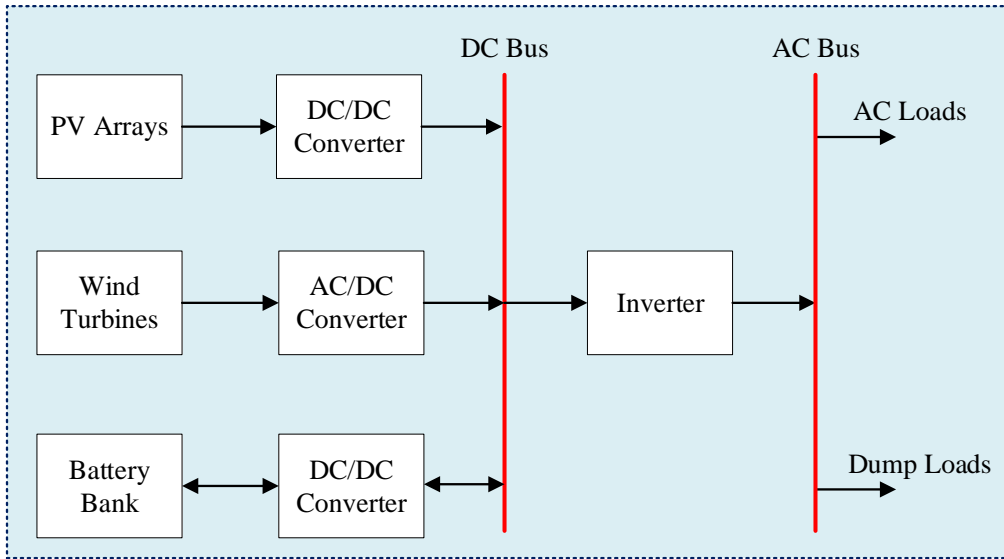


Figure 2.8: Hybrid PV-Wind-Battery system structure.

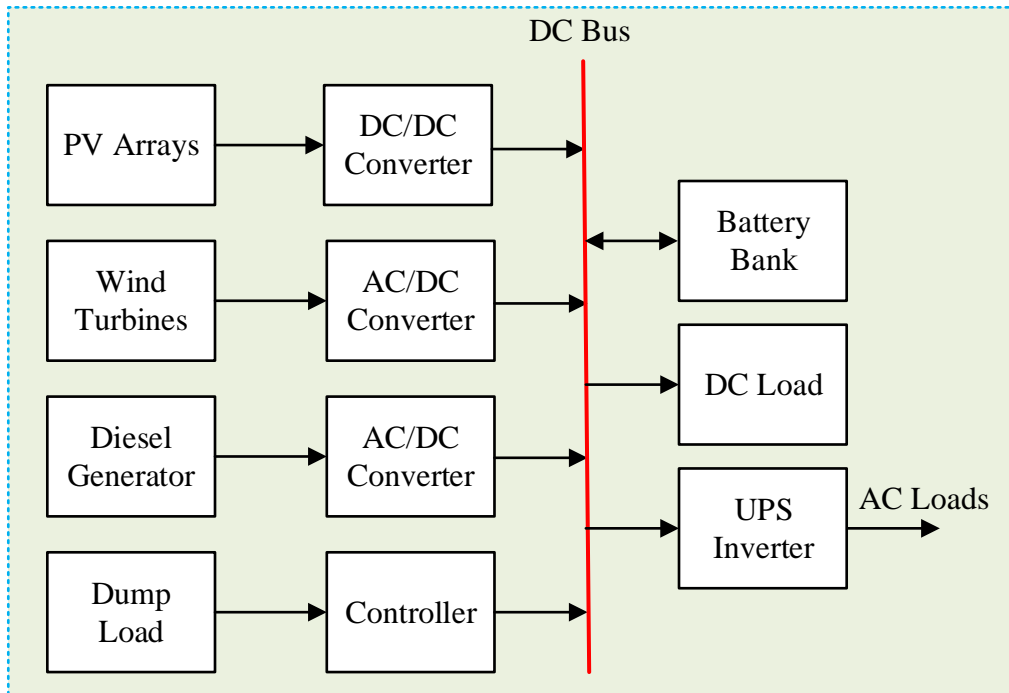


Figure 2.9: Hybrid PV-Wind-Diesel system structure.

### **2.1.3 Coupling Topologies of HRES**

#### **DC bus connected Wind-Solar HRES**

Here, the output from the WT is connected to the DC bus through an AC/DC converter, while the output from the PV array is coupled to the DC bus using a DC/DC converter. The ESS is tied-up to the DC bus using a bi-directional converter to allow its charging-discharging mechanism. This system framework can serve both AC and DC loads concurrently. A DC/AC converter is required when an AC load needs to be served. Here, other sources of RE can also be incorporated using the appropriate power electronic converters. This framework provides several operation advantages, such as simplicity and the elimination of challenges associated with synchronization. The main drawbacks of this architecture are the losses involved with the power conversion systems, particularly the losses associated with converting WT AC power to DC and then back to AC, which is approximately 10% of the WT power [27]. The DC bus connected wind-solar HRES topology is illustrated in Fig. 2.10.

#### **AC bus connected Wind-Solar HRES**

The AC-coupled HRES topology is demonstrated in Fig. 2.11, where the PV coupled to an AC bus using a DC/AC converter and the WT tied-up to the AC bus through an AC/AC converter. The ESS relates to a bi-directional electronic converter. In this scheme, an AC/DC converter is required to feed the DC loads. Other RE sources can be incorporated through the appropriate power converters interface. Here, each of the sources is connected to the AC bus via a separate power converter, allowing them to work even if one of them is disconnected, which can improve the system reliability [27]. Synchronization is the primary impediment of this configuration.

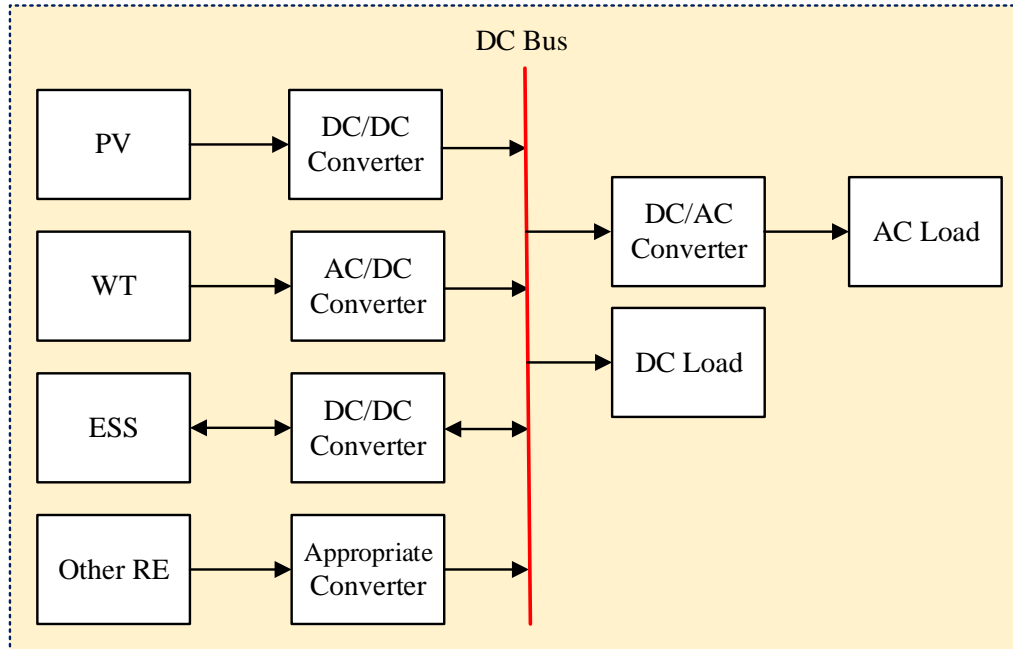


Figure 2.10: DC-Bus connected HRES.

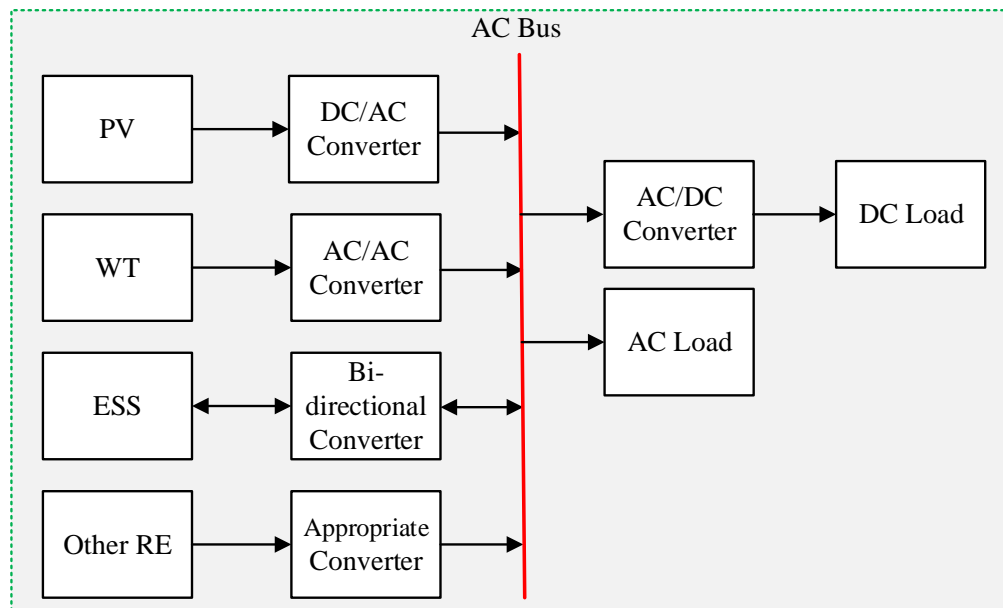


Figure 2.11: AC-Bus connected HRES.

### Dual bus connected Wind-Solar HRES

The dual bus-connected wind-solar HRES framework uses both the AC and DC bus. Here, RE sources with AC outputs are directly related to the AC bus, while RE

sources with DC outputs are directly coupled to the DC bus. Therefore, the dual-bus connected wind-solar HRES improves overall system efficiency by reducing the number of converters and limiting power losses due to conversion [28]. This configuration is the most widely adopted due to its flexibility to combine energy sources and load irrespective of features [29]. Fig. 2.12 and Fig. 2.13 illustrate the dual bus-connected wind-solar configurations.

## 2.2 Energy Storage System

By incorporating the ESS in the wind-solar HRES architectures, the uncertainty of renewable resources can also be diminished considerably. In particular, the ESS helps to provide ancillary services; peak regulation, voltage fluctuation and flicker mitigation, harmonic reduction, frequency stability, load leveling, and transient stability. Batteries and SC are the most frequently utilized components among the several types

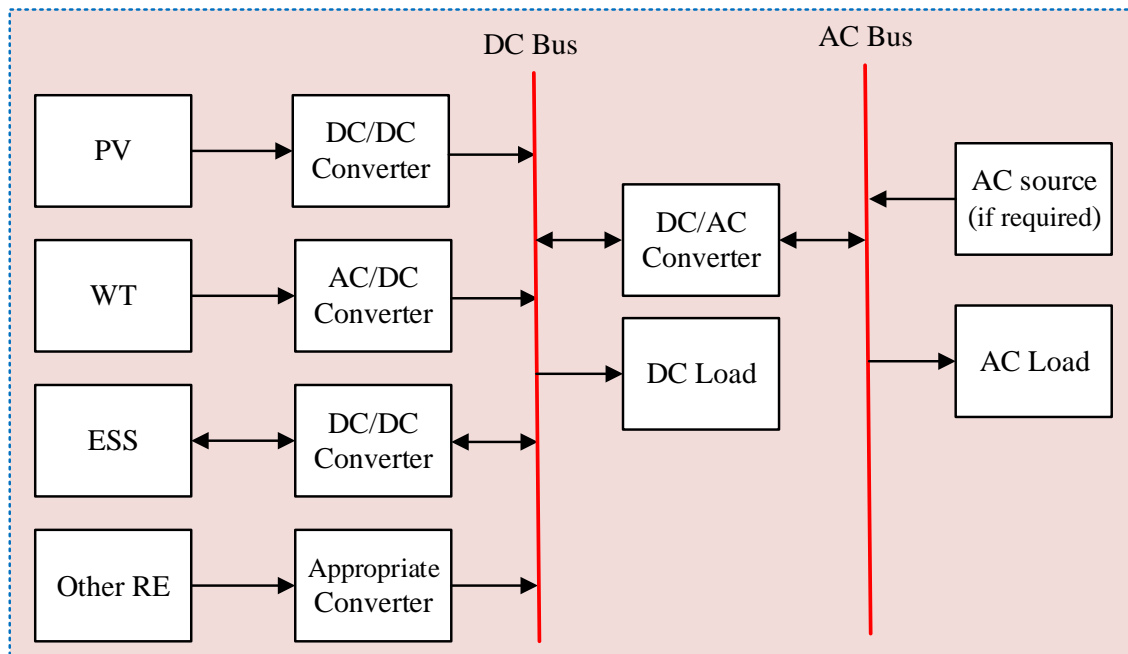


Figure 2.12: Dual-Bus connected HRES (Type 1).

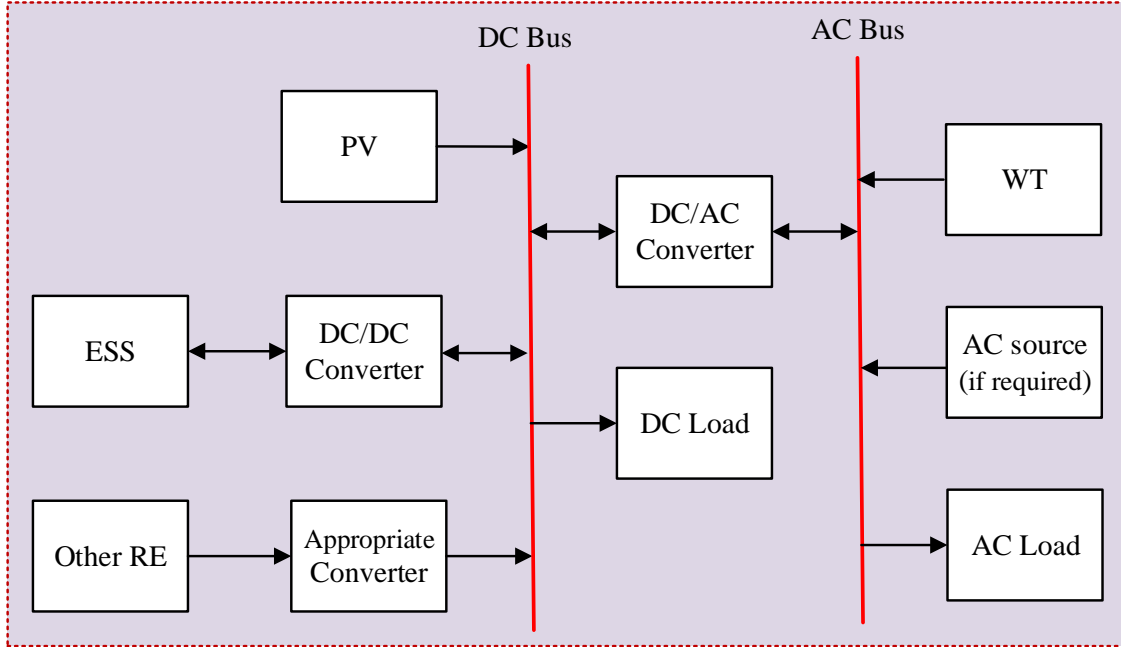


Figure 2.13: Dual-Bus connected HRES (Type 2).

of the ESS in the market. Different types of rechargeable batteries have been found in the market, such as lead-acid, nickel-cadmium, lithium-ion, and lithium-polymer. The design of the battery depends on some system requirements such as (a) voltage and current, (b) charging-discharging rates and duration, (c) operating temperature during charging and discharging, (d) lifetime in terms of the number of charging and discharging cycles, and (e) cost, size, and weight constraints [30].

Examples of practical utility-scale ESS include the 5 MW, 1.25 MWh Li-ion battery installed in the Pacific Northwest smart grid; the 32 MW Li-ion battery installed in a 98 MW wind farm by AES in Elkins, West Virginia; the 8 MW and the 32 MWh Li-ion battery installed in Tehachapi energy storage project in California [31], [32]. Table 2.2 shows the relative properties of the lead-acid battery and SC [33], [34], [35]. The conventional capacitor also exhibits similar characteristics to the SC except that its size is much larger and its cycle life is only half that of the SC [33].

From Table 2.2, it is noticeable that the battery has the high energy density

Table 2.2: Battery and SC performance comparison.

Properties	Battery	SC
Specific energy density (Wh/kg)	10-100	1-10
Specific power density (W/kg)	<1000	<10,000
Energy density (Wh/L)	50-80	2-10
Power density (W/L)	10-400	> 100,000
Power ratings (MW)	0-20	0-0.03
Power capital cost (\$/kW)	300-600	100-300
Energy capital cost (\$/kWh)	200-400	300-2000
Capital cost (\$/kWh-per cycle)	0.2-1	0.02-0.2
Cycle life	1000	>500,000
Charge/discharge efficiency (%)	70-80	85-98
Fast charge time	1-5 hr	0.3-30 sec
Discharge time	0.3-3 hr	0.3-30 sec
Self-discharge rate (% per day)	0.1-0.3	20-40
Operation range temperature ( $^{\circ}C$ )	-5 to 40	-40 to 75

property, but the low power ramp rate that means the charging-discharging rates of the battery are slow to meet the peak/pulse load demand. On the other hand, the SC has a high power ramp rate, but low energy density property. As a consequence, the SC cannot support the load demand for a long duration. It is evident that none of these two ESS has both the properties of high power density and high energy density. Thus, when only one type of ESS is used to meet both the power and energy capacity requirements, there is a possibility to incur high installation costs. A HESS consisting of a battery and SC can be leveraged to develop a more economical ESS, where the SC also helps to mitigate the high frequency power components passing through the battery, which is beneficial for extending the battery lifetime [36].

The HESS can be coupled to either a common DC or AC bus. Normally, the HESS can be categorized based on their connection topology as illustrated in Fig. 2.14 [37], [38].



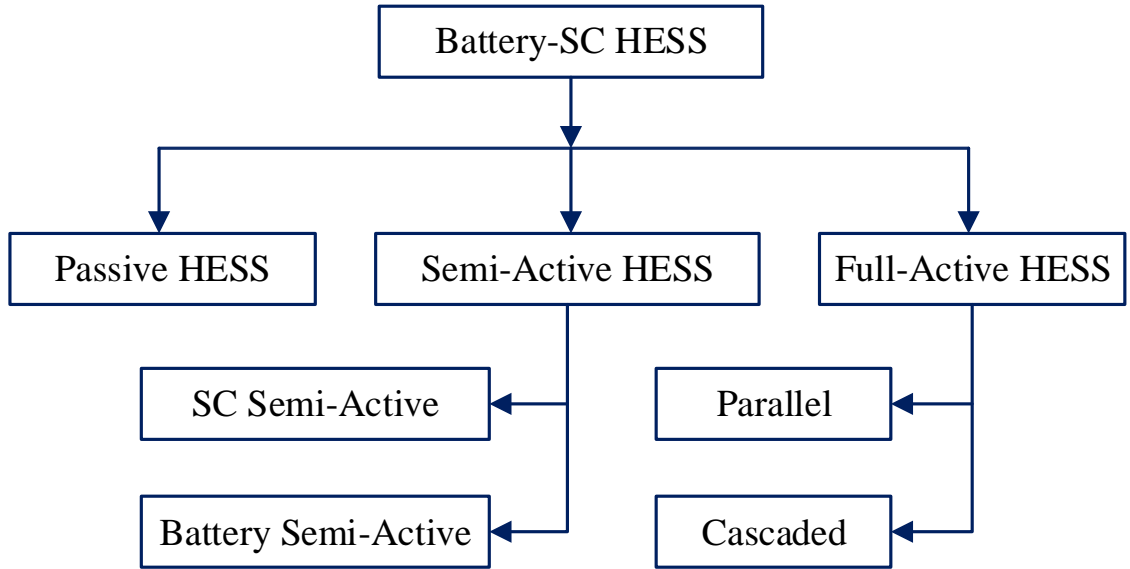


Figure 2.14: Classification of the battery-supercapacitor HESS topologies.

### Passive HESS

In the passive HESS framework, the battery and SC are directly connected to the DC bus, as shown in Fig. 2.15. They share the identical terminal voltage that depends on the SOC and charge-discharge characteristic of the battery. The passive HESS can effectively suppress transient current under pulse load conditions, diminish internal losses, and enhance the peak power. However, as the voltage deviation of the battery terminal is small, the SC can not be operated at its full SOC range, which yields poor volumetric efficiency [39], [40].

### Semi-Active HESS

The power electronic converters can be connected between the ESS and DC bus, which results in the power flow of the ESS to be actively controlled [41]. Either the battery or SC is actively controlled in semi-active HESS topology. A semi-active HESS configuration is illustrated in Fig. 2.16 (left), where only the SC is interfaced

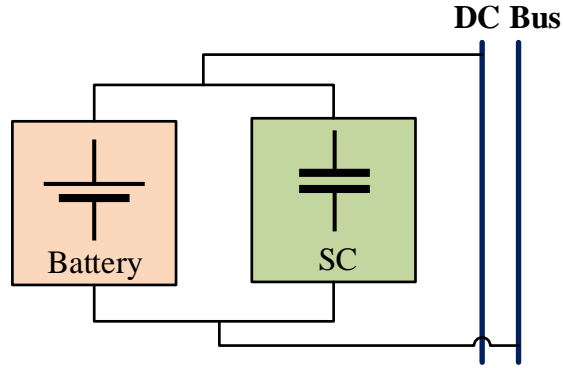


Figure 2.15: Passive HESS topology.

with the DC bus using a bidirectional DC-DC converter that isolates the SC from the DC bus and battery terminal [42]. Here, the SC can be operated within a wider range of voltages that improves its volumetric efficiency significantly. However, the battery is exposed to fluctuating high current in this setting that has an adverse impact on the battery's service life [43].

The other semi-active HESS framework is demonstrated in Fig. 2.16 (right). Here, the battery is isolated by a power converter, and the SC is directly connected to the DC bus [44], [45]. In this framework, the battery's current can be regulated at a moderately reasonable manner in any event of the variation in the power demand. The battery terminal voltage is not necessary to meet the DC bus voltage, which allows the adjustable and economical sizing of the battery bank [46]. However, the linear charge-discharge characteristic of the SC induces substantial fluctuation in the DC bus, which may deteriorate system stability and power quality. The capacity of the SC needs to be comparatively large to maintain a stable DC bus voltage, which leads to an increase in the energy storage expenditure.

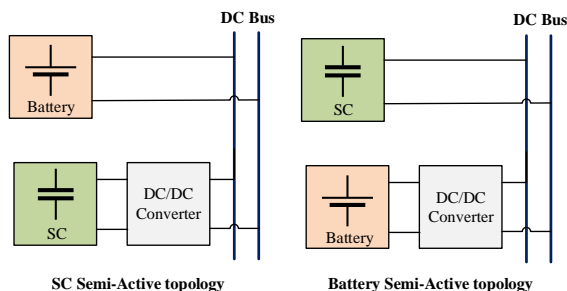


Figure 2.16: Semi-active HESS topology.

### Full Active HESS

The power flow of the battery and SC are both actively controlled through the bidirectional power converters in fully active HESS architecture, which results in enhancing the overall system flexibility and cycle life. Two of the most common full active HESS topologies—(i) parallel active HESS, and (ii) cascaded active HESS—are illustrated in Fig. 2.17.

Each of the ESS is connected to the DC bus via a bi-directional power converter in parallel active HESS framework [35]. Here, the battery lifetime and DC bus stability can be enhanced through a meticulously designed control strategy [47]. For instance, the frequency management technique can be deployed to increase the longevity of the batteries through comprehensively utilizing the high power density property of SC and the high energy density property of batteries. Besides, the decoupling of battery and SC facilitates both types of the ESS to operate at a comprehensive range of SOC that can make the system more efficient.

In the cascaded framework, two bidirectional power converters are cascaded to seclude the battery and SC from the DC bus [48]. The power converter that separates the battery is typically current-controlled to provide a smooth power transfer with the battery. This mechanism helps the battery to avoid the rapid charging-discharging process corresponding to increase in the battery service life. The power converter that

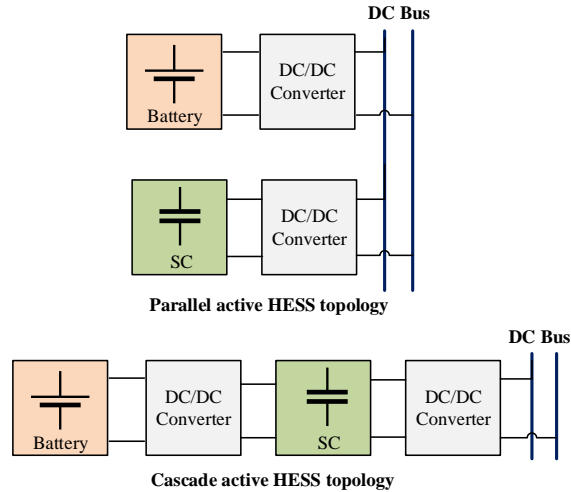


Figure 2.17: Active HESS topology.

segregates the SC from the DC bus is usually voltage-controlled to inhibit the DC bus voltage while absorbing the fast-changing power exchanges [49]. It is expected that a substantial voltage swing between the SC and DC bus due to the SC has a wide operating voltage. As a consequence, the power losses in the power converter considerably increase as it is challenging to regulate efficiency over a wide range of operating voltages.

The overall efficiency of the HESS substantially decreases as the number of DC/DC converter increases. Moreover, the performance of fully active HESS architecture is heavily dependent on the reliability of the power converters and their control system.

### 2.3 Modeling of HRES

According to the different parameters and constraints, modeling is the first step in designing a renewable energy system. In this section, the PV, WT, Battery, and SC mathematical modelings are documented, which will be useful to researchers to understand the characteristics of these components.

### 2.3.1 Modeling of PV System

In the literature, there are many mathematical models developed to describe the behavior of the PV [50], [51]. A PV cell is a nonlinear device that can be represented as a current source model. The V-I characteristic equation of a PV cell is shown in (2.1) and (2.2).

$$I = I_{sc} - I_d \quad (2.1)$$

$$I = I_{sc} - I_{os} \left( e^{\frac{q \cdot (V + I \cdot R_s)}{n \cdot K \cdot T}} - 1 \right) \quad (2.2)$$

where  $I_{sc}$  is the light generated current,  $I_{os}$  is the diode reverse saturation current,  $q$  is the electronic charge,  $k$  is the Boltzmann constant,  $T$  is the temperature,  $V$  is the terminal voltage of the module, and  $R_s$  is the series resistance.

The output of the PV array depends on two weather conditions: solar irradiation ( $\text{W}/\text{m}^2$ ) and solar cell temperature ( $^\circ\text{C}$ ). The PV array module in Matlab/Simulink provides power-voltage characteristic curves based on user-input parameters, such as solar cell type, the number of cells in parallel, and the number of cells in series, under various weather conditions. The power-voltage characteristic curves for 1 MW PV array are shown in Fig. 2.18 and Fig. 2.19. At maximum power point (MPP) operation, the PV arrays' output power is marked as a circle of their respective curves. The maximum power point tracking (MPPT) technique is generally employed to extract the maximum power from the PV array. The incremental conductance, perturb & observe (P&O), short circuit current (SCC), and open circuit voltage (OCV) are commonly MPPT approaches utilized in the PV system [52]. In general, especially for residential PV framework, the PV array provides power to the unidirectional boost

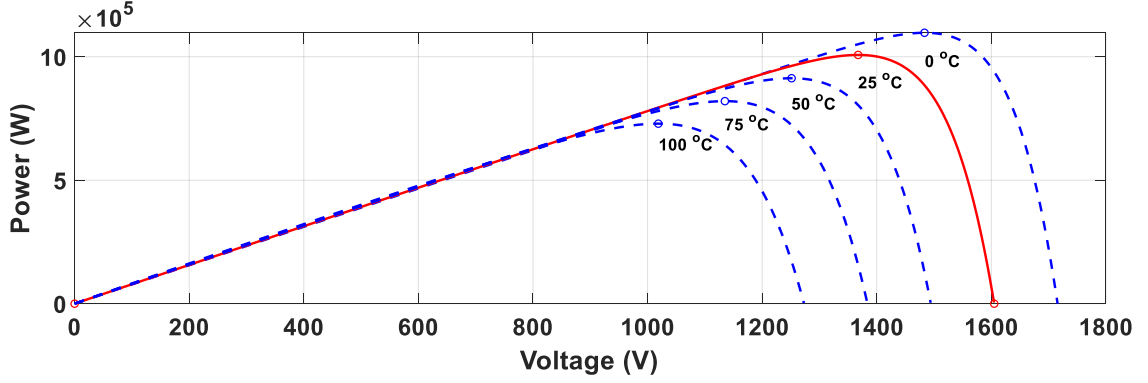


Figure 2.18: Power-Voltage characteristics of PV array at various temperatures.

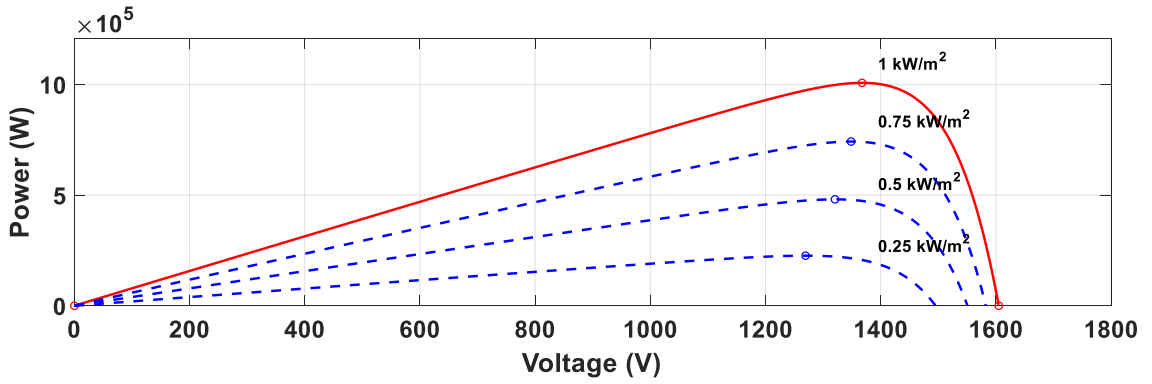


Figure 2.19: Power-Voltage characteristics of PV array at various irradiances.

converter, and an MPPT is utilized to control the duty ratio of the power converter to extract maximum power from the PV array.

The authors in [53] described a simplified technique to calculate the PV output power, which can be expressed as:

$$G(t, \theta_{pv}) = G_v(t) \times \cos(\theta_{pv}) + G_H(t) \times \sin(\theta_{pv}) \quad (2.3)$$

$$P_{pv} = \frac{G}{1000} \times P_{pv, \text{rated}} \times \eta_{MPPT} \quad (2.4)$$

where  $G$  is perpendicular radiation at the arrays' surface ( $\text{W}/\text{m}^2$ ).  $P_{pv, \text{rated}}$  is rated power of each PV array at  $G$  equal to 1000 ( $\text{W}/\text{m}^2$ ) and  $\eta_{MPPT}$  is the efficiency of PV's power converter and MPPT.

Another simple model is contemplated in [54] to predict the PV output power as a linear function of effective irradiance, as shown in (2.5). This model has the advantage of being parameterized from the PV panel datasheet and being simple to use, however it is not precise and does not account for environmental factors such as wind speed and solar cell temperature on PV performance.

$$P_{mp,array}(\rho_e) = N_s \times N_p \times \left( \frac{\rho_e}{\rho_s} P_{mp,s} \right) \quad (2.5)$$

where  $P_{mp,array}$  is the PV power at the maximum point for PV array,  $N_s$  and  $N_p$  are the number of panels and number of subarray, respectively,  $\rho_e$  is the effective solar irradiance,  $\rho_s$  is the solar irradiance under STC (1000 W/m<sup>2</sup>), and  $P_{mp,s}$  is the PV power at the maximum point for PV module.

Normally, the PV cell temperature is much higher than the ambient temperature, and it can decrease the PV output power as well as its capacity factor. An effective approach for estimating the PV cell temperature is formulated in [55]:

$$(T_m^\circ C) = a \times T_a + b \times I_r - c \times V_w + d \quad (2.6)$$

where,  $a$ ,  $b$ ,  $c$ , and  $d$  are system-specific regression coefficients,  $T_a$  refers to the ambient temperature given in (°C),  $I_r$  refers to the solar irradiation given in (W/m<sup>2</sup>), and  $V_w$  refers to the wind speed given in m/s.

The curve fitting tool is utilized to calculate the regression coefficients  $a$ ,  $b$ ,  $c$ , and  $d$ . Thus, the formula for prediction of the PV cell temperature can be expressed as:

$$(T_m^\circ C) = 0.943 \times T_a + 0.0195 \times I_r - 1.528 \times V_w + 0.3529 \quad (2.7)$$

Sandia National Laboratories proposed another PV cell temperature estimation model known as the Sandia Model [56]. The PV model estimates the impact of PV

cell temperature on PV performance using data from ambient temperature and wind speed. The public parameter databases as well as additional information about this model are available in [57]. The Sandia Model is highly accurate and can be expressed as:

$$I_{mp}(\rho_e, T_c) = I_{mp,ref} (C_0 \times \rho_e + C_1 \times \rho_e^2) [1 + \alpha(T_c - T_s)] \quad (2.8)$$

$$V_{mp}(\rho_e, T_c) = V_{mp,ref} + C_2 n_s \delta(T_c) \ln(p_e) + C_3 n_s [\delta T_c \ln(p_e)] + \beta_{mp} (T_c - T_s) \quad (2.9)$$

$$P_{mp,array} = N_s \times N_p \times V_{mp} \times I_{mp} \quad (2.10)$$

### 2.3.2 Modeling of WT system

There are several existing models in the literature to estimate the wind turbine power including linear, cubic, quadratic, Weibull parameters, and so on [58], [59], [60]. Generally, the output power of the wind turbine is a function of aerodynamic power efficiency, wind speed distribution of the selected sites, mechanical transmission and electrical energy conversion efficiency, and the hub height of the wind tower.

In [61], Sami et al. described a wind turbine model to calculate the WT power generation output, which can be expressed as follows:

$$P_W = \begin{cases} P_r \left( \frac{V^2 - V_c^2}{V_r^2 - V_c^2} \right), & V_c \leq V < V_r \\ P_r, & V_r \leq V < V_f \\ 0, & V \geq V_f \end{cases} \quad (2.11)$$

where  $P_W$  is the output power of the wind generator,  $P_r$  is the rated power of the wind generator,  $V_c$  is the cut in speed of the WT,  $V_r$  is the rated speed of the WT, and  $V_f$  is the cut-out speed at which the WT stops rotating.



When the meteorological data recorded is found at a different height from the WT height, (2.12) is utilized to calculate the wind speed:

$$V_h = V_{ref} \left( \frac{H}{H_{ref}} \right)^\alpha \quad (2.12)$$

where  $V_h$  is the wind speed at turbine height ( $H$ ),  $V_{ref}$  is the wind speed recorded by a meteorological station at height ( $H_{ref}$ ) and  $\alpha$  is the surface roughness factor which is around 1/7 in an open space surface [62].

The permanent magnet synchronous generator (PMSG) coupled WES has been reported in the studies [63], [64]. The PMSG based on WES can associate with the WT without utilizing a gearbox. The energy conversion in PMSG based on WES takes place through two stages. First, the kinetic energy is captured by the WT blades as mechanical energy. Second, the mechanical energy is transferred through the shaft to PMSG, which converts the mechanical energy to electrical energy. The mechanical output power of a PMSG wind turbine can be expressed as:

$$P_m = \frac{1}{2} \rho A v_w^3 C_p(\lambda, \beta) \quad (2.13)$$

where  $P_m$  is mechanical output power of the turbine (W),  $\rho$  is air density (kg/m<sup>3</sup>),  $A$  is turbine swept area (m<sup>2</sup>),  $v_w$  is wind speed (m/s),  $C_p$  is the performance coefficient of the turbine,  $\lambda$  is tip speed ratio of the rotor blade tip speed to wind speed and  $\beta$  is blade pitch angle (degree).

The mechanical output power ( $P_m$ ) depends significantly on the turbine performance coefficient  $C_p$ . In this study, the following generic  $C_p(\lambda, \beta)$  model is employed:

$$C_p(\lambda, \beta) = c_1 \left( \frac{c_2}{\lambda_i} - c_3 \beta - c_4 \right) e^{\left( \frac{-c_5}{\lambda_i} \right)} + c_6 \lambda \quad (2.14)$$

$$\frac{1}{\lambda_i} = \frac{1}{\lambda + 0.08\beta} - \frac{0.035}{\beta^3 + 1} \quad (2.15)$$

where,  $c_1 = 0.5176$ ,  $c_2 = 0.116$ ,  $c_3 = 0.4$ ,  $c_4 = 5$ ,  $c_5 = 21$ , and  $c_6 = 0.0068$ . The consequent  $C_p$ - $\lambda$  curve is illustrated in Fig. 2.20. The  $C_p$ - $\lambda$  curve shows that the maximum value of  $C_p$  is achieved for  $\beta = 0$  and  $\lambda = 8.1$ .

The WT model in MATLAB/Simulink provides the WT power characteristic curve based on user input parameters such as base wind speed, base rotational speed, blade pitch angle ( $\beta$ ), and maximum power at base wind speed. The WT power characteristics curve is illustrated in Fig. 2.21. In this power curve,  $\beta$  is assumed to be zero and wind speed varies from 5 m/s to 11 m/s. The maximum power points for each wind speed are labelled. The generator rotor speed should track the wind speed changes to extract the maximum power from the wind. In general, the back to back power converters are employed to meet the power quality criteria while the WES generated power is transferred to the utility.

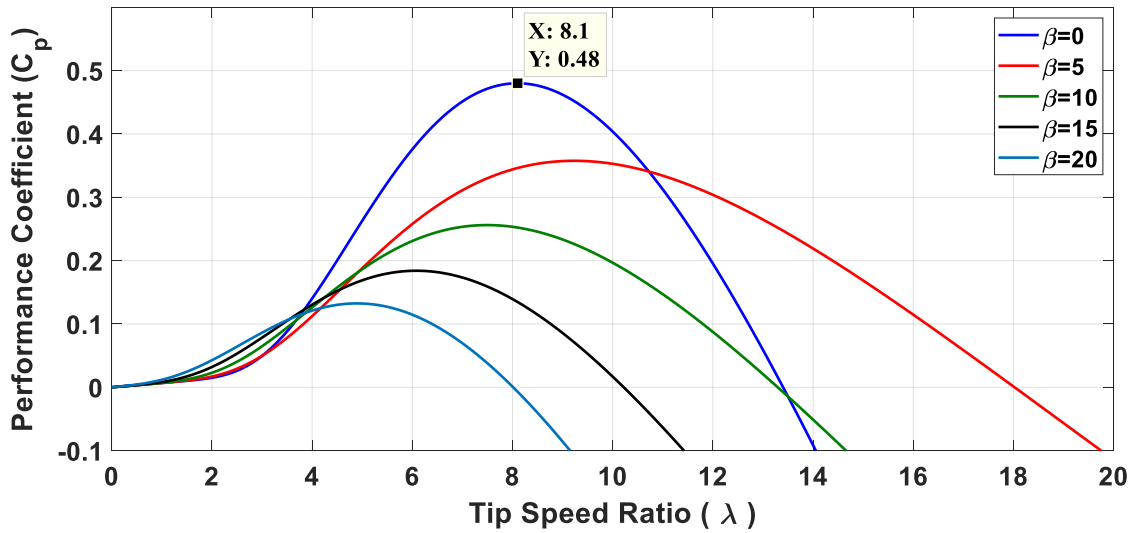


Figure 2.20: The  $C_p$ - $\lambda$  characteristics of PMSG wind turbine.

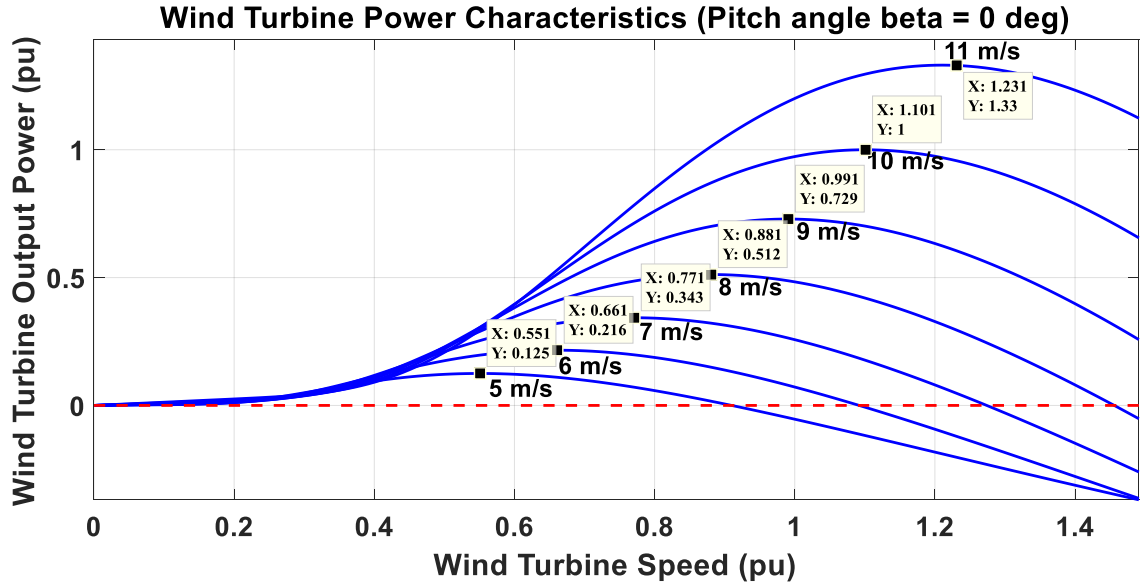


Figure 2.21: WT power characteristics curve.

### 2.3.3 Maximum Power Point Tracking

The maximum power generated by the PV generators varies with solar irradiance and temperature. Since the PV exhibits non-linear current-voltage and power-voltage characteristics, any alteration in solar insolation and temperature causes a change in terminal voltage, resulting in deviation from maximum power generation. The MPPT is utilized to adjust the solar operating voltage close to the MPP in response to changing atmospheric conditions in order to maximize power harvest from the PV array. As a result, it has become an essential component in evaluating the design performance of PV power systems.

In the literature, approximately 40 different methods are reported to track the maximum power point. This availability of multiple options as an MPPT makes its unambiguous selection a tougher nut to crack. The authors in [65] contemplated a summary of 31 different kinds of MPPT techniques, and a comparative comparison was documented among them based on 12 factors: category, dependency of PV array,

implementation methodology, sensor required, stages of energy conversion, partial shading enabled, grid integration, analog or digital, tracking efficiency, tracking speed, cost, and product availability on the market. The authors also classified MPPT techniques into three categories based on control strategy, such as indirect control methods (mathematical methods based on empirical data), direct control methods (modulation-based control strategies), and soft computing technique-based methods (genetic algorithm, particle swarm optimization, and artificial neural network).

A comprehensive review of MPPT techniques for PV systems under normal and partial shading conditions (PSC) was conducted in [66]. The selected MPPT strategies are classified further into three categories: artificial intelligence, hybrid, and other MPPT methods. It is reported that researchers have concentrated more on PSC in recent years in order to increase the power output and efficiency of PV systems. Another comparative study, which included the detailed classification and description of MPPT strategies for PV systems available until 2012, is summarized in [67]. The available MPPT strategies are classified based on the number of control variables involved, types of control strategies, circuitry, and cost of applications, which is useful for selecting an MPPT approach for a certain application.

In [68], the existing MPPT techniques are divided into two main categories: classical MPPT and modern MPPT, and the tactics of each category are briefly discussed. The modern MPPT category includes fuzzy logic, artificial neural network, and metaheuristic-based MPPT techniques, whereas the classical MPPT category includes perturb and observe, hill climbing, fractional open circuit voltage, and fractional short circuit current. The performance of each MPPT strategy is compared in both uniform and PSC insolation, and the metaheuristic-based MPPT technique outperformed the other MPPT approaches investigated in extracting the maximum

power from the PV array due to several advantages, including system independence, effective performance in PSC, and the absence of oscillations around the MPP.

The authors in [69] contemplated another survey on MPPT approaches by categorizing several existing MPPT techniques into three broad categories: offline, online, and hybrid methods. Offline MPPT techniques include open circuit voltage (OCV), short circuit current (SCC), and artificial intelligence (AI) based MPPT methods, which are referred to as model-based approaches because the physical values of the PV panel are utilized to generate control signals. On the other hand, the online category encompassed perturbation and observation (P&O), extremum-seeking control (ESC), and incremental conductance (IncCond) MPPT techniques, which are referred to as model-free methods where the relationship between the open circuit voltage and the maximum power point voltage is used to generate the control signals. Hybrid methods are a combination of online and offline approaches. The control signal associated with the hybrid method consists of two parts, where the first part is generated based on model-based techniques and the latter part is generated based on model-free approaches. The MPPT strategies are compared in terms of the dynamic response of the PV system, achievable efficiency, and implementation considerations, and hybrid methods outperformed model-based and model-free methods in extracting the maximum PV power.

Due to the variable nature of the wind, it is desirable in the wind energy conversion system to determine the optimal generator speed that assures maximum energy production. The MPPT approach is used to optimize the generator speed in relation to the wind velocity intercepted by the WT, ensuring the maximum energy is harvested from the available wind at any instance. Many MPPT strategies have been reported in the literature, and these methods differ in terms of technique employed,

complexity, number of sensors required, convergence speed, memory requirement, range of effectiveness, and so on. These MPPT techniques can be primarily classified as tip-speed ratio control (TSR), power-signal feedback (PSF), and hill climb search (HCS) based [70]. However, so many variations have been proposed over the last 30 years that it has become difficult to decide which strategy, newly proposed or existing, is best suited for a particular wind system.

The TSR control method regulates the rotational speed of a wind turbine generator to maintain an appropriate TSR, and this method requires the estimation of both wind speed and turbine speed, which is typically derived from turbine-generator characteristics and varies from system to system. Likewise, the PSF technique requires the knowledge of a wind turbine's maximum power curve to estimate the optimum turbine speed for a specific wind velocity to harvest the maximum available power from a WT [71]. Because both TSR and PSF control techniques involve substantial turbine knowledge as well as measurements of generator and wind speed, the practical implementation of the algorithm becomes highly complicated as the number of sensors and control complexity increase significantly. The HCS-based MPPT approaches are proposed to tackle these challenges, in which the algorithm continuously searches for a turbine's peak output power by altering the generator speed and adjusting the power direction. However, due to the constraints of deteriorated power quality, as power ripple constantly persists and the tracking speed is typically slow, its utilization is confined to small-scale wind turbine systems [72]. While each of these three strategies has advantages and disadvantages, a variety of versions of these methods have been presented over the years, each employing a different methodology to handle these concerns. The most significant aspects to consider while selecting a specific MPPT strategy are contemplated in Table 2.3 [73], [74].

Table 2.3: Comparison of characteristics of various MPPT techniques.

Technique	Complexity	Speed	Prior cognition	Wind estimation	Performance
TSR control	Simple	Fast	No	Yes	Very good
Optimal torque control	Simple	Fast	Yes	No	Very good
PSF control	Simple	Fast	Yes	Yes	Good
HCS control	Simple	Depends	No	No	Good
Adaptive HCS control	High	Medium	No	No	Good
Flux estimated	High	Slow	No	No	Moderate
Pitch control	Medium	Slow	Yes	Yes	Limited
Neural network	High	Fast	Yes	Depends	Very good
Fuzzy logic	High	Fast	Yes	Depends	Very good
Lookup table	Simple	Fast	Yes	Yes	Very good
Theoretical based	Simple	Fast	No	No	Limited
Other methods	High	Medium	Yes	No	Good

### 2.3.4 Degradation Model of ESS

In [75], Addoweesh et al. described a simple battery model where the SOC of the battery is calculated by a comprehensive analysis of the battery's charging-discharging modes, load profile, and output energy of the RE sources. This battery model is expressed as follows:

$$SOC(t) = SOC(t - 1)(1 - \sigma) + (E_{GA}(t) - \frac{E_L(t)}{\eta_{inv}})\eta_{bat} \quad (2.16)$$

where  $SOC(t)$  and  $SOC(t - 1)$  are the SOC of the battery bank at time  $t$  and  $t-1$ ;  $\sigma$  is hourly self-discharging rate;  $E_{GA}(t)$  is the total energy generated;  $E_L(t)$  is the

load demand;  $\eta_{inv}$  and  $\eta_{bat}$  are the efficiencies of inverter and battery.

### Li-ion Battery Degradation Model

To consider cycling and calendar aging for battery usage, a degradation model proposed in [76] is documented in this study. The expected lifetime of the battery decreases due to its degradation properties over the period, which can be expressed as:

$$\frac{1}{T_{life}} = \left[ \sum_{i=1}^N \frac{DOD_i^2}{2N_{cycles}^{ref}} + \frac{T}{T_{calendar}^{ref}} \right] \times e^{\left( \frac{\theta_c - \theta_c^{ref}}{\theta_0} \right)} \quad (2.17)$$

where  $T_{life}$  is the battery's service life, in years, decreases due to its degradation properties,  $N$  is the total number of half-cycles over the simulation period  $T$ ,  $i$  is the index of the half-cycle,  $DOD_i$  is the DOD during the half-cycle  $i$ ,  $\theta_c$  is the case temperature, and  $\theta_0$  is the ambient temperature.  $T_{calendar}^{ref}$  is the lifetime, in years, for a case temperature of  $\theta_c^{ref}$ . A rainflow-counting algorithm is generally employed to determine all half-cycles. The parameters  $N_{cycles}^{ref}$ ,  $T_{calendar}^{ref}$ ,  $\theta_0$  and  $\theta_c^{ref}$  are presented in Table 2.4 [76].

In [77], another degradation model is reported for battery usage where the calendar aging cost of the battery ( $C_{Bat,calendar}$ ) considering of its DOD usage and the initial cost is calculated as follows:

$$C_{Bat,calendar} = \frac{C_B}{C_{B,n} \times 2 \times DOD \times E_B \times m^2} \quad (2.18)$$

where  $C_{B,n}$  is the life cycle of the battery provided by the manufacturers,  $E_B$  is the battery capacity (kWh),  $C_B$  is the battery cost (\$/kWh), and  $m$  is the efficiency of the battery that was assumed 92% for a Li-ion battery.



Table 2.4: Parameters of the Li-ion battery aging model.

$N_{cycles}^{ref}$	16,000
$T_{calendar}^{ref}$	25 years
$\theta_c^{ref}$	25° C
$\theta_0$	22 K

### SC Aging Model

An aging model for the SC is contemplated in this study that considers both calendar aging and cycling aging [78]. The expected lifetime of the SC ( $T_{SC,life}$ ) can be expressed as:

$$\begin{aligned} \frac{1}{T_{SC,life}} &= \frac{1}{T_{life}^{ref}} \times \exp\left(\ln(2) \frac{\theta_c - \theta_c^{ref}}{\theta_0}\right) \\ &\times \left[ \exp\left(\ln(2) \frac{V - V^{ref}}{V_0}\right) + K \right] \times \exp\left(K_{RMS} \frac{I_{RMS}}{C_0}\right) \end{aligned} \quad (2.19)$$

where  $T_{SC,life}$  is the SC lifetime in hours,  $\theta_c$  is the case temperature and  $V$  is the voltage across the component.  $V_0$  and  $\theta_0$  are the respective decreases in voltage and temperature necessary to double the SC service life.  $T_{life}^{ref}$  is the lifetime, in hours, for a case temperature of  $\theta_c^{ref}$  with a voltage of  $V^{ref}$ .  $K$  is a dimensionless constant that replaces the voltage term whenever the voltage is low.  $C_0$  is the initial value of the SC capacitance, and  $K_{RMS}$  is an accelerator factor.  $I_{RMS}$  is the RMS current flowing through the component. The parameters of the SC aging model are given in Table 2.5 [78].

Table 2.5: Parameters of the SC aging model.

$\theta_0$	7.7 K
$V_0$	89 mV
$K$	$29 \times 10^{-3}$
$T_{life}^{ref}$	1470 h
$V^{ref}$	2.7 V
$\theta_c^{ref}$	65° C
$K_{RMS}$	68 s.V <sup>-1</sup>

## 2.4 Power Converter Configurations for HRES

Various power converters have been utilized in the HRES to extract the maximum power from the source, interface the different energy sources, and regulate the power quality at the load side. In general, the back-to-back AC-DC-AC power converter is employed to integrate the WT into the utility, and the unidirectional boost or buck-boost converter along with inverter is deployed to integrate the PV into the grid. In a hybrid PV-Wind configuration, the total cost with the semiconductor switches can be saved by up to 25% through the development of multi-port power converters where one single converter can interface several energy resources [79]. In general, the power converter configurations employed in the HRES can be classified into three categories, as follows: (i) AC shunt coupled HRES, (ii) DC shunt coupled HRES, and (iii) Multi-input coupled HRES.

### 2.4.1 AC Shunt Coupled HRES

The AC shunt coupled grid-connected HRES is illustrated in Fig. 2.22, where two separated inverters are deployed for the HRES grid integration. In this architecture, one DC-DC converter (e.g., buck-boost converters) embedded with MPPT algorithms is connected with the PV system, and one AC-DC active rectifier is generally config-

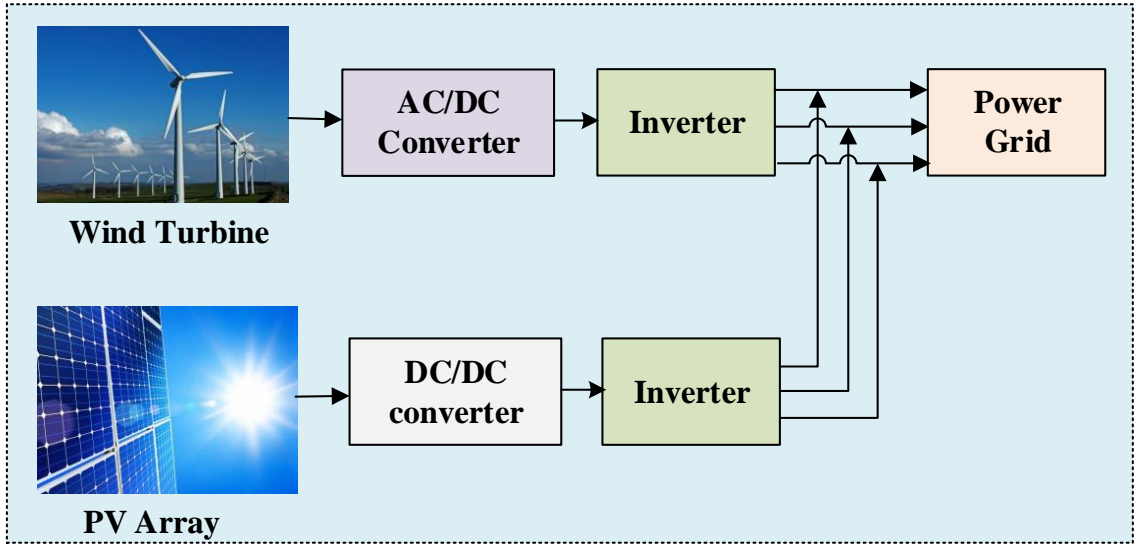


Figure 2.22: AC shunt coupled HRES.

used to interface the WT generator. Individual inverters are employed to convert the PV and WT system's DC power into the AC, and eventually incorporated at the AC bus and fed to the utility grid. The AC shunt coupled solution is straightforward and simple in controls, but one potential drawback is that it requires the synchronization of two energy sources.

#### 2.4.2 DC Shunt Coupled HRES

In DC shunt coupled HRES framework, one single common inverter is utilized for integrating the hybrid PV-Wind system into the utility grid, which is shown in Fig. 2.23. Here, the power converters are utilized for converting the PV and wind power into DC power. One common central inverter is employed to convert and manage the DC power into AC power and integrated for the utility grid. The inverter serves as an interface between the source and utility grid in this framework. This DC coupled solution yields higher efficiency and higher power density in many scenarios due to lower number of cascaded converters. However, one likely shortcoming is that, when

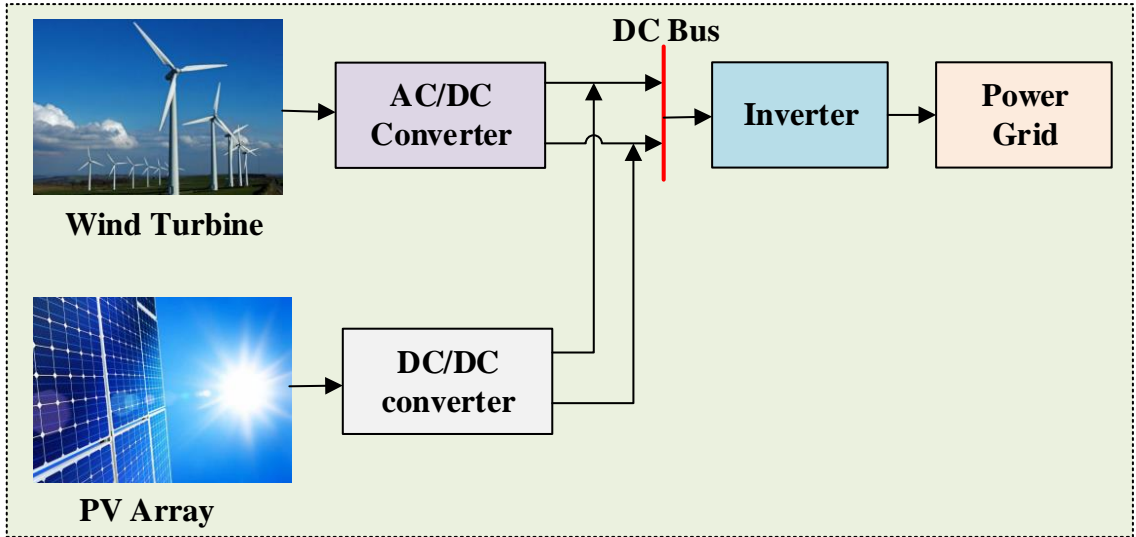


Figure 2.23: DC shunt coupled HRES.

the common inverter fails, the whole system will be malfunctioned.

### 2.4.3 Multi-input Coupled HRES

The AC or DC shunt coupled HRES requires multiple converters and the associated controllers as well as communication techniques between individual converters. As a result, the cost associated with the HRES increased substantially. To address this challenge, multi-input converter (MIC) have been proposed and developed, which is capable of interfacing different renewable energy sources and energy storage systems in one single power stage to achieve individual and simultaneous power transfer to the utility grid. The MIC offers several advantages, i.e., simple circuit topology with a reduced number of semiconductor switches, centralized control, and low manufacturing expense and size [80]. The MIC can be further divided into three categories, namely, (i) Non-isolated MIC, (ii) Isolated MIC, and (iii) Semi-isolated MIC.

Fig. 2.24 illustrates the non-isolated MIC, which is comprised of a buck and buck-boost fused multi-input DC-DC converter and an inverter [81]. In this topology, the

rectified WT output and PV output are fed as inputs to the MIC. The maximum power from renewable energy sources can be extracted individually and simultaneously by applying the appropriate switching scheme with a suitable MPPT algorithm in this framework. Then, the inverter with an appropriate control and modulation scheme is employed for converting the regulated DC power into AC power to meet the grid specifications. In this solution, galvanic isolation is unavailable between the source and load, which may induce significant common-mode current and EMI issues.

The isolated MIC is illustrated in Fig. 2.25, which consists of a multi-input isolated DC-DC converter and an inverter. The high-frequency transformer is utilized in the isolated MIC configuration to provide the galvanic isolation between the source and load. It can extract the maximum power from both energy sources individually and simultaneously, and meanwhile can regulate the low-level DC voltage. The required sinusoidal AC power can be obtained by utilizing the inverter with appropriate control and modulation strategies in this framework. The size of the high-frequency transformer can be reduced by leveraging the emerging wide bandgap switches and operating at high switching frequency (e.g., tens of kHz).

A semi-isolated MIC is shown in Fig. 2.26. It is comprised of both non-isolated converters for obtaining the maximum power from RE sources and isolated converters for galvanic isolation. The different types of power converter configurations employed in the state-of-the-art wind-solar HRES are summarized in Table 2.6.

#### **2.4.4 Inverter Configurations for HRES**

The grid inverters play a critical role in the HRES, not only converting the DC power into AC power to be integrated grid, but also may provide ancillary grid service if needed. Grid inverters can be classified into two broad categories: self-commutated

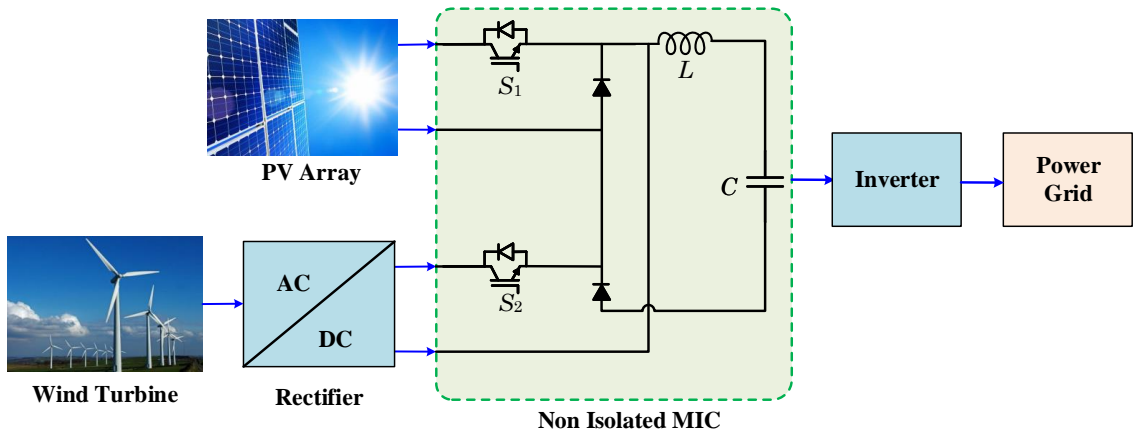


Figure 2.24: Non-isolated MIC coupled HRES.

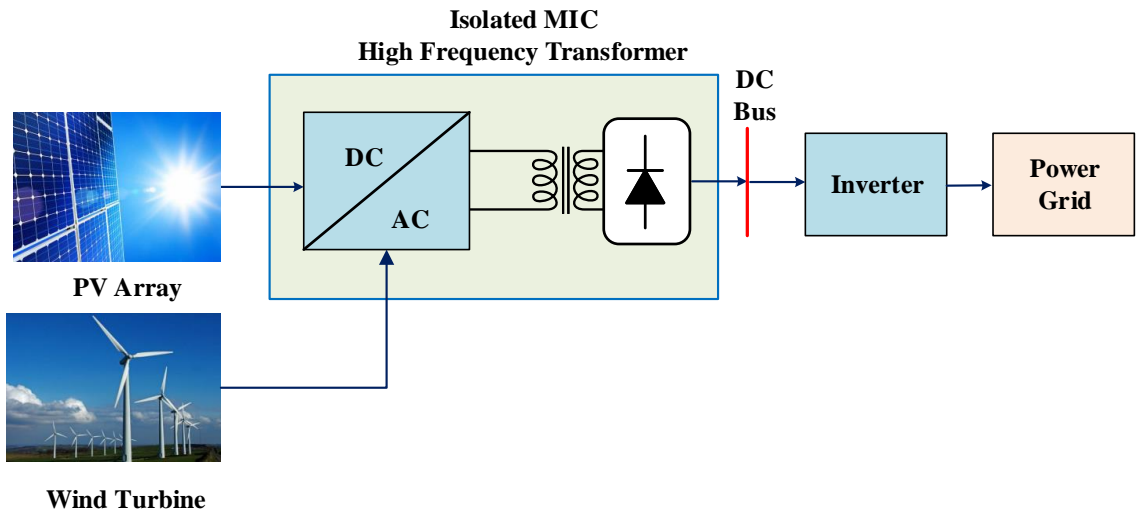


Figure 2.25: Isolated MIC coupled HRES.

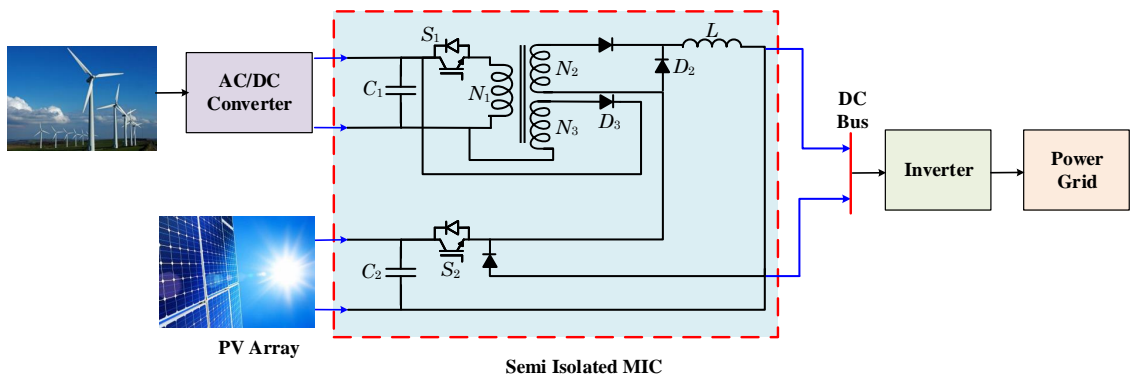


Figure 2.26: Semi-isolated MIC coupled HRES.

Table 2.6: Types of power converter configurations implemented in wind-solar HRES.

Ref.	System Topology	Converter Topology	Highlights
[82]	PV-WT-BESS	AC shunt	Improve smoothing performance of the HRES; Novel SOC control strategy of the BESS; Effectively regulate the HRES power output levels.
[83]	PV-Wind-ESS	AC shunt	Evaluate the ESS control strategy for HRES during fault-ride condition; Analyze the dynamic performance of superconducting magnetic energy storage system to protect the critical loads.
[84]	PV-WT-BESS	AC shunt	Economic analysis using genetic algorithm; Implement a supervisory controller to manage energy between the HRES units.
[85]	PV-WT-BESS	AC shunt	Flexible power control of each HRES unit; Decentralized power management strategy.
[86]	PV-WT	DC shunt	Extending PI controllers are employed to extract the maximum power from the PV-WT scheme; The total harmonic distortion is found within a grid compliance standard.
[87]	PV-WT-BESS	DC shunt	Investigate power-control techniques of a HRES with versatile power transfer; A supervisory strategy is employed to regulate the power generation of the individual HRES units.
[88]	PV-WT-BESS	DC shunt	Optimal BESS sizing; Cost minimization of the HRES; Improve power quality injected into the grid; Increase power supply reliability.
[89]	PV-WT-BESS	DC shunt	Simple power management technique; Reduce the number of power converter for HRES; Eliminate the need for dump loads; Improve HRES efficiency.
[90]	PV-WT-HESS	DC shunt	Hourly dispatching scheme of the HRES is demonstrated; Optimal scaling of the HESS is investigated; Economic analysis of the ESS is presented.
[79]	PV-WT	Non-isolated MIC	Unique nine-switch front end configuration for connecting HRES units; Reverse-boost mode; Accurate power dispatch.

Ref.	System Topology	Converter Topology	Highlights
[91]	PV-WT	Non-isolated MIC	Propose front-end rectifier configuration for hybrid PV-Wind framework; Eliminate the need for input filter; Adaptive MPPT is employed to extract the maximum power from the HRES.
[92]	PV-WT-FC-BESS	Non-isolated MIC	Improve reliability and dynamic response of the HRES; Proposed strategy works in both transient and steady-state power sharing modes.
[93]	PV-WT-FC-BESS	Non-isolated MIC	Five port DC-DC converter; Load dynamic regulation; Improve reliability of the HRES.
[94]	PV-WT	Isolated MIC	Simple framework; Energy management; Minimum number of power switches.
[95]	PV-WT-BESS	Isolated MIC	Four port DC-DC converter; Dynamic modeling and closed loop design; Feature low component count and zero-voltage switching operation.
[96]	PV-WT	Semi-isolated MIC	Simplify the power system; Deliver continuous power; Minimize the cost; Overcome high-voltage-transfer-ratio problem.
[97]	PV-WT-BESS	Semi-isolated MIC	Zero-voltage switching is realized for all primary switches; Bidirectional capability; Low component count; Achieved maximum power harvesting for PV and/or WT.
[98]	PV-WT-BESS	Non-isolated MIC	Utilizes only four power switches which are independently controlled with four different duty ratios; Newton-Raphson algorithm based maximum power point tracking strategy is proposed for PMSG variable speed WT generating system.
[99]	PV-WT-BESS	Semi-isolated MIC	Reduced number of power conversion stages; Less component count; Higher efficiency and reliability; Optimal charging of the ESS utilizing multiple sources; Simple control strategy.
[100]	PV-WT	Isolated MIC	Compact structure; Automatic load regulation; Soft switching; Regulates zero-current switched turn-off under a wide load, as well as input voltage variations.



inverter and line-commutated inverter. The turn-on and turn-off characteristics of the switching devices depend on the polarity of the current flow in the line-commutated inverter. However, the self-commutated inverter can be employed with full control of the switching devices.

The commutation process in the line-commutated inverter is initiated by the parameters of the grid, i.e., the reversal of AC voltage polarity and the flow of negative current. In general, the semi-controlled power switching devices, such as thyristors, are utilized in this scheme. Although the turn-on process of the semiconductor power switches can be controlled by the gate terminal of the device, an external circuitry, i.e., anti-parallel diode, is required to control the turn-off operation as well. The schematic diagram for a line-commutated current source inverter (CSI) is shown in Fig. 2.27 (left) [101].

The self-commutated inverter is the fully controlled power converter, as shown in Fig. 2.27 (right) [102]. The power switching devices, such as IGBTs or SiC MOSFETs, are utilized in the self-commutated inverter configuration. This framework also provides the facilitates to enable the current transfer from one switching device to another in a controlled manner. The self-commutated inverter can be divided into voltage source inverter and current source inverter.

Based on the existence or absence of the transformer, the inverter configuration can be classified into two categories, i.e., those with transformers and the transformerless ones. When a transformer is embedded in the inverter configuration, it provides galvanic isolation between the HRES and the utility grid. Since the transformers are bulky and costly, the overall expenditure of the HRES will be increased considerably in comparison with the transformerless inverter scheme. In transformerless inverter topology, the inverter output are generally medium-voltage levels, and additional cir-

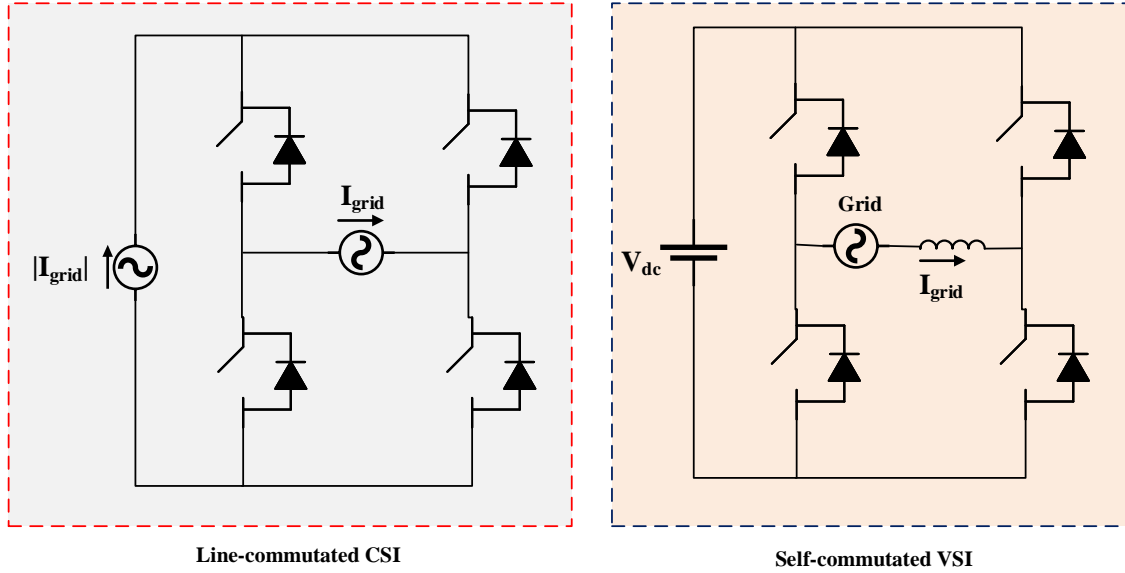


Figure 2.27: Grid-connected inverters.

cuitry may be needed to address the problem of DC current injection. Furthermore, as there is no galvanic isolation in the transformerless inverter architecture, it might induce voltage fluctuation, common mode voltage, and leakage current issues between the RE sources and the ground [103].

### Multilevel Inverters

Multilevel inverters are the power inverters that utilize a large number of semiconductor switches, which can withstand higher DC-link voltage and synthesize staircase quasi-sinusoidal waveforms. Thus, the output line voltages possess much lower THD, lower  $dv/dt$ , and lower common-mode voltage, in comparison to the conventional two-level voltage source inverters. Therefore, the size and cost of the harmonic and EMI filters will be dramatically reduced. There are several types of multilevel inverters, such as NPC inverters, cascaded H-bridge inverters, flying capacitor inverters, modular multilevel converters, as well as numerous derivatives of these topologies [103], [104]. Each multilevel inverter topology has its pros and cons, depending

on the specific HRES applications and power mission profiles. The selection of the inverter topology requires comprehensive performance analysis by concurrently considering the efficiency, cost, power density, and reliability.

The T-type converter is one of the advanced NPC converter configurations that have the benefits of reduced number of switching elements and higher efficiency compared to conventional I-type NPC converter [105]. The 3-level I-type NPC inverter (3L-INPCI) and 3-level T-type NPC inverter (3L-TNPCI) are the most extensively utilized topologies for grid-tied renewable energy applications. The circuit architecture of the 3L-INPCI is illustrated in Fig. 2.28. The clamping diodes linked to the neutral point enable producing a zero-voltage level, with which the three different output voltage levels are obtained. The 3L-TNPCI excludes the clamping diodes from the topology, as shown in Fig. 2.29. The inner switches ( $S_2$  and  $S_3$ ) are associated with the neutral point of the DC bus, blocking half of the DC-bus voltage. Therefore, the breakdown voltages of inner switches ( $S_2$  and  $S_3$ ) can be half of these with the outer switches ( $S_1$  and  $S_4$ ). In comparison with the 3L-INPCI, the 3L-TNPCI has the leverage of shorter commutation loops and reduced number of switches due to no clamping diodes.

The diode clamped, flying capacitor (FC), and cascaded H-bridge (CHB) topologies are the most frequently utilized multilevel inverter (MLI) configurations in grid-interfaced RE systems. These three MLI topologies are considered as the classic MLI topologies, and they are widely employed in industries due to their common advantages, including lower harmonic distortion, higher voltage withstanding capability, lower common mode voltage, and lower  $dv/dt$  in the output waveforms. [106]. The configuration of a single-phase leg of these three topologies is depicted in Fig. 2.30. The modular multilevel converter (MMC) is another popular MLI topology that has

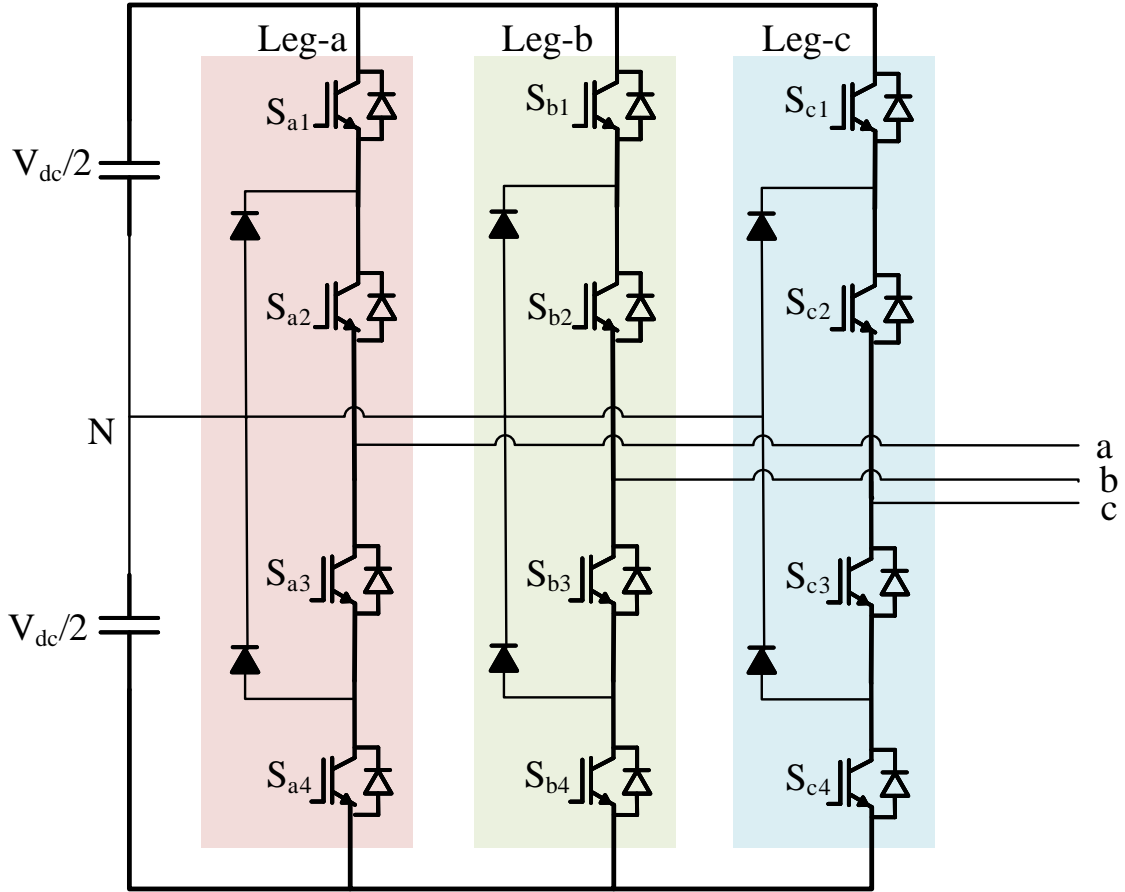


Figure 2.28: Circuit topology of 3-level I-type NPC inverter.

received increasing attention for renewable energy integration due to its superior features such as modularity, scalability, high efficiency, and high output waveform quality [107]. The general topology of an MMC is illustrated in Fig. 2.31. The submodule (SM) can be either a half-bridge or full-bridge circuit, depending on the performance requirements. Unlike half-bridge MMC, full-bridge MMC can be controlled to isolate and tolerate a DC short-circuit fault, which is preferred for safety-critical HRES applications, while at relative higher cost due to the larger number of power devices [108]. Furthermore, based on the number of employed DC sources, the classic MLI topologies can be classified into two main groups, as shown in Fig. 2.32. The classic MLI configurations have been thoroughly analyzed in the literature, and each has its own

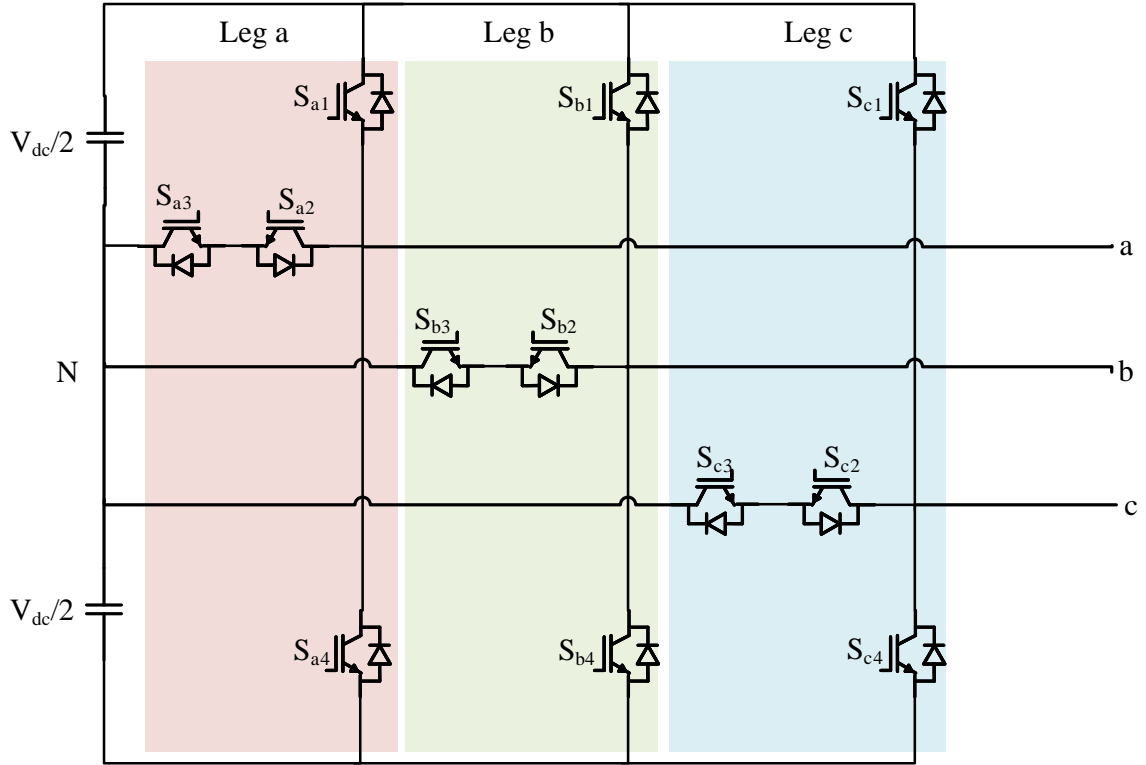


Figure 2.29: Circuit topology of 3-level T-type NPC inverter.

set of benefits and drawbacks. Here, a comparison between the classic MLI topologies is contemplated in terms of the advantages and disadvantages, as illustrated in Table 2.7 [109], [110], [111], [112], [113]. In the Table 2.7, the common advantages with MLI such as lower harmonic distortion and lower common-mode voltage are excluded, and only their unique characteristics are summarized.

#### 2.4.5 Grid Coupled Inverter Controller

In the grid-connected inverter control architecture, the grid synchronization to power flow management and pulse width modulation (PWM) of the inverter is occurred. This control topology employed an outer DC-link voltage control loop and an inner current control loop to secure decoupled regulation of active and reactive power components. The grid voltage-oriented reference frame utilized for transformations

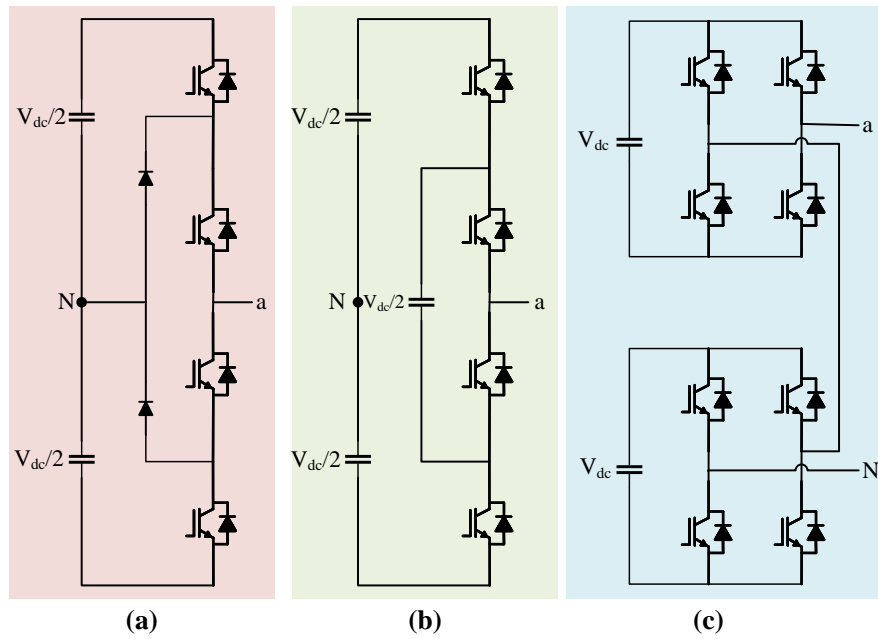


Figure 2.30: Classic multilevel inverter topologies (with one phase shown). (a) Three level diode clamped. (b) Three level flying capacitor. (c) Five level cascade H-bridge.

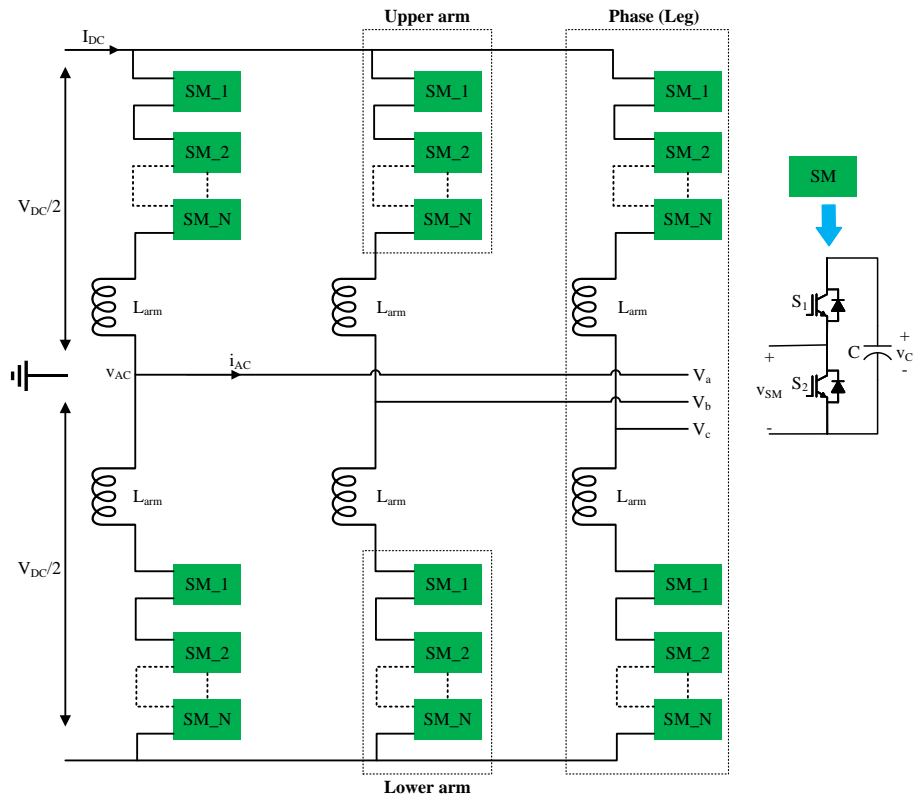


Figure 2.31: The topology of a modular multilevel converter.

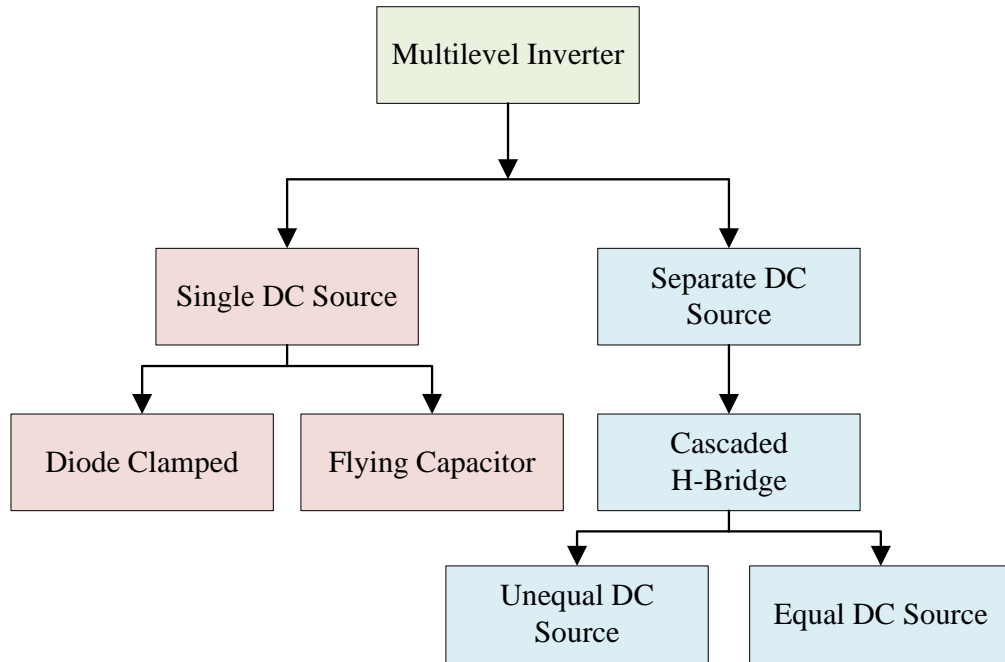


Figure 2.32: Multilevel inverter classification.

deploys the phase angle provided by instantaneous voltage measurements. The voltage control loop is responsible for maintaining the DC bus voltage and providing the active power current reference to the internal current loop. The current control loop, based on the active power current reference and reactive power current reference, yields the appropriate voltage reference signals. The desired voltage reference signals realized from the current controller are then employed to provide PWM pulses for the semiconductor switches in the inverter.

Nowadays, inverter-based resources are becoming an inevitable part of AC power systems due to the rapid advancement of hybrid PV-Wind grid integration. Inverter-based resources utilized in the HRES framework are responsible for providing active and reactive power to the grid. They can be categorized into two main groups: grid following inverter and grid forming inverter. The main discrepancy between the grid-forming and grid-following is the synchronization approach that gives the correct

Table 2.7: Summarized advantages and disadvantages of classical topologies.

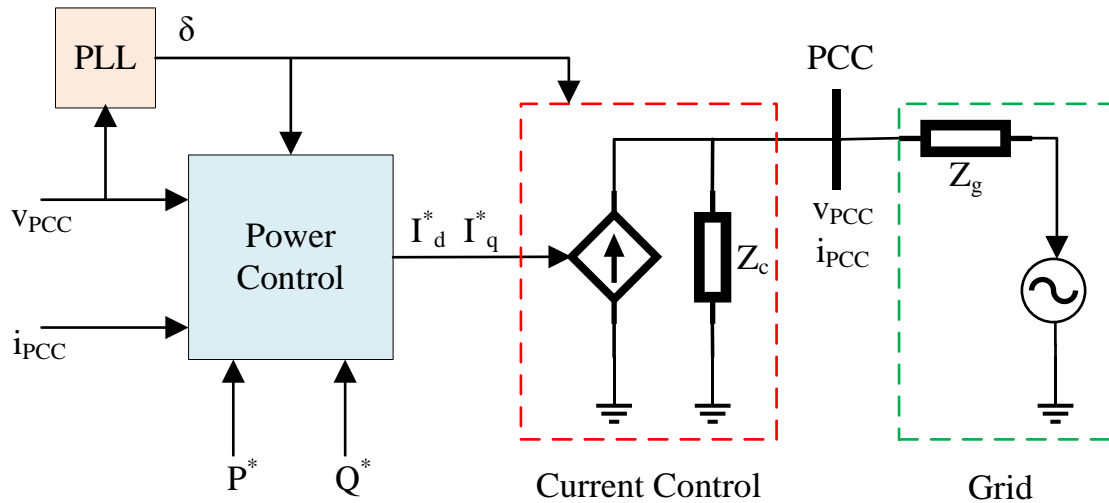
Topology	Advantages	Disadvantages
Diode-Clamped	<ul style="list-style-type: none"> <li>• Single DC source (no requirements for multiple isolated DC sources).</li> <li>• Switches experience less voltage stress.</li> <li>• Capable of pre-charging the capacitors as a group.</li> <li>• Straightforward control mechanism.</li> <li>• Capability for fault-tolerant operation.</li> </ul>	<ul style="list-style-type: none"> <li>• Uneven semiconductor loss distribution.</li> <li>• DC-bus neutral point voltage floating.</li> <li>• The complexity of voltage balancing circuit.</li> <li>• Increased number of clamping-diodes as the level increased.</li> <li>• Issues with balancing and stabilizing the DC voltage of the capacitor.</li> </ul>
FC	<ul style="list-style-type: none"> <li>• Single DC source (no requirements for multiple isolated DC sources).</li> <li>• Extra ride through capability during power outage.</li> <li>• Appropriate switching combination for balancing different voltage levels.</li> </ul>	<ul style="list-style-type: none"> <li>• High number of clamping capacitors which may cause reliability degradation in harsh environment.</li> <li>• Lower power density at low-frequency operation due to the size of the flying capacitors.</li> <li>• Unbalanced voltage among clamping capacitors.</li> <li>• High complexity of the voltage balancing circuit.</li> <li>• Packaging becomes more complex as the number of voltage levels increases.</li> </ul>
Cascaded H-Bridge	<ul style="list-style-type: none"> <li>• Good modularity.</li> <li>• Easy to extend it to higher levels by stacking up.</li> </ul>	<ul style="list-style-type: none"> <li>• More gate driver circuits are required.</li> </ul>



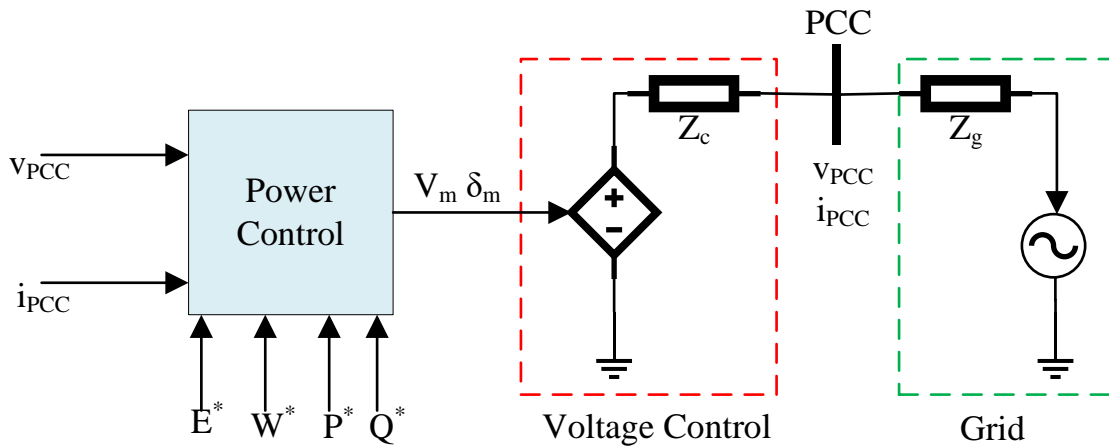
Topology	Advantages	Disadvantages
Cascaded H-Bridge	<ul style="list-style-type: none"> <li>• No need for extra diodes and capacitors.</li> <li>• Symmetric and asymmetrical topology options.</li> </ul>	<ul style="list-style-type: none"> <li>• It requires multiple isolated DC sources to increase the output voltage.</li> <li>• Switches must have a blocking voltage equal to the input voltage.</li> </ul>
MMC	<ul style="list-style-type: none"> <li>• Modularity and scalability.</li> <li>• Absence of additional bulky capacitors on the DC bus.</li> <li>• Fault tolerance for full-bridge MMC.</li> <li>• SM modules are composed of power devices with low voltage ratings at low cost.</li> </ul>	<ul style="list-style-type: none"> <li>• SM capacitor voltage balancing algorithm is required.</li> <li>• Control strategy needs to be implemented to reduce the AC components of the circulating currents under fixed-frequency operation.</li> <li>• Additional circuit arrangements are required to control the SM capacitor voltage ripple at low frequencies.</li> </ul>

rotation in the  $abc/dq$  transformation.

To this date, the grid following inverter is dominated where a phase locked loop (PLL) is employed to align with the grid voltage at the point of common coupling (PCC) of the converter. Therefore, it follows the measured voltage by aligning and utilizing the measured voltage as a reference. As a result, the grid following inverter is not expected to respond to grid frequency variations. This specific grid following characteristic resembles a current source. On the other hand, the primary objective of the grid forming inverter is regulating the voltage and frequency of the grid. The control of converters should be restructured from a grid-following to a grid-forming control to avoid the challenges associated with low inertia. In this way, it can provide damping to frequency variations and whose character is more similar to that of a



*Grid Following Inverter*



*Grid Forming Inverter*

Figure 2.33: Control working principles: (a) Grid Following Inverter (Top), (b) Grid Forming Inverter (Bottom).

synchronous machine. This is feasible since the grid forming system generates its own internal voltage reference angle based on the output power of the converter. A simplified representation of the working principles of the grid following inverter and grid forming inverter is documented in Fig. 2.33.

#### 2.4.6 Filter Topologies for HRES

High-frequency switching of power converters in the HRES framework produce considerable harmonics in the systems. Typically, for commercial and utility-scale power converters, the switching frequencies between 2 to 15 kHz can generate high-order harmonics that is responsible for inducing grid stability and harmonics issues. In general, a passive filter needs to be employed to mitigate or eliminate the harmonics around multiples of the switching frequency ( $f_{sw}$ ). Likewise, there are several factors to be concurrently considered during the filter development, namely, attenuation ratio, voltage drop, losses, cost, weight, and volume [114].

Different circuit topologies of the grid-connected filter, such as L-filter, L-C filter, and L-C-L filter, are analyzed in the literature. The most essential features—harmonic attenuation, system decoupling between the filter and grid impedance—are discussed while comparing different types of filter configurations. Due to its simple structure, the L-filter can easily be implemented. However, a high value of inductance or higher switching frequency needs to be selected for reducing the harmonics around the switching frequency. As a consequence, the system dynamic response may become sluggish, and the switching losses in the semiconductor power devices may increase significantly. Although the L-C filter has satisfactory performance in voltage-current conversion, the damping of the high-frequency noise has been a challenge.

In the L-C-L filter configuration, the damping of the high-frequency noise is improved due to its extra inductance. In addition, the capacitor in the L-C-L filter is not exposed to line current distortion at the fundamental frequency, unlike the L and L-C filters [115]. The utilization of the L-C-L filter in the HRES framework provides several advantages, i.e., relatively low switching frequency requires for a given harmonic attenuation, reduces the grid current distortion, decreases the reactive power

production, and so on [116], [117].

The LCL filter is a third-order filter with a  $-60 \text{ db/decade}$  attenuation that produces a resonance peak. Therefore, the LCL filter must be designed meticulously according to the parameters of the inverter. Several attributes, such as current ripple, filter size, and switching ripple attenuation, must be addressed while designing an LCL filter. The design approach of the LCL filter is documented in [118].

The first step in the procedure of designing LCL filter parameters is the estimation of the base impedance ( $Z_b$ ) and base capacitance ( $C_b$ ) values as expressed below:

$$\text{Base impedance, } Z_b = \frac{V_g^2}{P_n} \quad (2.20)$$

$$\text{Base capacitance, } C_b = \frac{1}{2 \times \pi \times f_g \times Z_b} \quad (2.21)$$

where  $V_g$  is the line to line RMS voltage (inverter output),  $P_n$  is the rated active power, and  $f_g$  is the grid frequency.

The next step in computing the filter components is the design of the inverter side inductance ( $L_i$ ), which can be indicated as:

$$L_i = \frac{V_{DC}}{16 \times f_{sw} \times \Delta I_L} \quad (2.22)$$

where  $V_{DC}$  is the DC bus voltage,  $f_{sw}$  is the switching frequency, and  $\Delta I_L$  is the current ripple specified by:

$$\Delta I_L = (1\% - 10\%) \frac{P_n \times \sqrt{2}}{V_g} \quad (2.23)$$

Then, the filter capacity ( $C_f$ ) is calculated as a multiplication of  $C_b$  by accounting the maximal power factor variation accepted by the grid 5%.

$$C_f = 0.05 \times C_b \quad (2.24)$$

The grid side inductance ( $L_g$ ) can be determined as:

$$L_g = r \times L_i \quad (2.25)$$

where  $r$  is the ratio between the  $L_i$  and  $L_g$ .

The final step in the design is to regulate the resonant frequency ( $f_{res}$ ) of the filter. Since the filter must have enough attenuation in the  $f_{sw}$  of the inverter, the  $f_{res}$  should be far above the grid frequency ( $f_g$ ) and lower than the switching frequency  $f_{sw}$ .

$$f_{res} = \frac{1}{2\pi} \times \sqrt{\frac{L_i + L_g}{L_i \times L_g \times C_f}} \quad (2.26)$$

$$10f_g \leq f_{res} \leq 0.5f_{sw} \quad (2.27)$$

The filter capacitor ( $C_f$ ) should be included with an in series connected resistor to diminish oscillations and unstable states of the filter. The value of the damping resistor ( $R_d$ ) can be expressed as:

$$R_d = \frac{1}{3 \times 2 \times \pi \times f_{res} \times C_f} \quad (2.28)$$

## 2.5 HRES Optimization

The primary objective of using optimization techniques in HRES is to achieve superior overall performance as well as to meet grid requirements and constraints. It is crucial to implement a systematic optimization algorithm to solve the optimal solution which provides the least annual cost as well as fulfilling the requirements. Recent survey has indicated that there are different types of optimization algorithms used by the researchers for HRES, such as the genetic algorithm (GA), PSO, the shuffled frog leaping algorithms, etc. [119]. Constrained by system cost, efficiency

target, and local weather conditions, a systematic sizing optimization method will be of paramount importance for HRES. Table 2.8 presents a summary of the analysis and sizing constraints employed for optimum sizing of the wind-solar HRES.

Furthermore, the widely utilized modelling and optimization approaches for the HRES can be categorized as: classical algorithms, metaheuristic methods, and hybrid of two or more optimization techniques. The differential calculus manner is used in the classical optimization algorithm to seek optimum solutions for differentiable and continuous functions. Therefore, it exhibits limited capabilities for applications whose objective functions are not continuous and/or differentiable [120]. Metaheuristic strategies have the potential to provide efficient, accurate, and optimal solutions, and it is extensively employed for optimizing the complex HRES. Metaheuristic approaches are nature-based, and their evolutions are based on the behavior of nature [121], [122]. In the hybrid techniques, two or more optimization approaches are combined to overcome the limitations of the individual strategies mentioned above. Consequently, it can provide more effective and reliable solutions for HRES [123]. The attributes of these optimization techniques are synopsised in Table 2.9.

The various criteria are contemplated in the literature for optimal sizing of the HRES can be mainly categorized as economic and technical. Economic criteria are employed to minimize the expenditure of the HRES. The cost optimization of the HRES, which objective is to seek the compromise solution between the costs and benefits, including minimizing energy cost, net present cost, and any other costs associated with the HRES. On the other hand, technical criteria deal with the reliability, efficiency, and environmental benefits of the HRES. The objective of the technical criteria fulfills the desired reliability levels based on loss of power supply probability, curtailing cost/efficiency ratio, minimizing carbon emissions and maximizing power.

Table 2.8: Optimization algorithms of “Wind+Solar” HRES.

Ref.	Optimization Technique	Optimization Constraints	Highlights
[84]	GA	Economic	Satisfy the load demand under all conditions.
[124]	GA	Minimum annualized cost; LPSP	Good optimization performance; Relationships between the system reliability and configurations are evaluated.
[125]	Multi-objective GA	LPSP; Annualized cost	Optimal sizing; Correlations between the cost of the optimal configuration and load profile are assessed.
[126]	PSO	Total cost	Address the equality constraints for power balance; Achieve the lowest accumulated cost.
[127]	PSO	Techno-socio-economic	Optimal sizing; System reliability evaluation is carried out using an analytical approach.
[128]	Multi-objective PSO	Reliability	Produce appropriate sizing of the HRES components for each location; Enhancing energy access for remote locations.
[61]	Forever power	Reliability; Cost; Environmental benefit	Economic analysis is carried out to seek the most feasible combination of the HRES components.
[75]	GA	PV array capacity; WT numbers; ESS numbers	Optimal sizing; Relationships between the HRES power fraction and the cost of energy are investigated.
[16]	Iterative filter selection	Minimization of unutilized surplus power	Yield minimum total cost and maximum reliability.
[26]	PSO	Economic and technical indexes	Minimize the life-cycle cost; Optimal capacity of the HRES.
[129]	Iterative	Deficiency of power supply probability; Unutilized energy probability	Optimize the size of HRES for a specific location.

Ref.	Optimization Technique	Optimization Constraints	Highlights
[53]	PSO	Economic and technical	Minimize the annualized cost; Improve the reliability index.
[26]	PSO	Economic and technical	Minimize the life-cycle cost; The influence of the optimal capacity of HRES on life-cycle cost is investigated.
[130]	PSO	Minimize the total cost	Reduce the time required to find the optimum solution.
[131]	OptQuest	Loss of load probability	Optimum sizes of the HRES components are investigated under various auxiliary energy unit costs.
[132]	GA	LPSP	Minimize the annualized cost of the HRES; Five decision variables are evaluated for optimal sizing of the HRES.
[133]	Multi-objective PSO	Net present cost; CO <sub>2</sub> emission.	Lower net present cost compared to HOMER.
[134]	Multi-objective GA	Techno-economic approach; CO <sub>2</sub> emission.	The HRES optimized while considering its size, cost, and availability criteria.
[135]	LPSP	Reliability; Power quality; loss of supply.	The performance of the HRES is evaluated based on cost and reliability.
[136]	Iterative	Techno-Economic	The WT-PV- Battery combination in the HRES is found to be a more cost-effective scheme compared with other hybrid systems.
[137]	Iterative	Deficiency of power supply probability; Levelized unit electricity cost.	Optimal sizing of the HRES components while fulfilling system reliability requirements.
[138]	Modified PSO	Optimal sizing	Faster convergence speed; Shorter computational time.
[139]	PSO	Total annual cost	The performance of different PSO variants are evaluated for optimal sizing of the HRES components; PSO with constriction factor is found to be more promising than other variants.



Ref.	Optimization Technique	Optimization Constraints	Highlights
[140]	Multi-objective PSO	Annualized cost; Loss of load expected; Loss of energy expected.	Reduce computation time; Technique for reliability evaluation of the HRES is investigated.
[141]	PSO	Total area occupied by the PV and WT; Number of batteries.	Minimize the life cycle cost with a certain level of system reliability; Adaptive inertia weight-based PSO provides more promising results than the other variants.
[142]	GA	Minimization of life-cycle cost; Minimization of pollutant emissions.	Optimal sizing of the HRES components.
[143]	GA	Minimization of life-cycle cost, CO <sub>2</sub> emissions, and dump energy.	Five different types of HRES configurations are investigated for a typical residential load profile to minimize the life-cycle cost of the HRES.
[144]	Improved GA	Service life of the HRES.	Better convergence speed than the standard GA.
[145]	Artificial bee swarm optimization	Minimizing the annual cost; LPSP.	Artificial bee swarm optimization technique utilizes the stochastic rules to escape local optima and find the global solution.
[146]	GA	Minimizing the unmet load.	The user socio-demographic profile is investigated for optimal sizing of the HRES components.
[147]	Curve fitting - PSO	Minimizing the annual cost.	Hourly dispatching scheme of the HRES; Optimal scaling of the HESS; HESS economic analysis.
[148]	Hybrid Iterative-GA	Loss of load probability.	Optimize the inverter size of the HRES.
[149]	Grey wolf optimizer	Reliability	Reduce the curtailment of the HRES generation.

Table 2.9: Comparative comparison among the commonly used optimization techniques for HRES.

Techniques	Algorithms	Advantages	Disadvantages
Classical	Linear programming model	Performs stochastically in reliability and economic analysis.	Energy delivery capability is severely affected by failure any of the RE sources to function effectively.
Classical	Nonlinear programming model	Enables solving complex problems with simple operations.	Increases the required number of iterations as well as computational burden of the problem.
Classical	Dynamic programming	Competent to address the complexity of large systems.	Implementation becomes complex and confusing due to high number of recursive functions.
Metaheuristic	GA	Efficient finding an optimal solution to a given problem.	Might converge in local optima if it is not initialized or designed perfectly.
Metaheuristic	PSO	Efficacious in solving the scattering and optimization problems.	Requires considerable modifications due to its complex and conflicted nature.
Metaheuristic	Simulated annealing (SA)	Independent from initial starting condition; Computer memory requirement is minimal.	Might accept an inferior solution based upon a probabilistic measure.
Metaheuristic	Ant colony (AC)	High convergence speed.	Requires long-term memory space.
Hybrid	PSO-Differential evolution; Monte Carlo simulation (MCS)-PSO; SA-Tabu search; Hybrid iterative-GA; Artificial neural fuzzy inference system; Artificial neural network-GA-MCS.	Ameliorate the overall performance of the optimization.	Increases the coding and design complexity; Might converge into suboptimal solution.

## 2.6 Benefits and Challenges of HRES

To sum up, the advantages of the HRES can be highlighted as follows:

- Continuous power supply.
- Utilize the renewable energy sources in an optimal way.
- Low maintenance cost.
- High efficiency.
- Load is supplied in the most optimal way.
- Improves the dispatch flexibility.
- Greater balance in energy supply.
- Yield greater economic and environmental returns.
- Reduces negative effects associated with burning fossil fuels.
- HRES can be synchronized to ameliorate the RE converter infrastructure.
- Enhance the system reliability.
- Decreases lifecycle costs for peaky loads or growing fixed loads.
- System energy service is enhanced.
- Truncates downtime during repairs or routine maintenance.
- Nearly zero pollutant emissions especially for PV-Wind-Energy storage HRES architecture.
- Relieved transmission and distribution congestion.

- Improved power quality.
- Provides more flexibility for future extension and growth.

Even though the HRES has come a long way in terms of research and development, there are still some impediments in terms of its efficiency and optimal utilization. The challenges associated with the HRES faced by practitioners can be summarized as:

- The HRES demands innovative technology to harness the optimal power from the RE sources.
- The poor efficiency of HRES is a significant hindrance in encouraging its deployment.
- Since the high capital cost leads to a prolonged payback time, the manufacturing expenditure of RE sources requires a substantial reduction.
- The power electronic devices interfaced with HRES should be a minimal amount of power loss.
- Geography plays a prominent role in the HRES deployment.
- Due to the high installation expenditure, government incentive policies are required to make the HRES economically viable.
- The energy storage technologies deserve more research attention and efforts to ease their durability and performance.
- Real-time energy management and robust communication between the respective energy sources of the HRES require to be ameliorated through cutting-edge investigation.

- Systematic approaches and standardization, e.g., IEEE Standard 1547, are demanded effective and safe deployment of the HRES.
- As the new advanced semiconductor devices such as silicon carbide and gallium nitride become available, research efforts are required to integrate them into the evolving HRES.
- System reliability and energy sustainability are needed to be improved to the maximum extent possible.

## **2.7 Future Trends of HRES**

In the future, operators would like RE plants to have the ability to operate more like traditional power plants in terms of capacity value, dispatchability, ancillary services, and reliability. As higher HRES capacity is connected to the power grid, it is expected that integration technology for high levels of HRES penetration will be an important research area in the following decade. Here, the future trends of the HRES are outlined as follows:

- Further advances in wind-solar technologies will significantly reduce the cost of HRES. As a result, HRES will be more cost-effective in the future. Aside from the expense, the environmental advantages are likely to make this hybrid system more widely used and accepted.
- A modern control technique can be employed to ensure optimal resource allocation based on load demand and RE resource forecast. Correspondingly, the total operating cost of HRES will be reduced substantially.

- Artificial intelligence as part of the energy management system has the potential to improve HRES operation.
- Advanced control methods implemented in a centralized system controller can ameliorate the performance of modular hybrid systems.
- Advanced research in the control and operation of HRES should be performed in the areas of grid code compliance and the potential to provide ancillary services to the grid.
- Developing an RE optimization model or toolset to survey and analyze market and resource conditions in order to assess the performance and cost of HRES.
- Evaluate HRES-specific design challenges and opportunities, e.g., economies of scale, technological innovation.
- Standard guidelines on the forecasting of hybrid power plant energy in commitment and dispatch operations must be defined for utilities.
- Most HRES plant designs are still in the early stages of development, which means that their long-term viability in terms of energy and capacity has yet to be established.
- Investigate various system architectures (AC coupled, DC coupled) and innovations related to inverters within the HRES.
- During the implementation of the HRES project, a systematic approach for optimizing the sizing of different assets and their layout to meet land constraints must be devised.

- As the penetration of the HRES increases, specifications for transient voltage and frequency become more critical. As a result, many countries' grid codes will need to be updated to accommodate the integration of the HRES generation and maintain a stable operation.
- The ESS becomes an indispensable component by strongly supporting ramp control and frequency regulation in HRES deployment. As a result, more detailed grid codes for ESS are expected in the future, including inertia emulation, power oscillation damping, and voltage control.
- Advanced weather forecasting techniques will reduce the uncertainty of HRES generation considerably and avoid HRES energy curtailment substantially.
- Both the sensitivity and reliability assessments of any proposed HRES configuration should be carried out.
- Develop a paradigm that would enable a feedback mechanism between end-users and grid operators to further improve the system's reliability and flexibility.
- There should be a minimal amount of power loss in the power electronic devices while interfacing the HRES to the utility.

## 2.8 Summary

In this chapter, a comprehensive review of existing wind-solar hybrid renewable energy resources is conducted, in which the system modeling, power converter configurations, and the optimal design algorithms are reviewed. The basic mathematical modeling of PV and WT, and the degradation model of batteries and supercapacitors are discussed in this study. A critical review of different HESS topologies is presented.

A comparative study on different power converter configurations employed in the wind-solar HRES is also reported. Commonly used optimization algorithms in the literature for optimizing the wind-solar HRES system are analyzed and summarized. Although considerable accomplishments have been achieved over the years on various HRES, a comprehensive review helps to identify and fulfill the technical gaps for improving the future HRES.



### Chapter 3 Cost Optimization of Battery-Supercapacitor Hybrid Energy Storage for Hourly Dispatching Wind-Solar Hybrid Power System

As more PV and WT are connected to the grid, overgeneration and curtailment become the rising concerns for the grid operators. There are primarily two causes, namely, local transmission constraints and supply-wide oversupply for RE curtailment. The range of the curtailment levels between 1% to 4% of wind generation has occurred, but higher levels of curtailment have also been reported [150]. Negative pricing and RE generation curtailment take place when the inflexible traditional generator, like nuclear and coal plants, cannot be employed to generate lower power.

It is well known that either wind or solar source cannot provide a continuous power supply to the load individually. It is also noted that the peak operating time for wind and solar system occur at different times of the day and the year. In fact, solar and wind energy resources are complementary to each other, due to the weather and climate patterns. As a consequence, the energy production by Wind-PV resources offset each other on a seasonal or day-to-day basis. Therefore, hybridization techniques can be developed to solve the variable nature of solar and wind power. The WSHPS incorporates the PV and WT subsystems together to provide increased systematic efficiency, lower required capacity of energy storage, and improved stability in power supply [4]. The uncertainty of RE resources can be reduced further by including the ESS in the WSHPS framework. Here, a HESS consisting of a BESS and a SESS is employed to develop a cost-effective ESS, where the SC facilitates to alleviate the fast-changing power components passing through the battery, which is beneficial for increasing the battery's service life [151].

The main objective of this chapter is to enhance the integration of RE that secures a desired hourly dispatching of the WSHPS output power at one-hour increments for an entire day to the power grid. Here, a HESS consisting of the lithium-ion batteries and SC is incorporated into the WSHPS architecture that can accumulate the harvested WSHPS energy and convert the sporadic energy into a dispatchable supply at an intended confidence level. The proposed dispatching scheme enables the WSHPS to be a reliable source of power for the utility, which can be regulated like any other conventional generators, i.e., thermal and hydropower plants. Furthermore, the WSHPS output power supplied to the grid using a dispatched scheme provides considerable flexibility to the utility grid, especially in the scheduling of generation units, grid operation economics, and grid ancillary services. Since most of the supply side adjustment in the utility grid takes place on an hour-to-hour basis, a one-hour dispatching interval is taken into account in this study.

Here, the LPF is employed to decouple the HESS power into two different categories: one has a fast-dynamic response specified to the SC while the other has a slow dynamic response specified to the battery. This technique assists the battery in avoiding the fast-changing charging-discharging cycles and a considerable magnitude of discharge current, accordingly prolonging the battery's lifetime. The battery lifetime comparison with and without the SC in the ESS architecture is also explored. Furthermore, the curve fitting and PSO approaches are applied to seek the optimum value of the LPF time constant that yields the most cost-effective HESS for hourly dispatching the WSHPS power. The objective function is minimizing the expenditure of the HESS with the constraint of regulating the SOC of the ESS within a specified range and successfully fulfilling the power demand for each dispatching period.

Besides, several control algorithms based on the battery SOC are developed to

achieve accurate estimation of the  $P_{\text{Grid,ref}}$  for each one-hour dispatching period. The SOC control algorithms also ensure the ESS to complete each dispatching period with the same SOC as it started. This mechanism plays a significant role in regulating the battery SOC within a specified range which helps to minimize the energy storage cost and ensures that the ESS has enough capacity available for next-day operation. An economic comparison is presented to investigate the impact of using different types of SOC control algorithms in the  $P_{\text{Grid,ref}}$  estimation.

In this research, the  $P_{\text{Grid,ref}}$  for the WSHPs is generated utilizing two different schemes, i.e., (i) dispatchable power reference case—estimating the  $P_{\text{Grid,ref}}$  utilizing the methodology described later in this chapter and (ii) load following case—load profile for 2.5 MW utility is collected from CAISO and is utilized as a  $P_{\text{Grid,ref}}$  for the entire system. A comparative economic assessment between the two schemes is also investigated in this work.

The expenditure associated with the ESS substantially depends on two aspects, namely, (i) lifetime of the ESS and (ii) minimum capacity required of the ESS. The service life of the ESS primarily relies on the utilization of DOD and the rate of charging-discharging power changes. In general, the ESS manufacturers specify energy storage cycle life as a function of DOD, and the deeper discharge of the ESS reduces the lifetime as well as increases its expense substantially. Hence, the SOC of the ESS has always been controlled to prevent the ESS depletion beyond its recommended DOD. This kind of constraint facilitates to prolong the lifespan of the ESS significantly. However, such SOC regulation is responsible for restricting the full utilization of the ESS, which is one contributing factor extending the required energy storage capacity. Thus, based on the usage of SOC, there is a trade-off between the service life and the minimum capacity required of the ESS. In this research, the op-

imum value of DOD has been investigated which exhibits the best competitive ESS cost for hourly dispatching the WSHPS power to the utility grid. In addition, after seeking the optimal value of DOD for the ESS, one secondary SOC control algorithm is also employed to regulate the ESS SOC in the optimal range.

The objective here is to develop a cost-effective ESS for the hourly dispatch of WSHPS power. An economic comparison is presented to investigate the impact of using three different types of energy storage systems: (i) battery only, (ii) HESS framework, i.e., the combination of a Li-ion battery and a SC, and (iii) SC only. Also, an economic comparison of using three different types of renewable energy sources—(i) PV only, (ii) WSHPS framework, i.e., the combination of the WT and the PV, and (iii) WT only, with HESS framework for the fulfillment of the  $P_{\text{Grid,ref}}$  is analyzed in this research. To obtain annual energy storage costs, the actual PV and WT data of four different days as representative of four seasons, which was recorded by U.S. NREL, is used in this research [152].

To exhibit the effectiveness of the proposed HESS control framework, a one-hour simulation is illustrated considering all possible cases of the availability of sources investigated in this study—(i) PV+WT+ESS, (ii) WT+ESS, (iii) PV+ESS, and (iv) ESS only, to dispatch the desired  $P_{\text{Grid,ref}}$  for the entire duration.

The rest of this chapter is organized as follows: Section 3.1 presents the state-of-the-art review on this same topic. Section 3.2 describes the proposed methodology for hourly dispatching the WSHPS power. Section 3.3 verifies the effectiveness of the proposed methodology and control methods through simulations. Finally, the summary of this chapter is drawn in Section 3.4.

### 3.1 State-of-the-Art Review

Various strategies have been contemplated in the literature to enable the PV and WT power to be dispatchable by deploying different types of ESS and control techniques. In [153] [154], a control technique has been proposed to smooth the output of the RE sources where the battery has been dispatched on an hourly basis. An iterative procedure has been utilized to calculate the required size of the battery. The control strategy is employed to maintain certain SOC of the battery in order to extend its lifetime. Therefore, a larger size of the battery is required to have an effective hourly dispatch. Another improved control approach for a grid-connected PV and battery energy system has been investigated in [155] to dispatch the PV power smoothly on an hourly basis to the utility grid. However, these control techniques do not take into account the daily cycling of the battery. Furthermore, the battery has been highly exposed to fast-changing components of intermittent PV power that would cause significant downtime cost once the battery fails. Consequently, these proposed techniques might not be feasible to develop cost-effective energy storage for hourly dispatching the PV power.

Wang et al. attempted to develop a BESS in a buffer scheme to attenuate the effects of unsteady input power from wind farms [156]. A computational procedure has been utilized to determine the BESS capacity that ensures a constant dispatched power from the wind farm to the connected grid. The power dispatched in a day was set to be a constant level while the optimal BESS capacity has been investigated. It has been found that the wind farm achieved a substantial profit at the optimal BESS capacity. Since the control strategy utilized in this study depends on the day that the wind was studied, the designed BESS capacity may not be unique.

The authors in [157] investigated a min-max RE dispatching approach where the dispatched power was set to the minimum available RE power during the battery charging phase. On the other hand, when the battery switches to the discharging phase, the dispatched power was set to the maximum available RE power. The complexity of the technique and the large-scale battery rating compared with other dispatching methods might be the downsides of this min-max dispatching method.

In [158], one modified min-max power dispatching method has been proposed to determine the optimal BESS capacity in order to effectively integrate the wind power into the grid. A short-term power dispatch control algorithm has been utilized to smooth the transient power between two consecutive dispatching intervals. Also, the battery SOC has been regulated within a safe range. Since the battery is the only ESS media employed to smooth the wind farm transient power, the charging-discharging cycles of the battery would be extremely high. Therefore, the overall economics of the system might lead to an unacceptable level.

A dual-battery scheme is proposed in [159] to enable a short-term dispatch commitment from the wind power station. In this framework, while the first battery is being charged by the generated wind power, the second battery power is being discharged to the utility grid. The function of the two batteries is shifted when the battery reaches its specified SOC or discharge limit. However, this approach demands the switch-over of battery modules, usually once every few hours, and additional arrangement to diminish the switch-over impact on the utility grid.

In [160], a statistical approach has been utilized to develop a dual-battery scheme in order to dispatch a controllable level of power from a wind power generating station. The expected BESS charging time dictates the scheduled constant discharge power from the BESS to the grid. In this scheme, the BESS is committed to accumulating

all the electrical power generated by the wind turbine, therefore, a large-scale battery is required to dispatch a steady power from an intermittent wind power generating station to the grid. Since the cost associated with the BESS is directly proportional to the size of the BESS, the resulting large-scale battery requirements make the system economically unfeasible.

Another HESS framework for the least-cost analysis to realize dispatchable wind power was discussed by Wee et al. [161]. A statistical approach is proposed to design a HESS for a wind farm to achieve a firm power dispatch objective while maximizing the wind energy harnessed without modeling power converters. Moreover, the power capacities of the battery and SC were limited in the HESS scheme to become economically viable. Therefore, the rated battery and SC power capacities utilized in this study cannot meet all the possible charging-discharging power requirements. Ref [162] presented a hybrid energy storage system consisting of a lead-acid battery and a SC to absorb or produce the necessary level of power so that constant power can be dispatched to the utility from PV generation. However, the average output power from the PV array might be overestimated.

In [163], various HESS frameworks are investigated to develop a cost-effective ESS for hourly dispatching solar power. Due to various assumptions, the annual cost of the required energy storage may be overestimated or underestimated. In [164], a low-cost ESS was proposed by evaluating reference generation algorithms for hourly dispatching solar power for 1 MW grid-connected PV arrays. The ambient temperature and PV cell temperature are assumed to be the same during annual energy storage cost calculation and this assumption might affect the estimation accuracy. Another HESS is described in [165] for dispatching solar power for grid-connected PV arrays, which uses an LPF to allocate the power between a battery and a SC.

However, LPF time constants may not be optimal.

It is important to note that none of the above studies investigated the capability of dispatching with the hybrid PV-WT scheme, which will be investigated in this chapter.

## **3.2 The Proposed Methodology**

### **3.2.1 WSHPS Framework**

The proposed WSHPS architecture that consists of a WES and a PVES is illustrated in Fig. 3.1. The PVES consists of PV arrays rated at 1 MW, a unidirectional DC/DC boost converter, and a MPPT controller. The WES is comprised of a 1.5 MW direct-drive three-phase PMSG coupled to a wind turbine, an AC/DC rectifier, and a pitch angle controller. The HESS is coupled in parallel with the WSHPS, and each of the ESS is connected with a bi-directional DC/DC converter. The WSHPS and HESS are connected in parallel to the DC-link capacitor bank that serves as the DC bus, which is tied to a three-level T-type inverter with high-quality output voltages. In this framework, the WSHPS and HESS are coupled to the DC bus as a current source, so controllable power flow is feasible by controlling the current flow through the power converters [166]. The three-level T-type inverter is utilized due to its high efficiency, low THD, and reduced common-mode voltage. A compact output harmonic filter is also demanded as an interface between the inverter and the grid to meet the grid code. In this research, an LCL filter has been designed for its higher efficiency and better harmonic attenuation.



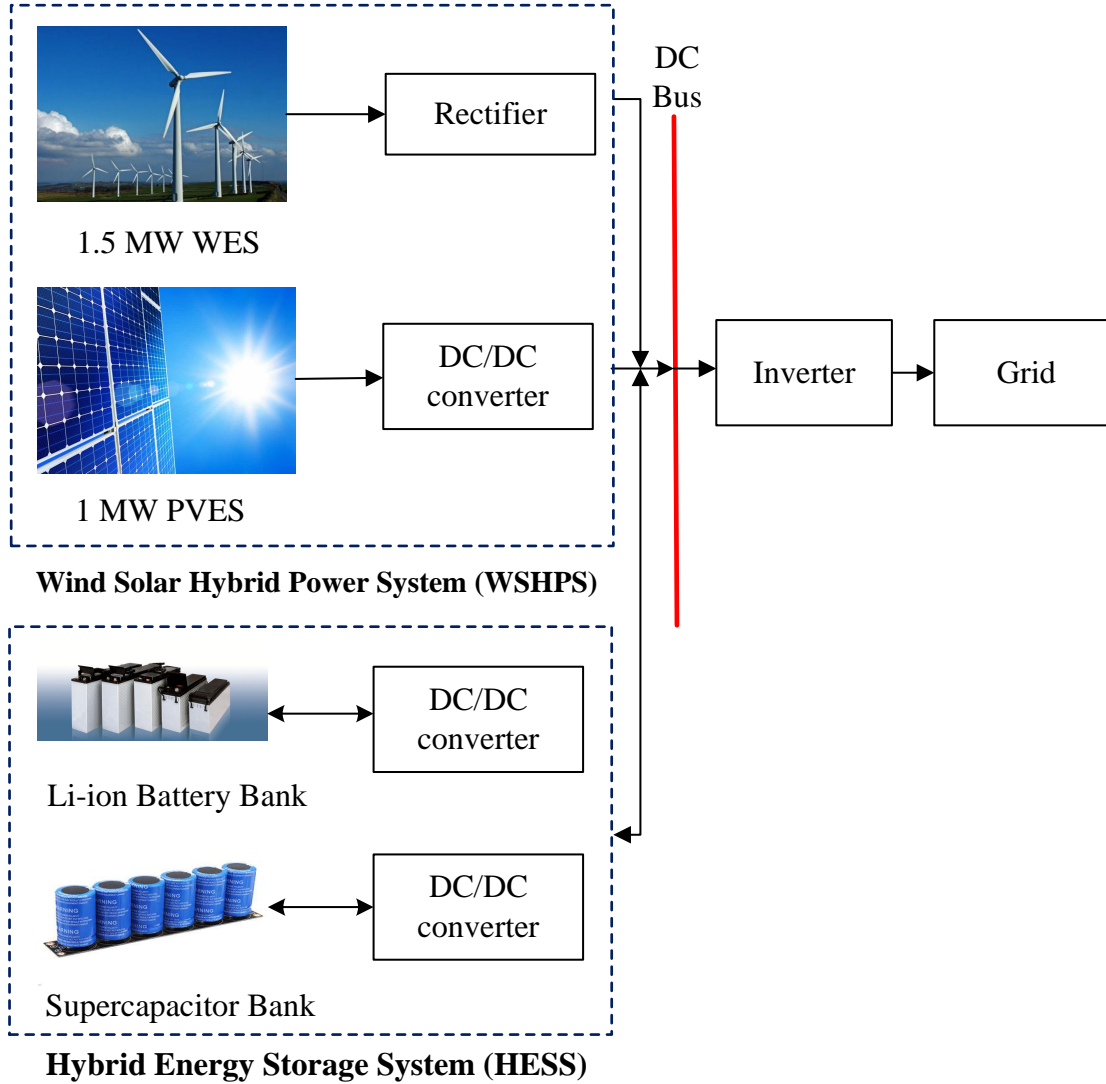


Figure 3.1: Structure of the wind-solar hybrid power system with HESS.

### 3.2.2 Control of PVES

The output of the PV array substantially relies on two weather conditions: PV irradiation ( $\text{W}/\text{m}^2$ ) and PV cell temperature ( $^{\circ}\text{C}$ ). This investigation is conducted using the actual solar data recorded by NREL. The PV array provides power to the unidirectional boost converter, whose duty ratio is controlled by an incremental conductance MPPT to extract the maximum power from the PV array. An incremental conductance MPPT is simple and more efficient compared to other approaches, i.e.,

perturb & observe, open circuit voltage, and short circuit current, which are commonly employed to extract maximum power from the PV systems [167]. Thus, the incremental conductance MPPT has been extensively utilized even though it can contribute to small oscillations next to the maximum power point while it is tracking power from the PV array.

### 3.2.3 Control of WES

In this study, the implemented WES consists of a WT, PMSG, pitch angle control, drivetrain, and power converter. The PMSG based on WES can associate with the WT without utilizing a gearbox. The energy conversion in PMSG based on WES takes place through two stages. First, the kinetic energy is captured by the WT blades as mechanical energy. Second, the mechanical energy is transferred through the shaft to PMSG, which converts the mechanical energy to electrical energy. The mechanical output power of a PMSG wind turbine can be expressed as:

$$P_{mech} = \frac{1}{2}\rho M v_{wind}^3 C_p(\lambda, \beta) \quad (3.1)$$

where  $P_{mech}$  is mechanical output power of the turbine (W),  $\rho$  is air density (kg/m<sup>3</sup>),  $M$  is turbine swept area (m<sup>2</sup>),  $v_{wind}$  is wind speed (m/s),  $C_p$  is the performance coefficient of the turbine,  $\lambda$  is tip speed ratio of the rotor blade tip speed to wind speed and  $\beta$  is blade pitch angle (degree).

The mechanical output power  $P_{mech}$  depends significantly on the turbine performance coefficient  $C_p$ . The generic  $C_p(\lambda, \beta)$  model documented in (2.14)-(2.15) is incorporated here. Equation (2.12) is utilized to calculate the wind speed when the meteorological data recorded is found at a different height from the WT height.

### 3.2.4 Modeling of ESS

The battery and SC energy storage systems are modeled in the MATLAB/SIMULINK environment in this research. The SOC formula for the battery and SC can be expressed using (3.2) and (3.3), respectively, where  $Q$  is the battery capacity,  $Q_T$  is the electric charge, and  $i$  is the charging/discharging current.

$$BESS(SOC) = \left(1 - \frac{1}{Q} \int_0^t i(t) dt\right) \times 100 \quad (3.2)$$

$$SC(SOC) = \frac{Q_{init} - \int_0^t i(t) dt}{Q_T} \times 100 \quad (3.3)$$

To consider cycling and calendar aging for battery usage, the Li-ion battery degradation model proposed in [76] is adopted in this study. The expected lifetime of the battery ( $T_{life}$ ) decreases due to its degradation properties over the period, which can be computed by using (2.17).

An aging model for the SC contemplated in [78] is incorporated in this research that considers both calendar aging and cycling aging. The expected lifetime of the SC ( $T_{SC,life}$ ) can be determined using (2.19).

### 3.2.5 Determination of Dispatch Power Reference

As mentioned earlier, the output of the PV array depends on two weather conditions: solar irradiation ( $W/m^2$ ) and solar cell temperature ( $^{\circ}C$ ). Besides, the output of the WT depends on the wind's speed (m/s) through the rotor. In this study, the actual solar irradiance, temperature, and wind speed data recorded at NREL is utilized to predict the dispatched power on an hourly basis for an entire day, which is referred to as the  $P_{Grid,ref}$ . The  $P_{Grid,ref}$  is estimated utilizing the average power that the WSHPS

can provide over each dispatching period, and it serves as a target power level for the entire system. Thus, the WSHPS and HESS are committed to providing this target power to the utility grid for each hourly dispatching period for the entire duration. The four different data sets with diverse PV and WT output regimes, recorded at NREL on January 30<sup>th</sup> 2019, May 15<sup>th</sup> 2019, June 9<sup>th</sup> 2019 and September 30<sup>th</sup>, are collected to use in this study [152].

Here, the WSHPS framework consists of a 1 MW PV array and a 1.5 MW WT system. Thus, the average output power of the WSHPS over each dispatching period is a combination of the PV array's and WT system's output power. The average irradiation and temperature of the NREL solar data is utilized as inputs to the PV array to calculate the PV array's average output power over each dispatching period. The PV array module in Matlab/Simulink provides power-voltage characteristic curves based on user-input parameters, such as solar cell type, the number of cells in parallel, and the number of cells in series, under various weather conditions. The power-voltage characteristic curves for 1 MW PV array are shown in Fig. 2.18 and Fig. 2.19. At MPP operation, the PV arrays' output power is marked as a circle of their respective curves. The resolution of the solar data recorded at NREL is one sample/minute. The cubic spline interpolation technique is employed to create a set of solar data with a resolution of 120 samples/minute and to map a value other than the four given maximum power points shown in Fig. 2.18 and Fig. 2.19. Afterwards, the average irradiation and temperature for each dispatching period are acquired utilizing the mean operation technique. The PVES estimated power from the average irradiation is referred as  $P_{PVES,est}$  and the estimated efficiency of the PVES provided by the average temperature is referred to as  $\eta_{PVES,est}$ . Therefore, the final estimated power dispatchable by PVES ( $P_{PVES}$ ) can be expressed as:

$$P_{PVES} = P_{PVES,est}(kW) \times \eta_{PVES,est}(\%) \quad (3.4)$$

Likewise, the estimated power dispatchable by WES ( $P_{WES}$ ) is calculated in this study. The WT model in MATLAB/Simulink provides the WT power characteristic curve based on user input parameters such as base wind speed, base rotational speed, blade pitch angle, and maximum power at base wind speed. The WT power characteristics curve is illustrated in Fig. 2.21. In this power curve,  $\beta$  is assumed to be zero and wind speed varies from 5 m/s to 11 m/s. The maximum power points for each wind speed are labelled. Then, cubic spline interpolation and mean operation techniques are implemented to acquire the average wind speed. The power level estimation from the average wind speed is referred to as the  $P_{WES}$ . Finally, the average output power of the  $P_{WSHPS}$  is calculated by using (3.5).  $P_{WSHPS}$  is also referred to as the  $P_{Grid,est}$ .

$$P_{Grid,est} = P_{PVES} + P_{WES} \quad (3.5)$$

Fig. 3.2 shows the block diagram deployed for the  $P_{Grid,ref}$  calculation. It is critical to adjust the  $P_{Grid,est}$  at the beginning of each period for achieving the desired  $P_{Grid,ref}$  estimation, and minimizing the ESS cost. The multiplication factor for the  $P_{Grid,est}$  correlates closely with the BESS SOC at the end of each dispatching period. This is accomplished by a rule-based algorithm that induces bounds represented by 10% SOC ranges that correspond to a multiplying factor. The ranges are from a battery SOC of 60% to 100% since one secondary SOC control algorithm is applied to guarantee the battery SOC regulates within this SOC limits. The resulting adjusted power level is referred as the  $P_{Grid,ref}$ . The primary SOC controller is employed to seek the desired multiplication factor for  $P_{Grid,est}$  that ensures the ESS to complete each

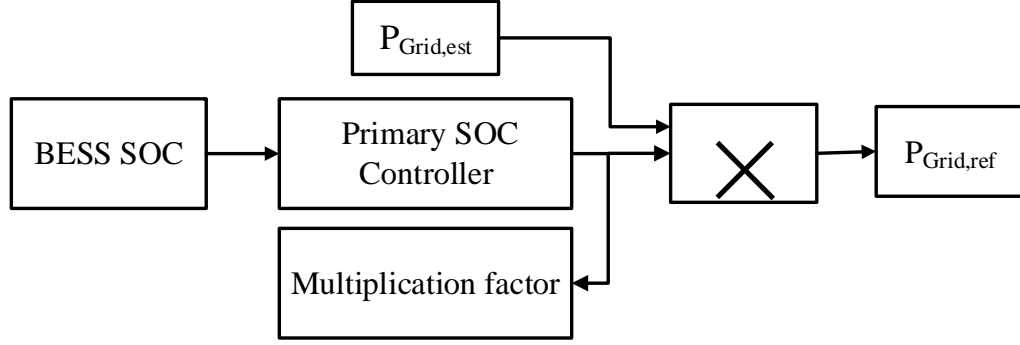


Figure 3.2: Block diagram of grid reference power calculation.

dispatching period with the same SOC as it starts. Thus, the multiplication factor that is employed to adjust the  $P_{\text{Grid,est}}$  plays a critical role in developing the most cost-effective ESS for hourly dispatching the WSHPS power.

To seek the appropriate multiplication factor to the  $P_{\text{Grid,est}}$ , a step rules algorithm, linearized step rules algorithm, and a fuzzy inference system are utilized as a primary SOC controller. Table 3.1 shows the rule-based control algorithm to calculate the  $P_{\text{Grid,ref}}$  from adjusting the  $P_{\text{Grid,est}}$  with BESS SOC [168]. The formula presented in (3.6) is employed to linearize the rule-based algorithm through regression analysis. Fig. 3.3 illustrates the linearization of the battery SOC. While implementing the fuzzy inference system, the BESS SOC is utilized as a fuzzy input, and the step rules algorithm shown in Table 3.1 is used in the rule editor. The output of the fuzzy inference system using the rules is shown in Fig. 3.4. Here, the fuzzy logic mechanism is utilized to implement a Mamdani type fuzzy inference system that exploits fuzzy logic for formulating the mapping from a given input to an output. Then the mapping provides a basis from which decisions can be made.

$$\text{Multiplication factor} = \frac{0.60 \times \text{SOC} + 51.7}{100} \quad (3.6)$$

Table 3.1:  $P_{Grid,ref}$  calculation from adjusting  $P_{Grid,est}$  with BESS SOC.

BESS	Multiplication factor
$100\% \geq SOC > 92\%$	1.10
$92\% \geq SOC > 84\%$	1.05
$84\% \geq SOC > 76\%$	1.00
$76\% \geq SOC > 68\%$	0.95
$68\% \geq SOC > 60\%$	0.90

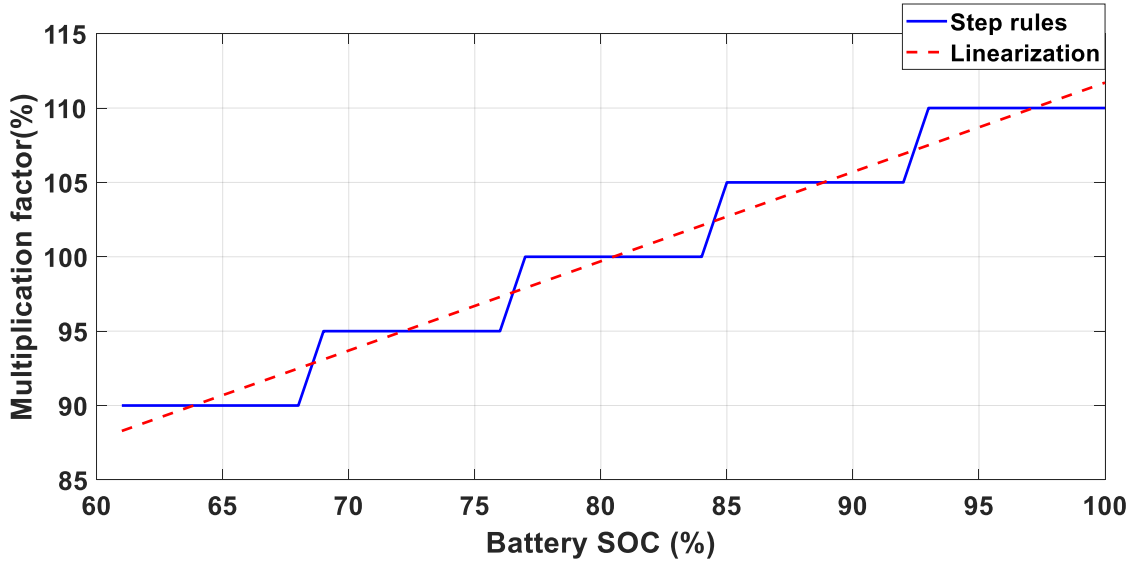


Figure 3.3: Linearization of step rules algorithm.

### 3.2.6 Control of HESS

Fig. 3.5 shows the HESS control framework that is implemented in this research. Here, the HESS is responsible for regulating the system power, which is injected into the utility grid. The reference power for the HESS ( $P_{HESS,ref}$ ) is the difference between the  $P_{Grid,ref}$  and the  $P_{WSHPS}$ , which can be stated as:

$$P_{HESS,ref} = P_{Grid,ref} - P_{WSHPS} \quad (3.7)$$

The lifetime of the battery can degrade significantly when the fast changing (i.e., high-frequency) power components flow through it. Thus, the  $P_{HESS,ref}$  is sent through

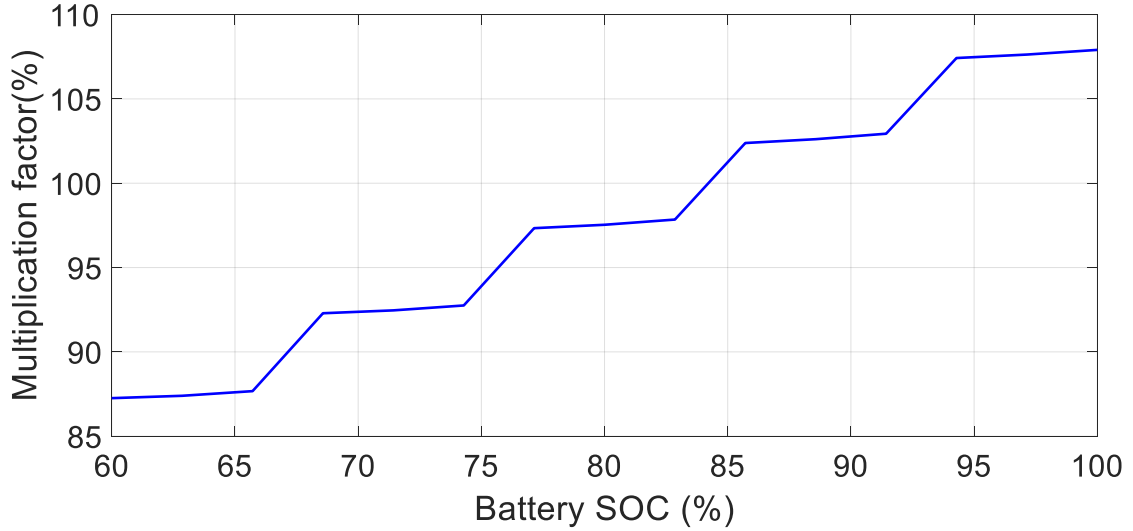


Figure 3.4: Output of the fuzzy inference.

the LPF to allocate high-frequency components of power reference for the SESS ( $P_{\text{SESS,ref}}$ ) and low-frequency components of power reference for the BESS ( $P_{\text{BESS,ref}}$ ). In addition, after obtaining the optimal value of DOD ( $\text{DOD}_{\text{optimum}}$ ) for the BESS, one rule-based SOC control algorithm is employed to regulate the BESS SOC in the optimal range. The block diagram of the rule-based algorithm for the BESS SOC control is illustrated in Fig 3.6. Likewise, another rule-based SOC control algorithm is implemented to regulate the SESS SOC after getting the optimal value of DOD for the SESS.

When the ESS is discharging (charging), the associated converter with the ESS acts in a boost (buck) mode in this HESS control architecture. The DC bus voltage demands to be set nearly twice as much as the ESS voltage for avoiding the discontinuity of the ESS input current induced by buck mode operation. The reference signals for the BESS and SESS are measured up to their instantaneous values ( $P_{\text{BESS}}$  for BESS, and  $P_{\text{SESS}}$  for SESS) to evaluate the duty ratio for the associated power converters. In this research, a pair of proportional integral (PI) controllers are ap-



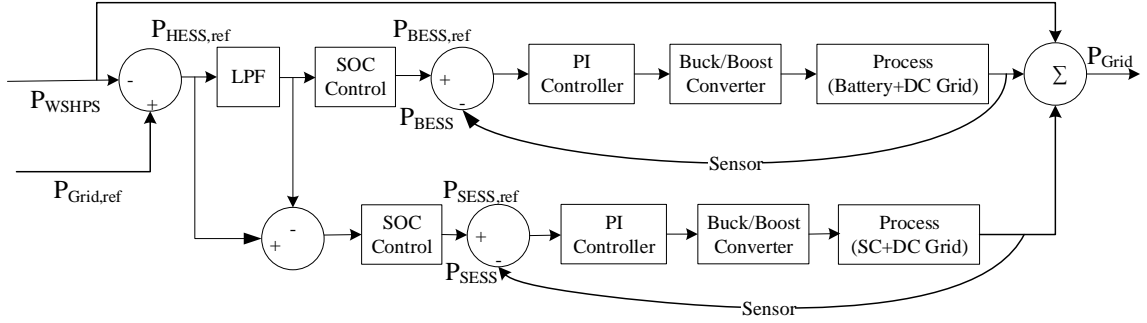


Figure 3.5: HESS power control framework.

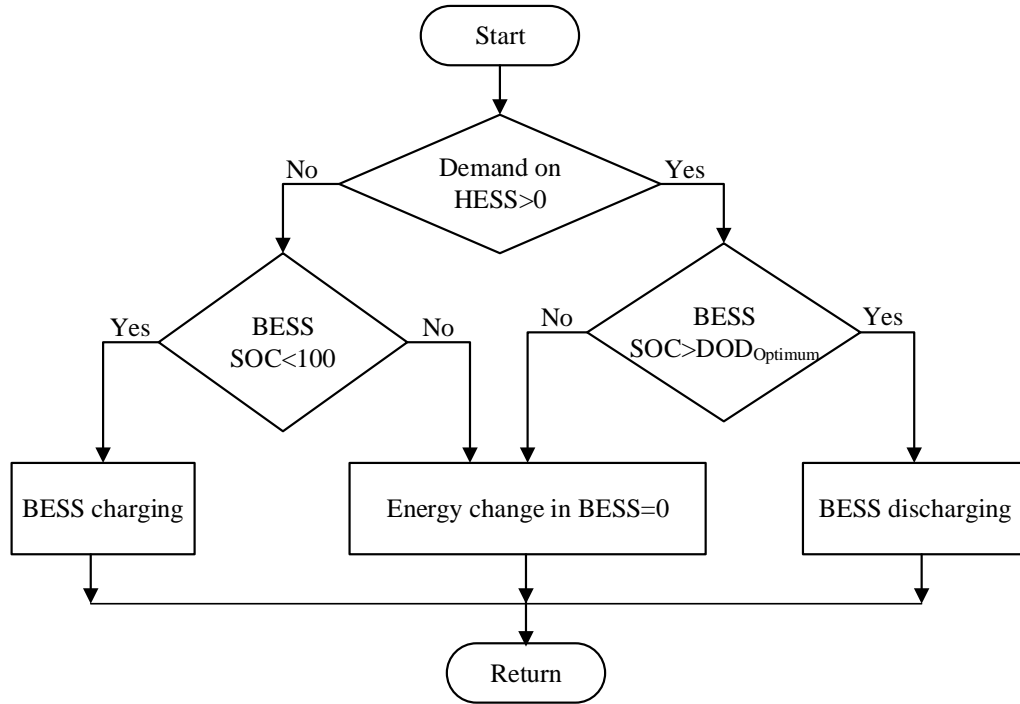


Figure 3.6: Rule-based algorithm for the BESS SOC control.

plied for determining the change in the duty ratio and reducing the proportional and integral error of the system.

### 3.2.7 HESS Energy and Power Capacity

To ensure the HESS can conform to the amount of energy that has to be charged or discharged, the minimum capacity demanded by the HESS needs to be determined.

The energy capacity needed for the BESS and SESS is exploited through integrating

the power profile of the BESS and SESS over each dispatching period respectively. At first, the absolute maximum amount of energy exploited by the BESS is computed through integrating the BESS power curve over each dispatching period and then in comparison to other dispatching period's maximum energy required for the BESS. Finally, (3.8) is utilized to determine the minimum capacity needed for the BESS to successfully dispatch the WSHPS power to the utility at one-hour increments for an entire day.

$$E_{BESS} = \frac{E_{sj}}{DOD_{max}} \quad (3.8)$$

where,  $E_{sj}$  is the total energy charged or discharged over the simulation period for the BESS, and  $DOD_{max}$  is the maximum DOD used by the BESS.

Likewise, the minimum capacity required for the SESS ( $E_{SESS}$ ) is computed. Specifically, (3.9) is employed to calculate the required SC energy capacity.

$$E = \frac{1}{2}CV^2 \quad (3.9)$$

where  $E$  is the energy measured in Joules,  $C$  is the supercapacitor's capacitance measured in Farads, and  $V$  is the supercapacitor's voltage measured in Volt.

In this HESS power coordinated scheme, the positive  $P_{BESS}$  dictates that the BESS is discharging whereas the negative  $P_{BESS}$  dictates that the BESS is charging. Thus, the rated power capacity required for the BESS can be statistically quantified. At first, the absolute values of  $P_{BESS}$  over the simulation period are calculated. Then, its probability density function (PDF) and cumulative density function (CDF) are computed. Finally, the BESS rated power capacity ( $P_{BESS, rated}$ ) is selected to be the values of  $|P_{BESS}|$  which corresponds to the CDF of 1. Hence, the BESS can be

expected to meet all the possible charging-discharging power requirements. Similarly, the rated power capacity for the SESS ( $P_{\text{SESS, rated}}$ ) is evaluated in this study.

### 3.2.8 DOD Optimization for HESS

The service life of the ESS primarily relies on the utilization of DOD and the rate of change of the charging-discharging power. The relationship between the cycle life and the DOD usage is close to exponential [169] and for the Li-ion battery it can be expressed as:

$$C_i = 28270e^{(-2.401DOD_i)} + 2.214e^{(5.901DOD_i)} \quad (3.10)$$

where  $C_i$  is the number of cycles when the depth of discharge is  $DOD_i$ . The relationship between DOD and cycle life calculated using (3.10) is shown in Fig. 3.7.

The expenditure associated with the ESS mainly depends on two factors, namely, (i) lifetime of the ESS and (ii) minimum capacity required for the ESS. Equation (3.8) illustrates that the minimum capacity required for the BESS is inversely proportional to the usage of its DOD. Nevertheless, deeper discharge of the BESS degrades its service life, as shown in Fig. 3.7. Thus, to determine the proper value of DOD that leads to the least expensive of the BESS (\$/kWh) for dispatching the WSHPS power, the simulations are carried out considering every possible value of the BESS DOD. Likewise, the optimum value of the DOD for the SESS has been explored. Unlike the Li-ion battery, SC can be practically charged- discharged an infinite number of times. Hence, the total number of charging-discharging cycles for the SESS is considered to be constant (i.e., 500,000) in this investigation [170].

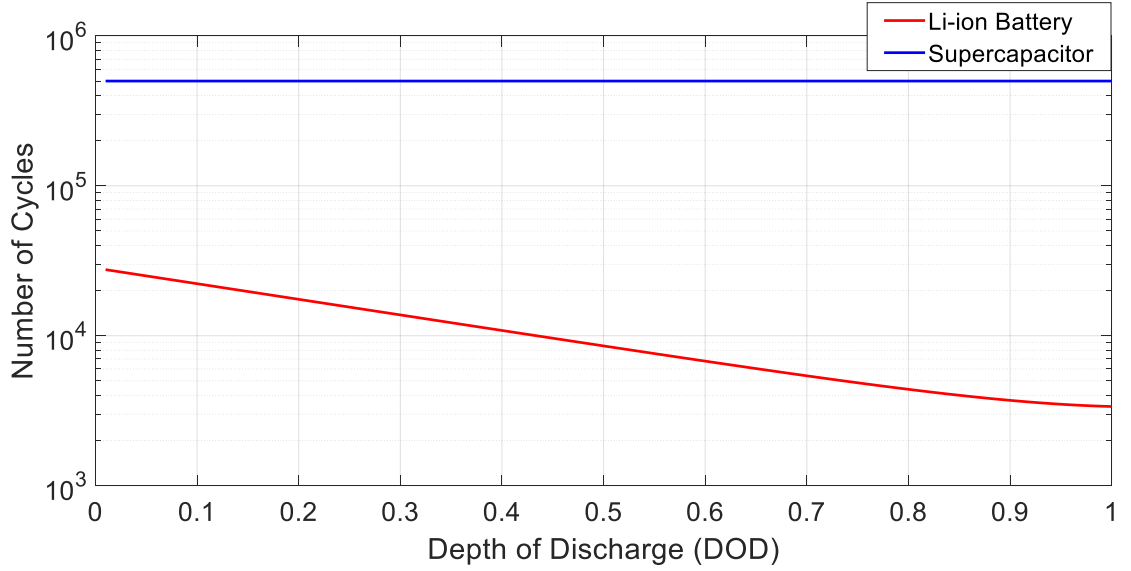


Figure 3.7: The relationship between DOD and cycle life.

### 3.2.9 Cost Optimization for HESS

The LPF is employed to provide the power reference for the BESS and SESS. The minimum capacity needed for the SESS is directly proportional to the LPF time constant, while the minimum capacity needed for the BESS is inversely proportional to the LPF time constant. A proper value of the filter time constant is required to minimize the total cost (\$/kWh) of the HESS. Here, after acquiring the appropriate cost formula of the HESS as a function of the LPF time constant by utilizing the curve fitting method, the PSO approach is implemented to identify the optimum LPF time constant, as shown in Fig. 3.8. The mathematical formula of the HESS expenditure as a function of the LPF time constant is shown in (3.11), which is obtained employing the 4<sup>th</sup> order polynomial curve fitting method.

$$HESS_{Cost,LPF}(x) = P_1x^3 + P_2x^2 + P_3x + P_4 \quad (3.11)$$

where  $P_1$ ,  $P_2$ ,  $P_3$  and  $P_4$  are regression coefficients, and  $x$  is the LPF time constant,

which is employed to distribute the power between the battery and SC in the HESS framework.

The PSO approach is incorporated due to its multiple advantages including: straightforward implementation, higher credibility in reaching the global optima, required for adaptation of few parameters, and speedy convergence. In general, the PSO offers a shorter evaluation time and better solution quality compared with a genetic algorithm, which is another optimization strategy usually deployed in renewable energy systems. The PSO performs a search for the feasible solutions, called particles, flying through the problem space by following the current optimum particles. The model of the particle's position can be expressed as:

$$V_i^{k+1} = wV_i^k + C_1rand_1 \times (pbest_i - S_i^k) + C_2rand_2 \times (gbest - S_i^k) \quad (3.12)$$

$$S_i^{k+1} = S_i^k + V_i^{k+1} \quad (3.13)$$

where  $V_i^{k+1}$  is the velocity of agent  $i$  at the iteration  $k$ ,  $w$  is the weighting function,  $C_j$  is the weighting factor,  $rand$  is the uniformly distributed random number between 0 and 1,  $S_i^k$  the current position of agent  $i$  at the iteration  $k$ ,  $p_{best_i}$  is the personal best position of agent  $i$ , and  $gbest$  is the global best position of the group.

### 3.2.10 Expected Lifetimes of the BESS and SESS

Due to the intermittent nature of the WSHPS output power, the charging-discharging characteristics of the BESS over a period is used to estimate the service life of the BESS. Here, the equation to compute the equivalent service cycle life ( $C_{B,T}$ ) of the BESS over the period  $T_s$  is shown below:

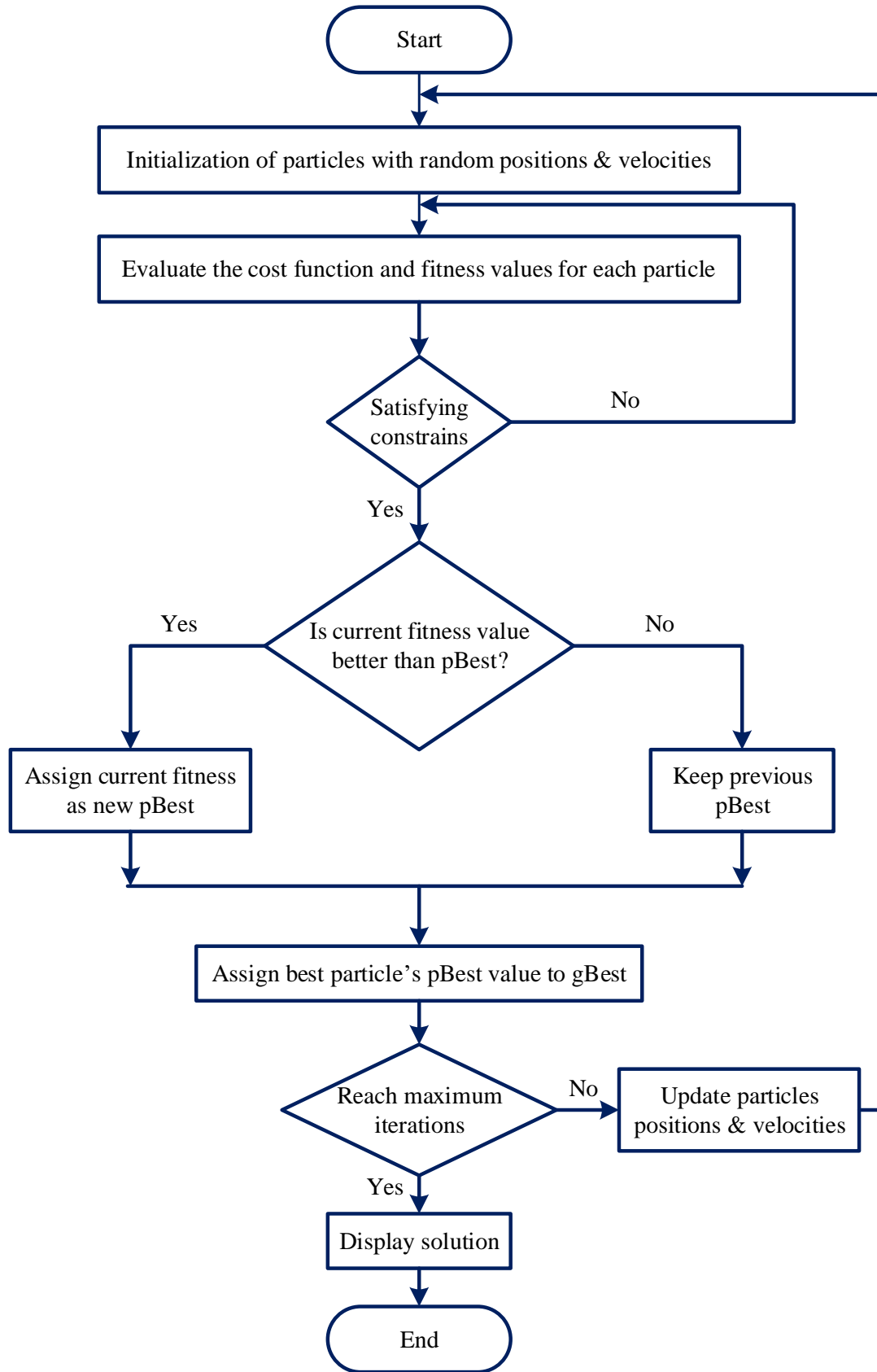


Figure 3.8: PSO functional flowchart.

$$C_{B,T} = \sum_{j \in T_s} \frac{E_{sj}}{E_{BESS}} \quad (3.14)$$

where,  $E_{sj}$  is the total energy charged or discharged (whichever is greater) over the simulation period  $T_s$ .  $E_{BESS}$  is battery's rated energy capacity multiplied by DOD and a correction factor to derate manufacturer's data (a correction factor of 0.8 is assumed in this study). Accordingly, the expected lifetime of the battery  $E|L_B|$  is calculated using (3.15).

$$E|L_B| = \frac{C_{B,n}}{C_{B,T}} \times T_s \quad (3.15)$$

where  $C_{B,n}$  is the life cycle of the battery provided by the manufacturers.

The expected lifetime of the BESS deteriorates due to its calendar aging and this is also contemplated here. The BESS degradation model has been explained in Section 3.2.4.  $T_{\text{life}}$  in (2.17) reflects the decline of the BESS service life due to its calendar aging. The SESS aging model that considers both cycling and calendar aging is adopted in this study. The SESS aging model has been fully documented in Section 3.2.4. Hence,  $T_{\text{SC,life}}$  in (2.19) indicates the expected lifetime of the SESS, while accounting for both cycling and calendar aging.

### 3.2.11 Cost Calculation for HESS

Both cycling and calendar aging expenses are considered while the ESS cost is investigated in this research. The overall expenditure of the ESS includes its capital cost, power conversion system cost, and operation and maintenance (O&M) cost. Therefore, the total expense associated with the BESS ( $C_{Bat,Total}$ ) can be estimated by using (3.16).

$$C_{Bat,Total}(\$) = C_{Cap} + C_{Conv} + C_{O\&M} \quad (3.16)$$

where  $C_{Cap}$  is the BESS capital cost,  $C_{Conv}$  is the BESS power conversion system cost, and  $C_{O\&M}$  is the BESS operation and maintenance cost.

The capital cost of the BESS ( $C_{Cap}$ ) can be expressed by:

$$C_{Cap} = C_{cycling} + C_{calendar} \quad (3.17)$$

$$C_{Cap} = \frac{E_{BESS} \times C_B}{E|L_B|} + \frac{E_{BESS} \times C_B}{T_{life}} \quad (3.18)$$

where  $C_{cycling}$  and  $C_{calendar}$  are the cycling and calendar expenses associated with the BESS respectively.  $E_{BESS}$  is the required energy capacity of the BESS in kWh,  $C_B$  is the BESS capital cost (\$/kWh),  $E|L_B|$  is the expected lifetime of the BESS and  $T_{life}$  is the expected lifetime of the BESS deteriorates due to its calendar aging.

The power conversion system expense of the BESS ( $C_{Conv}$ ) can be expressed by:

$$C_{Conv} = \frac{P_{BESS,rated} \times P_B}{E|L_B|} + \frac{P_{BESS,rated} \times P_B}{T_{life}} \quad (3.19)$$

where  $P_{BESS,rated}$  is the required power capacity of the BESS in kW and  $P_B$  is the BESS power conversion system cost (\$/kW). Likewise, the BESS O&M expenditure is evaluated in this research.

In this study,  $T_{SC,life}$  indicates the expected lifetime of the SESS that considers both cycling and calendar aging. Thus, the capital cost of the SESS ( $SC_{Cap}$ ) can be expressed by:



$$SC_{Cap} = \frac{E_{SESS} \times C_{SC}}{T_{SC,life}} \quad (3.20)$$

where  $E_{SESS}$  is the required energy capacity of the SESS in kWh and  $C_{SC}$  is the SESS capital cost (\$/kWh).

The power conversion system expenditure of the SESS ( $SC_{Conv}$ ) can be expressed by:

$$SC_{Conv} = \frac{P_{SESS,rated} \times P_{SC}}{T_{SC,life}} \quad (3.21)$$

where  $P_{SESS,rated}$  is the required power capacity of the SESS in kW and  $P_{SC}$  is the SESS power conversion system cost (\$/kW). Likewise, the SESS O&M expense ( $SC_{O\&M}$ ) is computed in this study.

Therefore, the total cost associated with the SESS ( $C_{SC,Total}$ ) can be calculated by using (3.22):

$$C_{SC,Total}(\$) = SC_{Cap} + SC_{Conv} + SC_{O\&M} \quad (3.22)$$

Finally, the normalized HESS cost per kWh can be expressed as follows:

$$C_{HESS}(\$) = C_{Bat,Total} + C_{SC,Total} \quad (3.23)$$

$$Cost_{Norm} = \frac{C_{HESS}}{(P_{PV} \times PV_{CF} + P_{WT} \times WT_{CF}) \times T} \quad (3.24)$$

where  $P_{PV}$  is the PV array capacity (kW),  $PV_{CF}$  is the PV capacity factor (20% is assumed in this study),  $P_{WT}$  is the wind turbine capacity (kW),  $WT_{CF}$  is the wind turbine capacity factor (35% is assumed in this study), and  $T$  is the number of hours

Table 3.2: Battery and SC cost comparison

Parameter	Battery	SC
Capital cost	271 (\$/kWh)	2500 (\$/kWh)
Power conversion system	271 (\$/kW)	350 (\$/kW)
O&M-Fixed	10 (\$kW-year)	1 (\$/kW-year)
O&M-Variable	3 (\$/kWh)	3 (\$/kWh)
Charging-discharging cycles	10,000 (40%DOD)	500,000

in a year. The unit price and life cycle of different energy storage exploited in this study are summarized in Table 3.2 [171].

### 3.3 Simulation Results

In this research, the hourly dispatching WSHPS has been developed and simulated in MATLAB/Simulink<sup>TM</sup> environment. Furthermore, bidirectional power converters, three-level T-type inverter, LCL filter, and the corresponding control algorithms have been modelled and analyzed to justify the performance and the economic evaluation of the HESS architecture.

Fig. 3.9 illustrates the power profiles of the WSHPS, HESS,  $P_{\text{Grid}}$ , and  $P_{\text{Grid,ref}}$ . Here, the  $P_{\text{Grid}}$  is the combination of the WSHPS and HESS power injected into the grid by an inverter, and the  $P_{\text{Grid,ref}}$  is utilized as a target power level for the WSHPS and HESS to supply to the grid. It is noticeable that the  $P_{\text{Grid}}$  remains constant in each dispatching period and successfully follows the desired  $P_{\text{Grid,ref}}$ . Hence, it can be concluded that the HESS successfully contributes the necessary power either by supplying or absorbing to provide a constant power to the utility from the intermittent WSHPS architecture. Further investigation into the simulation results also validates the fact that the fast-changing components of the power are charged-discharged by the SESS while the slow-changing components of the power are charged-discharged

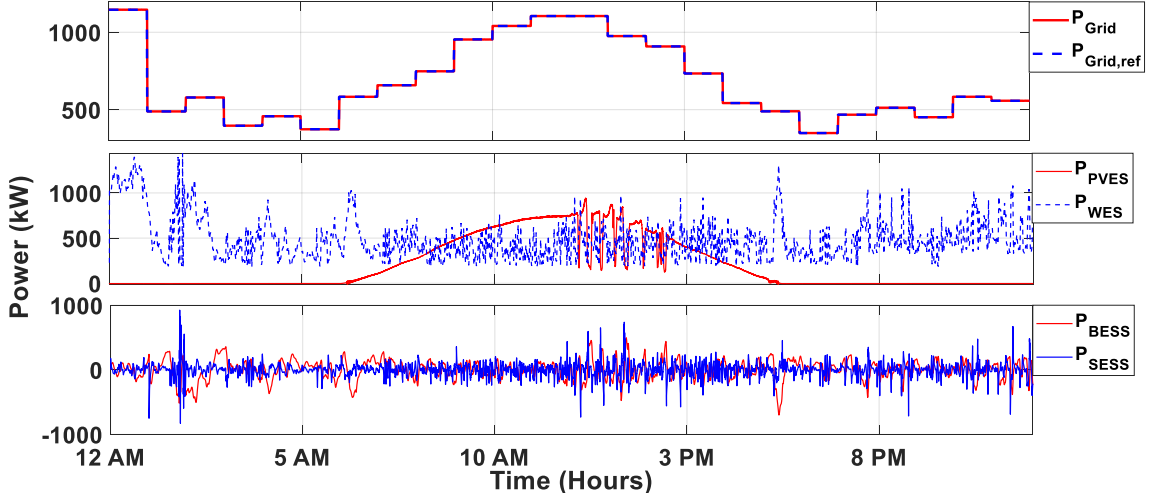


Figure 3.9: Dispatchable power reference case: Simulation results for one-hour dispatching for September 30<sup>th</sup>, 2019.

by the BESS.

The  $P_{\text{Grid,ref}}$  for the WSHPS is generated utilizing two different schemes, i.e., (i) dispatchable power reference case—estimating the  $P_{\text{Grid,ref}}$  utilizing the approach elucidated in Section 3.2.5 and (ii) load following case—load profile for 2.5 MW utility is collected from CAISO and is utilized as a grid reference power for the entire system. Fig. 3.9 illustrates the simulation result for the dispatchable power reference case and Fig. 3.10 demonstrates the simulation result for the load following case. It is worth mentioning that the  $P_{\text{Grid}}$  successfully follows the desired  $P_{\text{Grid,ref}}$  in both cases investigated in this study.

In addition, to validate the effectiveness of the proposed HESS control framework, a one-hour simulation has been carried out considering all possible cases of the availability of sources investigated in this study—(i) PV+WT+ESS (ii) WT+ESS (iii) PV+ESS (iv) ESS only—to dispatch the desired grid reference power for the entire duration. Fig. 3.11 illustrates the one-hour simulation results, and it is shown that the proposed control framework is capable of dispatching the desired  $P_{\text{Grid,ref}}$  irrespective

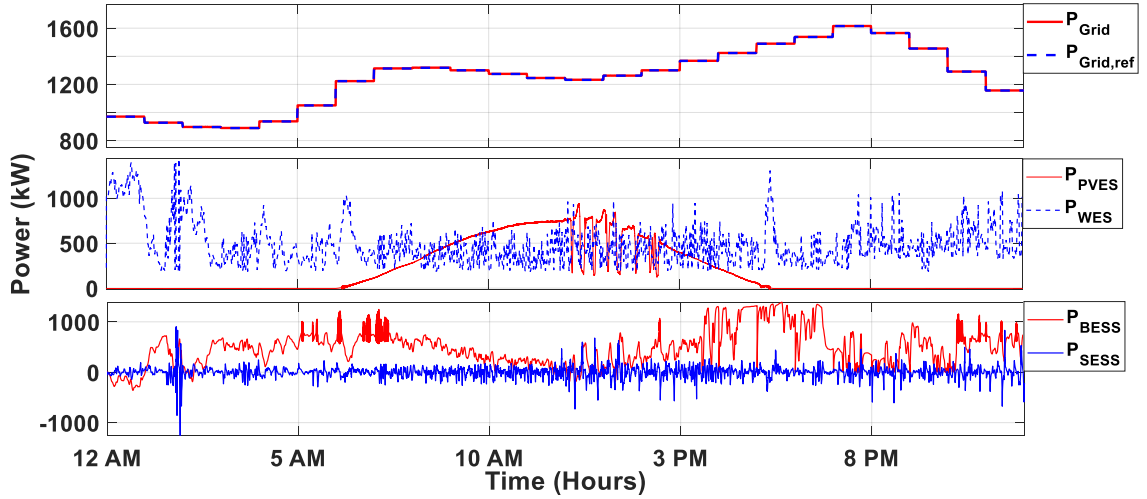


Figure 3.10: Load following case: simulation results for one-hour dispatching for September 30<sup>th</sup>, 2019.

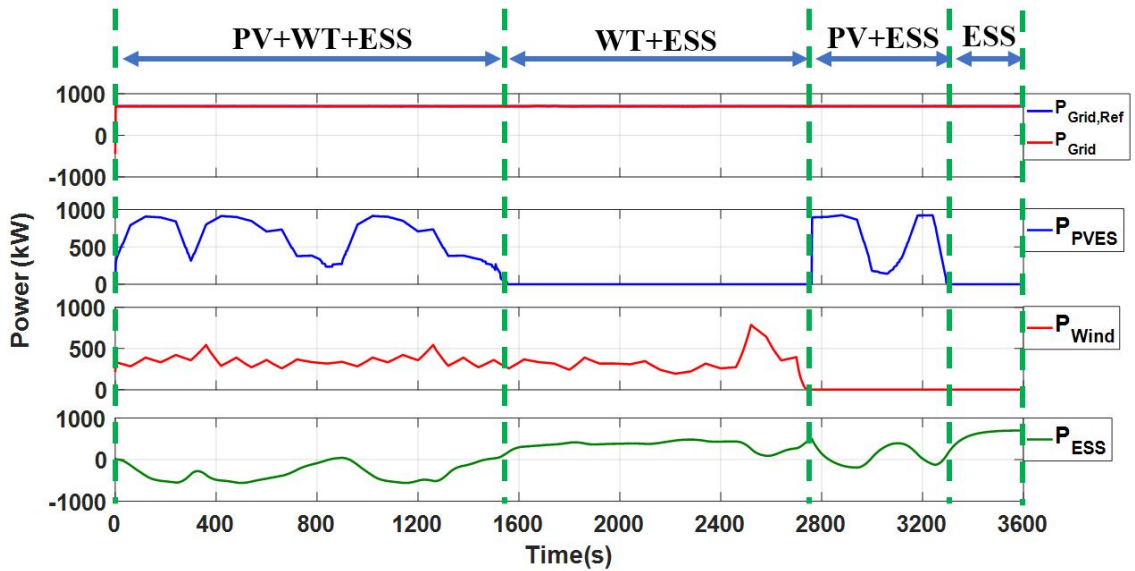


Figure 3.11: One-hour simulation results considering all possible cases of the availability of sources.

of the availability of renewable energy sources. Note that even though the proposed architecture can effectively operate in the ESS-only mode to fulfill the desired  $P_{\text{Grid,ref}}$  in each dispatching period, the required ESS capacity will become unnecessarily large in this scenario. Therefore, the ESS-only mode might not be cost-effective for hourly dispatching the WSHPS power to the grid.

The primary SOC controller as a function of the BESS SOC is developed to ensure the BESS finishes each dispatching period with the same SOC as it started. This type of SOC constraint is demanded for estimating the desired  $P_{\text{Grid,ref}}$ , minimizing the BESS cost, and ensuring the BESS has enough capacity to be available for the next-day operation. The simulation result of the BESS SOC variation on September 30<sup>th</sup> 2019 is illustrated in Fig. 3.12, which highlights the effectiveness of the primary SOC controller to regulate the BESS SOC within a specified range. As mentioned before, a step rules algorithm, linearized step rules algorithm, and a fuzzy interference system are employed as a primary SOC controller to seek the appropriate multiplication factor to the  $P_{\text{Grid,est}}$  in this study. The effect of those algorithms on the HESS cost assessment is demonstrated in Fig. 3.13 for September 30<sup>th</sup> 2019 meteorological data. The performances of the algorithms do not differ substantially, and fuzzy logic rule approach performs slightly better.

In this study, the simulations are carried out considering every possible value of the BESS DOD to seek the optimum value of DOD that exhibits the least cost

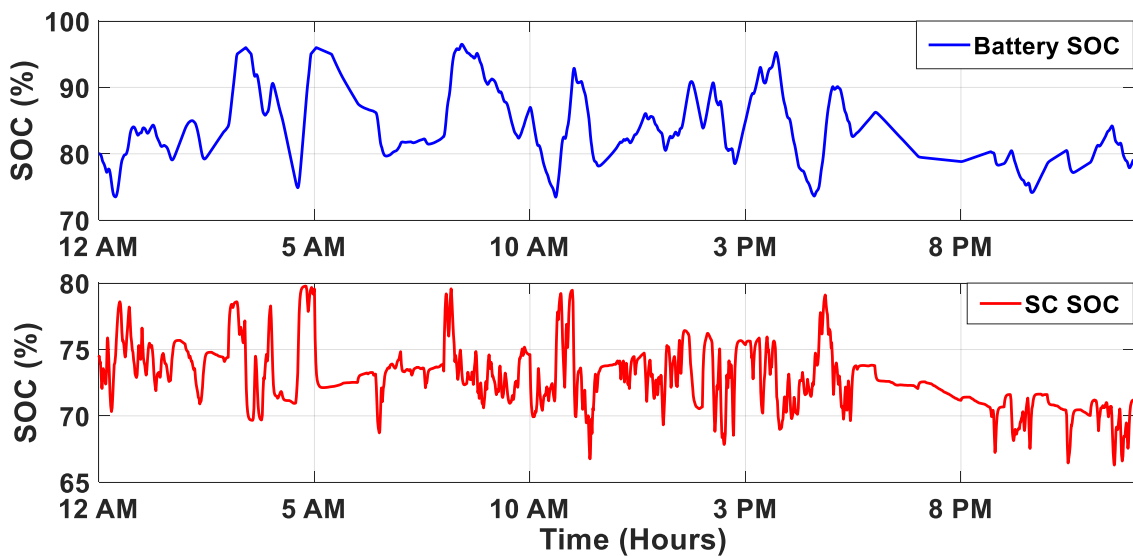


Figure 3.12: Simulation results of the SOC with the battery and SC.

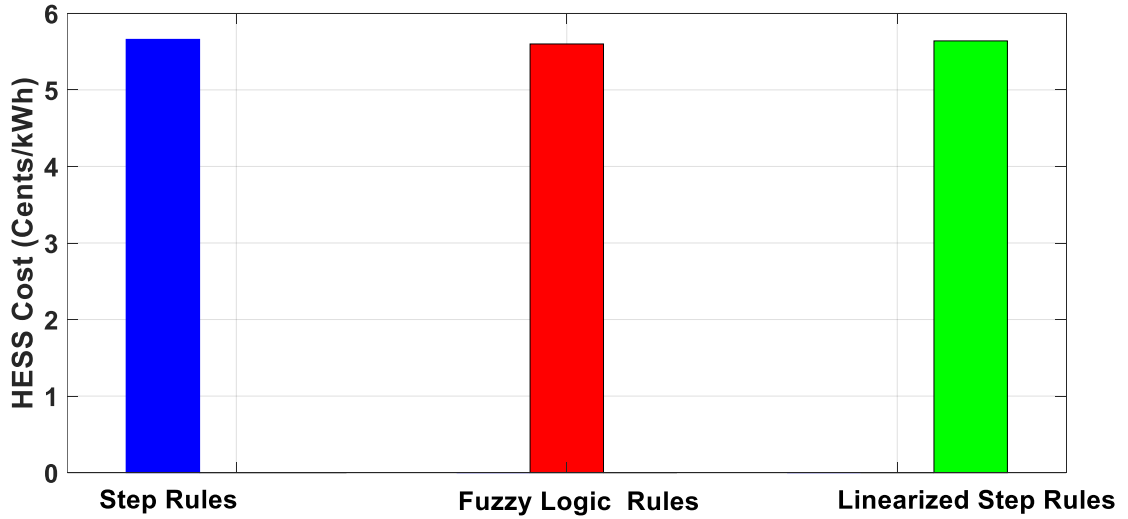


Figure 3.13: HESS cost comparison at different primary SOC control algorithms.

(\$/kWh) of the BESS for hourly dispatching the WSHPs power. The BESS cost per kWh as a function of its usage of DOD is illustrated in Fig. 3.14. As shown in Fig. 3.14, the optimum value of the BESS DOD that demonstrates the minimum cost is found at 42% DOD, which is approximately 9.85 ¢/kWh in the case of September 30<sup>th</sup> 2019 simulation.

The SESS cost per kWh as a function of its usage of DOD is also demonstrated in Fig. 3.14. It is observed that the full utilization of the SESS results in the least cost. The expenditure associated with the ESS is inversely proportional to the service life of the ESS and is directly proportional to the ESS capacity. Since the SC can be charged-discharged a virtually unlimited number of times, the total number of charging-discharging cycles of the SC as a function of its DOD usage, in any event, remained constant, as demonstrated in Fig. 3.7. Furthermore, the capacity needed for the SC becomes minimum when it is fully exploited. Consequently, at 100% DOD, the SESS demonstrates the least cost, approximately 17.2 ¢/kWh in the case of September 30<sup>th</sup> 2019 simulation. For better illustration, the ESS expense as a function of its DOD usage in the range between 10% to 100% is illustrated in Fig. 3.14.

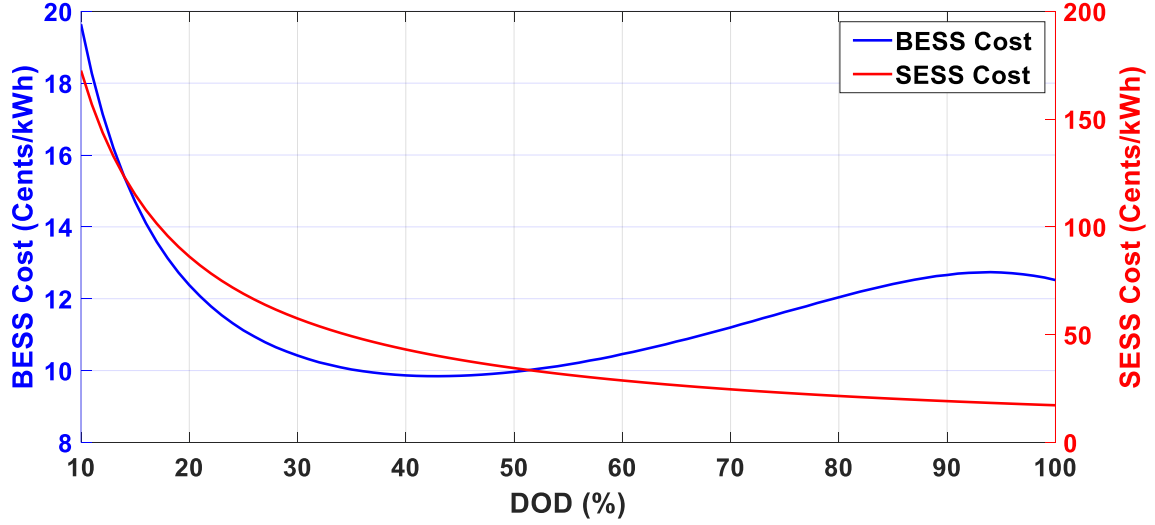


Figure 3.14: ESS cost ( $\text{¢}/\text{kWh}$ ) at different DOD levels.

In order to investigate the impact of utilizing different types of ESS for hourly dispatching the WSHPS power, an economic comparison is presented in Table 3.3. From Table 3.3, it is noted that the HESS can be the most cost-effective framework compared with the battery or SC-only operation. In addition, the following three steps are taken into account to seek the optimum LPF time constant. (1) A real meteorological dataset (i.e., September 30<sup>th</sup> 2019) with the solar irradiance, temperature, and wind speed profile that has considerable fluctuations is integrated into the Simulink model to carry out the simulations at different LPF time constants, as is presented in Table 3.3. (2) The curve fitting approach is executed to develop the best mathematical cost equation of the HESS as a function of the LPF time constants, as illustrated in Fig. 3.15. (3) Finally, the PSO strategy is applied by utilizing the HESS cost equation to seek the most feasible LPF time constant. In this study, the most optimum HESS cost is found at 62 s LPF time constant by using the 4<sup>th</sup> order polynomial HESS cost equation. The convergence rate of the PSO technique is illustrated in Fig. 3.16.

There are two main constraints took into account in the course of the cost op-

Table 3.3: Energy storage cost comparison at different LPF time constants

LPF time constant (s)	0	60	120	180	240	$\infty$
Cost ( $\text{¢}/\text{kWh}$ )	9.85	5.62	7.33	9.27	10.16	17.20

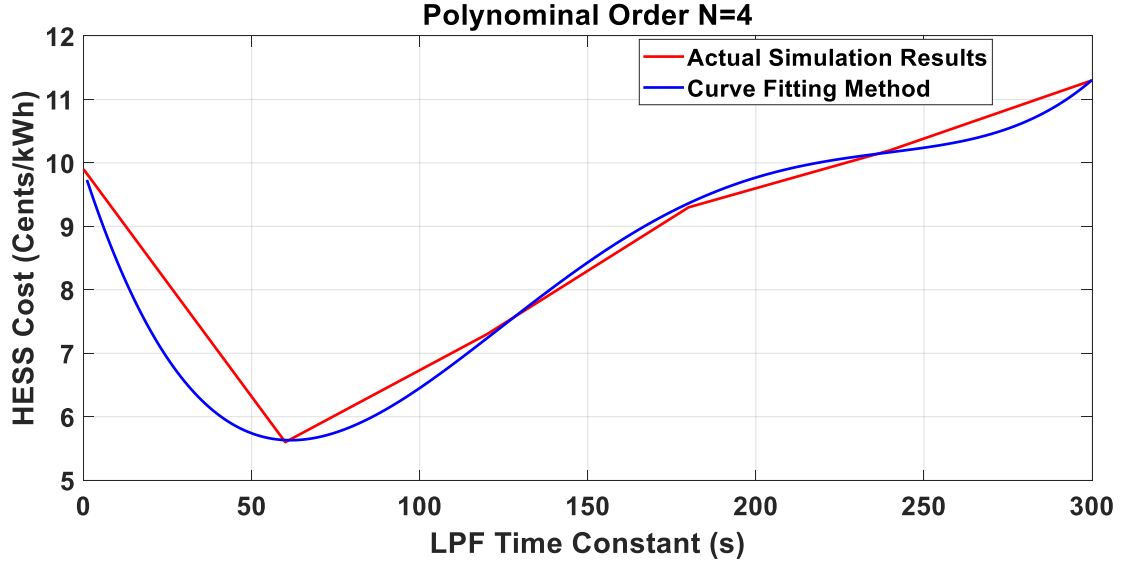


Figure 3.15: Simulation results using the optimization method.

timization process, namely, (i) total power supplied from the WSHPs farm ( $P_{\text{Grid}}$ ) must cover the desired  $P_{\text{Grid,ref}}$  in each dispatching period, and (ii) SOC of the BESS and SESS remains above the specified DOD. Fig. 3.9, Fig. 3.10 and Fig. 3.12 are presented to validate these optimization constraints.

To obtain the annual ESS cost for hourly dispatching the WSHPs power, the four different datasets as representative of four seasons recorded by U.S. NREL, are utilized in this study [152]. The annual HESS expenditure is estimated by the weighted average value of the four different seasons' energy storage costs. The HESS cost comparison at the optimum LPF time constant (i.e., 62 s) between the dispatchable power reference case and the load following case is illustrated in Fig. 3.17. In the dispatchable power reference case, the  $P_{\text{Grid,ref}}$  is determined by estimating the aver-



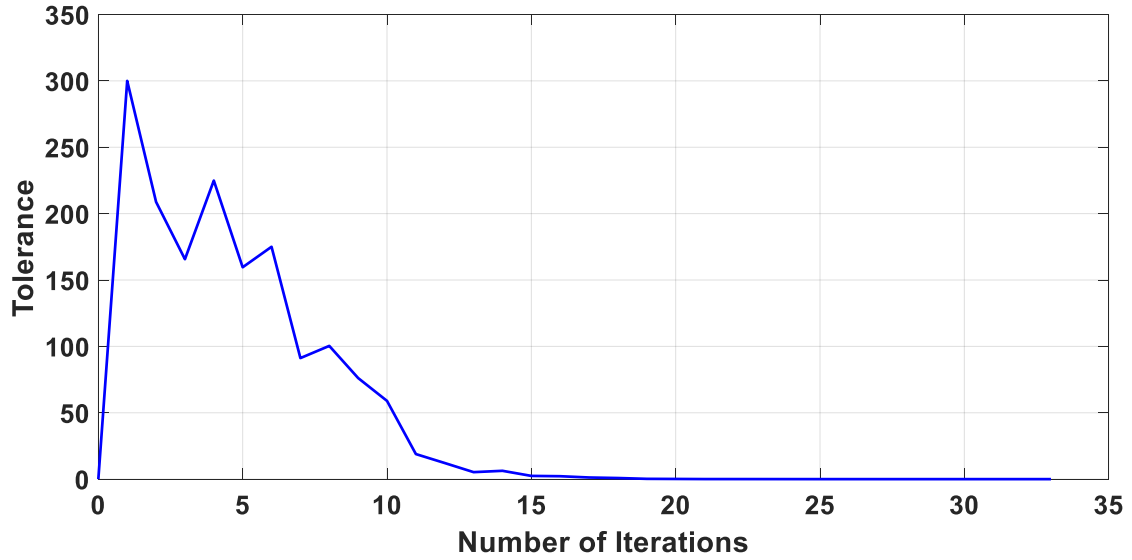


Figure 3.16: Convergence rate of the PSO technique.

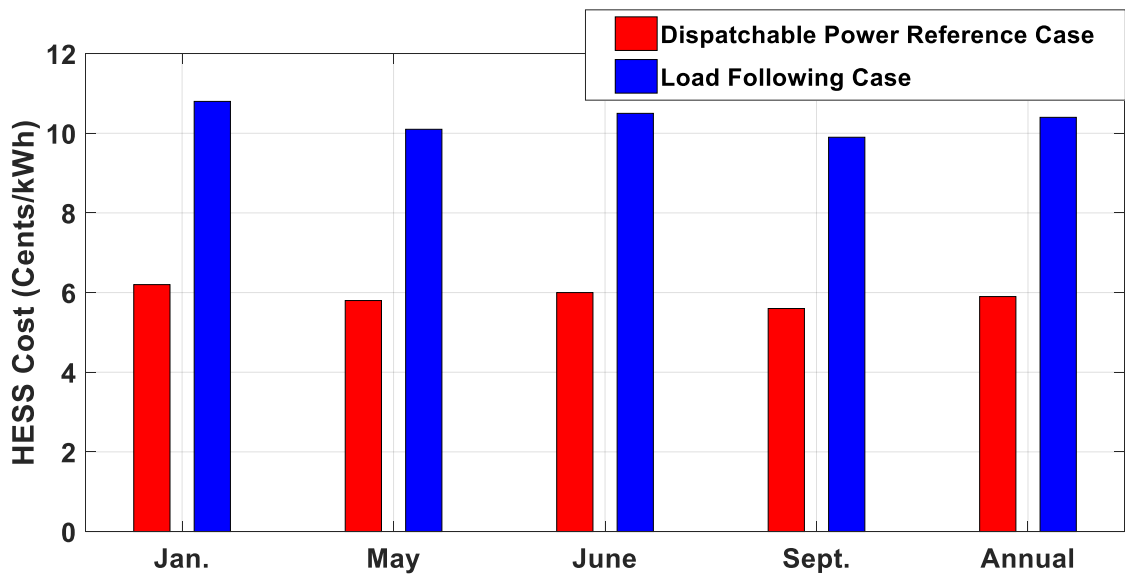


Figure 3.17: HESS cost (¢/kWh) at 62 s of the LPF time constants.

age power that the WSHPS can provide over each dispatching period. In the load following case, the load profile for 2.5 MW utility is collected from CAISO and is utilized as the  $P_{\text{Grid,ref}}$  for the entire system. The  $P_{\text{Grid}}$  successfully follows the desired  $P_{\text{Grid,ref}}$  in both cases investigated in this study, as shown in Fig. 3.9 and Fig. 3.10.

Due to the capacity factor constraints of RE sources, when the WSHPS framework

is assigned to meet the load demand that is equal to the WSHPS rated capacity, the WSHPS framework demands significant contribution from the ESS to successfully meet the utility load profile. Consequently, the required ESS capacity increases substantially for the load following case, as illustrated in Fig. 3.10. Thus, the HESS cost ( $\text{¢/kWh}$ ) is found to be more expensive for the load following case than the dispatchable power reference case. It is expected that the transmission system operator (TSO) assigns the load demand for the WSHPS framework considering the capacity factor constraints of RE sources. Since the WSHPS is utilized to fulfill its rated load demand without considering the capacity factor constraints, the HESS cost ( $\text{¢/kWh}$ ) reflects the worst-case scenario for the load following case.

The HESS expense is directly proportional to the required ESS size but is inversely proportional to the PV or WT capacity factor. The collaborative capacity factor of the WSHPS is higher than the individual PV or WT system. Also, the required ESS size is reduced in the WSHPS to fulfill the grid power demand due to the complementary power profiles of the WT and PV. Thus, the cost of the HESS becomes minimum in the WSHPS in comparison with a single PV or WT framework, which is verified in Fig. 3.18.

In this study, the statistical approach is performed to illustrate the required ESS capacities at different cumulative probability density function levels. The cumulative probability density function of the BESS energy capacities and the SESS energy capacities at 62 s LPF time constant for the dispatchable power reference case are demonstrated in Fig. 3.19, which shows that there is a trade-off between the loss of power supply probability and the minimum capacity required of the ESS. Since the ESS is committed to meet all of the possible charging-discharging energy requirements in this hourly dispatching scheme, the ESS rated energy capacity is chosen

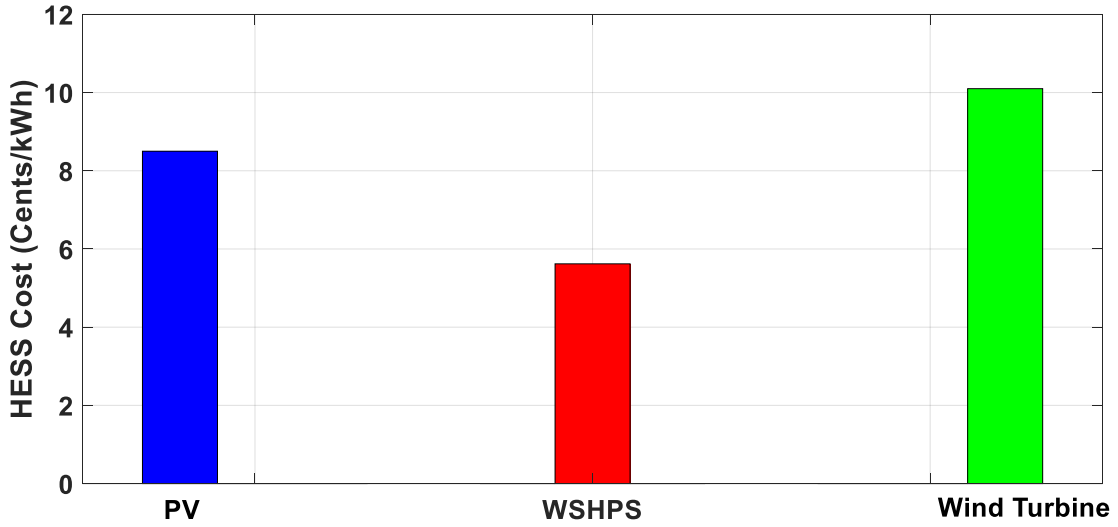


Figure 3.18: Annual HESS cost comparison at 62 s of the LPF time constants.

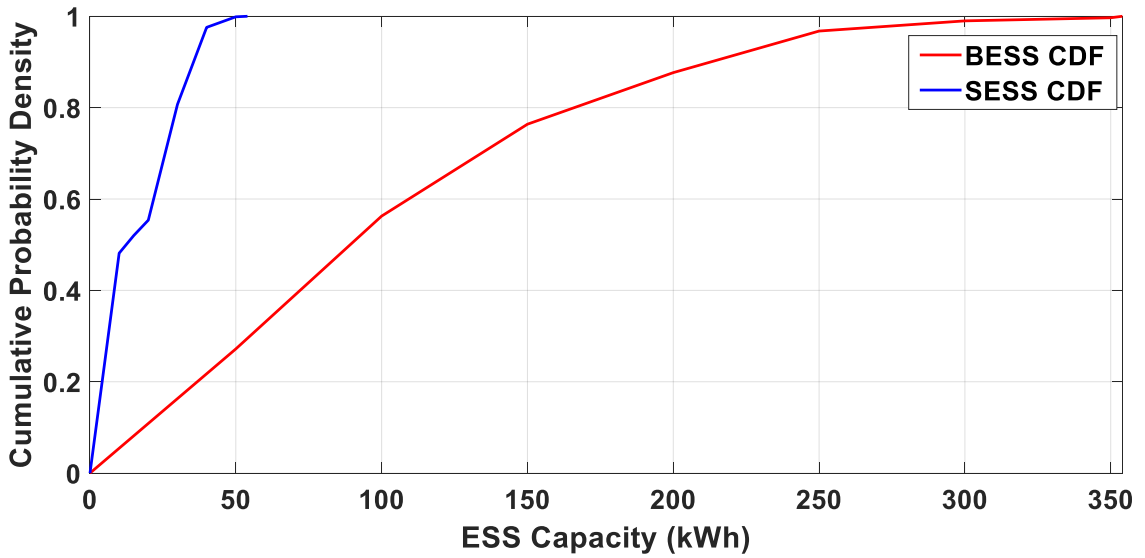


Figure 3.19: Cumulative probability density function of the BESS energy capacities.

corresponding to the CDF of 1, which is one factor to increase the required ESS capacity. Here, the most economical size of the BESS and SESS combination in the HESS scheme turns out to be 354 kWh and 55 kWh respectively at 62 s LPF time constant for the dispatchable power reference case. Likewise, the required power capacities of the BESS and SESS are evaluated for the HESS economic assessment.

The percentage of error between the  $P_{\text{Grid}}$  and  $P_{\text{Grid,ref}}$  is computed using (3.25) to

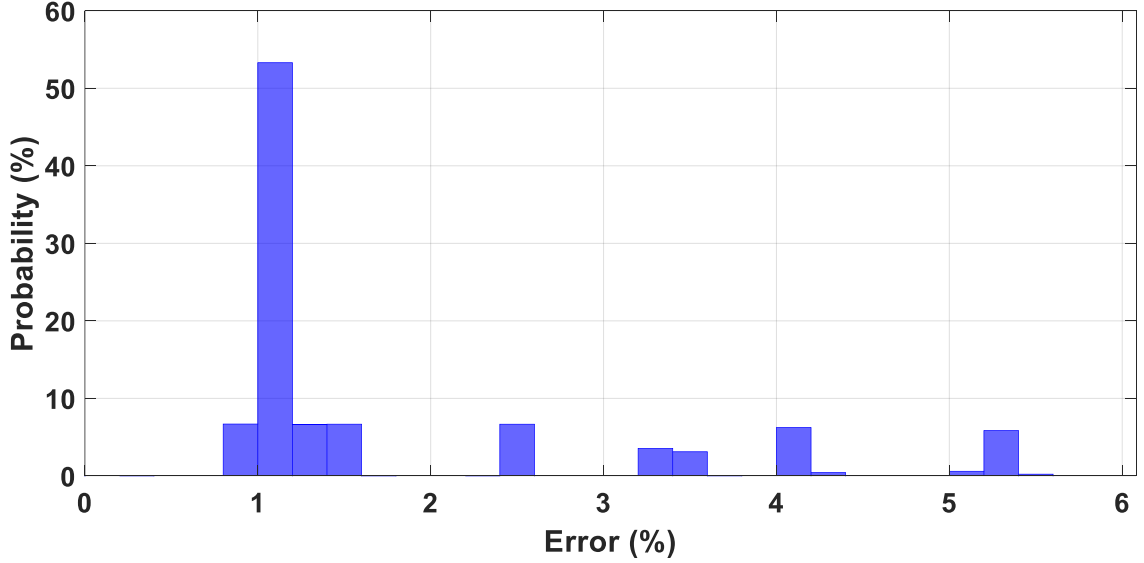


Figure 3.20: Histogram of hourly dispatching error results.

quantify the power quality criteria. The histogram of this error percentage is demonstrated in Fig 3.20. Since the  $P_{Grid}$  successfully tracks the desired  $P_{Grid,ref}$  closely in each dispatching period, the undesired deviation is found to be extremely low for the dispatchable power reference case. The similar phenomenon of the undesired deviation is also observed for the load following case. This attribute indicates the effectiveness of dispatchability provided by the WSHPS and HESS framework.

$$Error(\%) = \frac{|P_{Grid,ref} - P_{Grid}|}{P_{Grid,ref}} \quad (3.25)$$

Furthermore, IEEE 1547-2003 [172] provides the THD constraints of the grid voltage and current for the interconnection of distributed resources within electric power systems to maintain the power quality of the utility grid. The three-phase current injected into the grid is illustrated in Fig. 3.21, and the THD of the injected current is found to be 3.1 %, which is within reasonable limits. Furthermore, the three-phase grid voltage waveform is shown in Fig. 3.22, and the THD of the grid

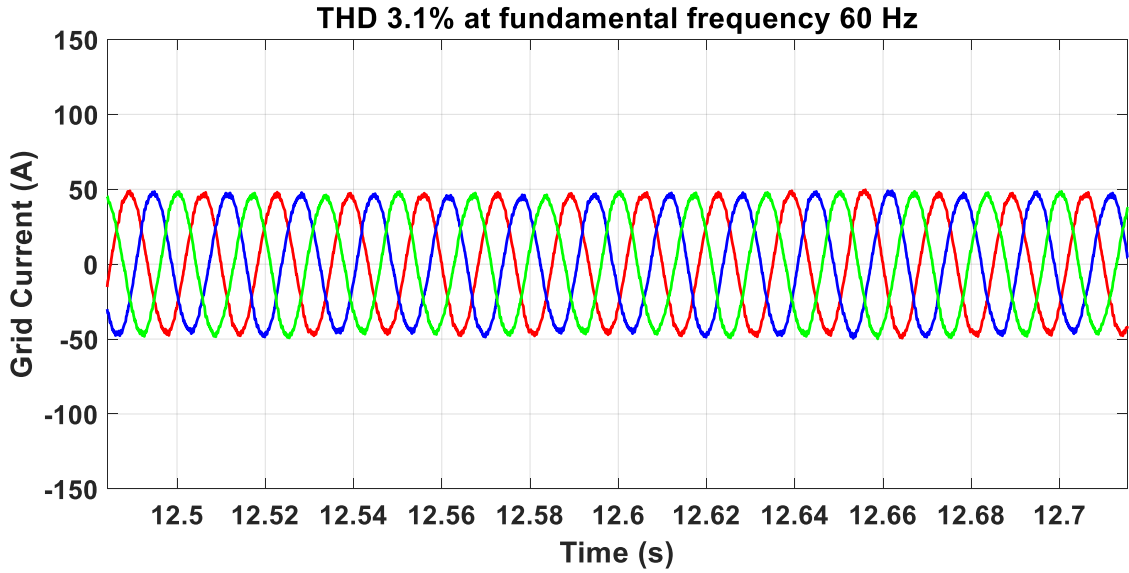


Figure 3.21: Injected current into the grid.

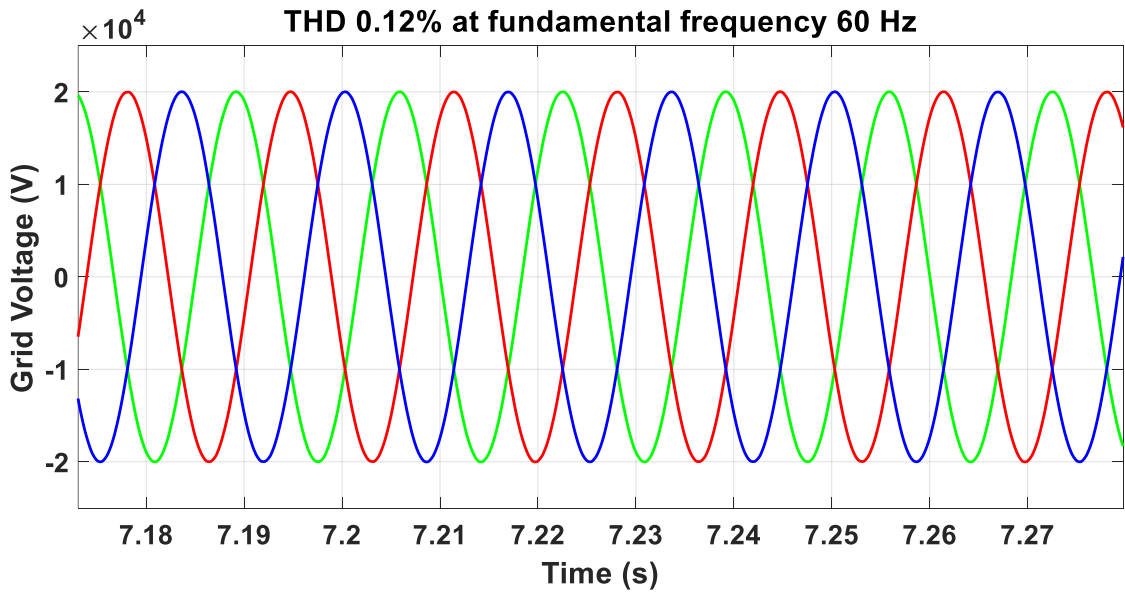


Figure 3.22: Three-phase voltage waveforms of the grid.

voltage waveform is found to be 0.12 %, which is within reasonable limits as well.

As mentioned earlier, the expenditure associated with the ESS is inversely proportional to its lifetime. The SESS helps to alleviate the fast-changing power components passing through the BESS in the HESS architecture, which is beneficial for prolonging the BESS service life. In the rainflow counting approach, cycle range signifies the ab-

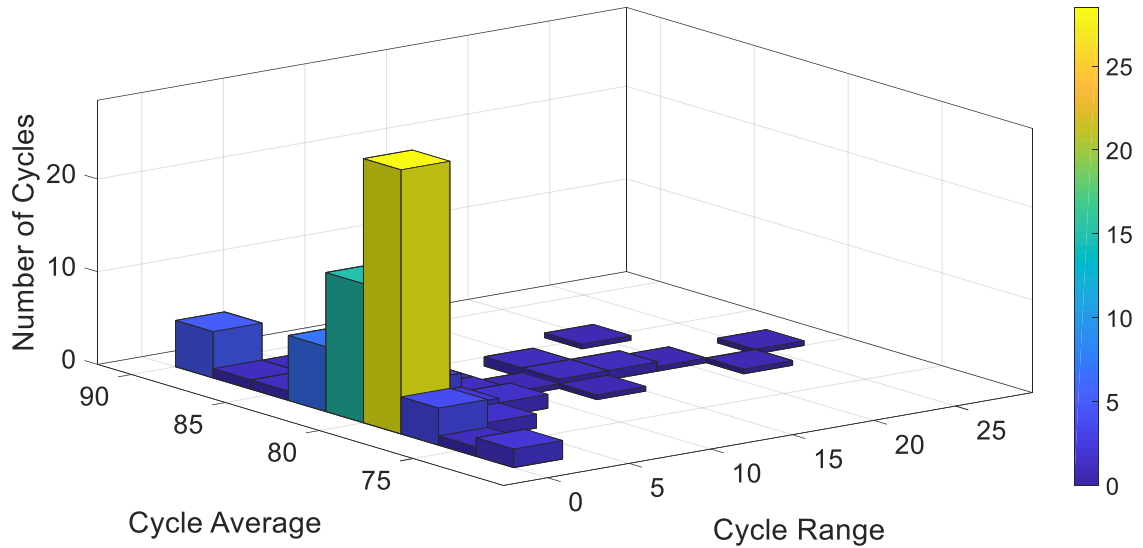


Figure 3.23: Rainflow matrix histogram of the BESS.

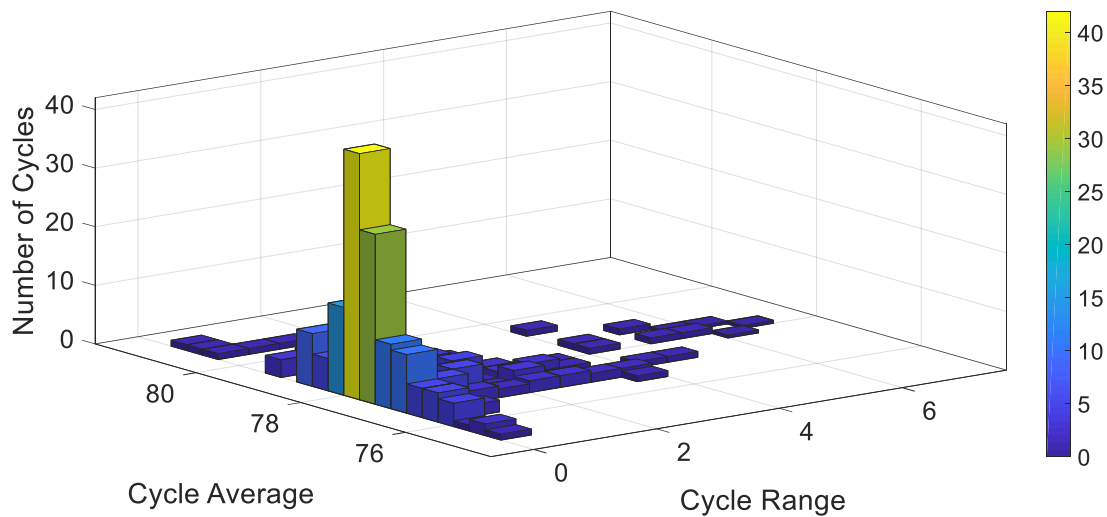


Figure 3.24: Rainflow matrix histogram of the SESS.

solute value of the difference between the amplitude of the first point and the second point when the cycle is considered. Fig. 3.23 illustrates the rainflow histogram of the BESS to validate the fact that the slow-changing components of the HESS power are charged-discharged through the BESS. Nevertheless, the fast-changing components of the HESS power are charged-discharged through the SESS. Fig. 3.24 is presented to justify this statement.

Furthermore, the power spectral density of the BESS and SESS shown in Fig. 3.25 and Fig. 3.26 exhibits the relative effectiveness of the SESS for absorbing high frequency components from the HESS. An estimated BESS lifetime comparison with and without the SESS in the energy storage framework is illustrated in Fig. 3.27. It can be observed that the BESS lifetime substantially increases when the SESS is part of the storage framework. Hence, the HESS is more cost-effective in comparison to using battery-only for dispatching the WSHPs.

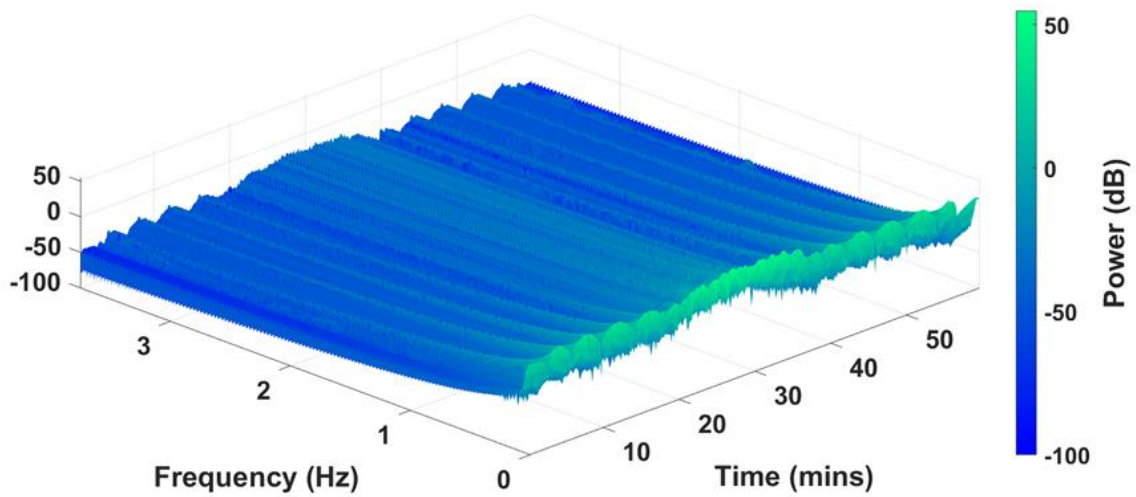


Figure 3.25: Spectrogram of the BESS.

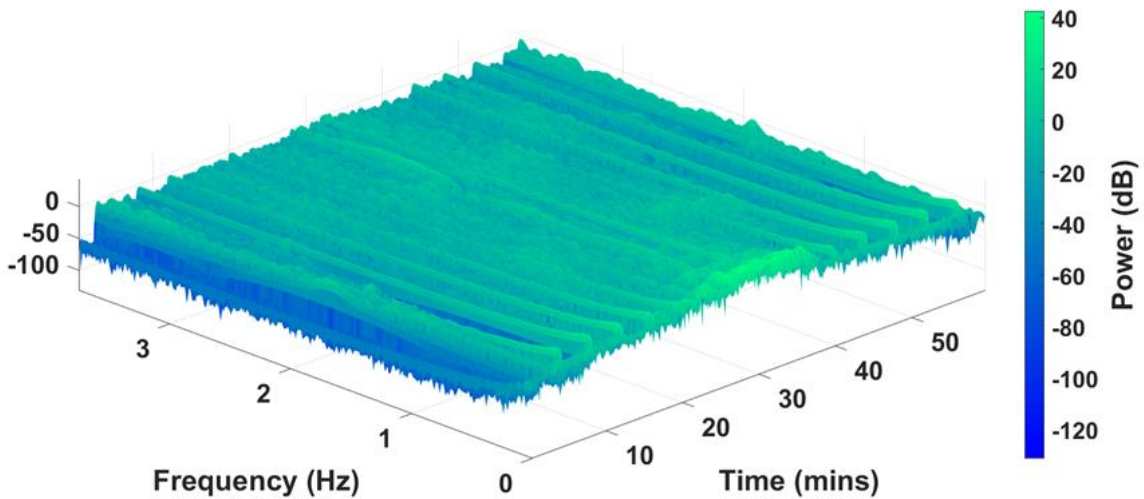


Figure 3.26: Spectrogram of the SESS.

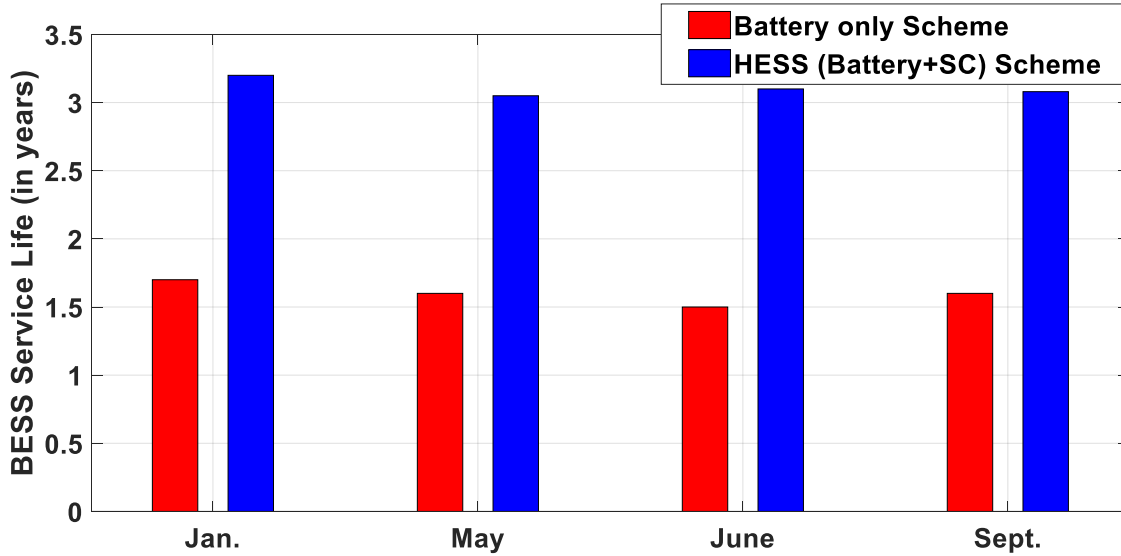


Figure 3.27: Battery lifetime (in years) comparison.

### 3.4 Summary

In this study, an hourly dispatching scheme of the WSHPS power has been presented. Simulation results exhibit that the WSHPS power can be successfully dispatched on an hourly basis at an error of less than approximately 1.5% most of the time. In this chapter, the energy storage life cycle cost is optimized as a function of its DOD usage. Furthermore, the optimum value of the LPF time constant in the HESS architecture has been found to be 62 s by implementing the curve fitting and PSO techniques that yield the most cost-effective HESS (i.e., annual HESS cost 5.9 ¢/kWh and 10.3 ¢/kWh for the grid dispatchable power case and the load following case, respectively). The significance of the SC on battery longevity when it is integrated into the HESS framework has been investigated. Also, the impact of the SOC control algorithms has been validated to develop a cost-effective HESS for a utility-scale hybrid PV-WT system.



## **Chapter 4 Cost, Reliability, and Power Converter Interface for Integrating PV into Utility with ESS**

This chapter explores the optimal scheduling for dispatchable utility-scale solar PV power with a battery-supercapacitor hybrid energy storage system. The expenditure of energy storage for hourly dispatching of utility-scale solar power using HOMER Pro is also investigated. Furthermore, this chapter contemplates a dispatching scheme of megawatt-scale solar PV power for a one-hour dispatching period for an entire day utilizing an isolated multiport converter configuration and a battery energy storage system.

Solar energy has been explored extensively in recent years to address significant global issues such as pollution and the depletion of fossil fuels. However, the PV output power exhibits intermittent characteristics since its insolation relies on the natural and meteorological conditions. Consequently, solar power plant's output can potentially vary between zero and the maximum available power. Thus, it is classified as a non-dispatchable energy source, which signifies that there is no guarantee the expected amount of power will be available on-demand for a specified period of time [173]. The ability of power system units to be turned on and off, as well as ramp up and ramp down their power output within the specified operational limits, is referred to as dispatchability. Dispatchable PV energy generation is the ultimate goal of 100 percent renewable-based power systems because it can provide a constant power dispatch, similar to what conventional fossil fuel power plants have done. The primary objective of this research is to develop a dispatching scheme that can provide a committed constant PV power into the utility grid at a specified confidence level

while also minimizing the costs associated with this system. As indicated before, when the ESS is incorporated into the PV framework, the uncertainty of PV power can be further decreased. In this research, the HESS comprised of a battery and a SC is employed to create a more cost-effective ESS, where the SC is also assisting in mitigating high frequency power components passing through the battery, which is helpful for increasing battery lifetime.

Here, the optimal scheduling for dispatchable utility-scale solar PV power with a hybrid energy storage system consisting of a battery and a SC is investigated. The optimal capacity of the ESS is assessed based on its usage of depth of discharge, which is critical for minimizing the cost of a dispatchable PV power scheme. The hybrid system can successfully dispatch the scheduled power at any dispatching horizon by leveraging the optimal ESS capacity. Both cycling and calendar expenses are taken into account during the cost optimization of the ESS to make it more practical.

Three different dispatching horizons are investigated for the desired  $P_{\text{Grid,ref}}$  calculation, which are 30-minutes (Semi-hour), 1-hour (Hourly), and 15-hour (Entire day). In general,  $P_{\text{Grid,ref}}$  is computed by averaging the power that the PV can provide over each dispatching period, and it serves as a target power level for the entire system. Accordingly, the minimum capacity required for the ESS to secure reliable dispatched power is the maximum discrepancy between the  $P_{\text{Grid,ref}}$  and PV output power. Besides, the battery capacity rating has a significant impact on the charging-discharging characteristics, such as total number and depth of charging-discharging cycles, which are used to determine ESS lifetime. Evidently, the dispatching horizon is strongly related to the ESS capacity and lifetime, which are the essential elements in determining the ESS expenditure. Thus, selecting the optimum dispatching horizon duration for a dispatchable PV power is critical for developing a cost-effective

ESS. An economic analysis is presented here to evaluate the effect of dispatching horizon selection on ESS cost estimation. Besides, an economic comparison is conducted utilizing the HOMER Pro software, which was developed by NREL, to design a cost-effective ESS for an hourly PV power dispatching scenario.

The expenditure of the ESS is directly proportional to the capacity required but inversely proportional to its service life. Because the ESS lifetime is substantially reduced with deeper discharge, the SOC of the ESS has always been controlled to prevent the ESS from being depleted beyond its suggested DOD, i.e., the lowest depletion SOC of ESS. However, such SOC regulation is responsible for limiting the full utilization of the ESS, which is one contributing factor to the required energy storage capacity being extended. Therefore, there is a trade-off between the service life and the minimum capacity required of ESS depending on its SOC utilization. This research explores the value of DOD that has the best competitive ESS cost for dispatching the PV power to the utility. During this economic analysis, both the cycling and calendar aging expenses associated with the ESS are taken into account. Furthermore, after determining the optimal DOD value for the ESS, one secondary SOC control technique is implemented to keep the ESS SOC within the optimal range.

Accurate forecasting of PV power is vital for generation scheduling and cost-effective operation. A multilayer perceptron ANN is utilized to predict PV irradiance one hour ahead of time, which performs well with good convergence mapping between input and target output data. Here, the  $P_{\text{Grid,est}}$  is determined by computing the average power that the PV can provide for each dispatching period, and the solar farm is in charge of supplying this reference power to the utility. A multilayer perceptron ANN is used to predict the PV insolation one hour ahead of time so that the grid operators can be informed beforehand about the  $P_{\text{Grid,est}}$ , which will provide more

flexibility to the grid operators' scheduling of their generation units.

As mentioned before, it is vital to ensure that the ESS ends each dispatching period with the same SOC that it began with in order to reduce ESS expenditures and ensure sufficient capacity is available to handle next-day operations. As a function of both battery and SC SOC in the HESS framework, this chapter proposes an ANFIS based SOC controller that can adjust the  $P_{\text{Grid,est}}$  at the start of each dispatching period, thereby aiding in achieving the desired  $P_{\text{Grid,ref}}$  for each dispatching period. In addition, this controller would ensure the ESS ends each dispatching period with the same SOC that it began with.

This chapter also investigates a dispatching scheme of megawatt-scale solar PV power for a one-hour dispatching period for an entire day utilizing an isolated multiport converter configuration and battery energy storage system. A multilevel TAB DC-DC converter has been developed where a NPC H-bridge is employed in the high-voltage side, and the conventional two-level full-bridge is configured in the low-voltage side across the high-frequency transformer. The power losses between the developed TAB-NPC converter and conventional TAB converter are compared to identify the superior multiport converter topology for this application.

Also, multilevel inverters, T-type and I-type NPC inverters, are investigated due to their superior attributes: high efficiency, low total harmonic distortion, and reduced common-mode voltage. The power losses between the three-level T-type and I-type NPC inverters are compared, to identify the superior grid inverter topology for this application. This study also deals with the optimized design procedure of an LCL filter for a grid-connected RE system.

TAB converter acts as a viable option to address the intermittent issue of solar energy by incorporating a battery energy storage system in the PV framework for a

large-scale PV-BESS grid integration. TAB DC-DC converter has attracted more and more attention due to its salient advantages: multiple interfacing ports, high-power density, galvanic isolation, bidirectional power flow, and soft-switching capability. Typically, separate DC-DC converters employed for individual sources are linked together at the DC bus and controlled independently. However, this type of power electronic interface is inherently complex and less efficient due to multiple conversion stages. In the multiport power converter architecture, both the DC link and the magnetic coupling are combined together; thereby the entire system is treated as a single power converter. Thus, the centralized control can be deployed with a minimal number of conversion steps since here the system resources are shared.

Nowadays, the multiport converter is preferable to connect multiple energy sources to the grid due to its lower cost, centralized control, and higher power density. In the literature, a number of multiport converters have been proposed for renewable energy systems [174], [175]. The multiport converter configurations can be classified into two categories: non-isolated topologies and isolated topologies. Non-isolated multiport converters are usually employed in applications that do not demand galvanic isolation. In contrast, an isolated converter, which incorporates a transformer, is desirable for applications that require galvanic isolation between the energy sources and the grid. In this study, high frequency transformer-coupled isolated multiport converter is utilized for a PV-BESS grid integration.

The authors in [176] investigated a triple port dual active bridge converter for the integration of solar energy into the utility grid. Another triple port dual active bridge converter configuration was discussed in [177] for the PV integration into the grid. However, with the power capacity increased, PV systems with higher voltage level such as 1.5 kV or above are preferred due to higher efficiency and lower cost,

which may impose significant voltage stress across the semiconductor switches and induce higher  $dv/dt$ , if the conventional two-level converter bridges are used. In this research, two three-level NPC switching poles will be used in the high-voltage side of the developed TAB-NPC converter configuration. Thus, a five-level voltage waveform in the high-voltage bridge is produced, which leads to semiconductor switches being exposed to only half of the DC bus voltage, resulting in lower  $dv/dt$  stress and ameliorating converter efficiency.

As the integration of PV energy into the utility increases substantially, the efficient energy conversion of the power converter has gained more attention. This research incorporates a comparative power loss analysis between the developed TAB-NPC converter and conventional TAB converter for dispatching solar PV power at 1-hour increments for an entire day for a 1-MW grid-connected PV array. IGBT and silicon carbide (SiC) MOSFET are the most popular semiconductor devices for multilevel converter design and construction. Selecting the appropriate device for the selected converter topology at different power specifications is also crucial for efficient and reliable converter design. This study also analyses the multiport converter power losses and resulting efficiencies with the above-mentioned semiconductor devices so that an efficient converter topology could be obtained for hourly dispatching PV power scheme.

## **4.1 Proposed Methodology**

### **4.1.1 System Structure for PV Farm**

The proposed PV-ESS system configuration is shown in Fig. 4.1. The PVES consists of 1 MW PV arrays, a MPPT, and a unidirectional DC/DC boost converter. The

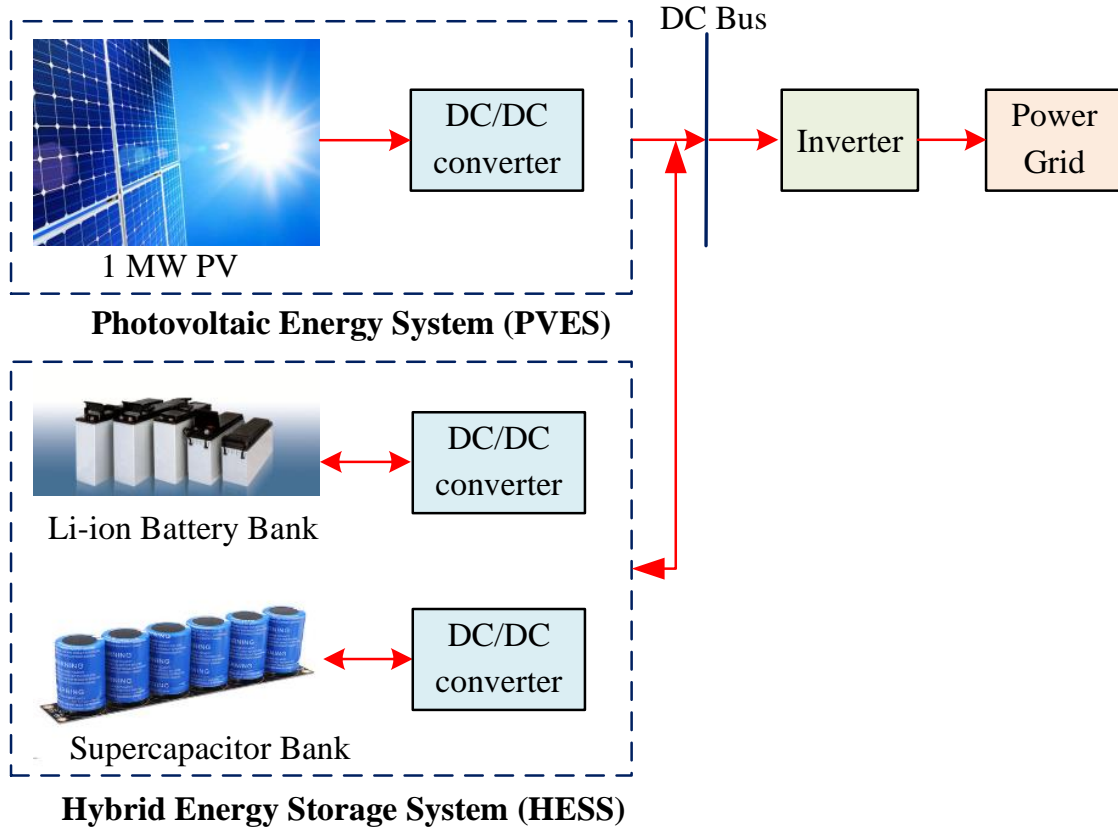


Figure 4.1: Structure of the dispatching PV-ESS system.

HESS, which is comprised of a Li-ion battery and a SC, is connected to the PVES in parallel, and each of the ESS is coupled to a bi-directional power converter. The PVES and HESS are linked to the DC bus as a current source in this framework, and the inverter regulates the DC bus voltage. Hence, controllable power flow is obtained by managing current flow via power converters.

The actual solar irradiance, temperature, and wind speed data recorded at ORNL on June 10<sup>th</sup> 2019 [178] are utilized to estimate dispatched power for an entire day on the investigated dispatching horizon basis, and it is referred to as the  $P_{\text{Grid,est}}$ . The  $P_{\text{Grid,est}}$  is determined by estimating the average power that the PVES can provide for each dispatching period, and the solar farm (PVES and HESS) is responsible for supplying this reference power to the utility. Here, three different dispatching horizons

are investigated for the  $P_{\text{Grid,est}}$  calculation, which are 30-minutes (Semi-hour), 1-hour (Hourly), and 15-hour (Entire day), which is illustrated in Fig. 4.2. Also, Fig. 4.3 shows the  $P_{\text{Grid,est}}$  profiles for each one-hour dispatching period corresponding to the solar irradiance data at one sample/minute on July 16, 2019. The objective is to investigate the effects of the dispatching horizon duration on the ESS cost assessment for a dispatchable PV power scheme.

This study uses the ANN to estimate solar insolation one hour in advance, which is suitable to describe the intermittent phenomenon of solar irradiance due to its non-linear nature. In the MATLAB environment, a feed-forward seven-layer perceptron ANN is used to forecast hourly solar insolation one hour ahead of time, where the Levenburg-Marquardt algorithm is employed in training. The “tansig” and “logsig” transfer functions are implemented at the hidden layer and output layer, respectively. The following steps are taken into account to forecast PV insolation one hour ahead of time using the ANN. (1) The hourly solar irradiance and the time of day index

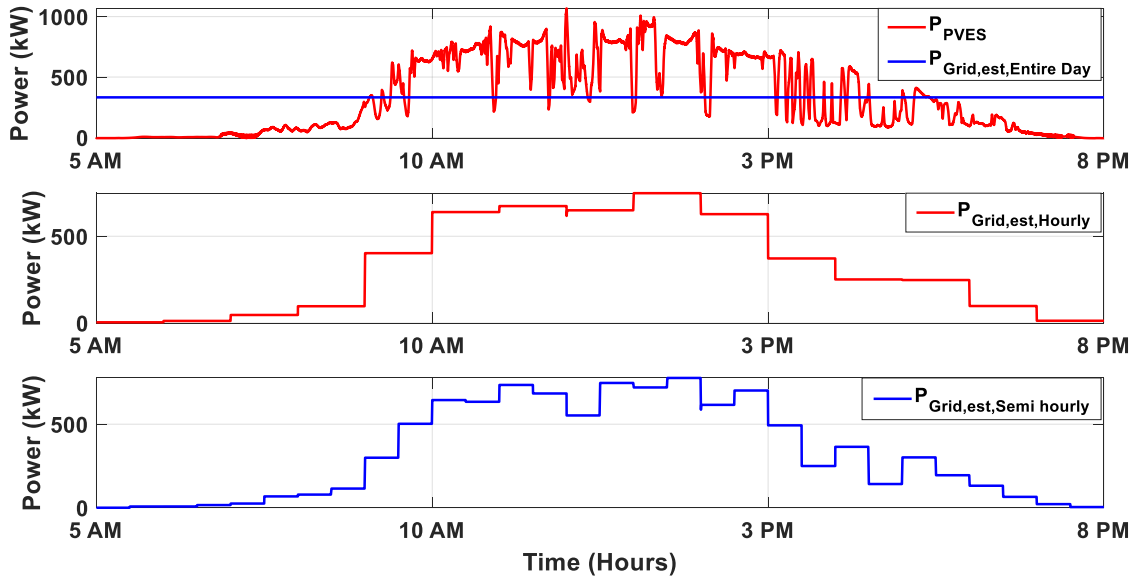


Figure 4.2: Grid estimated power calculation on June 10, 2019.



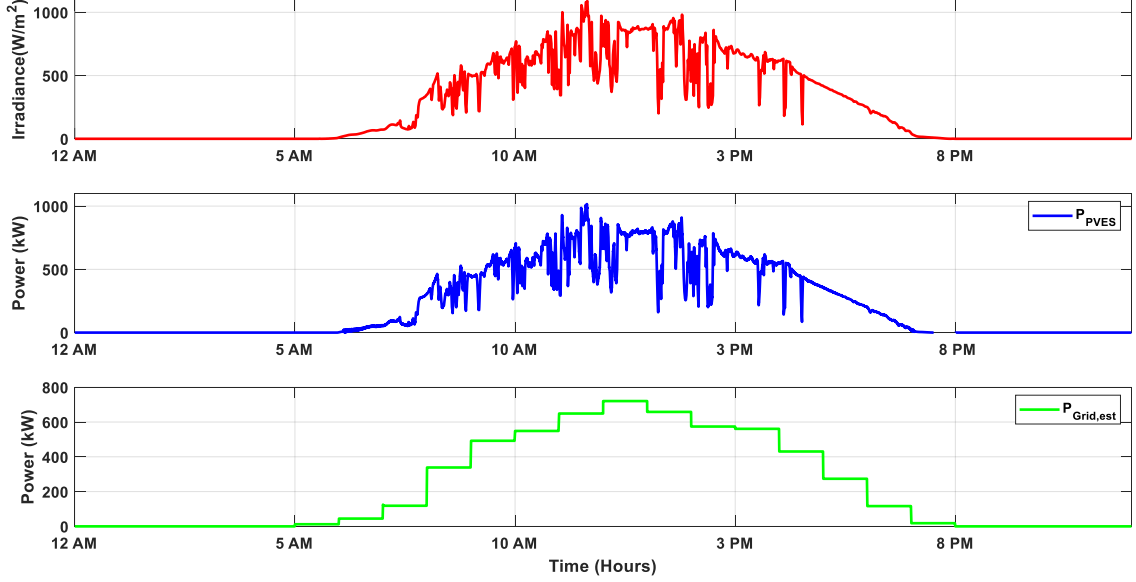


Figure 4.3: Grid estimated power calculation on July 16, 2019.

are utilized as inputs. (2) Hourly PV irradiance data recorded at ORNL from July 1, 2019, to July 15, 2019, is utilized for training the ANN model to estimate hourly PV irradiance on July 16, 2019. (3) After training the ANN, the model is evaluated to forecast the hourly PV insolation on July 16, 2019. (4) Finally, the ANN model's performance is measured by comparing forecasted solar irradiance data to historical solar irradiance data in terms of Root Mean Square Error (RMSE), as shown in (4.1). Table 4.1 presents the detailed specifications of the ANN model.

$$RMSE = \sqrt{\frac{1}{N} \sum_{m=1}^N \left( y_f^{i,L} - y_r^{i,L} \right)^2} \quad (4.1)$$

where  $y_f^{i,L}$  is the forecasted PV irradiance,  $y_r^{i,L}$  is the actual PV irradiance, and  $N$  is the total number of forecasting cases.

Here, the following steps are taken into account while determining the desired  $P_{\text{Grid,ref}}$  for each dispatching period. First, the mean operation technique is employed to compute the PV power on an hourly basis, which is referred to as the  $P_{\text{Grid,est}}$ .

Table 4.1: ANN model specifications.

Parameter	Value
Training function	Trainlm
Performance function	RMSE
Number of layers	7
Number of hidden layers	5
Number of neurons in each layer	[1 20 20 20 20 1]
Activation function hidden layer	Tansig
Activation function output layer	Logsig
Epochs	1000

The primary SOC controller is then used to find the appropriate multiplication factor in order to adjust the  $P_{\text{Grid,est}}$  at the start of each dispatching period to achieve the desired  $P_{\text{Grid,ref}}$ , ensuring that the ESS bank’s SOC stays within an acceptable range. Fig. 4.4 depicts the primary SOC controller in which the ANFIS is implemented to calculate the appropriate multiplication factor for the  $P_{\text{Grid,est}}$ . The multiplication factor is directly tied to the ESS SOC at the end of each dispatching period, and it is critical in ensuring that the ESS finishes with its starting SOC so that ESS expense can be decreased. The ANFIS is trained using the MATLAB “Neuro-Fuzzy Designer” tool, which generates a single output fuzzy inference system (FIS) and tunes the system parameters using given input (ESS SOC) and output (multiplication factor) training data. A combination of least-squares and back-propagation gradient descent is used to model the training data set. The training data set and output of the ANFIS are illustrated in Fig. 4.5 and Fig. 4.6, respectively, while considering the ESS SOC as an input and the multiplication factor as an output.

The HESS power control framework is shown in Fig. 4.7. The discrepancy between the  $P_{\text{Grid,ref}}$  and the  $P_{\text{PVES}}$  represents the  $P_{\text{HESS,ref}}$ , as demonstrated in (4.2). In this case, the  $P_{\text{Grid}}$  is the combination of the PV output power and the HESS power, which may be expressed as (4.3). The HESS is responsible for maintaining the  $P_{\text{Grid}}$  either

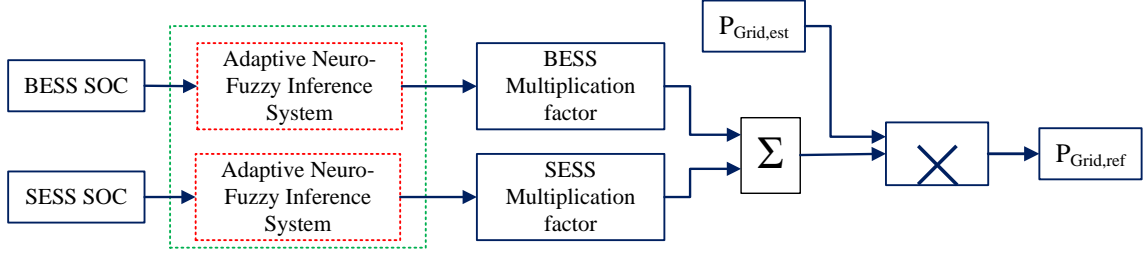


Figure 4.4: Block diagram of the primary SOC controller with ANFIS.

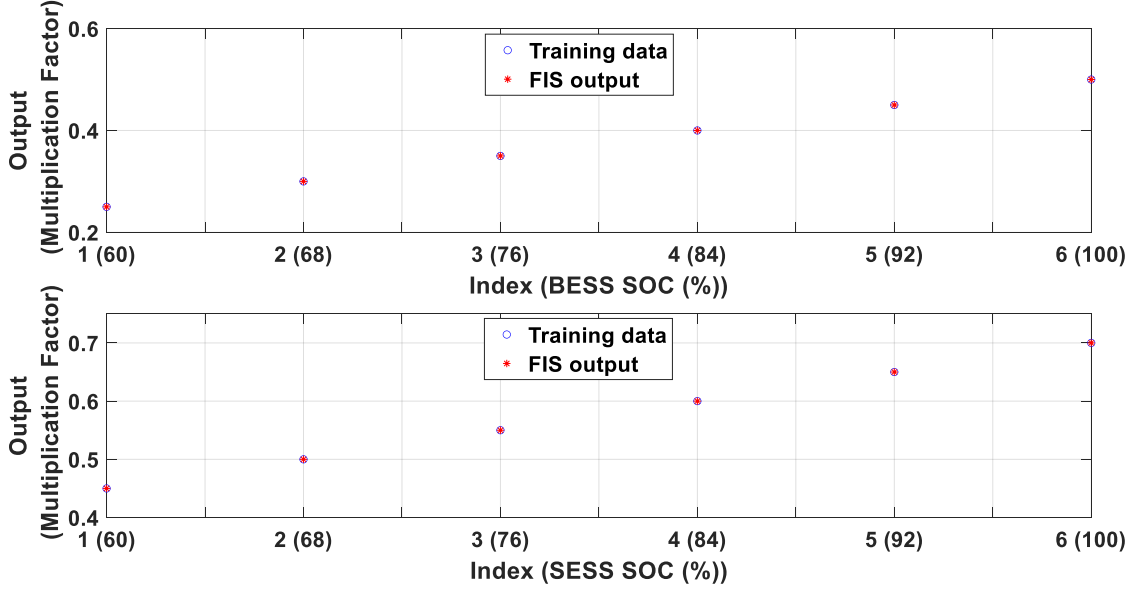


Figure 4.5: ANFIS training data set as a function of ESS SOC.

by supplying or absorbing the required power so that the  $P_{Grid}$  is able to follow the desired  $P_{Grid,ref}$  in each dispatching period. In this research, the  $P_{HES,ref}$  is decoupled by employing the LPF with a filter time constant of 30 s to provide high-frequency components of power reference for the SESS and low-frequency components of power reference for the BESS [165]. This type of frequency management technique assists in extending the battery lifetime and reducing the overall system expenditure. In the HESS scheme, the power converter connected to the ESS operates in a buck mode when the ESS is charging and acts in a boost mode when the ESS is discharging.

$$P_{HES,ref} = P_{Grid,ref} - P_{PVES} \quad (4.2)$$

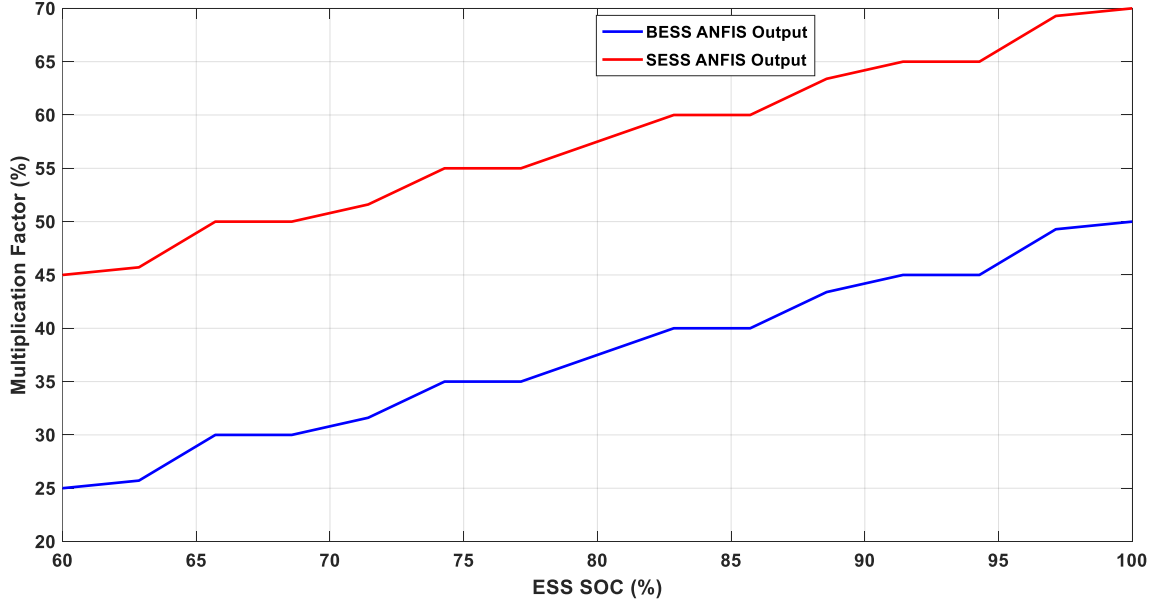


Figure 4.6: ANFIS output for ESS (from 60% SOC to 100% SOC).

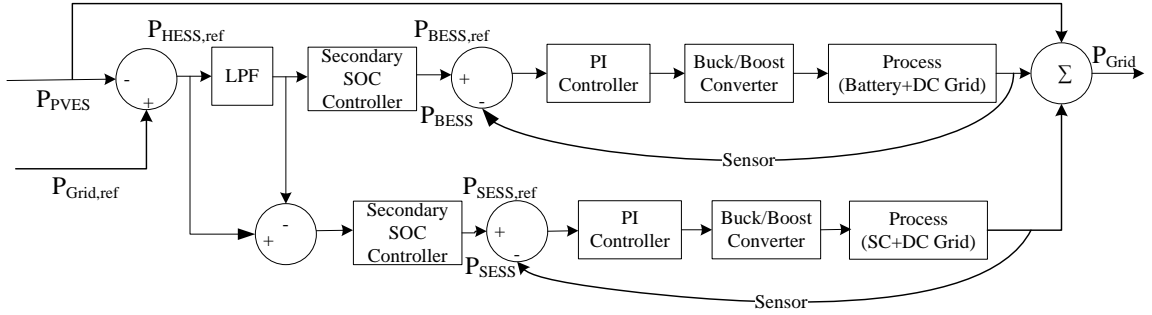


Figure 4.7: HESS power control framework for PV farm.

$$P_{Grid} = P_{PVES} + P_{HESS} \quad (4.3)$$

Another SOC control algorithm called secondary SOC control, as shown in Fig. 4.8, is also employed to ensure that the ESS SOC remain within their optimal ranges. Here, after seeking the optimal DOD usage for the ESS, the upper and lower bounds of the ESS SOC are selected. Then, the secondary SOC algorithm utilizes a rule-based approach to prevent the ESS SOC from going above its upper bound (100 % SOC) or going below its lower bound (optimal DOD level).

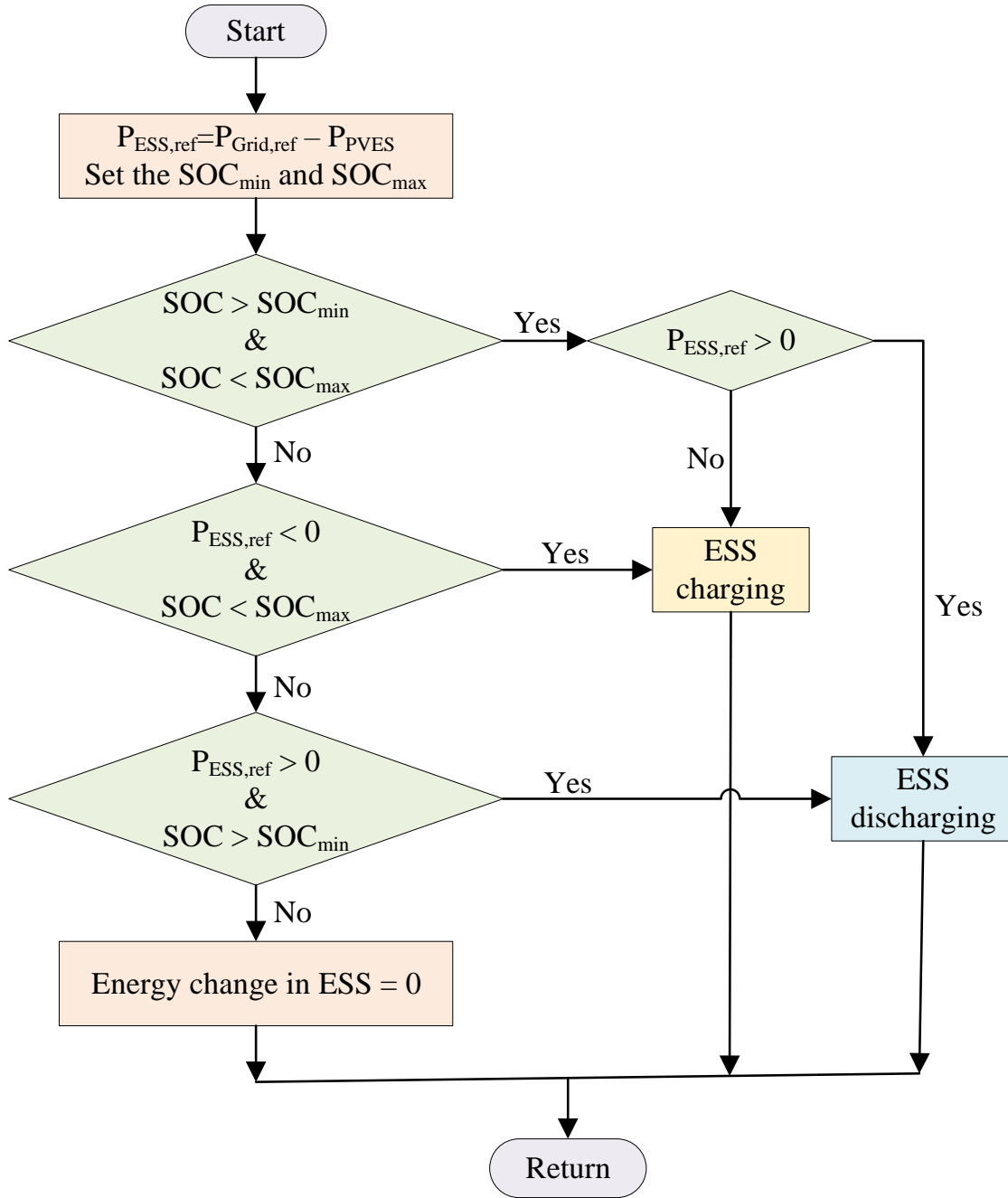


Figure 4.8: Modified secondary SOC control algorithm.

#### 4.1.2 Cost Optimization for HESS

The cost of the ESS is mostly determined by two factors, e.g., lifetime and the minimum capacity required of the ESS. The minimum capacity required for the ESS to secure reliable dispatched power is the maximum discrepancy between the  $P_{Grid,ref}$

and PV output power. Here, the capacity required for the ESS is computed by the integrated ESS power profile with respect to time. First, the absolute maximum amount of energy utilized by the ESS during each dispatching period is calculated and compared. Second, the maximum of these maximums yields the minimum energy capacity required for the ESS to successfully dispatch the PV power to the utility.

$$E_{ESS}^r = \frac{\text{Max}_{0 \leq t \leq T} \int_0^t |P_{Grid,ref}(\tau) - P_{PVES}(\tau)| d\tau}{DOD_{max}} \quad (4.4)$$

where,  $E_{ESS}^r$  is the ESS capacity,  $DOD_{max}$  is the maximum DOD used by the ESS, and  $T$  is the simulation time.

The ESS's service life is mostly determined by the amount of DOD used and the rate of change of the charging-discharging power. Fig. 3.7 depicts the relationship between cycle life and DOD utilization for the Li-ion battery and SC [169]. As the minimum capacity required and service life of the ESS are strongly related to its DOD usage, it is extremely important to seek the proper value of DOD that yields the least expensive ESS for dispatching the PV power. In this research, the 3<sup>rd</sup> order polynomial curve fitting technique is executed to acquire the appropriate cost formula for the ESS as a function of its DOD utilization, as shown in (4.5).

$$ESS_{Cost,DOD}(y) = Q_1 y^2 + Q_2 y + Q_3 \quad (4.5)$$

where  $Q_1$ ,  $Q_2$  and  $Q_3$  are regression coefficients, and  $y$  is the DOD level utilized by the ESS.

The total expense of the ESS is primarily comprised of its cycling and calendar costs, and both of these expenses are taken into account while the ESS cost is explored in this study. Here, the ESS cycling aging is calculated using [147], and the ESS

calendar aging is computed using the degradation model described in [76]. The normalized HESS cost per kWh is then determined considering both the battery and SC expense utilizing the following formulas.

$$C_{HESS,cost} = \frac{E_{BESS} \times C_{BESS}}{T_{BESS,life}} + \frac{E_{SESS} \times C_{SESS}}{T_{SESS,life}} \quad (4.6)$$

$$Cost_{Norm} = \frac{C_{HESS,cost}}{P_{PV} \times PV_{CF} \times T} \quad (4.7)$$

where  $E_{BESS}$  and  $E_{SESS}$  are the required capacity (kWh) for the battery and SC, respectively, and  $C_{BESS}$  and  $C_{SESS}$  are the cost (\$/kWh) for the battery and SC, respectively.  $T_{BESS,life}$  and  $T_{SESS,life}$  represent the battery and SC's expected lifetimes while accounting for both cycling and calendar aging.  $P_{PV}$  is the PV capacity (kW),  $PV_{CF}$  is the PV capacity factor (20% is assumed in this study), and  $T$  is the number of hours in a year. The unit price of Li-ion battery and SC are considered to be \$271/kWh and \$2500/kWh, respectively.

#### 4.1.3 Techno-economic Optimization using HOMER Pro

In this study, three distinct system frameworks are studied for hourly dispatching of PV power, i.e., (i) PV+BESS (battery-only scheme), (ii) PV+SESS (SC-only scheme), and (iii) PV+HESS, and the techno-economic optimization of these system architectures is evaluated using HOMER Pro. The HOMER Pro tool is designed and developed by the NREL and is used to assess the economics and technical feasibility of distributed generation applications. The HOMER Pro is an efficient application to optimize small power systems using a variety of equipment options based on various constraints and sensitivity levels [179].

The optimization of the hybrid system is performed with the objective to minimize total net present cost (NPCs) and levelized cost of energy (LCOE) to the system constraints, such as the fulfillment of the  $P_{\text{Grid,ref}}$  in each dispatching period so that the unmet electrical load is found to be zero. The *NPCs* and *LCOE* can be evaluated in HOMER Pro using (4.8) and (4.9). The PV irradiance and the  $P_{\text{Grid,est}}$  profiles illustrated in Fig. 4.3 are fed in HOMER Pro as input for the PV and electrical load data, respectively, and the load following dispatch strategy is employed. Here, the PV irradiance and  $P_{\text{Grid,est}}$  profiles are assumed to be the same for other days of the year during the techno-economic optimization. The specifications of different components exploited in this research for economic evaluation are summarized in Table 4.2 [180].

$$NPCs = \frac{C_{\text{annual}}}{CRF(i, T_{\text{project}})} \quad (4.8)$$

$$LCOE = \frac{C_{\text{annual}}}{L_{\text{primary}}} \quad (4.9)$$

where  $C_{\text{annual}}$  is the annualized total cost,  $i$  is the interest rate,  $T_{\text{project}}$  is the lifetime of the project,  $CRF(.)$  is the capital recovery factor, and  $L_{\text{primary}}$  is the total primary load.

Furthermore, the relationship between the cycle life and DOD usage for the Li-ion battery is computed using (3.10), and the total number of charging-discharging cycles as a function of the DOD for the SC is assumed to be constant (i.e., 500,000) since

Table 4.2: Summary of the PV system component specifications.

<b>Parameter</b>	<b>PV</b>	<b>Inverter</b>	<b>BESS</b>	<b>SESS</b>
Capital cost (\$)	1000	114	189	2500
Replacement cost (\$)	820	106	175	2325
O&M cost (\$/year)	10	0	10	1
Lifetime (years)	25	15	15	16



SC can be virtually charged-discharged an infinite number of times [170]. Fig. 3.7 demonstrates the relationship between cycle life and DOD usage for the Li-ion battery and SC. These specifications of the ESS are also fed to the HOMER Pro during the economic assessment.

## 4.2 Isolated Multiport Power Converter Interface

### 4.2.1 System Structure for PV Farm with TAB-NPC Converter

The TAB-NPC converter topology has been developed for a large scale PV-BESS grid integration, as shown in Fig. 4.9. The developed converter has two low-voltage H-bridge ports to interface the PV and BESS (port 1 refers to the PV, Port 2 refers to the BESS), and one high-voltage NPC-based H-bridge port for connecting high voltage DC bus (2500 V is considered here). A three-winding high-frequency transformer provides electrical galvanic isolation and matches the high voltage–low voltage ports with its turn ratio. Each full bridge on the low voltage side operates at a fixed switching frequency (5 kHz in this scenario) and a 50 % duty cycle.

A phase shift control is employed for controlling the power flow between the ports of the three-port TAB-NPC DC-DC converter. The phase shift control is the most straightforward technique, which is extensively implemented in the multiport converters. The bidirectional power flow is executed by appropriate phase angles with respect to the reference port, which is the PV connected port (i.e., port 1) in this study. The MPPT controller is implemented to extract the maximum power from the PV array, which sets one of the phase shifts,  $\phi_{13}$ , between the reference port and port 3 (high-voltage side port). The phase shift between the BESS port and the reference port is assumed  $\phi_{12}$ , and the phase shift between the BESS port and the high-voltage

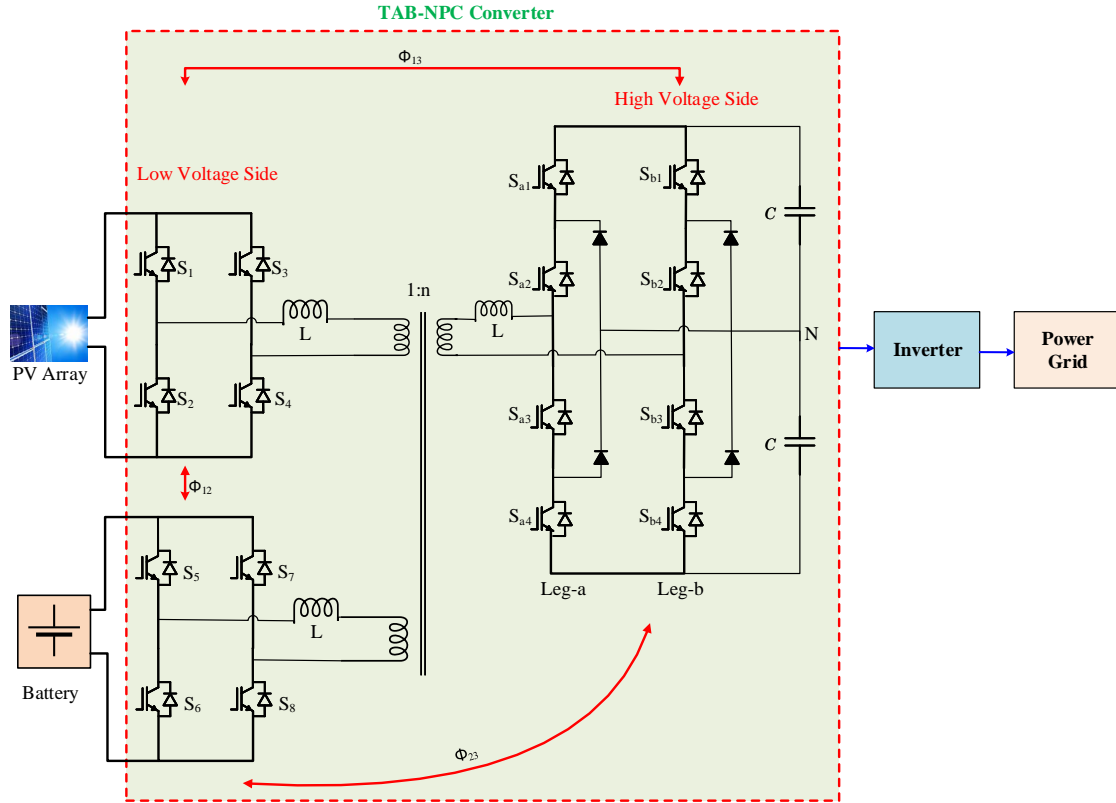


Figure 4.9: Hourly dispatching PV system with the TAB-NPC converter.

side port is assumed  $\phi_{23}$ . The power always flows from the voltage-leading bridge to the voltage-lagging bridge with respect to the reference bridge in the TAB-NPC converter architecture. In this research, a multilevel inverter is utilized to control the voltage level at the DC-bus due to its high efficiency, low THD, and reduced common-mode voltage.

#### 4.2.2 TAB-NPC Converter Power Flow Control

The power flow from the low voltage side to the high voltage side is conventionally controlled using the phase shift between the active bridges. In the developed converter configuration, the low voltage bridges are switched so as to produce a two-level square waveform across the transformer, and a three-level NPC diode clamped bridge

operates in the high voltage side. The modulation technique introduced in [181] for 2L-to-5L bridge voltages with an NPC-based secondary bridge is incorporated in this study, which has the advantage of having a simple mathematical representation and a minimum number of parameters to define the voltage waveforms and to control the power flow through the multiport converter. The voltage waveform of the low side and high side bridges across the multi-winding transformer is shown in Fig. 4.10. These angles  $\alpha$ ,  $\beta$  are measured symmetrically at zero,  $\pi$ , and  $2\pi$  within a switching period. The phase-shift angle  $\phi$  is independent of  $\alpha$ ,  $\beta$  and acts as the control parameter to control the power flow in the multilevel TAB-NPC converter. The average power flow between low and high voltage bridges can be expressed as:

$$P = \left( \frac{V_L V_H}{2\pi f_s n L_{eq}} \right) \gamma \quad (4.10)$$

where  $V_L$  is the low side bridge voltage,  $V_H$  is the high side bridge voltage,  $f_s$  is the switching frequency,  $n$  is the transformer turns ratio, and  $L_{eq}$  is the equivalent leakage inductance between two bridges at the high frequency link.

$$\gamma = \begin{cases} \left( \phi - \frac{\alpha\phi}{\pi} - \frac{\beta\phi}{\pi} \right); & 0 < \phi \leq \alpha \\ \left( \phi - \frac{\phi^2}{\pi} - \frac{\alpha^2}{2\pi} - \frac{\alpha\beta}{\pi} \right); & \alpha < \phi \leq \beta \\ \left( \phi - \frac{\phi^2}{\pi} - \frac{\alpha^2}{2\pi} - \frac{\beta^2}{2\pi} \right); & \beta < \phi \leq \frac{\pi}{2} \end{cases} \quad (4.11)$$

Here,  $\gamma = \gamma_{13}$  and  $\phi = \phi_{13}$  when the power is transferred from the PV connected port (i.e., port 1) to the DC bus connected port (i.e., port 3). On the other hand,  $\gamma = \gamma_{23}$  and  $\phi = \phi_{23}$  when the power is transferred from the BESS connected port (i.e., port 2) to the DC bus connected port (i.e., port 3).

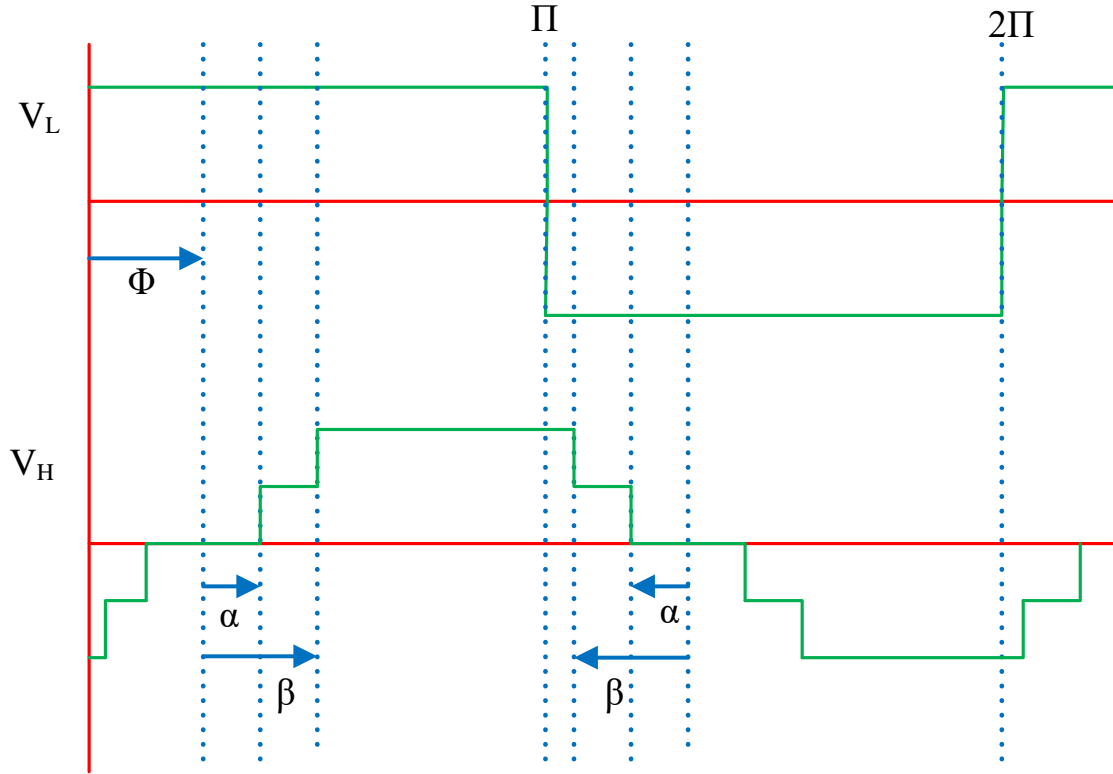


Figure 4.10: Voltage waveforms of the low voltage and high voltage side bridges.

### 4.2.3 Decoupled TAB-NPC Topology Analysis

In the TAB-NPC converter framework, it is evident that the inductor plays the role of power transfer between two ports. The relationship between the transmission power of the TAB-NPC converter port and phase angles is not very straightforward because of strong coupling and non-linearity. The transmission path between every two ports is the direct cause of the strong coupling of the TAB-NPC converter; therefore, this coupling can be mitigated by cutting off one of the power transmission paths. The power decoupling approach for the multiport converter proposed in [182] is incorporated in this research. Here, when the leakage inductance connected to port 3 (i.e., DC bus port) is set to the minimal compared with the leakage inductance connected to the other ports across the multi winding transformer, the coupling

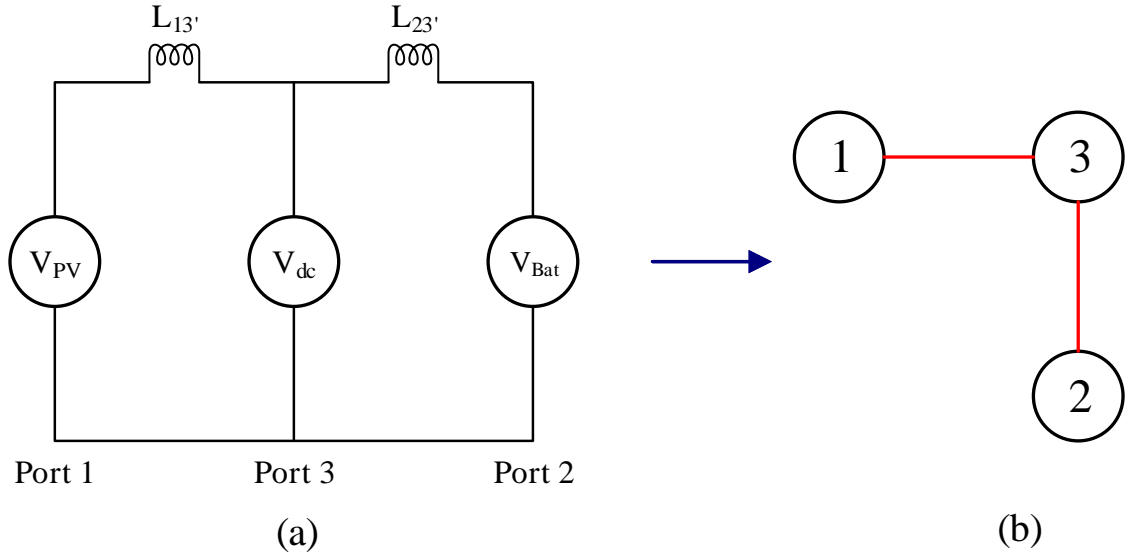


Figure 4.11: (a) Equivalent circuit of decoupled TAB-NPC converter (b) Equivalent topology diagram of TAB-NPC converter with three vertexes and two edges.

relationship between the port power and phase shift angle is significantly weakened, which can be expressed using (4.12). The circuit diagram of the decoupling TAB-NPC converter is shown in Fig. 4.11, where  $L_{13'}$  is the equivalent inductance between the PV connected port and DC bus connected port, and  $L_{23'}$  is the equivalent inductance between the BESS connected port and DC bus connected port.

$$\begin{aligned}
 P_1 = P_{13} &= \left( \frac{V_1 V_3}{2\pi f_s n L_{eq}} \right) \gamma_{13} \\
 P_2 = P_{23} &= \left( \frac{V_2 V_3}{2\pi f_s n L_{eq}} \right) \gamma_{23} \\
 P_3 &= -P_{13} - P_{23} = -P_1 - P_2
 \end{aligned} \tag{4.12}$$

#### 4.2.4 BESS Power Controller

As mentioned earlier, the MPPT controller is implemented to extract the maximum power from the PV array, which sets one of the phase shifts,  $\phi_{13}$ , between the reference

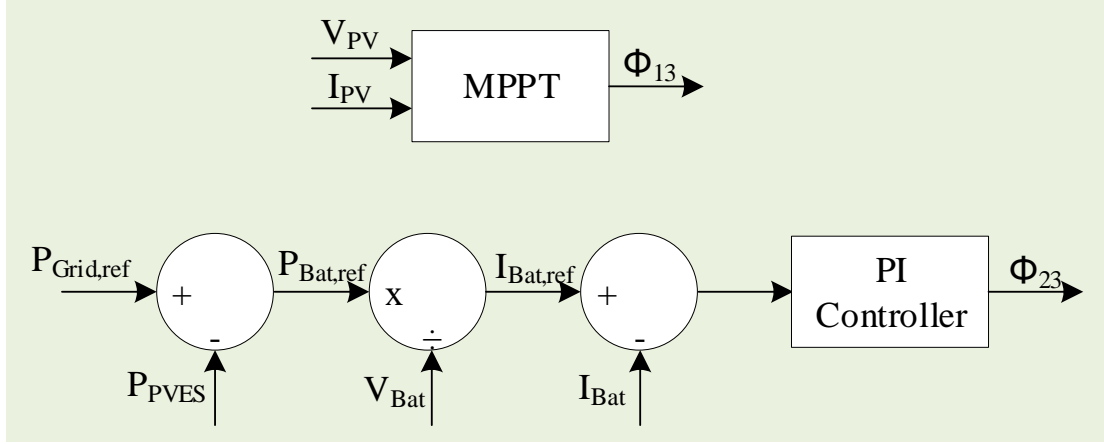


Figure 4.12: BESS power flow controller in TAB framework.

port and port 3. The phase shift between the BESS port and the reference port is assumed  $\phi_{12}$ , and the phase shift between the BESS port and the high voltage side port is assumed  $\phi_{23}$ . The BESS power control framework is shown in Fig. 4.12. The reference power for the BESS ( $P_{\text{Bat,ref}}$ ) is the difference between the  $P_{\text{Grid,ref}}$  and  $P_{\text{PVES}}$ . In this scheme, power always flows from the voltage-leading bridge to the voltage-lagging bridge. Therefore, when the power generated by the PV is lower than the grid reference power, the BESS acts in discharging mode, and  $\phi_{12}$  leads the  $\phi_{13}$ . On the other hand, when the power generated by the PV is higher than the grid reference power, the BESS acts in charging mode, and  $\phi_{12}$  lags the  $\phi_{13}$ . In this study, PI controller is employed to determine the desired phase shift between the BESS port and the reference port to regulate the system's power injected into the utility grid.

$$\text{BESS charging constraint, } \phi_{12} = \phi_{13} + \phi_{23} \quad (4.13)$$

$$\text{BESS discharging constraint, } \phi_{12} = \phi_{13} - \phi_{23} \quad (4.14)$$

#### 4.2.5 TAB-NPC Converter Performance Analysis

The multiport converter is the most promising topology for grid-tied renewable energy applications due to its several advantages. The conduction and switching losses of the semiconductor devices are the dominant power losses in the power converter operation. In this research, the power losses between the traditional TAB converter and the developed TAB-NPC converter are investigated for the hourly dispatching PV power architecture. Please note that only semiconductor losses are considered for the efficiency analysis, and the transformer losses are ignored, assuming that ultra-efficient Litz wires and nanocrystalline cores will be used for the transformer windings and cores, respectively. Here, the MATLAB/SIMULINK thermal module is utilized to explore the converter power losses. The power losses are computed based on the thermal attributes of the semiconductor modules chosen for the simulation and then imported into a thermal RC network of the power converter. Finally, thermal blocks of the Simscape foundation library are employed to create an external thermal network simulating the heat dissipated by the heat sink.

Currently, SiC devices are attracting wide attention for power electronic applications due to their extremely robust and stable behavior even at high frequency operations, high voltage ratings, and high operating temperatures. In particular, they appear very promising in those applications where traditional silicon semiconductors are affected by severe limitations such as energy storage devices, power converters for renewable energy, and all those high-power applications operating at high temperatures or requiring high switching operations [183]. This research also investigates the multiport converter power losses and resulting efficiencies with the IGBT and SiC MOSFET semiconductor devices so that an efficient converter topology could be obtained for hourly dispatching PV power scheme. Based on the voltage and current

Table 4.3: Semiconductor devices specifications

Devices	Manufacturer	Parts No.	Rating
IGBT	ABB	5SNE0800M170100	1700 V/ 800 A
IGBT	Infineon	FD400R33KF2C	3300 V/ 400 A
SiC	Hitachi	MSM900FS17ALT	1700 V/ 900 A
Diode	Infineon	DD800S17H4_B2	1700 V/ 800 A

ratings across the semiconductor switches, the performance data and characteristic curves in the datasheets of the semiconductor devices are utilized to extract the necessary output, and switching and output characteristic curves used to calculate the converter losses are summarized in Table 4.3 [184], [185], [186], [187].

#### 4.2.6 Multilevel Inverters

The circuit architecture of the 3L-INPCI is illustrated in Fig. 2.28. The clamping diodes linked to the neutral point enable producing a zero-voltage level, with which the three different output voltage levels are obtained. The 3L-TNPCI excludes the clamping diodes from the topology, as shown in Fig. 2.29. The inner switches ( $S_2$  and  $S_3$ ) are associated with the neutral point of the DC bus, blocking half of the DC-bus voltage. Therefore, the breakdown voltage of inner switches ( $S_2$  and  $S_3$ ) can be half of that with the outer switches ( $S_1$  and  $S_4$ ). In comparison with the 3L-INPCI, the 3L-TNPCI has the leverage of shorter commutation loops and reduced number of switches due to no clamping diodes.

The total power losses of semiconductor devices in the inverters mainly consist of two parts: conduction loss and switching loss. Here, the power losses of the 3L-INPCI and 3L-TNPCI are analyzed and compared for hourly dispatching PV power scheme. In this study, the power loss is analyzed by using the MATLAB/SIMULINK thermal module. Based on the thermal characteristics of the IGBT modules selected for the



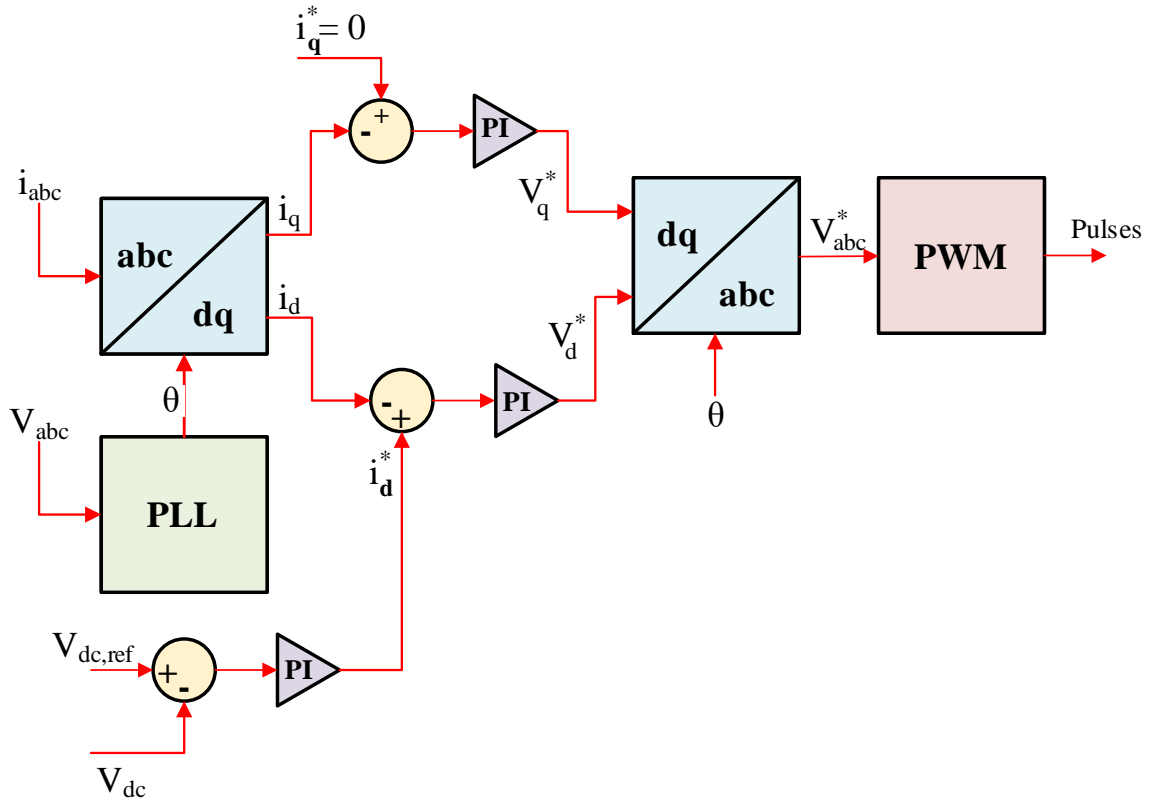


Figure 4.13: Inverter controller block diagram.

simulation, both switching and conduction losses are calculated and imported into a thermal RC network of the inverter. Thermal blocks of the Simscape foundation library are then used to build an external thermal network simulating the heat dissipated by the heat sink. The IGBT module (Infineon FD400R33KF2C) datasheet is utilized to extract the necessary output and switching characteristics curves to calculate the inverter power losses [185].

Fig. 4.13 shows the control structure of the grid-connected inverter where the grid synchronization to power flow management and PWM of the inverter is taken place. This control framework utilizes an outer DC-link voltage control loop and an inner current control loop to ensure decoupled regulation of active and reactive power components. The grid voltage-oriented reference frame employed for transformations

uses the phase angle provided by instantaneous voltage measurements. The voltage control loop is responsible for regulating the DC bus voltage and providing the active power current reference to the internal current loop. The current control loop, based on the active power current reference and reactive power current reference (taken as 0 in this model, as the system only supplies active power to the grid), provides the desired voltage reference signals. The desired voltage reference signals obtained from the current controller are then utilized to generate PWM pulses for the semiconductor switches in the inverter.

Furthermore, the design procedure of the LCL filter contemplated in Section 2.4.6 is adopted here, which is depicted in Fig. 4.14.

### 4.3 Simulation Results

#### 4.3.1 Optimal Dispatch Scheduling

The 1-MW grid-connected PV array is developed in the MATLAB/Simulink environment to validate the performance and economic assessment of the HESS framework. Fig. 4.15 and Fig. 4.16 illustrate the power profile of  $P_{\text{Grid,ref}}$ ,  $P_{\text{Grid}}$ ,  $P_{\text{PVES}}$ ,  $P_{\text{BESS}}$ , and  $P_{\text{SESS}}$  on June 10, 2019 for the entire day (15-hours) dispatching horizon and semi-hourly (30-minutes) dispatching horizon, respectively. The combination of the power of PV and HESS reflects the actual dispatched grid power ( $P_{\text{Grid}}$ ), which is supplied into the utility by the inverter. Here, the  $P_{\text{Grid}}$  remains constant during each specified dispatching horizon and successfully follows the desired  $P_{\text{Grid,ref}}$ . This attribute validates the fact that the HESS successfully absorbs or supplies the required power to supply the intended power to the utility from the intermittent PV framework. Furthermore, a similar phenomenon is observed when the  $P_{\text{Grid}}$  follows

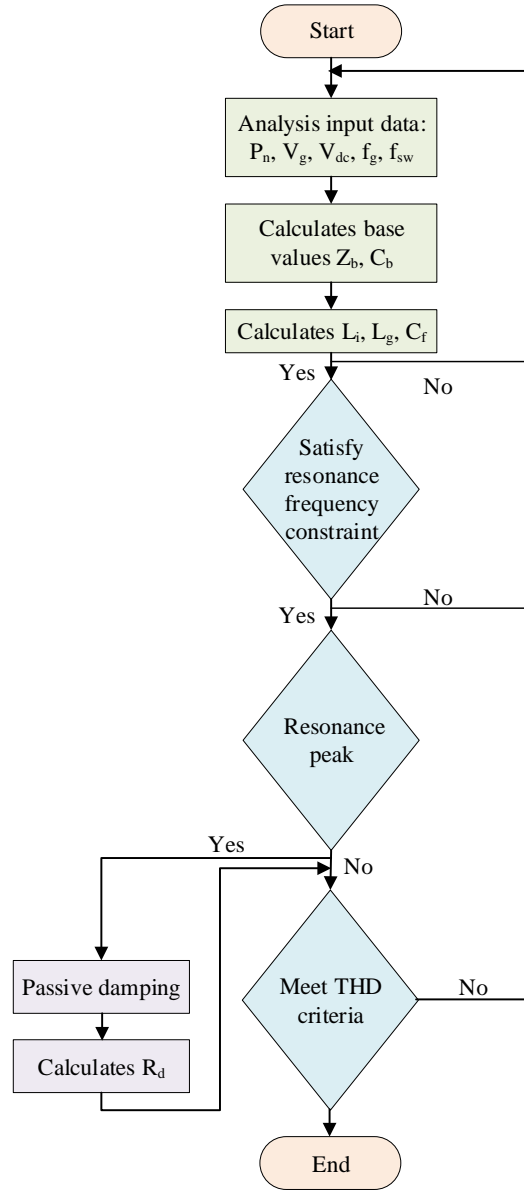


Figure 4.14: Design flowchart of the LCL filter.

the  $P_{\text{Grid,ref}}$  at a one-hour dispatching period for the entire duration, which is defined as an hourly dispatching scenario in this study. It is important to mention that the solar farm framework demands a significant contribution from the HESS to successfully meet the desired  $P_{\text{Grid,ref}}$  in the entire day dispatching horizon instance due to the higher discrepancy between the  $P_{\text{Grid,ref}}$  and  $P_{\text{PVES}}$ . As a result, the required HESS capacity increases substantially for the entire day dispatching horizon scenario

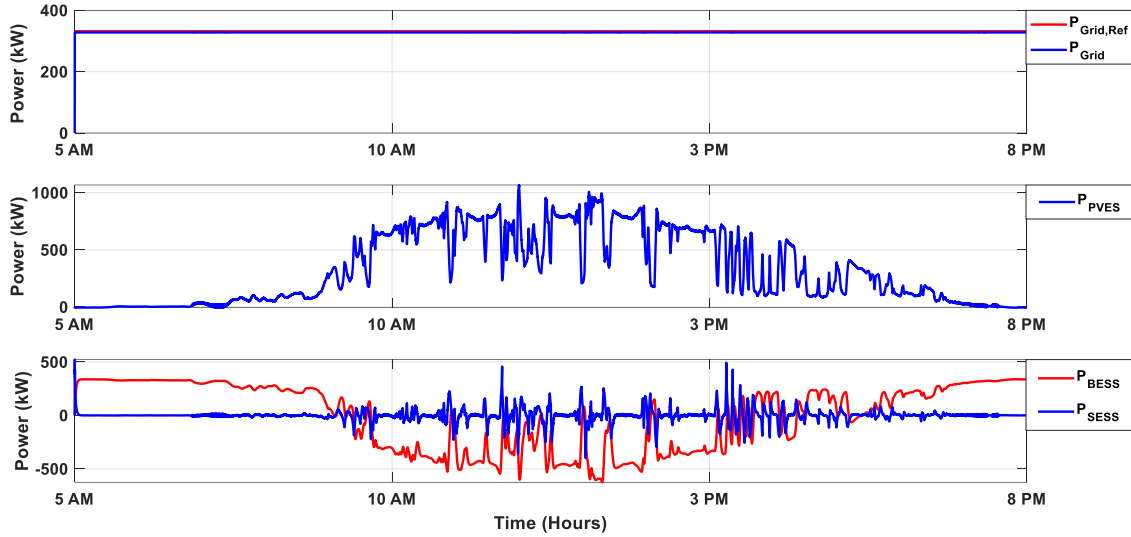


Figure 4.15: Simulation results with entire day dispatching horizon considered.

as compared to the semi-hourly or hourly dispatching case.

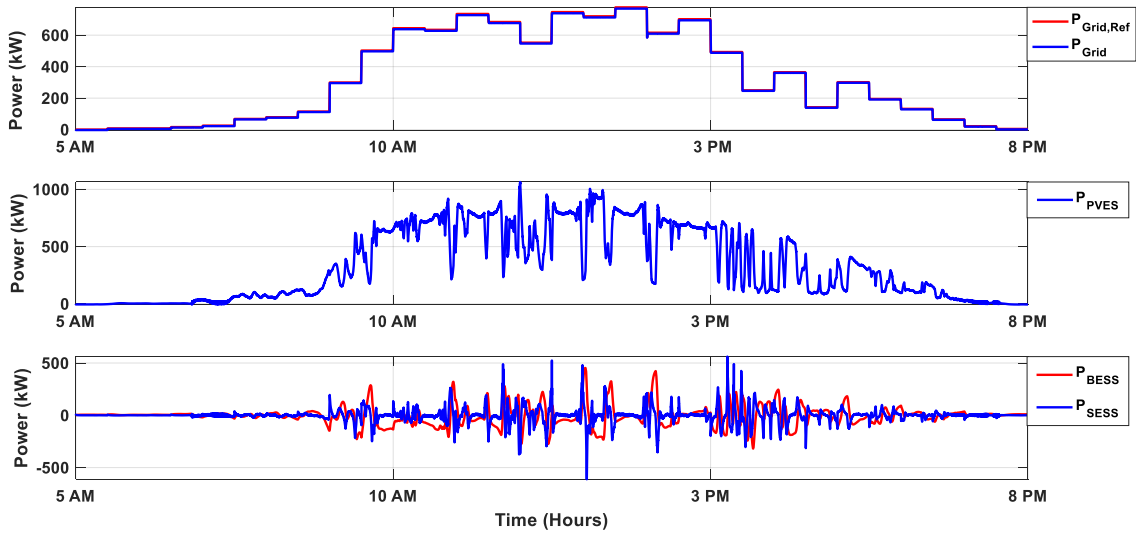


Figure 4.16: Simulation results with semi-hourly dispatching horizon considered.

Here, the following steps are taken into account to seek the optimal value of DOD that exhibits the least cost of ESS for dispatching PV power. (1) The simulations are carried out with actual meteorological PV dataset (June 10, 2019) at different levels of DOD utilization by the ESS, as documented in Table 4.4 for the hourly dispatching case. (2) Then, the curve fitting strategy is utilized to develop the ESS mathematical

Table 4.4: ESS cost comparison at different DOD levels.

DOD (%)	20	40	60	80	100
BESS cost (¢/kWh)	2.34	2.04	2.12	2.33	2.40
SC cost (¢/kWh)	15.52	7.76	5.17	3.88	3.10

expenditure equation as a function of its DOD usage, which best fits in a least-square sense. The BESS and SC cost per kWh as a function of their DOD utilization after employing the 3<sup>rd</sup> order polynomial curve fitting approach is shown in Fig. 4.17 for the battery-only and SC-only operations in the hourly dispatching scenario. The optimal value of DOD usage for the BESS is found to be around 44 %, whereas full utilization (100 % DOD) of SC provides the optimal value of DOD usage for the SESS in terms of the cost assessment. Since the SC can be charged-discharged virtually an unlimited number of times, the capacity required for the SC becomes minimum when it is fully exploited. It is noted that when the SC is fully utilized, the resulting minimum capacity required may be insufficient to ensure enough charge or discharge to successfully finish the entire dispatching period. Here, it was found that approximately 50 % DOD usage for the SC can make sure that it has enough capacitance to meet all of the charging-discharging requirements. Hence, SC DOD usage is limited to 50 % here during the HESS cost investigation.

As previously stated, the battery and SC are utilized in the HESS architecture, and the LPF is employed to allocate the power between them so that fast-changing components of power are charged-discharged through the SC, and slow-changing components of power are charged-discharged through the battery. This technique helps to significantly extend the BESS service life and substantially reduce ESS expenditure. At the optimal DOD utilization, the estimated service life (in years) of the battery is found to be around 4.4 in the battery-only scheme and approximately 7.1 in the

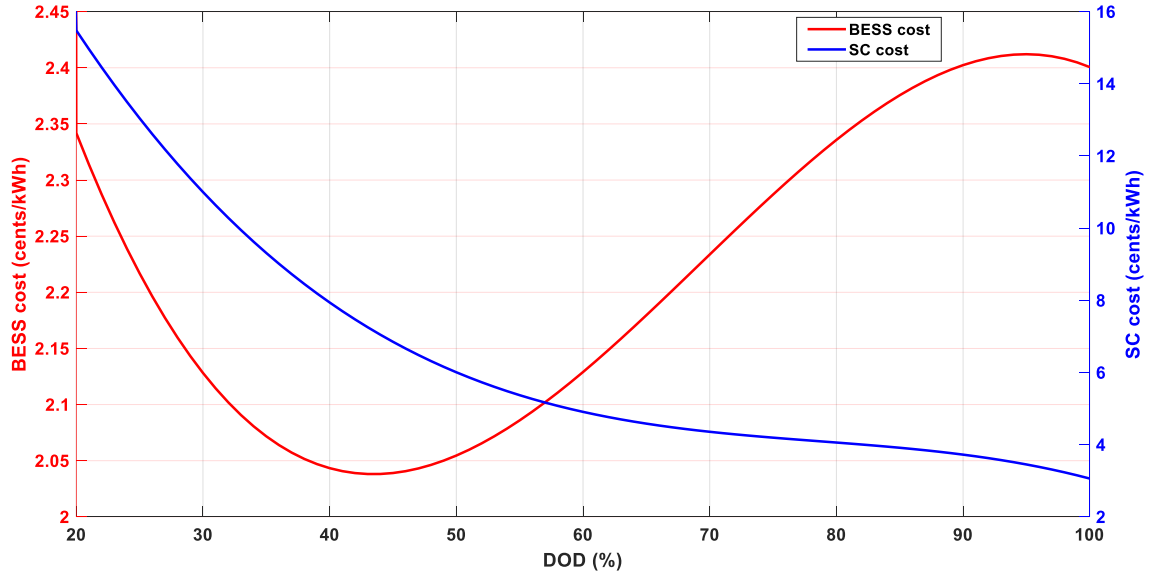


Figure 4.17: ESS cost (¢/kWh) at different DOD levels with a curve fitting approach.

HESS (Battery + SC) framework in the case of an hourly dispatching scenario. As a result, the HESS is more economical in comparison to using a battery-only for dispatching the PV power to the utility grid. According to the simulation results, the HESS cost per kWh at the optimal DOD usage is found to be around 1.5 cents/kWh in the hourly dispatching case, which is more cost-effective than the battery-only or SC-only framework, as illustrated in Fig. 4.17. Even though the battery-only or SC-only architecture can successfully follow the desired  $P_{\text{Grid,ref}}$  in each dispatching period, the HESS architecture seems to be cheaper for this application.

The cost optimization of the HESS is made as a function of DOD utilization levels of the battery and SC in the HESS scheme. Fig. 4.18 and Fig. 4.19 illustrate the HESS cost at various DOD levels of the battery and SC for the entire day dispatching and semi-hourly dispatching horizon scenarios, respectively. The most cost-effective HESS is found to be 1.3 cents/kWh when employing the semi-hourly dispatching case, which is approximately 200 % and 16 % lower than the entire day dispatching and hourly dispatching instances, respectively. The most optimal scaling of the battery and SC

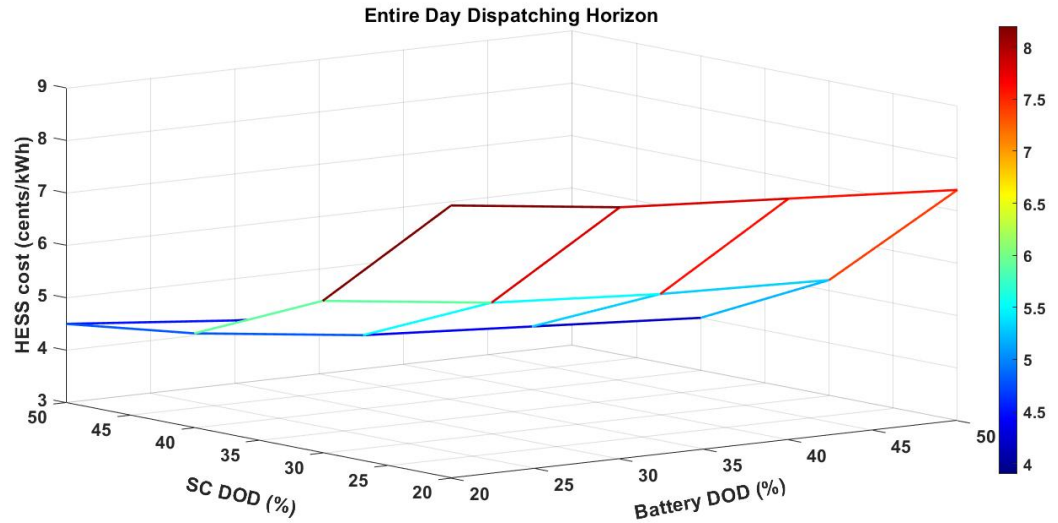


Figure 4.18: Entire day dispatching case: HESS cost as a function of DOD.

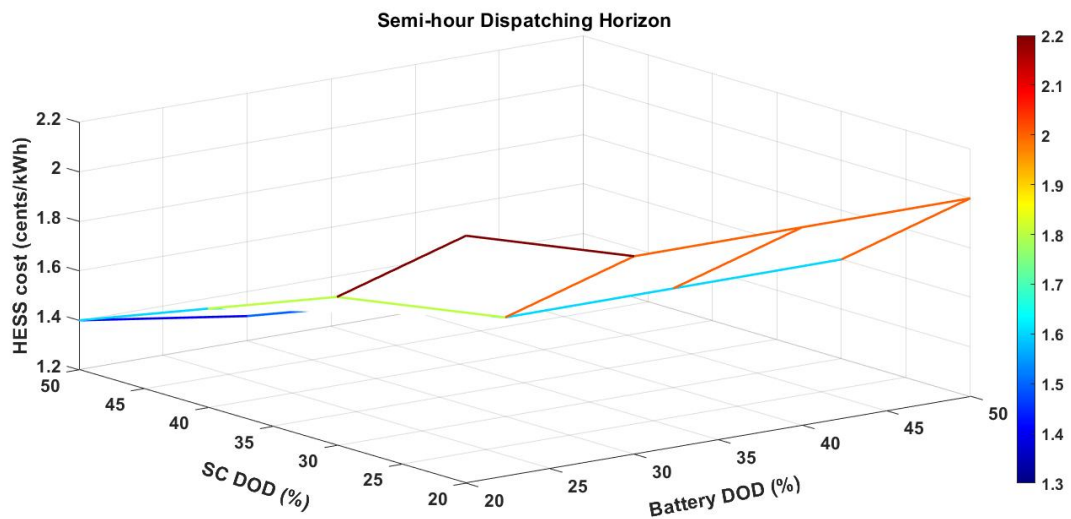


Figure 4.19: Semi-hourly dispatching case: HESS cost as a function of DOD.

in the HESS architecture is found to be 225 kWh and 20 kWh, respectively, with a semi-hourly dispatching horizon approach for a 1 MW grid-connected PV array.

The authors in [163] studied one HESS for dispatching PV power to the utility, and the HESS's optimal cost was found to be around 1.9 cents/kWh for hourly dispatching of PV power. However, optimal DOD usage for the ESS was not explored, which is investigated in this research to evaluate the impact of the ESS DOD utilization in

developing the cost-effective ESS for dispatching solar PV power scenario.

### 4.3.2 ESS Cost Investigation using HOMER Pro

Fig. 4.20 illustrates the power profile of  $P_{\text{Grid,ref}}$ ,  $P_{\text{Grid}}$ ,  $P_{\text{PVES}}$ ,  $P_{\text{BESS}}$ , and  $P_{\text{SESS}}$  for hourly dispatching PV power scheme on July 16, 2019. The  $P_{\text{Grid}}$  is the combination of the power of PV and HESS, and the inverter supplies this power to the utility. In each dispatching horizon, the  $P_{\text{Grid}}$  remains nearly constant and closely follows the intended  $P_{\text{Grid,ref}}$ , which also verifies the proposed framework’s dispatch capability. A similar phenomenon is realized when the BESS or SESS is employed as an energy storage system, which is specified as a battery-only or SC-only scheme in this study.

In this study, the ANN has been simulated in the MATLAB environment. Fig. 4.21 shows the 1-hour ahead solar irradiance forecast on an hourly basis from 7 AM to 7 PM on July 16, 2019, using the ANN compared to the measured actual historical solar irradiance data. The simulation result illustrates that the forecast values of the ANN model reasonably match with the measured values, and the RMSE is found to be around 6.3%. Moreover, the regression value is found to be close to 1, which indicates

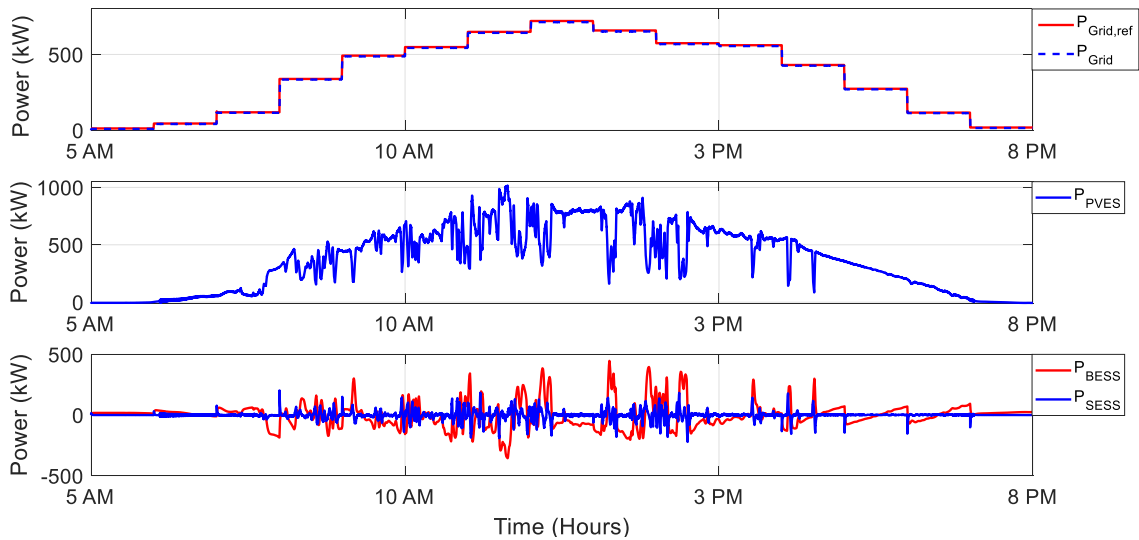


Figure 4.20: Simulation results for 1-hour dispatching on July 16, 2019.



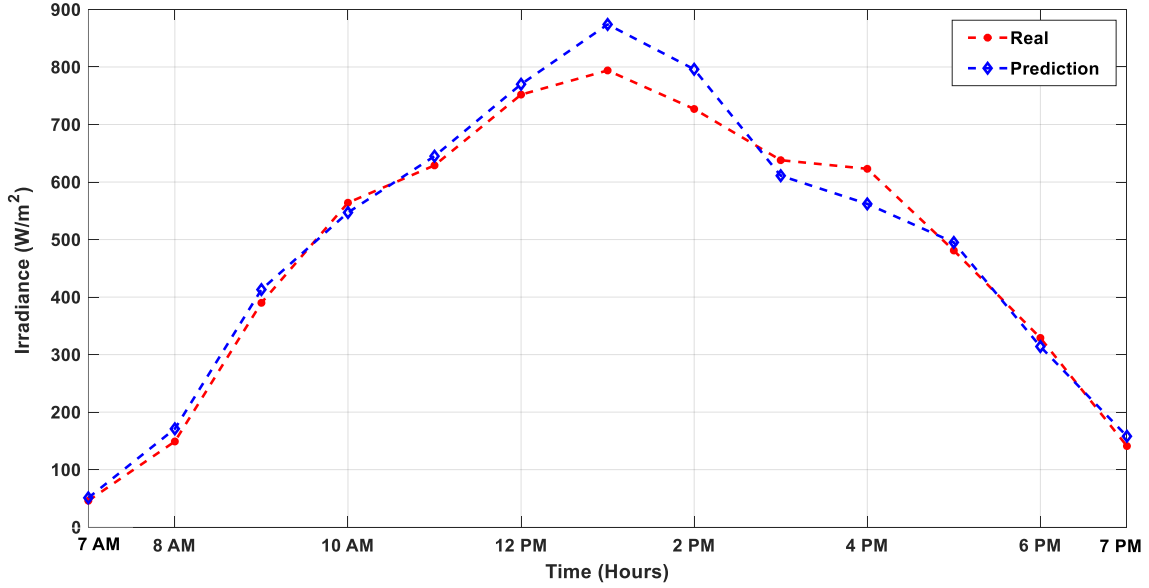


Figure 4.21: Solar irradiance forecasting result using ANN.

good convergence between the forecasted and measured values of solar insolation.

Fig. 4.22 depicts the ESS SOC fluctuation on July 16, 2019, demonstrating the proposed SOC controller’s effectiveness in guaranteeing that the ESS finishes each dispatching horizon with its initial SOC. This type of SOC constraint is required to predict the desired  $P_{\text{Grid,ref}}$ , minimize ESS cost, and ensure the ESS has enough capacity to function the following day. Fig. 4.23 presents the BESS SOC fluctuation with and without the primary SOC controller. This verifies the SOC controller’s effectiveness in ensuring the BESS finishes with its starting SOC, which is highly desirable in developing the most cost-effective ESS for hourly dispatching PV power.

In the HOMER Pro platform, an economic comparison is carried out to select the most techno-economically hybrid system for hourly dispatching PV power. Fig. 4.24 and Fig. 4.25 show the NPC of various components utilized in the hybrid system for battery-only and SC-only scenarios, respectively. According to the HOMER Pro results, the total NPC and LCOE are found to be \$1,551,076 and 5.95 cents/kWh, respectively, for the battery-only scheme, and the total NPC and LCOE are found to

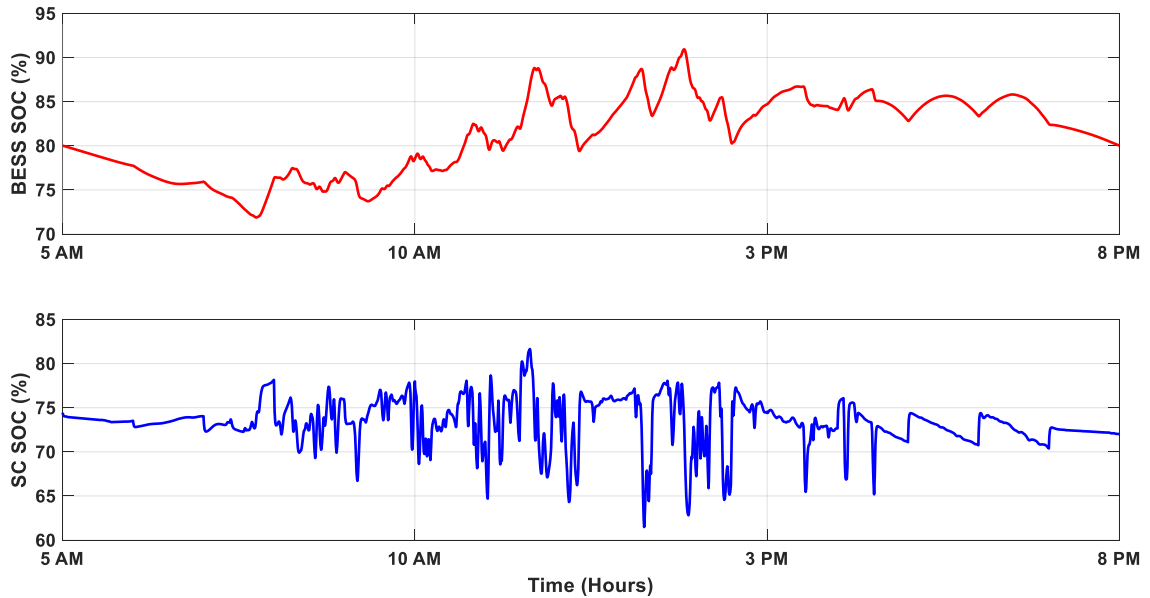


Figure 4.22: Simulation results of the ESS SOC on July 16, 2019.

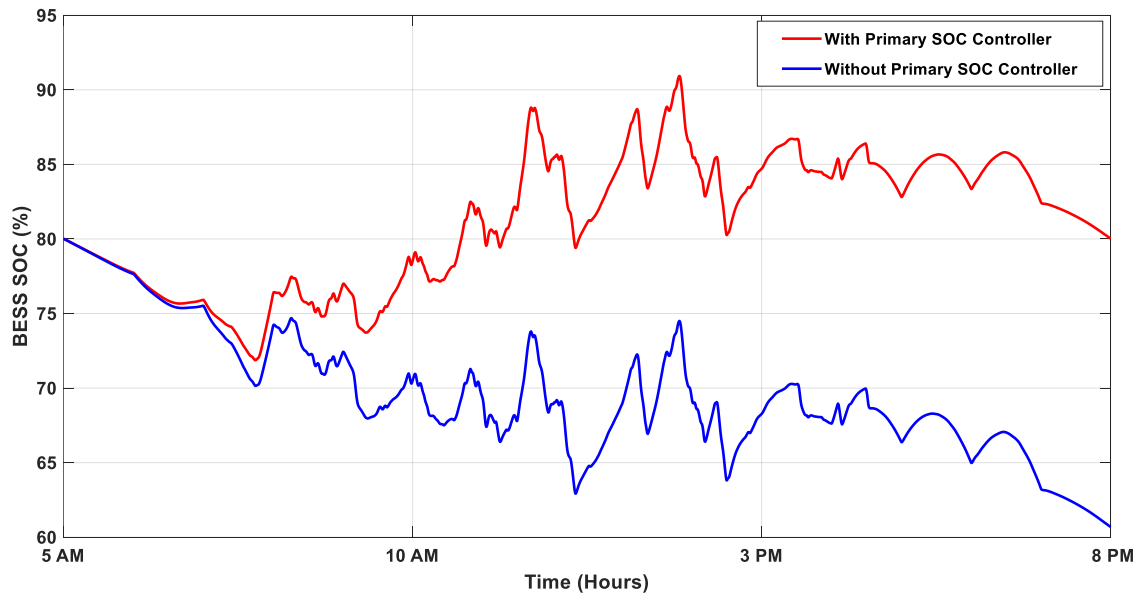


Figure 4.23: Proposed primary SOC controller effectiveness on July 16, 2019.

be \$2,654,416 and 10.19 cents/kWh, respectively, for the SC-only scheme. In both scenarios, the annual electrical energy production of the hybrid system is found to be around 2,335,492 kWh/yr with a 100 % RE fraction, and the unmet electrical load is found to be very minimal, which also reflects the higher reliability of the system. Here, the LPF is employed to decouple the power reference for the battery

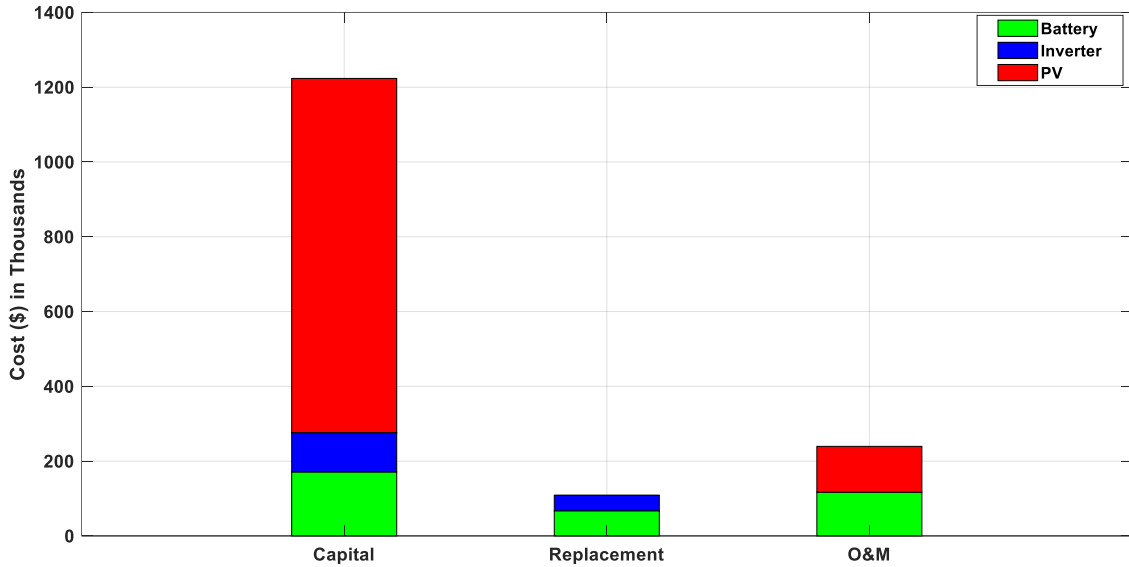


Figure 4.24: Cost summary for the battery-only scheme.

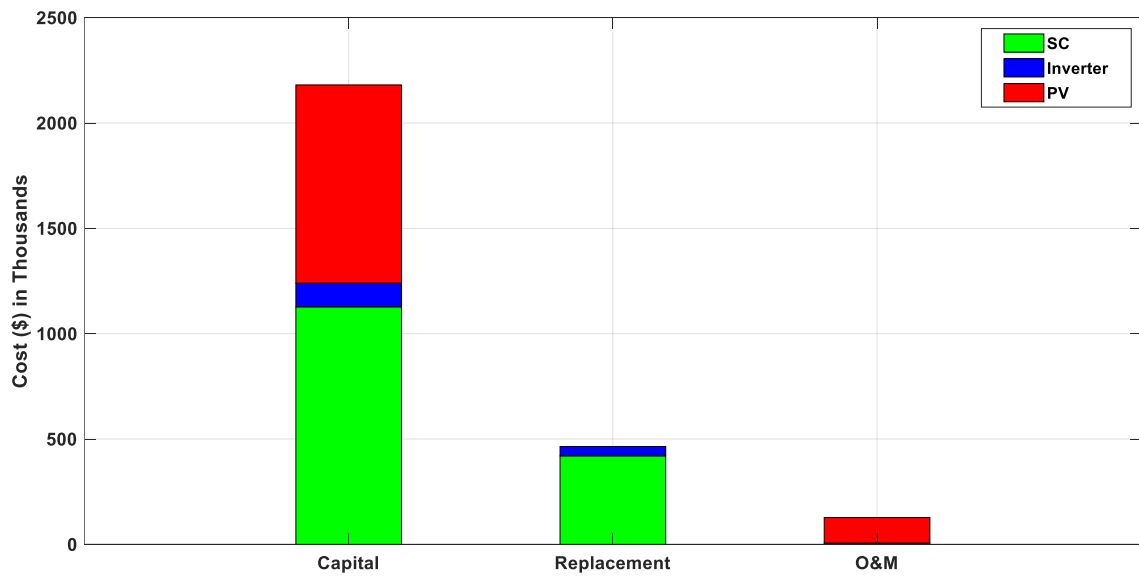


Figure 4.25: Cost summary for the SC-only scheme.

and SC in the HESS framework, as shown in Fig. 4.7. However, the HOMER Pro simulation does not support this type of frequency management approach between two ESS during the techno-economic optimization. Hence, the economic evaluation of the HESS is not possible in the HOMER Pro platform.

The authors in [188] investigated a techno-economic evaluation of a hybrid system

using HOMER Pro, and it was found that the most economical configuration has an LCOE of approximately 14 cents/kWh. Here, the optimal LCOE (5.95 cents/kWh) is found to be significantly lower when the electrical load/grid demand is modeled utilizing the proposed dispatching strategy. This attribute demonstrates the superior performance of the proposed dispatching technique over conventional strategies for meeting the load demand from the intermittent PV framework.

### 4.3.3 TAB Power Converter Interface for the PV-BESS System

Simulations have been carried out in MATLAB/Simulink environment to justify the performance of the developed TAB-NPC converter for the PV-BESS system structure. The power profile data of 1 MW PV, BESS,  $P_{\text{Grid}}$ , and  $P_{\text{Grid,ref}}$  collected on June 30, 2019, is shown in Fig. 4.26. Here, the combination of the power of PV and BESS reflects the  $P_{\text{Grid}}$ , which is injected into the utility grid by the inverter. As shown in Fig. 4.26, it is noticeable that the  $P_{\text{Grid}}$  remains constant and successfully tracks the  $P_{\text{Grid,ref}}$  in each dispatching period. To sum, the BESS successfully absorbs or supplies the required power for providing the desired power to the grid at a one-hour dispatching period for an entire duration from the intermittent PV architecture.

For a better illustration of the BESS charging-discharging mechanism, the zoomed version of the simulation results is shown in Fig. 4.27. Here,  $V_{11}$  is the reference bridge voltage profile (PV connected port),  $V_{22}$  is the BESS connected bridge voltage profile, and  $V_{13}$  is the high side bridge voltage profile referred to as the reference bridge side. The power always flows from the voltage-leading bridge to the voltage-lagging bridge with respect to the reference bridge in the TAB-NPC architecture. Fig. 4.27 is presented here to justify this fact.

Fig. 4.28 shows the simulation results of power losses for the traditional TAB

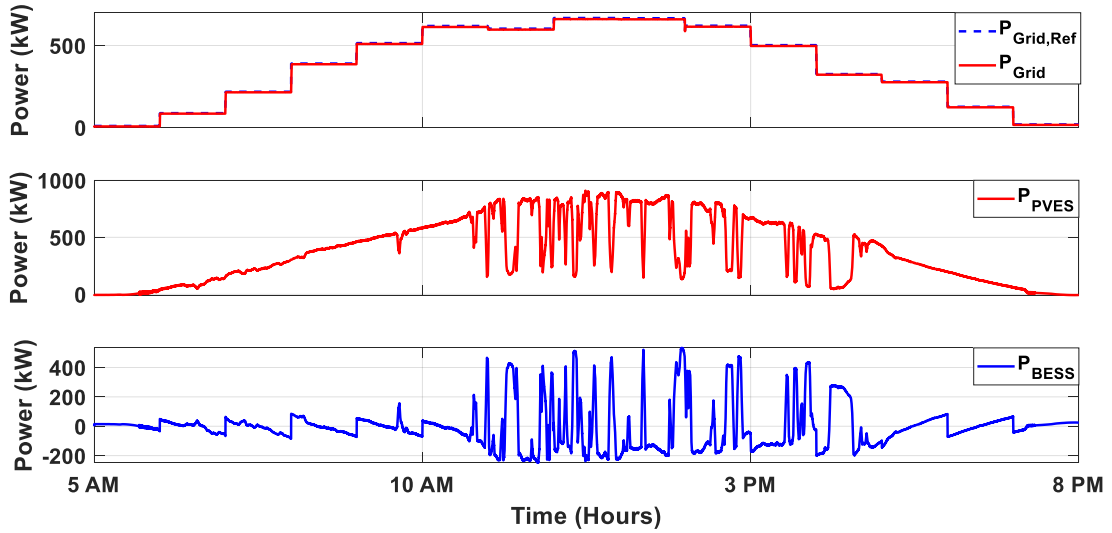


Figure 4.26: Simulation results for 1-hour dispatching on June 30, 2019.

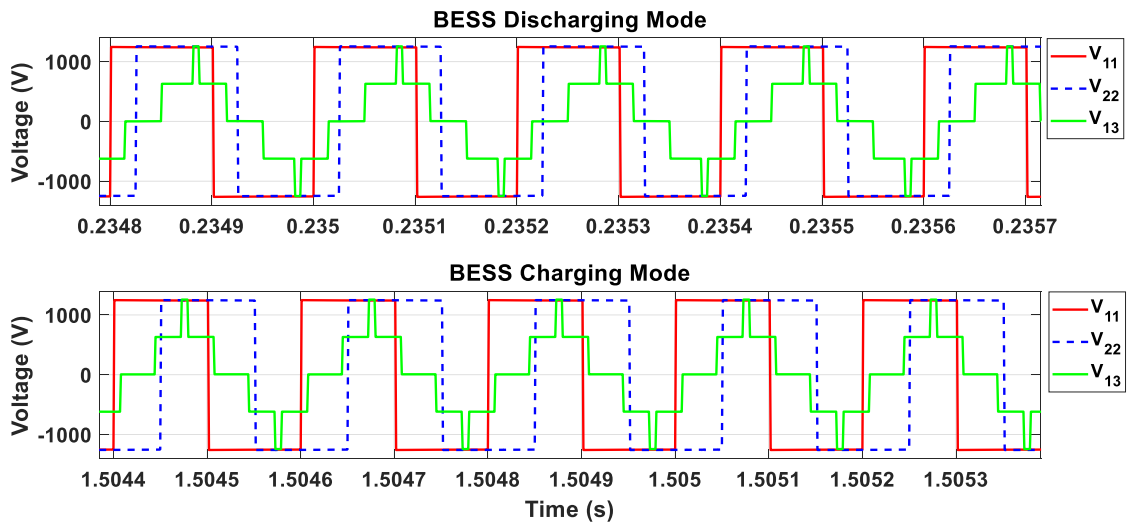


Figure 4.27: BESS charging-discharging zoomed view.

converter and developed converter at different PV irradiance levels. It is observed that the power losses of the developed TAB-NPC converter are lower at different solar insolation than that of the traditional TAB one. Also, the developed TAB-NPC converter with SiC MOSFET devices performs slightly better in the power loss reduction than the developed converter with IGBT devices. Furthermore, the power losses of the switching devices are proportional to the magnitude of the converter

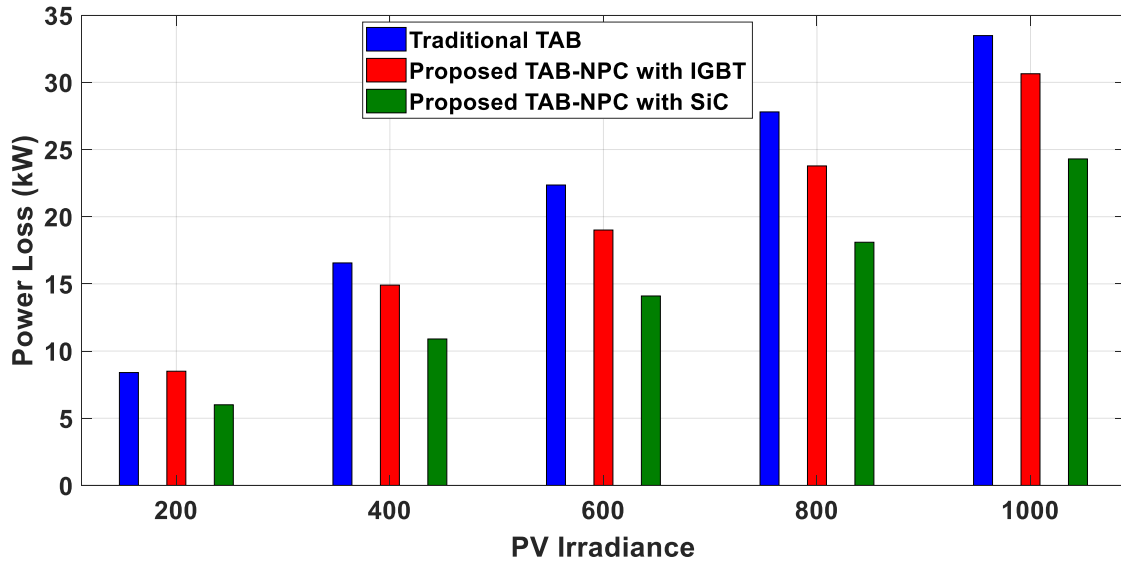


Figure 4.28: Power losses comparison at different PV irradiance levels.

current. Therefore, it is expected that the maximum power losses incur at the highest PV irradiance level, which is the 1000 W/m<sup>2</sup> in this investigation. The presented simulation result also validates this fact.

To further understand the converter performance, the efficiency of the traditional TAB and developed converter are also compared at different solar irradiance levels. The comparison of the efficiencies at different solar insolation for different topologies of the power converter investigated in this research is demonstrated in Fig. 4.29. From the simulation results, it can be verified that the developed converter is more efficient than the traditional TAB converter under different solar insolation considered in this study. It is also evident that the developed TAB-NPC converter with SiC MOSFET devices exhibits superior performance than using the IGBT devices for megawatt-scale grid-connected PV arrays.

Fig. 4.30 shows the simulation results of power losses for 3L-INPCI and 3L-TNPCI with SPWM at 2 kHz switching frequency for each dispatching period on July 20, 2019. It is observed that the power losses of the 3L-TNPCI are lower in each dis-

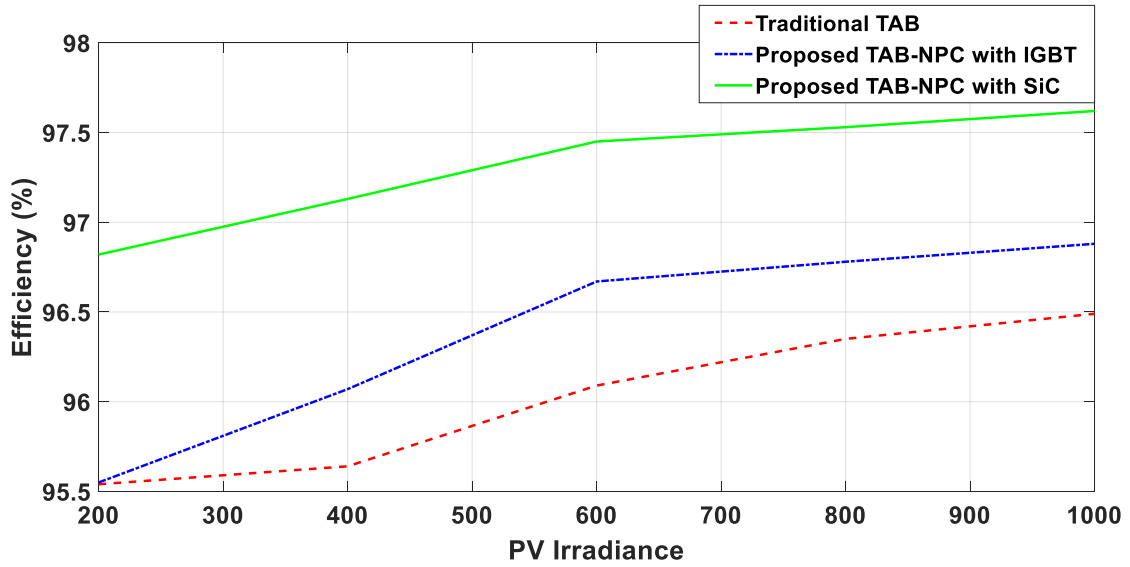


Figure 4.29: Efficiency comparison at different PV irradiance levels.

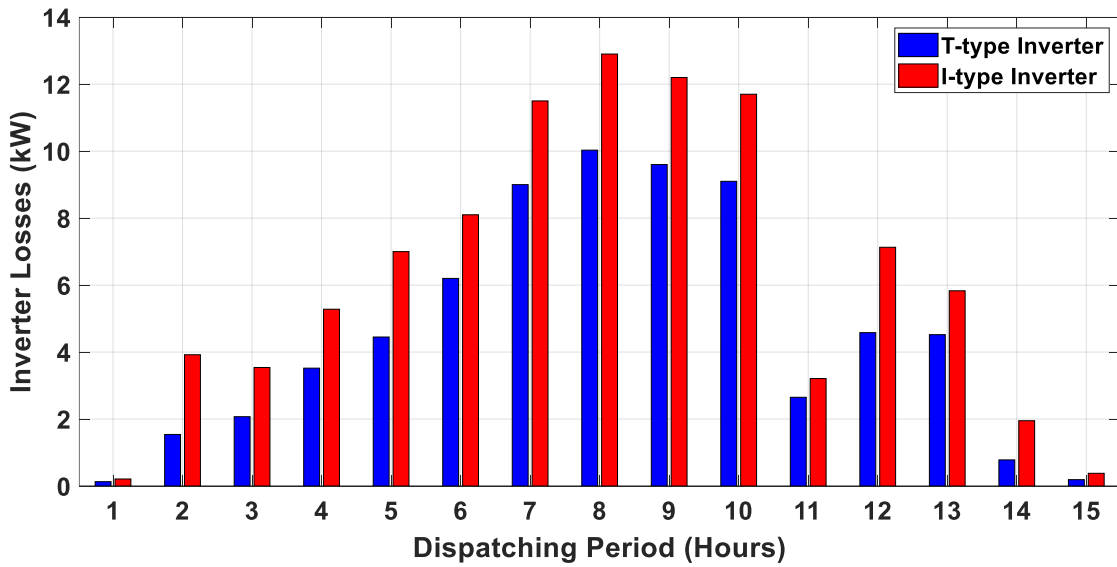


Figure 4.30: Comparison of power losses between 3L-TNPC and 3L-INPCI.

patching period than that of the 3L-INPCI one. Furthermore, the power losses of the switching devices are proportional to the magnitude of the inverter current. Therefore, it is expected that the maximum power losses incur at the highest grid demand power, which is the 8<sup>th</sup> dispatching period in this investigation. The presented simulation result also validates this fact.

To further understand the inverter performance in the hourly dispatching PV power scheme, the power losses of the 3L-TNPCI and 3L-INPCI are also compared at different switching frequencies. The comparison of the power losses at different switching frequencies for 3L-TNPCI and 3L-INPCI on July 20, 2019 is demonstrated in Fig. 4.31 and Fig. 4.32, respectively. From the simulation results, it can be verified that the 3L-TNPCI is more efficient than the 3L-INPCI under different switching frequencies considered in this study. In addition, the power losses that appeared in the different semiconductor switches of the 3L-TNPCI Phase-A leg at 10 kHz switching frequency for the 8<sup>th</sup> dispatching period are presented in Fig. 4.33

Fig. 4.34 compares the value of grid current THD between the two multilevel inverter topologies on July 20, 2019. It shows that increasing the switching frequency will significantly decrease the THD (in percentage), while the inverter switching losses will inevitably increase. It is also evident that the 3L-TNPCI performs slightly better in terms of grid current THD reduction than the 3L-INPCI. This THD comparison also justifies the effectiveness of the LCL filter compiles with the IEEE 1547 standard for the grid-connected PV system.

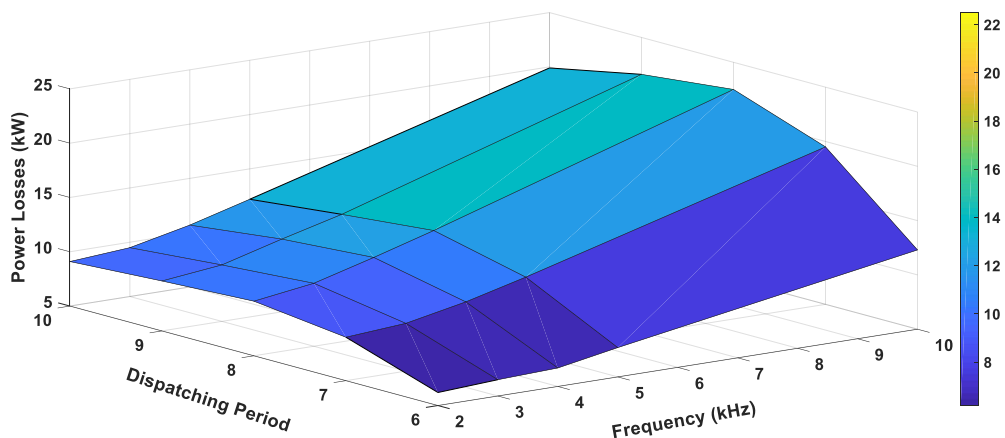


Figure 4.31: Power losses of 3L-TNPCI at different switching frequencies.



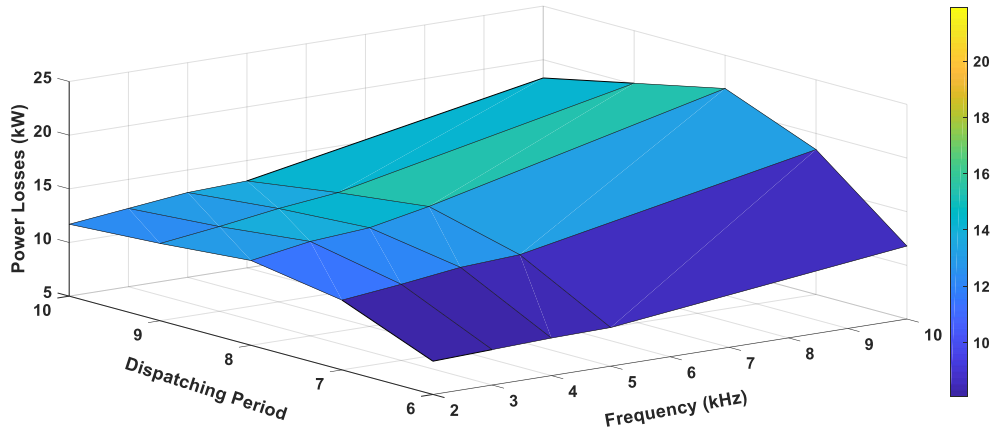


Figure 4.32: Power losses of 3L-INPCI at different switching frequencies.

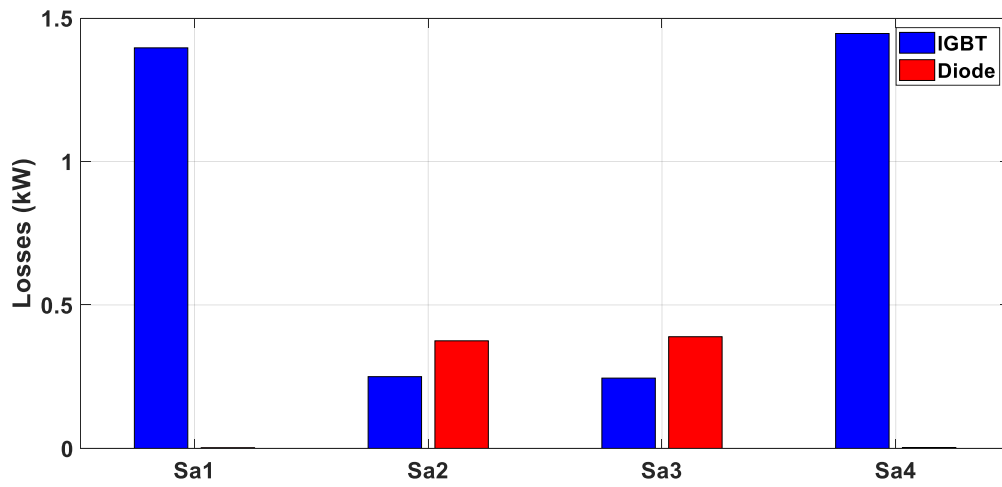


Figure 4.33: Power losses breakdown in Phase-A leg of the 3L-TNPCI.

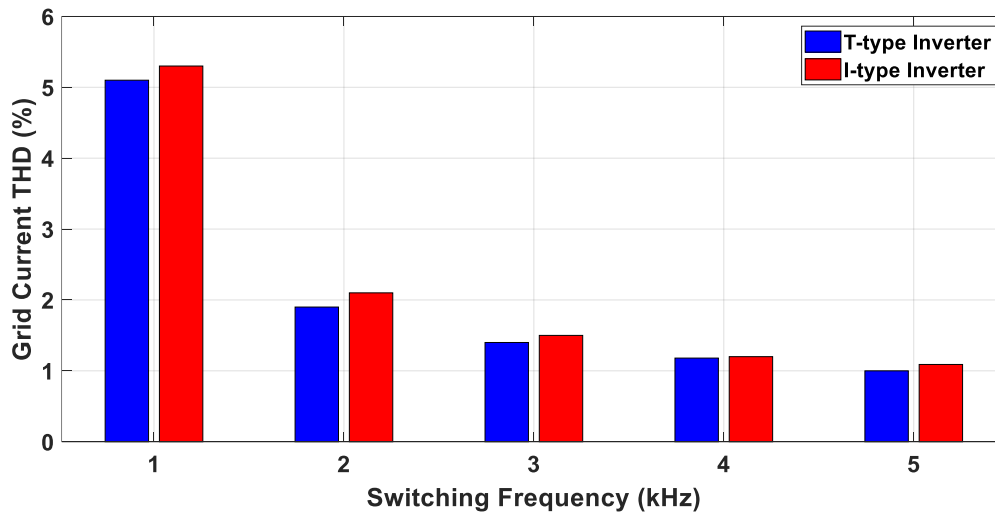


Figure 4.34: THD comparison of the inverters at different frequencies.

#### 4.4 Summary

In this chapter, the proposed PV-HESS framework can dispatch power at any intended dispatching horizon. Besides, the life cycle cost of the ESS is optimized as a function of its DOD utilization, and economic comparison is presented to evaluate the impact of dispatching horizon selection on ESS expenditure estimation. The machine learning strategy ANN is also implemented to predict the solar insolation 1-hour ahead of time to predict the PV output power. Moreover, the effectiveness of the proposed SOC controller in the grid reference power estimation is explored in this research to make the system more practical. Based on the NPC and LCOE, an economic comparison is investigated in the HOMER Pro environment, and it is found that the battery-only scenario is more economical than the SC-only scenario for hourly dispatching PV power scheme.

The developed TAB-NPC DC-DC converter is an attractive solution for integrating a large-scale PV-BESS into the grid, which has the advantages of high efficiency, flexible control for power flow, and high voltage operation with lower voltage rated devices. The power losses of the 3L-TNPCI and 3L-INPCI are also analyzed and compared, which shows that the losses of the 3L-TNPCI are lower for hourly dispatching PV power scheme. Besides, this chapter systematically studied the optimal design of an LCL filter for the grid-connected PV system.

## Chapter 5 Economic Dispatch Analysis of Wind Power Integration into Utility with Battery-Supercapacitor Hybrid Energy Storage System

This chapter demonstrates an effective dispatching scheme of utility-scale wind power at one-hour increments for an entire day with a hybrid energy storage system consisting of a battery and a supercapacitor. Accurate forecasting of wind power is crucial for generation scheduling and economic operation. Here, wind speed is predicted by one hour ahead of time using a multilayer perceptron Artificial Neural Network, which exhibits satisfactory performance with good convergence mapping between input and target output data. Furthermore, an adaptive neuro-fuzzy inference system is employed to devise a state of charge controller to accurately estimate the  $P_{\text{Grid,ref}}$  for each one-hour dispatching period. This type of desired  $P_{\text{Grid,ref}}$  estimation is critical to ensure the energy storage system completes each dispatching period with its starting SOC and has adequate capacity available for next-day operation. Also, the PSO technique is implemented to optimize the life cycle cost of the ESS based on its depth of discharge usage, which is vital for minimizing the cost of a dispatchable wind power scheme. The actual wind speed data of four different days as a representative of each season recorded at ORNL are utilized in the simulations to provide a realistic economic assessment for dispatching the wind power.

As a fast-growing RE source, wind energy has been playing an increasingly important role in power generation [189], [190]. With the output of the WT significantly dependent on natural and meteorological conditions, its output power exhibits highly intermittent characteristics. Therefore, the WT output can potentially vary between zero and the maximum available power. As a result of the fluctuating nature of the

resource, the WT is classified as a non-dispatchable energy source, which means there is no guarantee that the expected amount of power will be available on-demand for a specified period of time.

Every country has its own grid connection requirements specified by the transmission system operator. As a result, grid operators must comply with these grid regulations, particularly on voltage and frequency variations, and active and reactive power responses and control. Also, due to the considerable penetration of RE in the utility, grid operators are increasingly concerned about over-generation and curtailment. Hence, RE plant operators will be pressured to maintain a consistent power dispatch, similar to what conventional fossil fuel power plants have done.

In this chapter, wind power is dispatched on an hourly basis using the battery-supercapacitor HESS, which can exploit technical advantages of both the battery and the SC ESS medium. Furthermore, an economic evaluation associated with the HESS is presented. The contributions of this chapter can be summarized as below:

- Implementing the ANN to predict the wind speed one-hour ahead of time.
- Developing an ANFIS based primary SOC controller to compute the desired  $P_{\text{Grid,ref}}$  for each dispatching period.
- Optimize the ESS life-cycle cost by employing the PSO technique to determine the optimal DOD usage.
- Detailed investigations of the annual ESS life-cycle cost, including the actual WT speed data of four different days, representing each season.

The rest of this chapter is organized as follows: The methodology and control techniques utilized for hourly dispatching of the WT power are contemplated in Section

5.1. Section 5.2 verifies the effectiveness of the proposed methodology and control methods through simulations. A comparative study of the ESS for dispatching WT power is contemplated in Section 5.3. Finally, the summary of this chapter is summarized in Section 5.4.

## **5.1 Proposed Methodology for WT Farm**

### **5.1.1 System Architecture of WES**

The WES is comprised of a 1.5 MW direct-drive three-phase permanent magnet synchronous generator coupled to the WT, a pitch angle controller, and a rectifier, as shown in Fig. 5.1. The WES and HESS are connected in parallel, and each ESS is connected to a bi-directional power converter. The WES and HESS are parallelly associated with the capacitor bank that serves as the DC bus, which is then linked to a multilevel inverter with improved output voltages. In this framework, the inverter is responsible for maintaining the desired DC bus voltage, and the WES and HESS are connected to the DC bus as current sources, which allows achieving controllable power by regulating the current flow through power converters. An LCL filter is also used for superior harmonic attenuation and greater efficiency. The control methodology and associated power flow equations of the WT contemplated in [191] are incorporated in this study.

### **5.1.2 Wind Speed Forecasting**

This research predicts wind speed 1-hour in advance using the ANN, which is well suited to describe the intermittent nature of wind, considering its non-linear nature. Furthermore, the ANN exhibits superior performance in handling noisy data and non-iterative, speedy computation in the prediction task once the ANN is success-

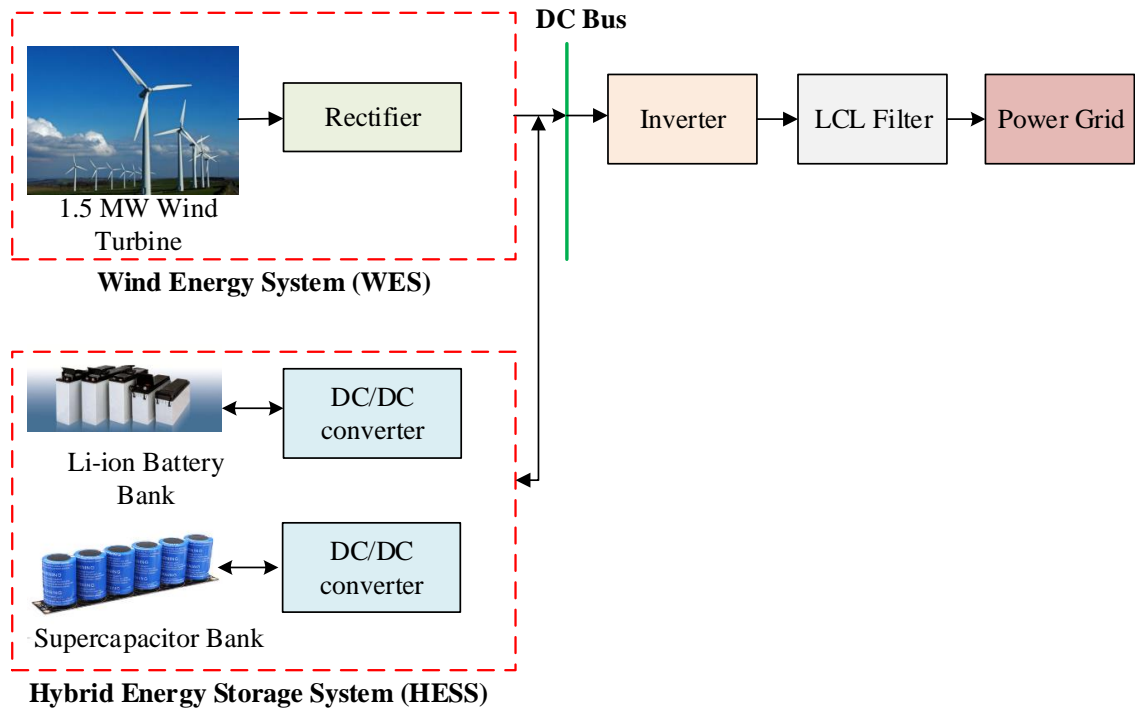


Figure 5.1: Hourly dispatching wind turbine framework.

fully trained [192]. A feed-forward seven-layer perceptron ANN is implemented in MATLAB environment to predict the hourly wind speed one-hour ahead of time. The Levenburg-Marquardt algorithm is used in training. The “tansig” and “logsig” transfer functions are used at the hidden layer and output layer, respectively. The detailed specifications of the ANN model utilized are presented in Table 4.1. There is no established guidance in the literature on how to select the optimal parameters of the ANN model, such as the number of hidden layers, the number of neurons in each layer, and epochs. However, it is a common practice to keep the numbers as low as possible to ensure simplicity and robustness of the model. Here, simulations were carried out with different combinations/configurations of the ANN model, and the best results were obtained with the ANN model specifications that are documented in Table 4.1. The real wind data speed recorded at ORNL is utilized in this study [178]. The wind speed varies from season to season, so the wind speed is forecasted by

selecting four days corresponding to each season, namely January 16, 2019, April 16, 2019, July 16, 2019, and October 16, 2018. The following steps are considered to predict the wind speed one-hour in advance using the ANN. (1) The hourly wind speed, the season of the year index, and the time of day index are used as inputs. (2) Hourly wind speed data recorded at ORNL from January 1, 2019, to January 15, 2019, is used for training the ANN model to predict hourly wind speed on January 16, 2019. (3) After completing the training, the ANN model is tested to predict the hourly wind speed on January 16, 2019. (4) Finally, the forecasted wind speed data is compared with historical wind speed data in terms of RMSE, as illustrated in (5.1), to measure the performance of the ANN model. Likewise, the hourly wind speed for other selected days is predicted 1-hour ahead of time.

$$RMSE = \sqrt{\frac{1}{N} \sum_{m=1}^N \left( y_{fw}^{i,L} - y_{rw}^{i,L} \right)^2} \quad (5.1)$$

where  $y_{fw}^{i,L}$  is the forecasted WT speed,  $y_{rw}^{i,L}$  is the actual WT speed, and  $N$  is the total number of forecasting cases.

In addition to wind speed data, when other atmospheric variables such as temperature, pressure, wind direction, moisture content, rainfall, and turbulence intensity of wind are incorporated as inputs to the training of an ANN model for forecasting the wind speed, the performance of the ANN model might be enhanced. However, adding more input parameters to the ANN would increase the complexity of the model and time required for processing and training. In this research, the reported ANN model provides a comparative result compared to [193] to predict the wind speed one-hour ahead of time by using a relatively small set of historical hourly wind speed data as well as a smaller number of input parameters for training the model, which also

significantly reduces the model complexity and computational burden.

### 5.1.3 Grid Reference Power Calculation

As indicated before, the ESS capacity and service life are strongly related to the amount of power transferred in and out of the ESS, which is largely determined by the characteristics of the WT output power. Since the output power of the WT substantially depends on the wind speed, this study selected the highest windy day to calculate the  $P_{\text{Grid,ref}}$  in order to get the worst-cost scenario about the ESS expenditure. The actual peak wind speed data recorded at ORNL at one sample/minute on January 20, 2019 (winter season), April 26, 2019 (spring season), July 21, 2019 (summer season), and October 31, 2019 (fall season) is collected to use in this research to compute the  $P_{\text{Grid,ref}}$  for each dispatching horizon for an entire day [178]. Four different days are chosen to reflect each season of the year. The following steps are considered for computing the desired  $P_{\text{Grid,ref}}$  for each dispatching period. First of all, the  $P_{\text{Grid,est}}$  for each 1-hour dispatching period is determined by averaging the WT power on an hourly basis. Then, the primary SOC controller is implemented to seek the appropriate multiplication factor in order to adjust the  $P_{\text{Grid,est}}$  at the beginning of each dispatching period to obtain the desired  $P_{\text{Grid,ref}}$ , which will guarantee the ESS bank's SOC remains within a desirable range.

The primary SOC controller is illustrated in Fig. 4.4. Here, ANFIS is utilized to determine the suitable multiplication factor to the  $P_{\text{Grid,est}}$ , where the multiplication factor is directly correlated to the ESS SOC at the end of each dispatching period. This multiplication factor plays an important part in ensuring that the ESS finishes with its starting SOC, so that the ESS expenditure can be reduced. The MATLAB “Neuro-Fuzzy Designer” tool is used to train the ANFIS, which generates a single



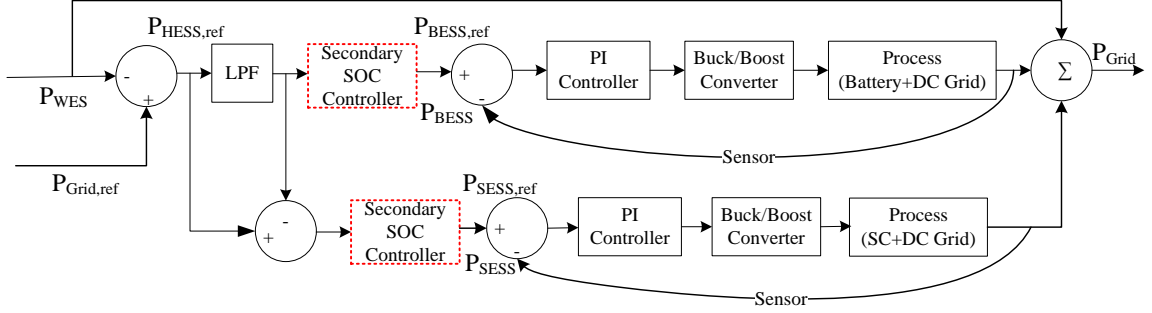


Figure 5.2: HESS power control framework for WT farm.

output FIS and tunes the system parameters utilizing the specified input (ESS SOC) and output (multiplication factor) training data. Modeling the training data set is done using a combination of least-squares and back-propagation gradient descent. Considering the ESS SOC as an input and the multiplication factor as an output, the training data set and output of the ANFIS are illustrated in Fig. 4.5 and Fig. 4.6, respectively.

#### 5.1.4 Control and Sizing of HESS

Fig. 5.2 shows the HESS control architecture, where the  $P_{\text{HESS,ref}}$  is the difference between the  $P_{\text{Grid,ref}}$  and  $P_{\text{WES}}$ . The LPF with a filter time constant of 48 s is employed to allocate the  $P_{\text{HESS,ref}}$  between the battery and SC [191]. Using this frequency management technique, high-frequency power components are charged and discharged by the SC, while low-frequency power components are charged and discharged via the battery, thereby extending battery service life and lowering overall system expense. The secondary SOC control, as shown in Fig. 4.8, employs a rule-based method to prevent the ESS SOC from exceeding its upper bound (100 % SOC) or going below its lower bound (optimal DOD level).

The maximum difference between the  $P_{\text{Grid,ref}}$  and  $P_{\text{WES}}$  results in the ESS capacity required to satisfy the grid demand for an entire day. By integrating the ESS

power profile with respect to time, the ESS capacity is determined. At first, the absolute maximum amount of energy used by the ESS during each dispatching period is determined and compared. Then, the maximum of these maximums provides the energy capacity that the ESS needs to dispatch WT power successfully. Finally, (5.4) is employed to take into account the DOD utilization by the ESS in its needed capacity computation.

$$E_{ESS}(t) = \int_0^t |P_{Grid,ref}(\tau) - P_{WES}(\tau)| d\tau \quad (5.2)$$

$$E_{ESS}^r = \underset{0 \leq t \leq T}{MAX} [E_{ESS}(t)] \quad (5.3)$$

$$C_{ESS} = \frac{E_{ESS}^r}{DOD_{max}} \quad (5.4)$$

where,  $C_{ESS}$  is the ESS required capacity,  $DOD_{max}$  is the maximum DOD utilization, and  $T$  is the simulation time.

### 5.1.5 Cost Optimization for ESS

The charging-discharging rate and DOD utilization are the primary factors determining the ESS service life. Fig. 3.7 shows the number of charging-discharging cycles as a function of DOD usage for the Li-ion battery and SC.

The expenditure associated with the ESS is related to its capacity and lifetime, which may be stated as (5.5). Detailed explanations with required mathematical formulas for calculating the ESS capacity and the ESS lifetime are documented in Section 5.1.4 and Section 5.1.6, respectively. It is evident that the ESS capacity and lifetime are strongly dependent on its DOD utilization levels. For instance, deeper

discharge of the Li-ion battery reduces its required capacity, but at the same time, the battery service life is also reduced. Therefore, it is recommended to select the optimal DOD, which can provide the most economical ESS for dispatching the WT power. Here, the contemporary PSO technique is implemented to find the optimal DOD in order to reduce the ESS expenditure. The optimization is performed with the objective to minimize the ESS cost to the constraints, i.e., (i) the ESS SOC remains within the lower bound (0 % SOC) and upper bound (100 % SOC), and (ii) the ESS successfully satisfies its reference power in each dispatching period. These constraints are also documented in (5.6) and (5.7). After finding the optimum DOD level for the ESS, the secondary SOC controller is responsible for maintaining the ESS SOC within a desirable range. Also, the various combinations of the battery and SC DOD usage levels in the HESS architecture are explored to realize the most economical ESS for dispatching the WT power.

$$ESS\ Cost = \frac{ESS\ Capacity}{ESS\ Lifetime} \quad (5.5)$$

$$SOC_{Lower\ bound} \leq SOC \leq SOC_{Upper\ bound} \quad (5.6)$$

$$P_{ESS} = P_{ESS,ref}; P_{Grid,ref} = P_{WES} + P_{ESS} \quad (5.7)$$

The contemporary PSO strategy is incorporated for its several advantages, e.g., higher convergence speed, simple and easy implementation, effective in global search, insensitive to scaling of design variables, and no overlapping or mutation computation [194], [195]. The mathematical model of the contemporary PSO can be expressed as follows:

$$V_i^{k+1} = \chi[V_i^k + C_1rand_1 \times (pbest_i - S_i^k) + C_2rand_2 \times (gbest - S_i^k)] \quad (5.8)$$

$$S_i^{k+1} = S_i^k + V_i^{k+1} \quad (5.9)$$

$$\chi = \frac{2}{\left|2 - \phi - \sqrt{\phi^2 - 4\phi}\right|} \quad (5.10)$$

where the optimization parameters utilized in the above mentioned equations are documented in [194].

### 5.1.6 Cost Calculation for ESS

The overall cost of the ESS includes its capital ( $S_{cap}$ ), power conversion ( $S_{conv}$ ), operation and maintenance ( $S_{O\&M}$ ), and replacement ( $S_{rep}$ ) expenses, which can be determined by using (5.11). The ESS capital cost is calculated by taking into account both cycling and calendar aging expenditure.

$$S_{ESS,Total}(\$) = S_{cap} + S_{conv} + S_{O\&M} + S_{rep} \quad (5.11)$$

$$S_{cap} = S_{ESS,cycling} + S_{ESS,calendar} \quad (5.12)$$

The BESS charging-discharging characteristics are utilized to compute the equivalent service life of the battery ( $T_{bat,z}$ ) since the charging-discharging cycles of the battery are demonstrated to be irregular in the WT scheme.

$$T_{bat,z} = \sum_{j \in T_s} \frac{C_{sj}}{C_{BESS} \times DOD} \quad (5.13)$$

where  $C_{BESS}$  is the BESS required capacity,  $C_{sj}$  is the total charged or discharged energy, and  $T_s$  is the simulation period.

Equation (5.14) is employed to calculate the expected service life of the BESS ( $T_{bat,life}$ ), where  $T_{bat,n}$  is the total number of cycles at the specific DOD provided by the manufacturers.

$$T_{bat,life} = \frac{T_{bat,n}}{T_{bat,z}} \times T_s \quad (5.14)$$

Then, the cycling cost of the BESS ( $S_{BESS,cycling}$ ) is calculated by using (5.15).

$$S_{BESS,cycling} = \frac{C_{BESS} \times Y_b}{T_{bat,life}} \quad (5.15)$$

where  $Y_b$  is the BESS capital cost (\$/kWh). Likewise, the SESS cycling expense ( $S_{SESS,cycling}$ ) is computed.

The calendar cost of the battery ( $S_{BESS,calendar}$ ) is calculated utilizing the degradation model proposed in [77], as shown in (5.16). The lithium-ion battery efficiency ( $m$ ) is assumed to be 92% in this study.

$$C_{BESS,calendar} = \frac{Y_b}{T_{bat,n} \times 2 \times DOD \times C_{BESS} \times m^2} \quad (5.16)$$

Ref. [78] is employed to compute the SC lifetime reduction due to its degradation properties, and the calendar aging cost for the SC is determined by using following formulas.

$$\frac{1}{T_{SC,calendar}} = \frac{1}{T_{SC,life}} \times \exp\left(\ln(2) \frac{\theta_c - \theta_c^{ref}}{\theta_0}\right) \times \left[ \exp\left(\ln(2) \frac{V - V^{ref}}{V_0}\right) + K \right] \quad (5.17)$$

$$S_{SESS,calendar} = \frac{C_{SESS} \times Y_s}{T_{SC,calendar}} \quad (5.18)$$

where  $C_{SESS}$  is the SESS capacity (kWh) and  $Y_s$  is the SESS capital cost (\$/kWh). The SC aging parameters are documented in [78].

The power conversion expenditure of the ESS ( $S_{conv}$ ) is evaluated as follows:

$$S_{conv} = \frac{P_{ESS} \times P_{ESS,conv}}{T_{ESS,life}} \quad (5.19)$$

where  $P_{ESS}$  is the ESS required power capacity in kW,  $P_{ESS,conv}$  is the power conversion expense (\$/kW), and  $T_{ESS,life}$  is the lifetime of the ESS considering both cycling and calendar aging. Similarly,  $S_{O\&M}$  is computed for the ESS.

The  $S_{rep}$  expenditure for the ESS is determined utilizing the methodology described in [161]. The capacity recovery factor ( $CRF$ ) is computed using (5.20), where  $I$  is the interest rate assumed to be 8.5 % and  $T_{WF}$  is the WT life span considered to be 20 years. Equation (5.21) is used to evaluate the replacement cost for the battery ( $S_{rep,bat}$ ), where  $M$  is the number of times the BESS is required to be replaced during the WT lifetime. Likewise, the replacement cost for the SC is determined.

$$CRF = \frac{[I \times (1 + I)^{T_{WF}}]}{[(1 + I)^{T_{WF}} - 1]} \quad (5.20)$$

$$S_{rep,bat} = (Y_b \times C_{BESS} \times CRF) \times \sum_{N=1}^M \left[ (1 + I)^{-N \times T_{bat,life}} \right] \quad (5.21)$$

Finally, the normalized HESS cost per kWh is computed utilizing the following formulas, taking into account the capital, power conversion, operation & maintenance (O&M), and replacement expenditures associated with the ESS.

$$S_{HESS}(\$) = S_{BESS,Total}(\$) + S_{SESS,Total}(\$) \quad (5.22)$$

$$HESS_{Norm,Cost} = \frac{S_{HESS}}{P_{WT} \times WT_{CF} \times T} \quad (5.23)$$

where  $P_{WT}$  is the WT capacity (kW),  $WT_{CF}$  is the WT capacity factor (35% is considered), and  $T$  is the number of hours in a year. Table 5.1 shows the price information associated with the ESS utilized in this research [171]. The high-level representation of the proposed methodology is also illustrated in Fig. 5.3.

## 5.2 Simulation Results

The hourly dispatching WT farm is developed and simulated in the MATLAB/Simulink platform. Furthermore, the power converter interface and associated control algorithms are modeled and studied in order to justify the performance and economic analysis of the grid-connected WT-HESS scheme.

Fig. 5.4 illustrates the power profile of  $P_{Grid,ref}$ ,  $P_{Grid}$ ,  $P_{WES}$ ,  $P_{BESS}$ , and  $P_{SESS}$  on January 20, 2019. The WES and HESS combined power constitutes the  $P_{Grid}$ , and the

Table 5.1: BESS and SESS cost information.

Parameter	BESS	SESS
Capital cost	189 (\$/kWh)	2500 (\$/kWh)
Power conversion system	211 (\$/kW)	211 (\$/kW)
O&M-Fixed	10 (\$kW-year)	1 (\$/kW-year)
O&M-Variable	3 (\$kWh)	3 (\$/kWh)

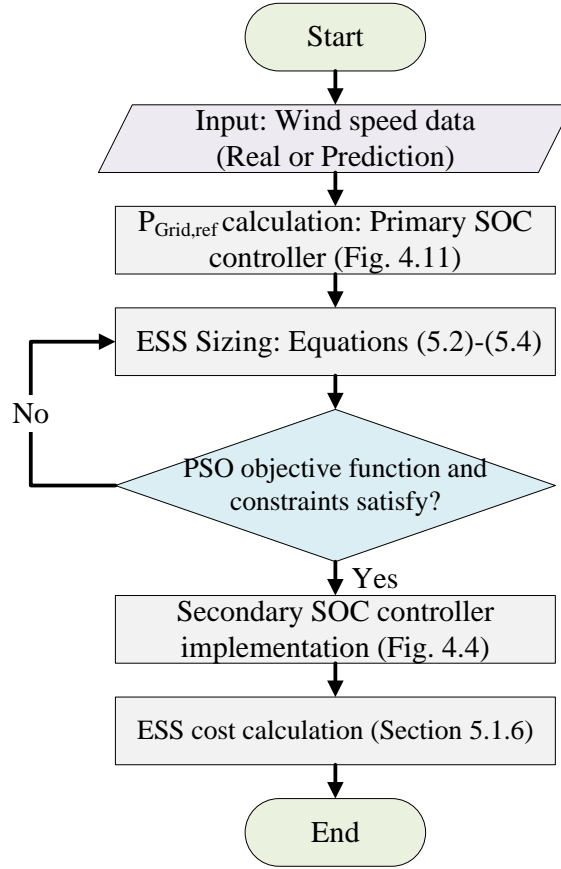


Figure 5.3: Overall workflow of the proposed methodology.

grid-connected converter provides  $P_{\text{Grid}}$  to the utility. In each dispatching period, the  $P_{\text{Grid}}$  remains steady and follows the desired  $P_{\text{Grid,ref}}$ . This confirms that the HESS effectively absorbs or supplies the required power to supply the intended power to the grid in each dispatching period from the highly intermittent WT framework. Furthermore, a similar phenomenon is observed regarding the tracking capability of the WT farm (WES + ESS) to the desired  $P_{\text{Grid,ref}}$  on an hourly basis when the battery or SC is integrated instead of HESS in the ESS architecture, which is defined as a battery-only or SC-only scenario in this research. Also, the error percentage between the  $P_{\text{Grid,ref}}$  and the  $P_{\text{Grid}}$  is computed using (3.25), which is also depicted in Fig. 5.5, in order to assess power quality. In each dispatching horizon, the  $P_{\text{Grid}}$  follows the  $P_{\text{Grid,ref}}$  closely; hence the undesirable deviation is observed to be exceedingly low.



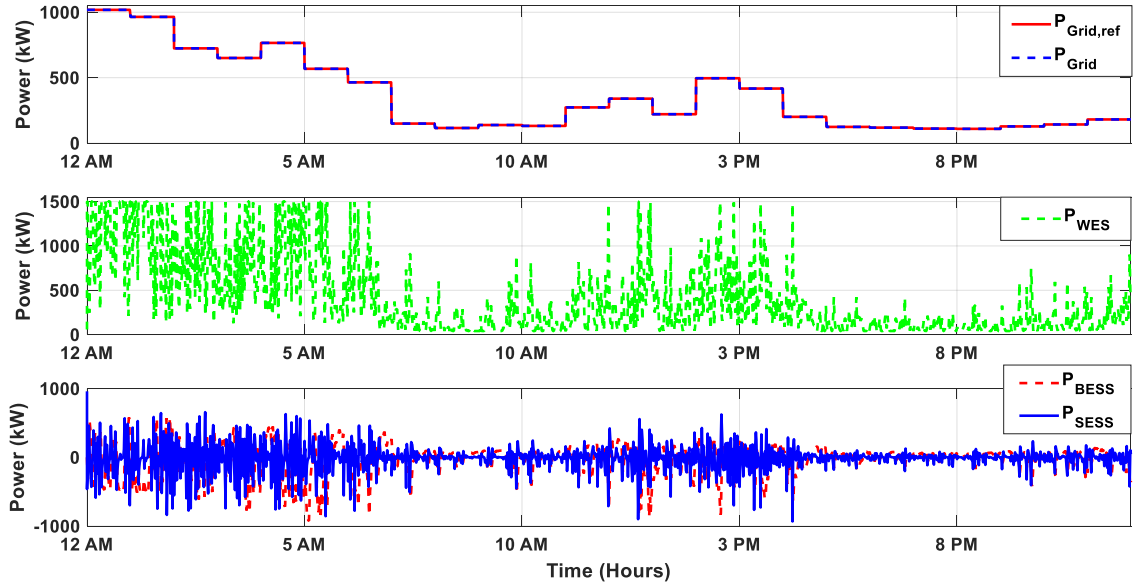


Figure 5.4: WT farm 1-hour dispatching results on January 20, 2019.

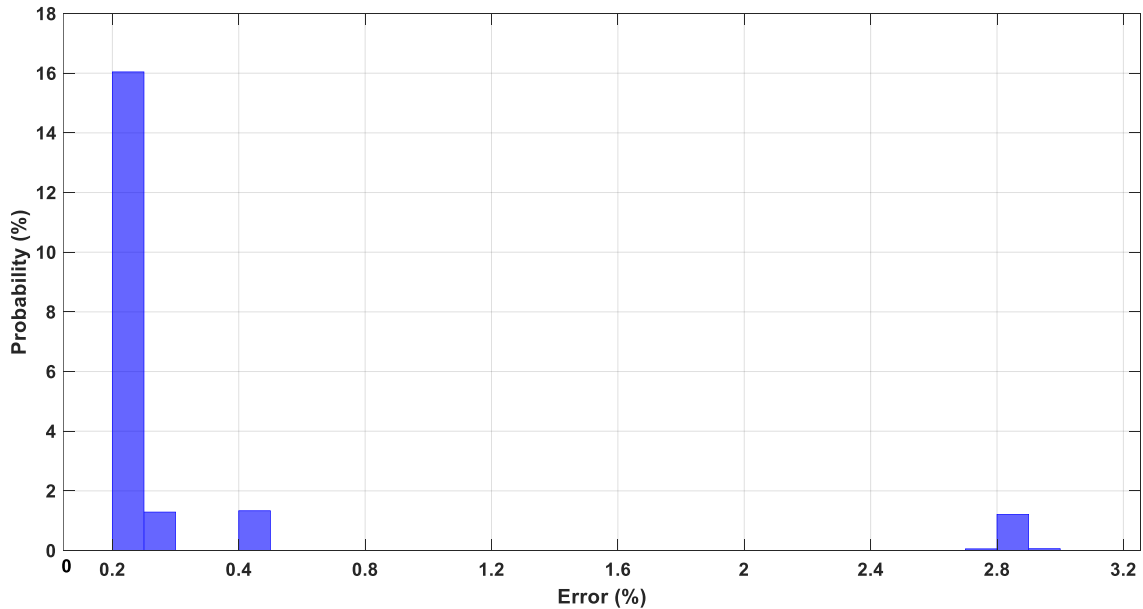


Figure 5.5: Histogram error results on January 20, 2019.

This attribute reflects the proposed architecture’s (WES + ESS) dispatch capability.

Fig. 5.6 illustrates the ESS SOC fluctuation on January 20, 2019, indicating the effectiveness of the primary SOC controller in ensuring that the ESS completes each dispatching horizon with its initial SOC. Such an SOC restriction is demanded to predict the desired  $P_{Grid,ref}$ , minimize the ESS cost, and guarantee the ESS has suf-

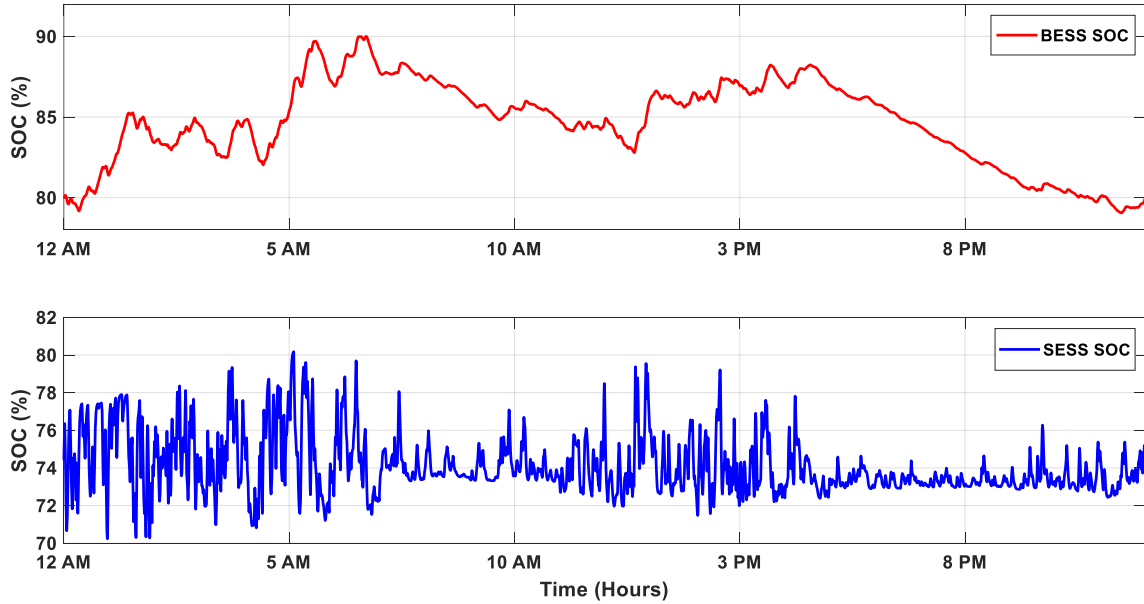


Figure 5.6: The ESS SOC variation profile on January 20, 2019.

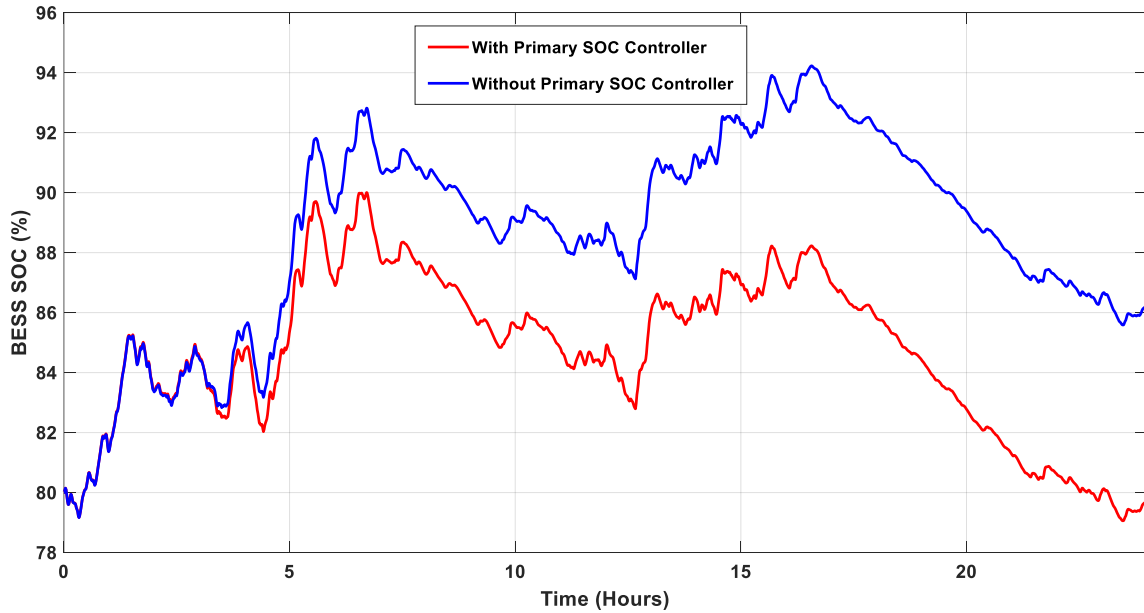


Figure 5.7: Proposed primary SOC controller effectiveness on January 20, 2019.

sufficient capacity to operate for the next day. The BESS SOC fluctuation with and without the primary SOC controller is also depicted in Fig. 5.7. This justifies the effectiveness of the SOC controller to ensure the BESS finishes with its starting SOC, which is highly desirable in developing the most economical ESS for this application.

The BESS and SESS expense as a function of their DOD utilization for the battery-only and SC-only operations on October 31, 2019, is illustrated in Fig. 5.8. After implementing the contemporary PSO, the optimal value of DOD usage for the BESS is found at 44 %, where the BESS cost is found to be around 2.7 ¢/kWh. However, full utilization (100 % DOD) of the SC provides the optimal value of DOD usage for the SC in terms of the cost assessment. Because the SC may be charged and discharged nearly indefinitely when it is completely exploited, the capacity needed for the SC is reduced to the minimum. It is noted that when the SC is fully utilized, the resulting minimum capacity required may be insufficient to ensure enough charge or discharge to successfully finish the entire dispatching period. Here, it was found that approximately 50 % of DOD usage for the SC can make sure that it has enough capacitance to meet all of the charging-discharging requirements. Hence, SC DOD utilization is limited to 50 % during the SC cost investigation. At 50 % DOD utilization, the optimal cost of SESS is found to be approximately 5.9 ¢/kWh.

Here, the annual ESS cost is calculated by the weighted average of the four differ-

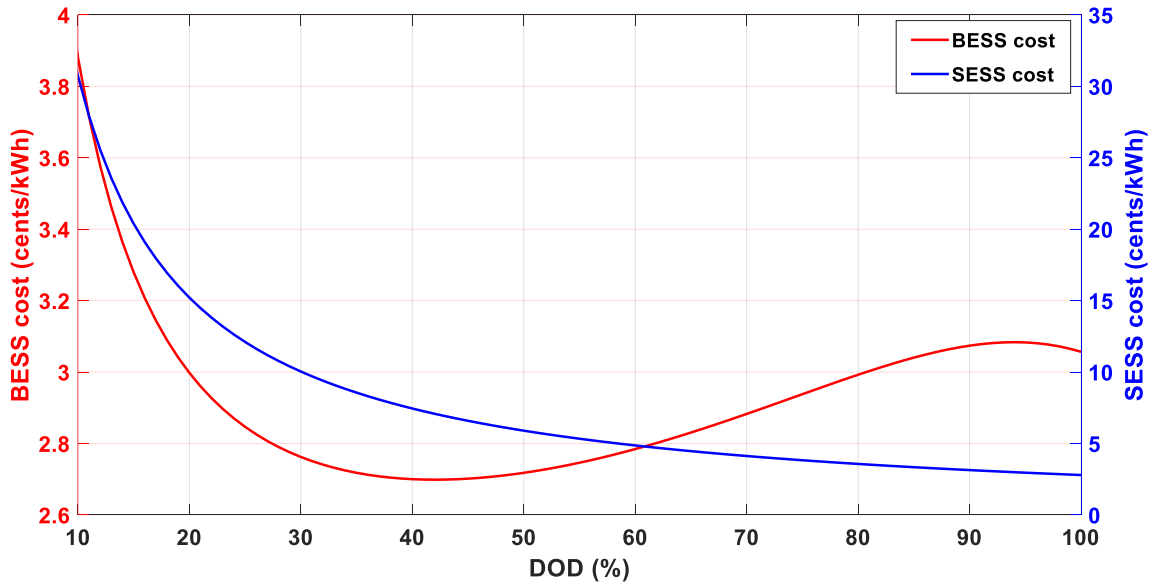


Figure 5.8: BESS and SESS cost (¢/kWh) at different DOD levels with WT farm.

ent seasons' ESS expenditure. The ESS expenditure comparison among various ESS frameworks considered in this study, i.e., battery-only, HESS with 48 s LPF time constant, and SC-only, is documented in Fig. 5.9. The optimal DOD utilization for the battery and 50 % DOD usage for the SC in the HESS framework are considered during this economic comparison. The HESS with 48 s LPF time constant provides the most competitive cost per kWh, which is approximately 2.2 ¢/kWh annually. It is also noticeable that the HESS scheme outperforms both battery-only and SC-only architectures considerably.

The various combinations of the SC and battery DOD utilization levels in the HESS framework are also explored to get a better idea of the HESS expenditure aspect. The HESS cost at various DOD levels of the battery and SC on January 20, 2019, is illustrated in Fig. 5.10. The objective is to investigate the effects of the combinations of the battery and SC DOD usage levels on the economic perspective of the HESS framework. The lower DOD utilization combination of the SC and battery in the HESS architecture significantly increased the overall HESS expenditure. As

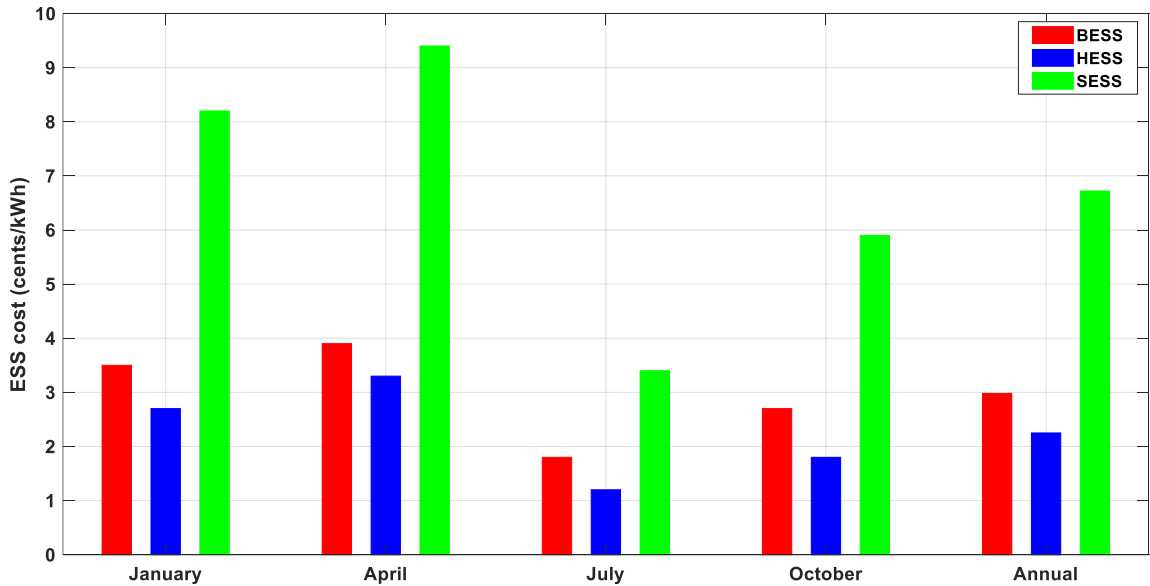


Figure 5.9: Annual ESS cost (¢/kWh) comparison with WT farm.

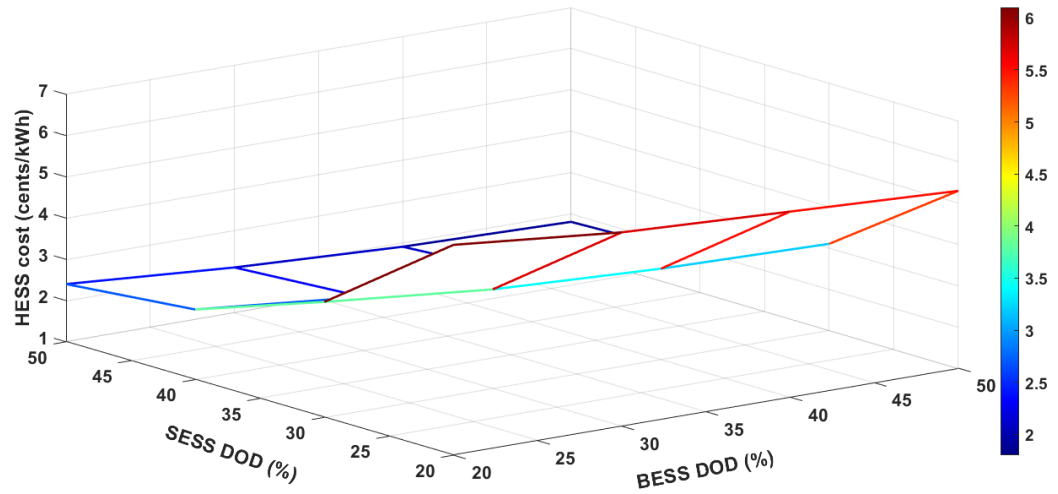


Figure 5.10: HESS cost as a function of DOD utilization on January 20, 2019.

the ESS capacity is directly related to its DOD utilization, the sizing of the HESS for any specific application can be made by exploring the optimal combinations of the battery and SC DOD usage levels, which significantly reduces system cost. Here, the optimal combination of DOD usage levels for the battery and SC, which is 44 % DOD utilization for the battery and 50 % DOD usage for the SC, is selected to design the most economical HESS architecture for dispatching the WT power.

The battery service life comparison with and without the SC in the ESS architecture is presented in Fig. 5.11. In this battery lifetime comparison, optimal DOD utilization for the BESS is considered. The high-frequency power components charged-discharged by the BESS are considerably reduced when the SC is part of the ESS framework. Hence, the battery service life increases significantly. Since the BESS life cycle cost is inversely proportional to its lifetime, the HESS appears to be more economical than the battery-only scheme for hourly dispatching of WT power.

Fig. 5.12 shows the 1-hour ahead WT speed forecast on an hourly basis on January 16, 2019 (top) and April 16, 2019 (bottom), using the ANN compared to the

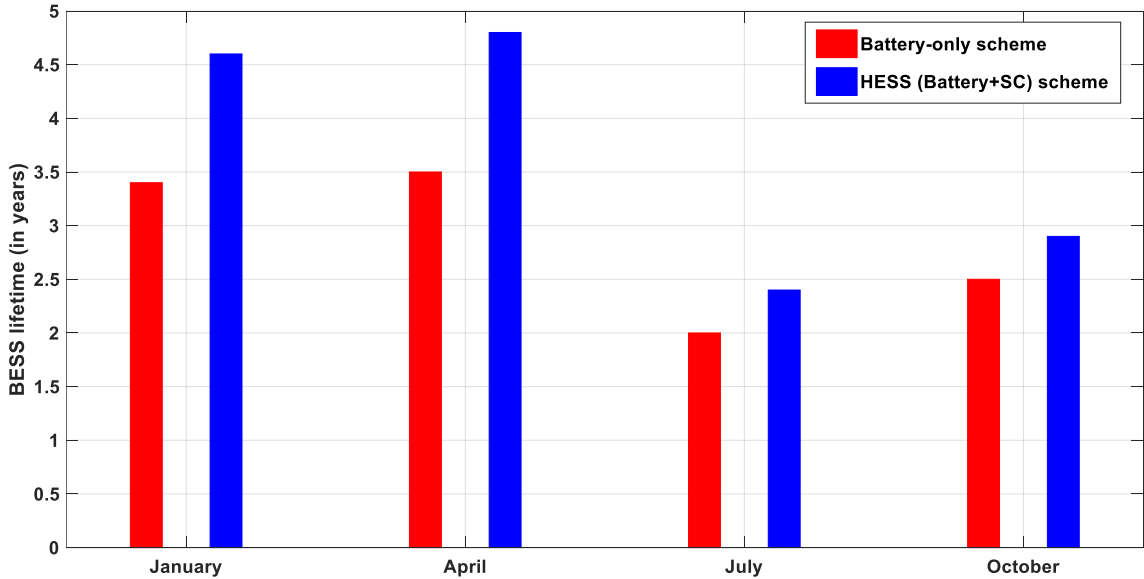


Figure 5.11: Battery service life (in years) comparison.

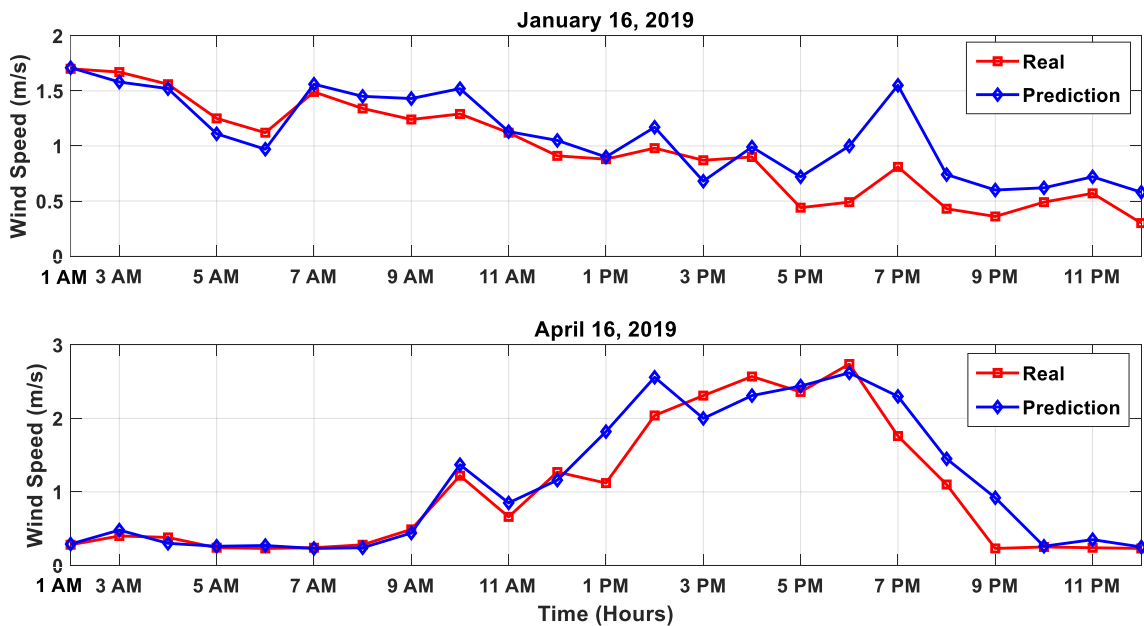


Figure 5.12: Hourly wind speed forecasting results using the ANN method.

measured actual historical wind speed data. The simulation results demonstrate that the forecast values of the ANN model reasonably match the measured values, and the RMSE is found to be around 10 %. A similar trend is observed while forecasting hourly WT speed data on July 16, 2019, and October 16, 2018. Therefore, it can be

concluded that the simulated ANN shows good convergence between the forecasted and measured values of hourly wind speed data.

### 5.3 Comparative Study on ESS Cost

According to [196], the average cost of producing electricity at thermal power plants ranges between 5 ¢/kWh and 10 ¢/kWh, whereas onshore wind farms cost between 6 ¢/kWh and 15 ¢/kWh. Here, the annual HESS expenditure is found to be approximately 2.2 ¢/kWh for hourly dispatching of WT power while selecting four different days with significant wind variability as a representative of each season. Typically, the levelized cost of energy for WT is between 3 ¢/kWh to 5 ¢/kWh [197]. Hence, the WT-HESS architecture with the proposed hourly dispatching scheme could be an appealing alternative type of reliable power generation, particularly in areas with abundant wind resources.

This study attempted to compare the expenditure associated with the HESS for hourly dispatching WT power scheme with existing literature. Nevertheless, to the best knowledge of the author, no prior studies explored the HESS expense for dispatching the WT power on an hourly basis. Nonetheless, one HESS is studied in [165] for hourly dispatching solar PV power to the utility, and the cost associated with HESS for this purpose was found to be around 1.5 ¢/kWh. As the WT power is inherently more intermittent in nature than the solar PV power, the required charging-discharging cycles of the HESS are expected to be substantially increased to track the desired  $P_{\text{Grid,ref}}$  in each dispatching period in the WT-HESS framework. As a result, higher HESS costs will be incurred in the WT architecture. Furthermore, the replacement and calendar aging expenditures related to the ESS were not taken into account during the ESS cost assessment in [165].

In [76], the ESS life cycle cost was compared to smooth out the power produced by the wave energy converter in order to satisfy the flicker constraint. However, the goal was to smooth out the RE power rather than dispatch RE power, as explored in this study. The proposed dispatching strategy demands a significant contribution from the ESS to meet the load demand in each dispatching period, resulting in higher capacity and lower service life due to the higher number of charging-discharging cycles in comparison with the flicker constraint technique. As the ESS expense mainly depends on its required capacity and lifetime, the ESS life cycle cost evaluation between the dispatching strategy and flicker constraint technique may not provide sufficient information to perform a like-for-like comparison.

#### 5.4 Summary

This chapter has proposed and demonstrated an hourly dispatching scheme for WT power. Employing the proposed methodology, the WT farm (WES+ESS) can successfully dispatch a pre-determined constant power hourly with an error of less than 1 %. Furthermore, an ANN based algorithm is implemented to predict the wind speed 1-hour ahead of time to predict the WT output power. Besides, the primary SOC technique is employed to estimate the desired  $P_{\text{Grid,ref}}$ , which helps to improve the system reliability and reduce the system expenditure. The effectiveness of the primary SOC control strategy is thoroughly investigated to design the most economical ESS for an hourly dispatching WT power scheme. The ESS life cycle cost is optimized based on its DOD usage using an advanced optimization approach. The HESS is found to be the most cost-effective (2.2 ¢/kWh annually) ESS for hourly dispatching of WT power. At the optimal configuration, the HESS expense per kWh is also more economical than the battery-only or SC-only scenarios.



Even though decentralized ESS, which can help reduce transmission losses, is considered during this investigation, the proposed methodology is suitable for both centralized and decentralized ESS. The objective is to present the worst-case scenario of the ESS expenditure for hourly dispatching of WT power. Therefore, the highest wind variation day for each season is selected to compute the expenditure associated with the ESS for successfully dispatching WT power on an hourly basis.

## Chapter 6 Hardware-in-loop Experimental Verifications for Hourly Dispatching Wind-Solar Power with Battery Energy Storage

The Hardware-in-Loop (HIL) technique allows to reproduce the behavior of a dynamic system in real time. This quality makes HIL a useful tool in the controller validation process and is widely used in multiple areas. This chapter presents a Control-HIL (CHIL) based test system for testing the proposed BESS controller for dispatching the WSHPS power. With the CHIL, the actual controller used in the real hardware system can be tested for its operation with a simulation based WSHPS. The CHIL has been used to validate the proposed BESS controller performance under various conditions of the BESS charging-discharging for maintaining the desired  $P_{\text{Grid,ref}}$ . For the CHIL, the WSHPS farm is modeled in the RTDS and the BESS controller is designed in the DSP. Here, the power converter coupled to the BESS is controlled by the DSP, which is connected between the GTA0 card and the GTDI card in the RTDS interface circuit boards.

Real time power system simulators provide continuous, actual real time, Electro-magnetic Transient (EMT) simulation results. It is essential to use EMT simulations in order to obtain instantaneous results when testing protection, control, and power equipment. In the early 1990s, RTDS Technologies Inc. released the first commercial real-time EMT simulator. These simulators' hardware and software have experienced numerous upgrades over the years, increasing their performance and broadening their scope of applications [198]. The RTDS simulator is being used to research various aspects of the electric power system, as well as to develop and test new equipment to be deployed in power systems. The growing need for RE sources and their integration

into the existing grid, in particular, highlights the importance of reliable real-time simulation models. These models enable the network operator to assess all of the aspects presented by the integration or linked with the RE source controllers.

As RTDS solves the power system equation at high speeds, it can produce output conditions that accurately reflect actual power grid conditions. In general, RTDS consists of both hardware and software. The RTDS hardware consists of processing and communicating cards that are put into the device and attached to a common plate situated in the RTDS's rear. The parallel processing architecture of the processing cards is specifically designed to simulate with one or more processors for the equation solution for the power system and its constituent parts. The communicative cards handle communication between RTDS and its software, which is installed on the guest machine. Additional dedicated interface cards in RTDS enable physical and logical connections between simulated power systems and actual devices. The RTDS software, known as RSCAD, has a graphical user interface and enables users to create, compile, run, and examine simulation instances. This software includes a large library of power system components, control, and automated protection systems, as well as a user-friendly interface, making the assembly and analysis of a wide range of AC and DC systems easier and more integrated. Users can create a model of the power system using the RSCAD program, load that model into the RTDS for EMT simulation, and then download the modified states of that model for analysis.

However, there is some concern about the trade-off between the complexity of the systems modeled in software and the available hardware resources required by real-time simulations. The key problem is to create low-cost (in terms of hardware) simulation models while maintaining high accuracy of the results.

Real-time power system simulators are frequently employed by utilities, equipment

makers, and research institutions in the electric power sector. The simulators are used to research power systems as well as to develop and test new equipment that will be deployed in power systems. The hardware and software that make up the RTDS simulator were specifically created and produced for real-time applications.

When the results for each timestep are calculated and the necessary communication with external physical equipment is accomplished in a real-world time less than or equal to the simulation timestep, a digital simulation is deemed to run in “real time”. Furthermore, data exchange with external physical equipment must occur at equidistant real-world time points (i.e., once each timestep) throughout the simulation [199].

The RTDS simulator performs EMT simulations with a typical timestep of 50  $\mu\text{s}$ . The RTDS is also capable of performing simulations with smaller timestep in the range of 1-3  $\mu\text{s}$ . It is necessary to use small time steps when modeling power electronic converters with switching frequencies greater than 40 kHz, which require a lower time resolution. RTDS hardware cards arranged in card cages, also referred to as racks, make up the RTDS Simulator. The racks, together with other RTDS add-ons equipment and power supply components, are housed in cubicles.

The hardware for the RTDS simulator was created expressly to use specialized, high-speed parallel processors to solve the Dommel Algorithm for EMT in real time.

The Dommel Algorithm permits parallel processing at two different levels:

- Components connected to a common admittance matrix are processed in parallel (i.e., within one subsystem).
- Subsystems are processed in parallel (i.e., decoupled admittance matrices).

The RTDS simulator emulates the first level by solving components connected to

a common admittance matrix utilizing tightly coupled processors (communicating via a shared backplane) within a rack. The second level is realized by utilizing distinct racks to solve various simulation subsystems (communicating via dedicated gigabit per second communication channels). The second level of parallel processing enables practically infinite system expansion.

Each RTDS simulator hardware device is referred to as a NovaCor chassis. Each chassis includes a high-performance multi-core processor, Workstation Inter-Face (WIF) capabilities, communication connections, and analogue output channels. NovaCor is the hardware that is utilized to solve the equations that represent the power and control system components modeled in the RTDS. It contains optical connections that can be used to link to high resolution digital and analog I/O cards as well as for direct communication amongst NovaCor processor cards. As indicated earlier, the simulation software used with the RTDS simulator is called RSCAD. The Graphical User Interface (GUI) utilized by the Simulator is included in the RSCAD, which was created specifically for real-time digital simulation. With the help of RSCAD, users can carry out all the tasks required to set up, run, and examine the outcomes of a real-time simulation.

The rest of this chapter is organized as follows: Section 6.1 presents the detailed modeling of the testbed created using RTDS to verify the BESS controller for dispatching the WSHPS power. The detailed specification of the individual equipment employed in the CHIL is documented in Section 6.2. The CHIL results to justify the BESS controller are contemplated in Section 6.3. Finally, the synopsis of this chapter is summarized in Section 6.4.

## 6.1 RTDS-Based Testbed

### 6.1.1 RTDS-Based Representative WSHPS Model

The WSHPS topology shown in Fig. 6.1 is modeled in the RSCAD platform. The WSHPS topology consists of a PVES and a WES. The PVES is comprised of solar PV arrays rated at 1 MW, a MPPT controller, and a unidirectional DC/DC boost converter. The WES consists of a direct-drive 1.5 MW three-phase PMSG coupled to a wind turbine, a pitch angle controller, and an AC/DC rectifier. The BESS is connected in parallel with the WSHPS using a bi-directional DC/DC converter. The WSHPS and BESS are connected in parallel to the DC-link capacitor bank that serves as the DC bus. Here, the WSHPS and BESS are connected to the DC bus as a current source, and the inverter controls the DC-bus voltage. Therefore, controllable power flow is feasible by controlling the current flow through the power converters.

### 6.1.2 PVES Model

An ideal solar cell is represented as a current source with a paralleled diode. In the single-diode and solar cell models, the current-voltage relationship is as follows:

$$I = I_{ph} - I_o \times e^{\left(\frac{V+R_s I}{V_t \times a}\right)-1} - \frac{V + R_s I}{R_{sh}} \quad (6.1)$$

where  $I_{ph}$  is photocurrent of the solar cell,  $I_D$  is the diode current;  $R_s$  is the sum of several structural resistances in the solar cell,  $R_{sh}$  is to model the leakage current of the semiconductor material,  $I_o$  is the diode reverse saturation current,  $a$  is called diode ideality factor and is a measure of how closely the diode matches the ideal diode equation, and  $V_t$  is the diode thermal voltage which is a constant defined at

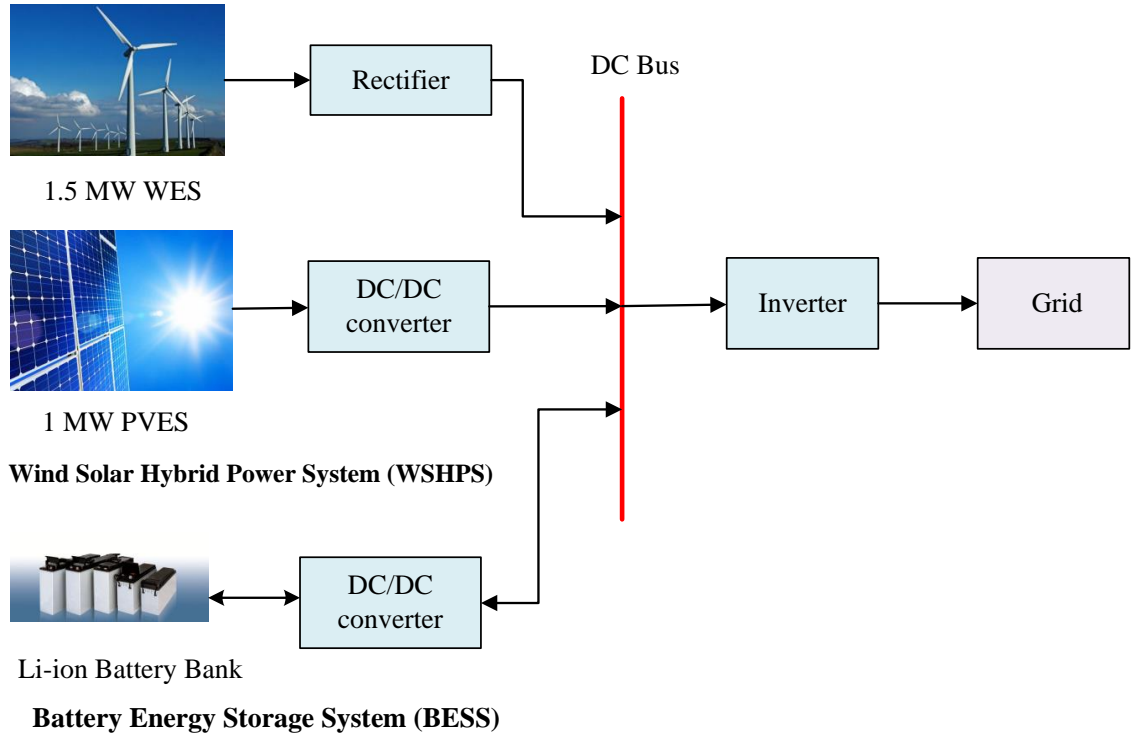


Figure 6.1: Overview of the WSHPS framework.

any given temperature  $T$  (in K) by:

$$V_t = \frac{kT}{q} \quad (6.2)$$

where  $k$  is the Boltzmann constant and  $q$  is the magnitude of an electron charge.

In this work, the RSCAD single-diode and five-parameter PV array models are used, and the current-voltage curve with the provided insolation  $G$  and temperature  $T$  for the constructed PV array may be represented as:

$$I_{ph} = \frac{G}{G_{ref}} I_{phref} (1 + k_i (T - T_{ref})) \quad (6.3)$$

$$I_o = I_{oref} \left( \frac{T}{T_{ref}} \right)^3 e^{\left( \frac{E_g}{a_{ref} \frac{kT}{q}} \left( \frac{T}{T_{ref}} - 1 \right) \right)} \quad (6.4)$$

where the nominal (standard) test conditions are referred to the standard temperature  $T_{ref} = 25^\circ\text{C}$  and the standard solar intensity  $G_{ref} = 1000$  ( $\text{W}/\text{m}^2$ ), and  $E_g$  is the energy gap of the selected solar cell semiconductor material.

The incremental conductance Method algorithm serves as the foundation for the RTDS MPPT model since it reduces the amount of computation required. The Hill-Climbing Method is the foundation of the incremental conductance Method (Perturbation & Observation Method). With a minor modification, this algorithm becomes slightly more robust. A boost converter is used to introduce a desirable DC voltage because the terminal voltage of a PV panel may vary in a wide range due to environmental changes, such as temperature or solar intensity variations.

### 6.1.3 WES Model

The power extracted from the WT can be represented using (2.13), where  $\lambda$  reflects the tip-speed ratio that can be defined as:

$$\lambda = \frac{r \times w_{tur}}{V_w} \quad (6.5)$$

$r$  is the WT radius,  $V_w$  is the wind speed and  $w_{tur}$  is the turbine angular speed.

The WT model in the RTDS simulator library adopts (6.6) to represent the performance coefficient  $[C_p(\lambda, \beta)]$  where the recommended values of  $c_1$  to  $c_6$  are listed in Table 6.1.

$$C_p(\lambda, \beta) = c_1 (c_2 \lambda_i - c_3 \beta - c_4) e^{-c_5 \lambda_i} + c_6 \lambda \quad (6.6)$$

$$\lambda_i = \frac{1}{\lambda + 0.08\beta} - \frac{0.035}{\beta^3 + 1} \quad (6.7)$$



Table 6.1: Coefficients for the WT model.

Coefficient	$c_1$	$c_2$	$c_3$	$c_4$	$c_5$	$c_6$
Value	0.5176	116	0.4	5	21	0.0068

If the turbine power generation is less than its nominal value, the optimal pitch angle is adjusted to zero in order to maximize turbine power generation. The blades are pitched to reduce the rotor speed and the power drawn from the wind when the wind speed exceeds the nominal value.

#### 6.1.4 Battery Model

The RTDS Li-ion battery model (Min/Rincon-Mora) is adopted in this study, which is shown in Fig. 6.2. This model allows for an accurate representation of the device in real-time simulation.

In Fig. 6.2,  $R_{\text{transient\_S}}$  and  $C_{\text{transient\_S}}$  are responsible for the battery's short-term transients, whereas  $R_{\text{transient\_L}}$  and  $C_{\text{transient\_L}}$  are responsible for the battery's long-term transients. It is observed that the optimal trade-off between the accuracy and complexity of the model is achieved by using two RC time constants as used in the

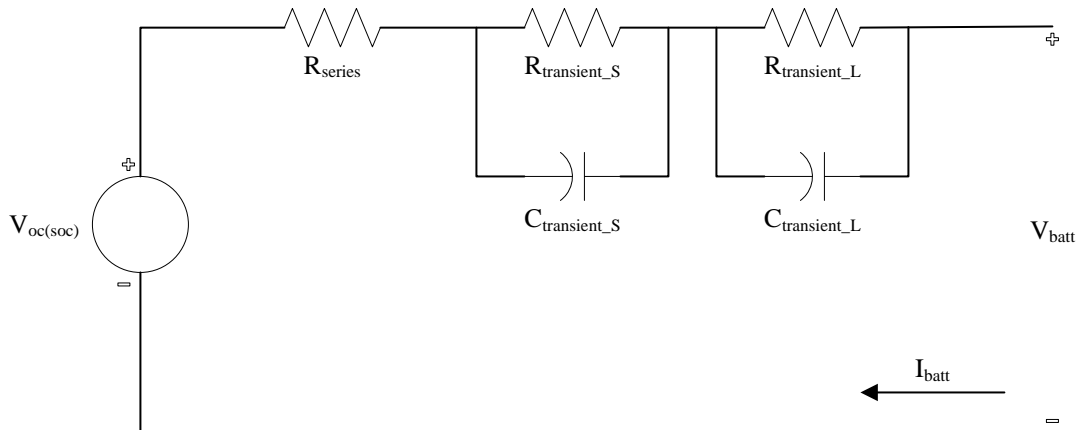


Figure 6.2: Electrical equivalent circuit of Min/Rincon-Mora model.

model [200]. All the non-linear circuit parameters in the Min/Rincon-Mora model can be expressed as functions of the SOC. The behavior of such parameters was mathematically described by single variable functions, which are shown as below:

$$V_{OC}(SOC) = -1.031 \times e^{-35 \times SOC} + 3.685 + 0.2156 \times SOC - 0.1178 \times SOC^2 + 0.3201 \times SOC^3 \quad (6.8)$$

$$R_{Series}(SOC) = 0.1562 \times e^{-24.37 \times SOC} + 0.07446 \quad (6.9)$$

$$R_{Transient\_S}(SOC) = 0.3208 \times e^{-29.14 \times SOC} + 0.04669 \quad (6.10)$$

$$C_{Transient\_S}(SOC) = -752.9 \times e^{-13.51 \times SOC} + 703.6 \quad (6.11)$$

$$R_{Transient\_L}(SOC) = 6.603 \times e^{-155.2 \times SOC} + 0.04984 \quad (6.12)$$

$$C_{Transient\_L}(SOC) = -6056 \times e^{-27.12 \times SOC} + 4475 \quad (6.13)$$

### 6.1.5 BESS Controller

Fig. 6.3 illustrates the BESS controller implemented in the RSCAD environment. Here,  $P_{WSHPS}$  reflects the power generated by the hybrid WT-PV system, and  $P_{Grid,ref}$  is the desired power, which is intended to be supplied to the grid at this instant. The difference between  $P_{Grid,ref}$  and  $P_{WSHPS}$  represents the battery's power reference. The  $P_{BESS,ref}$  value is compared to the battery's instantaneous value ( $P_{BESS}$ ) to determine the desired duty ratio for the power converter. In this re-

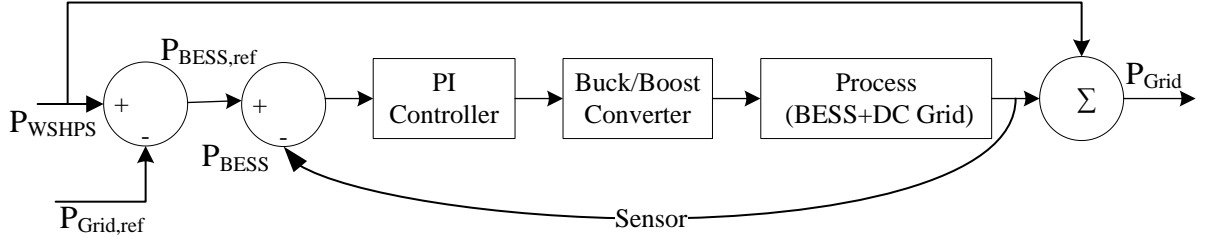


Figure 6.3: BESS controller framework.

search, a PI controller is employed to track the desired duty ratio and to reduce the proportional and integral errors of the system.

## 6.2 Controller Hardware-in-the-loop for WSHPS

Testing control algorithms against the real system can be time-consuming, costly, and possibly insecure. Testing engineers have replaced traditional testing methods with HIL testing in order to achieve rapid prototyping and high-quality controller software. HIL testing allows users to validate the controller design without requiring the entire system hardware. The RTDS simulator is an excellent tool for evaluating power system controls in situations where real-time closed-loop interaction between the power system simulation and the control hardware is required.

In the RTDS, the HIL testing of converter controllers is implemented through electrical connections and does not use any GTNET communication. In this case, the current and voltage measurements from RTDS are sent through the GTA0 card to the controller, and the firing pulses from the controller are brought into the simulation through the GTDI card. Fig. 6.4 illustrates a typical CHIL setup for validating the converter controller.

Analogue signals from the RTDS simulator are interfaced to external devices via the GTA0. The GTA0 card has sixteen 16-bit analogue output channels with a 10 V output range. A large dynamic range is offered by the 16-bit Digital to Analog

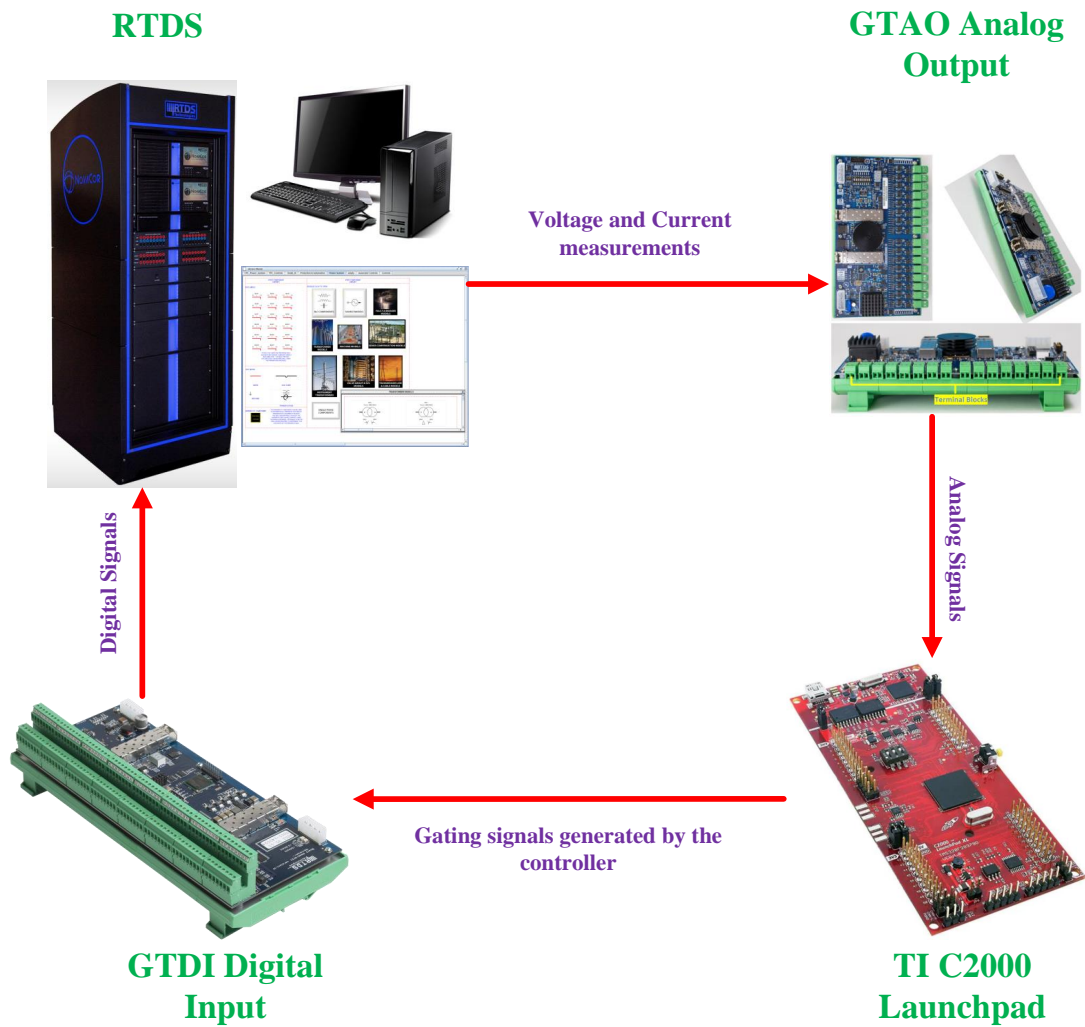


Figure 6.4: Typical CHIL setup.

Converters (DAC). When employing the GTA0 to transmit measured current signals to an external protection device via RTDS, such a broad dynamic range might be necessary. An optical cable linked between the optical ports of the GTA0 card and the NovaCor is used to transfer data between the two devices. The scale factor for each channel is adjustable from the RSCAD/Draft component connected to the GTA0 card. For a specific floating-point input value, the scaling factors decide what voltage the GTA0 channel will output. The scale value is entered as a floating-point number, which equals the GTA0's output of +5V.

Digital signals from an external device are interfaced to the RTDS using the GTDI card. There are 64 digital input channels on the GTDI card. Each bank of eight input channels is isolated from the other banks as well as the RTDS system. An optical cable linked between the card's optical ports is used to transfer data between the GTDI and a NovaCor. Any of the 20 GT Fiber Communication connections that are accessible can be used to connect the GTDI card. In the GTDI component that references the GTDI card in RSCAD, the GTIO port number to which the GTDI card is linked must be given as a parameter. The terminal block connectors on the GTDI card are wired for digital signals. The GTDI card has 64 input channels, each of which has a channel number. Channel 1 corresponds to the least significant bit (LSB), while channel 64 corresponds to the most significant bit (MSB). A simple constant current source connected in series with a resistor describes how the input section of the GTDI card operates. If an input voltage of between 3 and 50 volts is given, current will flow, yielding a logic 1. If the supplied voltage input falls between the range of 0-1.5V, current won't flow and a logic 0 will result.

Here, the microcontroller unit (MCU) used to model the BESS controller in real time is the C2000 F28379D Launchpad, developed by Texas Instruments. It is a simple and low-cost development board and has four independent 12-bit/16-bit analog-to-digital (ADC) converter modules. The ADC modules are employed for sampling the BESS power signal, with a resolution of 4,096 levels.

Fig. 6.5 demonstrates the overall structure of WSHPS with CHIL setup in detail. The WSHPS is modeled in the RSCAD platform and the BESS controller is embedded in F28379D Launchpad. An automatic code generator is incorporated to embed the BESS controller in the MCU, utilizing the MATLAB/SIMULINK coder in this study. Considering the F28379D Launchpad characteristics, Simulink blocks are used to

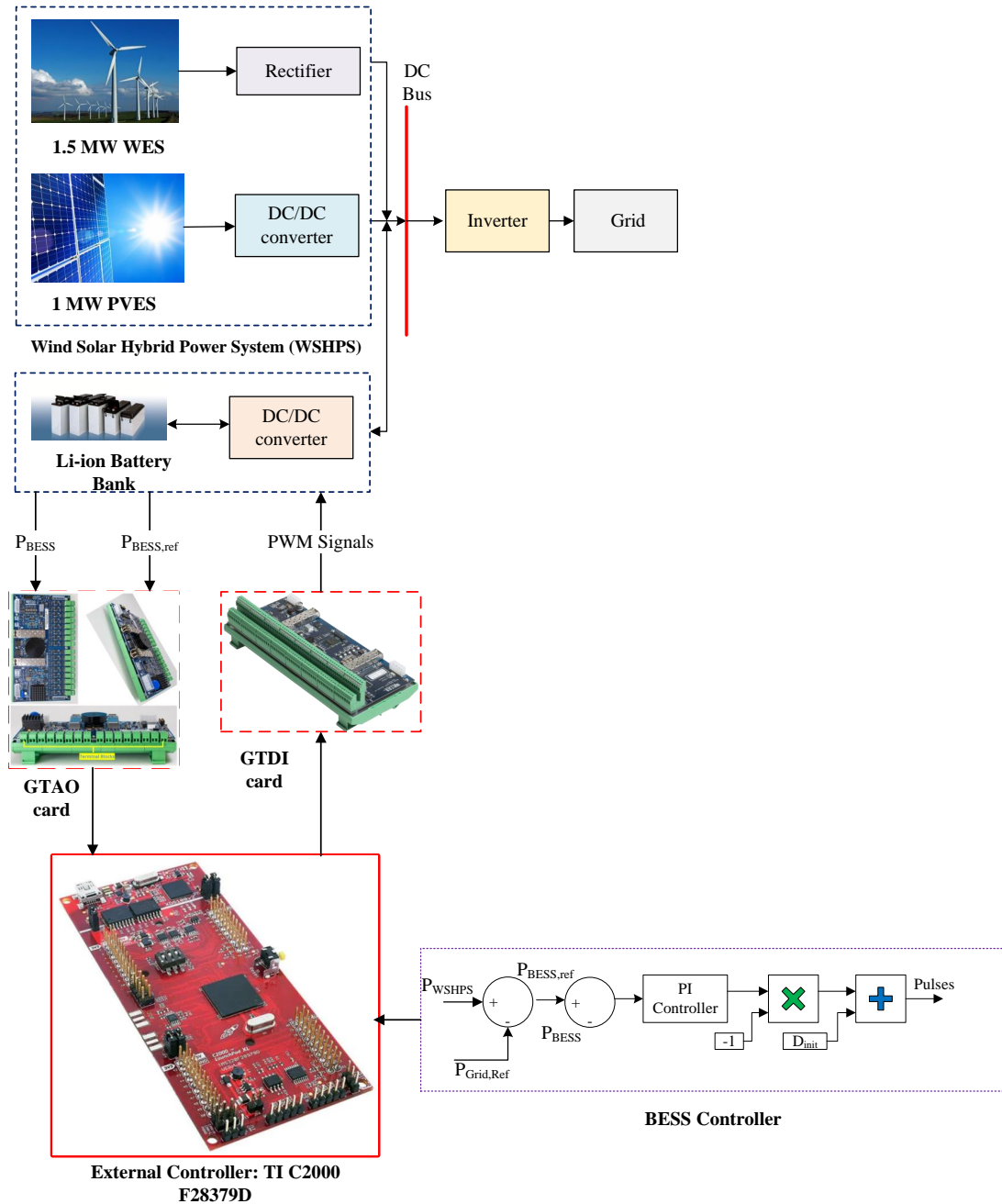


Figure 6.5: Overall structure of the WSHPs with a CHIL setup.

develop the BESS controller, which is utilized to control the duty ratio of the power converter associated with the battery energy storage system shown in Fig. 6.5. The RTDS is utilized to conduct real-time experiments by injecting the analog signal into the F28379D through the GTA0 card. The RTDS receives the digital signal (firing

pulses) from the F28379D by the GTDI card, which leads to closing the loop.

### 6.3 Experimental Setup and Results

Fig. 6.6 shows the experimental setup in the lab to justify the effectiveness of the proposed BESS controller utilizing the CHIL platform. The RTDS simulator consists of one cubicle with two NovaCor Chassis. The GTA0 card and GTDI card are attached to NovaCor using fiber cables and mounted on a DIN rail in the back of the RTDS cubicle. The BESS controlled is modeled in C2000 F28379D Launchpad. As mentioned earlier, the simulation software employed with the RTDS simulator is called RSCAD, which is installed on the workstation to perform the real-time simulation. In the CHIL environment, the RTDS measured signals (voltage, current, power, etc.) are injected into the F28379D Launchpad through the GTA0 card. Then, the firing pulses generated by the F28379D Launchpad are brought back into the RSCAD simulation via the GTDI card to control the duty ratio of the power converter.

In the proposed BESS controller scheme, when the power generated by the hybrid PV-WT system is found to be higher than the  $P_{\text{Grid,ref}}$ , the battery operates in charging mode. On the other hand, when the power generated by the hybrid PV-WT system is found to be lower than the  $P_{\text{Grid,ref}}$ , the battery acts in discharging mode. The power converter connected to the BESS operates in a buck mode when the BESS is charging and acts in a boost mode when the BESS is discharging. Here, the BESS is responsible for maintaining the desired  $P_{\text{Grid,ref}}$  by absorbing or supplying the required power. The combination of the power generated by the WSHPS and BESS is defined as the  $P_{\text{Grid}}$ , which is actual power supplied to the grid from the proposed WSHPS framework. In this research, both the charging and discharging scenarios



Figure 6.6: RTDS Control-Hardware-in-Loop experimental setup.

of the BESS are taken into account while justifying the proposed BESS controller utilizing the CHIL platform with RTDS.

### **BESS Discharging Case:**

Two different scenarios are investigated for the BESS discharging instance. Case 1:  $P_{\text{Grid,ref}}$  is set to 704 kW, and Case 2:  $P_{\text{Grid,ref}}$  is set to 729 kW. Fig. 6.7 and Fig. 6.8 illustrate the CHIL results for the BESS discharging Case 1 and Case 2, respectively. The power generated by the hybrid PV-WT system is found to be 679 kW. In both



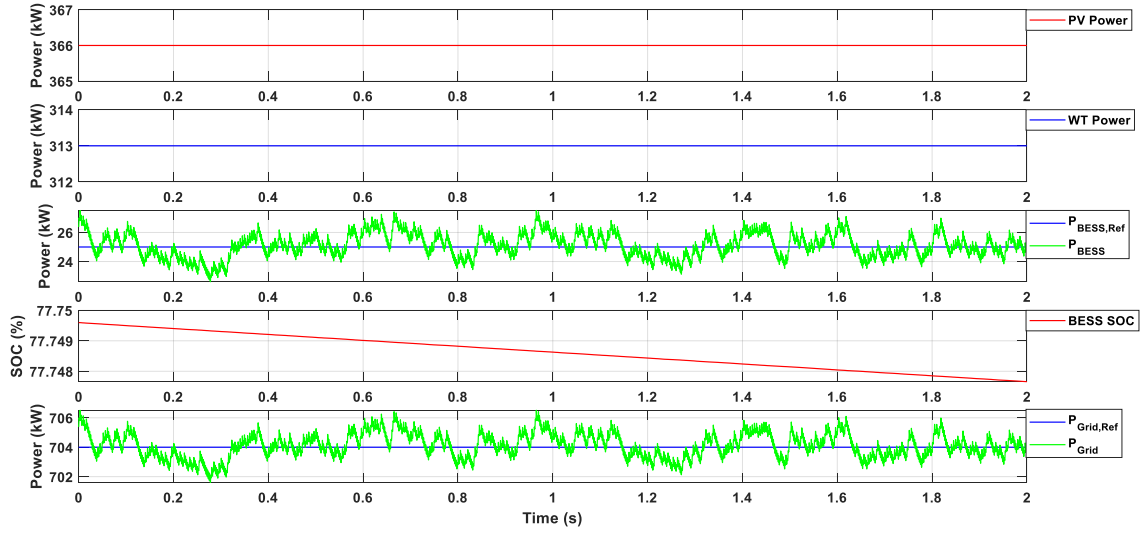


Figure 6.7: Case 1: BESS discharging instance.

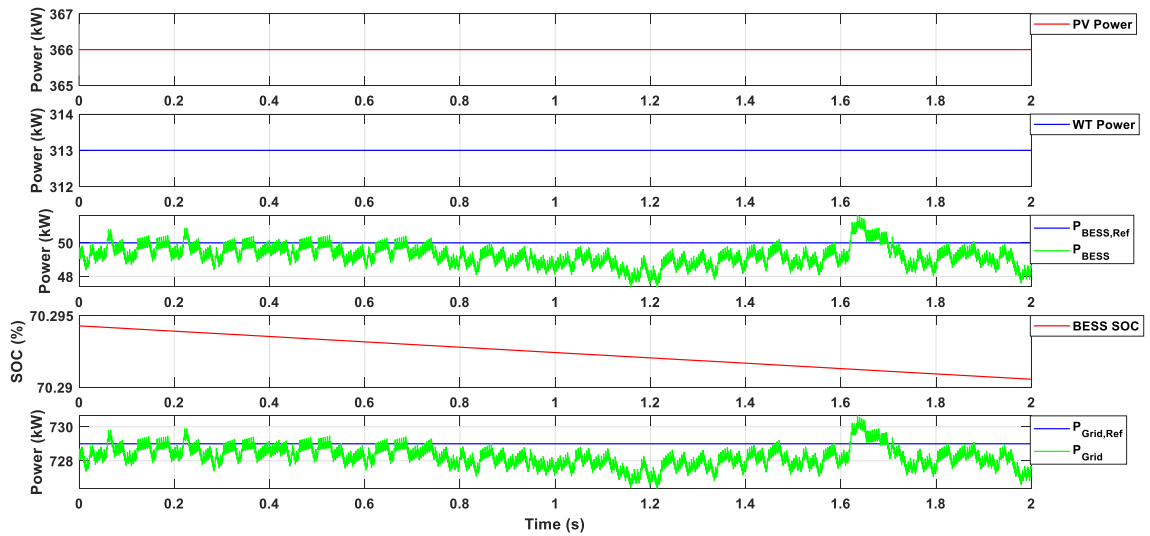


Figure 6.8: Case 2: BESS discharging instance.

scenarios, the BESS successfully supplies the necessary power to follow the desired  $P_{\text{Grid,ref}}$  with acceptable undesired deviation, which also justifies the proposed BESS controller effectiveness with the CHIL platform. The BESS SOC variation also verifies the BESS is in discharging mode for both instances.

### BESS Charging Case:

For the BESS charging scenario, two different cases are also exploited. Scenario 1:  $P_{\text{Grid,ref}}$  is set to 654 kW, and Scenario 2:  $P_{\text{Grid,ref}}$  is set to 629 kW. Fig. 6.9 and Fig. 6.10 illustrate the CHIL results for the BESS charging Scenario 1 and Scenario 2, respectively. The power generated by the hybrid PV-WT system is found to be 679 kW. Therefore, the required power demand for the BESS is found to be -25 kW and -50 kW, respectively, for Scenario 1 and Scenario 2. From Fig. 6.9 and Fig. 6.10, it is evident that the BESS is able to absorb the required power to follow the desired  $P_{\text{Grid,ref}}$  with acceptable undesired deviation. This phenomenon supports the proposed BESS controller effectiveness, which is verified by the CHIL environment in this research. The negative power supplied by the BESS signifies that the battery operates in charging mode. Furthermore, the BESS SOC variation justifies the BESS is in charging state for both instances.

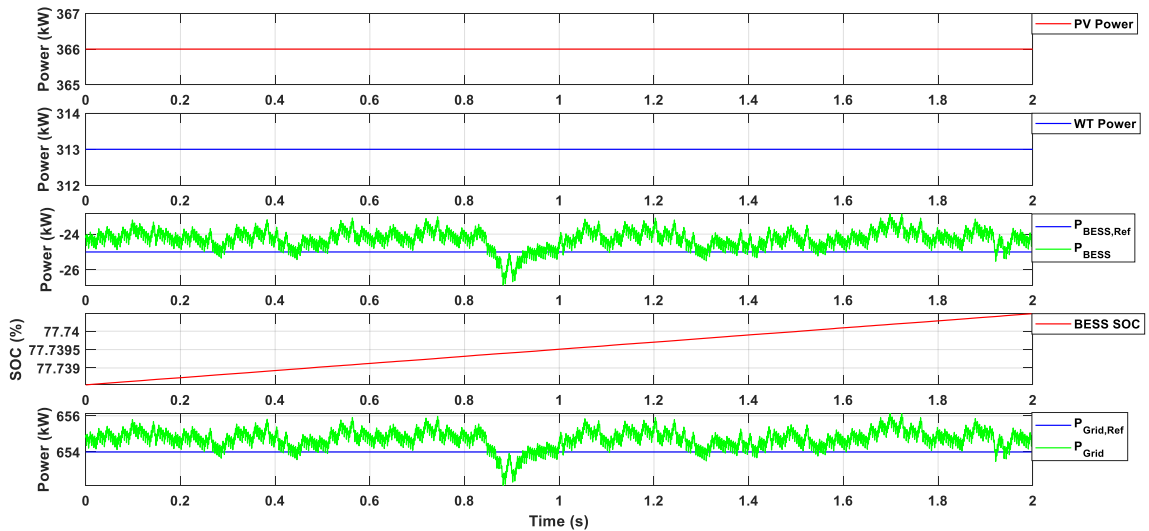


Figure 6.9: Scenario 1: BESS charging mechanism.

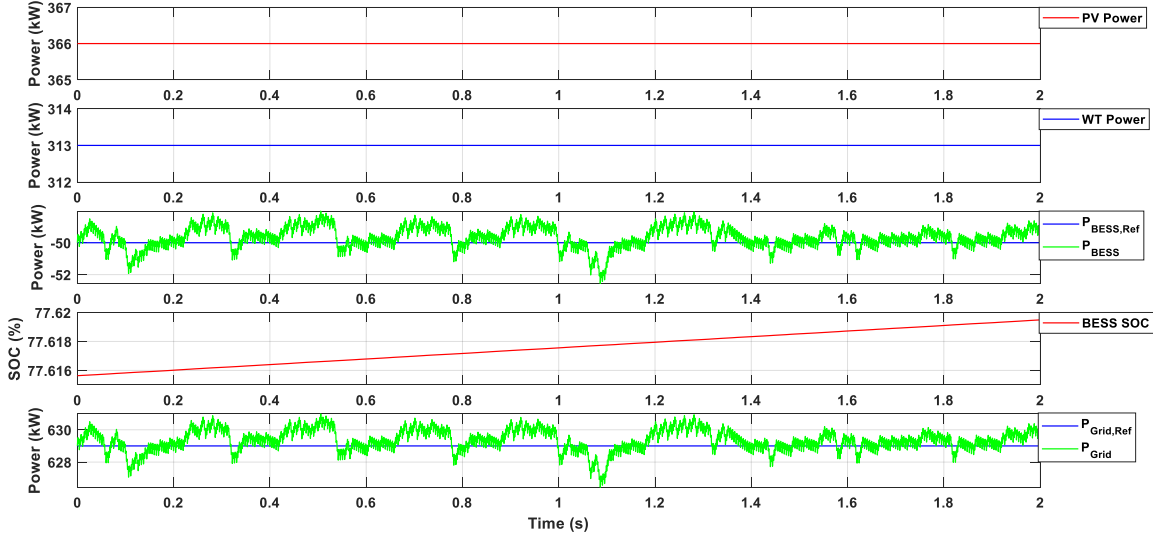


Figure 6.10: Scenario 2: BESS charging mechanism.

#### 6.4 Summary

This chapter presents a CHIL-based test system for testing the proposed BESS controller for dispatching the WSHPs power. The RTDS is used to model the WSHPs farm, and the BESS controller is designed in the C2000 F28379D launchpad. Here, the DSP, which is connected between the GTA0 card and the GTDI card in the RTDS interface boards, controls the duty ratio of the BESS power converter in order to follow the  $P_{\text{BESS,ref}}$ . The CHIL has been utilized to test the performance of the proposed BESS controller under various BESS charging-discharging scenarios in order to maintain the desired  $P_{\text{Grid,ref}}$ . The experimental results presented in this chapter verify the fact that the BESS is able to supply or absorb the necessary power to follow the  $P_{\text{Grid,ref}}$  utilizing the proposed control architecture. While justifying the proposed BESS controller in the CHIL platform, both the charging and discharging mechanisms of the BESS are taken into account.

## Chapter 7 Conclusions and Future Work

The conclusions of this dissertation can be summarized as follows:

- A dispatching scheme has been proposed to provide a pre-determined constant RE power to the utility grid from the intermittent RE framework. The proposed dispatching technique enables the RE architecture to be a reliable source of power for the utility that can be regulated in the same way as any other traditional generator, while also providing greater flexibility, particularly in grid operating economics, generation unit scheduling, and grid ancillary services (**Chapter 3, Chapter 4, and Chapter 5**).
- The wind speed and solar insolation are forecasted one-hour ahead of time by using a relatively small set of historical hourly wind speed and solar insolation data as well as a smaller number of input parameters for training the ANN model, which also significantly reduces the model complexity and computational burden (**Chapter 4 and Chapter 5**).
- The primary state of charge controller as a function of both battery and supercapacitor SOC in the HESS framework has been proposed to adjust the  $P_{\text{Grid,est}}$  at the start of each dispatching period, which aids in achieving the desired  $P_{\text{Grid,ref}}$  for each dispatching period. This controller would also make sure that the energy storage system finishes each dispatching period with the same SOC it started with (**Chapter 3, Chapter 4, and Chapter 5**).
- The particle swarm optimization approach has been implemented to seek the optimum value of the low pass filter time constant that yields the most cost-

effective HESS for hourly dispatching the RE power scheme (**Chapter 3**).

- The energy storage system life-cycle cost has been optimized by employing an advanced optimization technique to determine the optimal depth of discharge usage. In addition, after seeking the optimal value of depth of discharge for the ESS, one secondary state of charge control algorithm is also employed to regulate the ESS state of charge in the optimal range (**Chapter 5**).
- Detailed investigations of the annual ESS life-cycle cost have been conducted, including the actual wind speed and solar insolation data of four different days, representing each season (**Chapter 3, Chapter 5**).
- A cost comparison analysis has been presented to assess the impact of dispatching horizon selection on energy storage system cost estimation. The optimal scheduling for dispatchable RE power is determined by the ESS depth of discharge utilization levels, which is critical for minimizing the cost of a dispatchable scheme (**Chapter 4**).
- An isolated multiport converter has been developed for interfacing the RE framework to the utility and presents a comparative power loss analysis between the conventional TAB converter and the developed TAB-NPC converter for dispatching the RE power scheme (**Chapter 4**).
- An economic comparison has been presented utilizing the HOMER Pro software to develop a cost-effective ESS for an hourly PV power dispatching scenario (**Chapter 4**).
- The proposed BESS control algorithm has been verified for dispatching the WSHPS power, employing CHIL testing in the RTDS platform (**Chapter 6**).

Based on the results of this dissertation and recent research, future work to consolidate this research topic is recommended as follows:

- The technique presented in Chapter 3 to optimize the ESS cost for hourly dispatching WSHPS power does not consider the self-charging and discharging rates of the ESS. In the next step of this work, controllable charging and discharging rates of the ESS may be incorporated to further optimize the ESS sizing. Subsequently, it will help to reduce the expenditure associated with the ESS for hourly dispatching RE power scheme.
- In Chapter 4, HOMER Pro software is employed to conduct a techno-economic evaluation for hourly dispatching of PV power with an energy storage system. Further studies may investigate the techno-economic analysis for hourly dispatching of wind-solar hybrid power using HOMER Pro software. In addition, an economic comparison of the ESS for dispatching different types of RE sources, i.e., PV only, WSHPS (PV+WT), and WT only, should be conducted in the HOMER Pro platform to identify the superior RE framework to meet the load demand.
- The RE meteorological data (solar insolation and wind speed) is predicted one-hour ahead of time utilizing the feed-forward ANN model in Chapter 5. Further studies may be carried out to examine the impact of the forecasted meteorological data as an input to the WSHPS farm; correspondingly, the effect of prediction on the ESS cost analysis and HESS control architecture should be investigated. Furthermore, multiple local meteorological data such as wind speed, temperature, wind direction, and weather pressure values might be utilized as inputs to the ANN model. Subsequently, the performance of the mul-

tivariable ANN model to forecast the wind speed may be analyzed. Also, the hybrid method, i.e., a combination of the conventional statistical method and a machine learning method, may be explored to further improve the accuracy of wind speed and solar insolation forecasting. Furthermore, an idealized forecasting model is developed in [201], where the expected values and variance of the RE sources are assumed to be known over the next period of time, but the moment-by-moment source power injections are not assumed to be known in advance. This proposed model may be investigated in the future to improve the accuracy of the RE power prediction. Also, the multi-time scale coordinated economic dispatch model may be explored to optimize the cost of the WSHP architecture.

- Chapter 6 presents a CHIL-based test system for testing the proposed BESS controller for dispatching the WSHP power. In this dissertation, the frequency management technique is employed to decouple the power reference for the battery and SC in the HESS framework to exploit the technical benefits of both apparatuses. However, the SC built-in model is not available in the RSCAD software. In the future, an SC generic model may be built to verify the proposed frequency management approach utilizing the CHIL platform in the RTDS environment.

## Bibliography

- [1] Z. Zhongming, L. Linong, Y. Xiaona, Z. Wangqiang, L. Wei *et al.*, “World energy outlook special report 2013: Redrawing the energy climate map,” 2013.
- [2] REN21, “Renewables 2019 global status report,” 2019. [Online]. Available: <https://wedocs.unep.org/20.500.11822/28496>
- [3] B. K. Sovacool, “The intermittency of wind, solar, and renewable electricity generators: Technical barrier or rhetorical excuse?” *Utilities Policy*, vol. 17, no. 3-4, pp. 288–296, 2009.
- [4] J. L. Bernal-Agustín and R. Dufo-Lopez, “Simulation and optimization of stand-alone hybrid renewable energy systems,” *Renewable and sustainable energy reviews*, vol. 13, no. 8, pp. 2111–2118, 2009.
- [5] F. Ongaro, S. Saggini, and P. Mattavelli, “Li-ion battery-supercapacitor hybrid storage system for a long lifetime, photovoltaic-based wireless sensor network,” *IEEE Transactions on Power Electronics*, vol. 27, no. 9, pp. 3944–3952, 2012.
- [6] W. A. Omran, M. Kazerani, and M. Salama, “Investigation of methods for reduction of power fluctuations generated from large grid-connected photovoltaic systems,” *IEEE Transactions on Energy Conversion*, vol. 26, no. 1, pp. 318–327, 2010.
- [7] L. Bird, M. Milligan, and D. Lew, “Integrating variable renewable energy: Challenges and solutions,” National Renewable Energy Lab. (NREL), Golden, CO (United States), Tech. Rep., 2013.
- [8] W. Ur Rehman, A. R. Bhatti, A. B. Awan, I. A. Sajjad, A. A. Khan, R. Bo, S. S. Haroon, S. Amin, I. Tlili, and O. Oboreh-Snapps, “The penetration of renewable and sustainable energy in Asia: A state-of-the-art review on net-metering,” *IEEE Access*, 2020.
- [9] D. Gielen, F. Boshell, D. Saygin, M. D. Bazilian, N. Wagner, and R. Gorini, “The role of renewable energy in the global energy transformation,” *Energy Strategy Reviews*, vol. 24, pp. 38–50, 2019.
- [10] S. Koebrich, T. Bowen, and A. Sharpe, “2018 Renewable Energy Data Book,” *U.S. Department of Energy (DOE), Office of Energy Efficiency & Renewable Energy (EERE)*, 2018.
- [11] H. Bahar and J. Moorhouse, “Renewable Energy Market Update; Outlook for 2021 and 2022,” *International Energy Agency*, May 2021, [Online]. Available: <https://iea.blob.core.windows.net> [Accessed: 5-Nov-2021].



- [12] W. Thomas, “FY22 Budget Outlook: DOE Applied Energy RD&D,” *American Institute of Physics*, August 2021, [Online]. Available: <https://aip.org> [Accessed: 5-Nov-2021].
- [13] S. Ray, “Renewables account for most new U.S. electricity generating capacity in 2021,” *U.S. Energy Information Administration (EIA)*, January 2021, [Online]. Available: <https://www.eia.gov/todayinenergy/> [Accessed: 11-Nov-2021].
- [14] P. L. Joskow, “Challenges for wholesale electricity markets with intermittent renewable generation at scale: the us experience,” *Oxford Review of Economic Policy*, vol. 35, no. 2, pp. 291–331, 2019.
- [15] P. Denholm et al., “(2015). Overgeneration from Solar Energy in California: A Field Guide to the Duck Chart,” *National Renewable Energy Laboratory; NREL Report No. NREL/TP-6A20-65023*, 2015, [Online]. Available: <https://nrel.gov/publications> [Accessed: 7-Nov-2021].
- [16] S. Hussain, R. Al-ammari, A. Iqbal, M. Jafar, and S. Padmanaban, “Optimisation of hybrid renewable energy system using iterative filter selection approach,” *IET Renewable Power Generation*, vol. 11, no. 11, pp. 1440 – 1445, 2017.
- [17] A. Andreas and T. Stoffel, “(1981). NREL Solar Radiation Research Laboratory (SRRL): Baseline Measurement System (BMS),” *Golden, Colorado (Data); NREL Report No. DA-5500-56488*.
- [18] R. A. Badwawi, M. Abusara, and T. Mallick, “A review of hybrid solar PV and wind energy system,” *Smart Science*, vol. 3, no. 3, pp. 127–138, 2015.
- [19] M. A. Alotaibi and A. M. Eltamaly, “A smart strategy for sizing of hybrid renewable energy system to supply remote loads in Saudi Arabia,” *Energies*, vol. 14, no. 21, p. 7069, 2021.
- [20] H. K. Trabish, “Solar Wind Storage Developers ‘gearing up’ as Hybrid Projects Edge to Market,” *Utility Dive*, July 2019, [Online]. Available: <https://www.utilitydive.com> [Accessed: 30-Sep-2020].
- [21] E. Bellini, “Danish Fjord to Host 400 MW of Solar,” *PV magazine International*, March 2020, [Online]. Available: <https://www.pv-magazine.com> [Accessed: 30-Sep-2020].
- [22] R. Walton, “NextEra Inks 700 MW Wind Solar Battery Project, Largest in the US,” *Utility Dive*, July 2019, [Online]. Available: <https://www.utilitydive.com>. [Accessed: 30-Sep-2020].
- [23] S. Munuswamy, K. Nakamura, and A. Katta, “Comparing the Cost of Electricity Sourced from a Fuel Cell-based Renewable Energy System and the National Grid to Electrify a Rural Health Centre in India: A Case Study,” *Renewable Energy*, vol. 36, no. 11, pp. 2978 – 2983, 2011.

- [24] C. Li, X. Zhu, G. Cao, S. Sui, and M. Hu, “Dynamic Modeling and Sizing Optimization of Stand-alone Photovoltaic Power Systems using Hybrid Energy Storage Technology,” *Renewable Energy*, vol. 34, no. 3, pp. 815 – 826, 2009.
- [25] G. Graditi, S. Favuzza, and E. R. Sanseverino, “Technical, Environmental and Economical Aspects of Hybrid System including Renewables and Fuel Cells,” in *International Symposium on Power Electronics, Electrical Drives, Automation and Motion, 2006. SPEEDAM 2006.*, May 2006, pp. 531–536.
- [26] C. Zhu, F. Liu, S. Hu, and S. Liu, “Research on Capacity Optimization of PV-Wind-Diesel-Battery Hybrid Generation System,” in *2018 International Power Electronics Conference (IPEC-Niigata 2018 -ECCE Asia)*, 2018, pp. 3052–3057.
- [27] A. M. Eltamaly and A. A. Al-Shamma’a, “Optimal configuration for isolated hybrid renewable energy systems,” *Journal of Renewable and Sustainable Energy*, vol. 8, no. 4, p. 045502, 2016.
- [28] M. H. Nehrir, C. Wang, K. Strunz, H. Aki, R. Ramakumar, J. Bing, Z. Miao, and Z. Salameh, “A review of hybrid renewable/alternative energy systems for electric power generation: Configurations, control, and applications,” *IEEE Transactions on Sustainable Energy*, vol. 2, no. 4, pp. 392–403, 2011.
- [29] K. Anoune, M. Bouya, A. Astito, and A. B. Abdellah, “Sizing Methods and Optimization Techniques for PV-Wind based Hybrid Renewable Energy System: A Review,” *Renewable and Sustainable Energy Reviews*, vol. 93, pp. 652 – 673, 2018.
- [30] L. Lu, H. Yang, and J. Burnett, “Investigation on Wind Power Potential on Hong Kong Islands—an Analysis of Wind Power and Wind Turbine Characteristics,” *Renewable Energy*, vol. 27, no. 1, pp. 1 – 12, 2002.
- [31] R. Carnegie, D. Gotham, D. Nderitu, and P. Preckel, “Utility Scale Energy Storage Systems Benefits, Applications, and Technologies,” *State Utility Forecasting Group*, June 2013.
- [32] “SCE Unveils Largest Battery Energy Storage Project in North America,” *Edison International*, [Online]. Available: <https://newsroom.edison.com> [Accessed: 30-Sep-2020].
- [33] H. Chen, T. N. Cong, W. Yang, C. Tan, Y. Li, and Y. Ding, “Progress in Electrical Energy Storage System: A Critical Review,” *Progress in Natural Science*, vol. 19, no. 3, pp. 291 – 312, 2009.
- [34] B. Zakeri and S. Syri, “Electrical Energy Storage Systems: A Comparative Life Cycle Cost Analysis,” *Renewable and Sustainable Energy Reviews*, vol. 42, pp. 569 – 596, 2015.

- [35] S. K. Kollimalla, M. K. Mishra, and N. L. Narasamma, "Design and Analysis of Novel Control Strategy for Battery and Supercapacitor Storage System," *IEEE Transactions on Sustainable Energy*, vol. 5, no. 4, pp. 1137–1144, 2014.
- [36] B. R. Ravada, N. R. Tummuru, and B. N. L. Ande, "Photovoltaic-wind and hybrid energy storage integrated multisource converter configuration-based grid-interactive microgrid," *IEEE Transactions on Industrial Electronics*, vol. 68, no. 5, pp. 4004–4013, 2020.
- [37] A. Kuperman and I. Aharon, "Battery–Ultracapacitor Hybrids for Pulsed Current Loads: A Review," *Renewable and Sustainable Energy Reviews*, vol. 15, no. 2, pp. 981 – 992, 2011.
- [38] T. Ma, H. Yang, and L. Lu., "Development of Hybrid Battery-Supercapacitor Energy Storage for Remote Area Renewable Energy Systems," *Applied Energy*, pp. 153:56–62, 2015.
- [39] R. A. Dougal, S. Liu, and R. E. White, "Power and Life Extension of Battery-Ultracapacitor Hybrids," *IEEE Transactions on Components and Packaging Technologies*, vol. 25, no. 1, pp. 120–131, 2002.
- [40] J. P. Zheng, T. R. Jow, and M. S. Ding, "Hybrid Power Sources for Pulsed Current Applications," *IEEE Transactions on Aerospace and Electronic Systems*, vol. 37, no. 1, pp. 288–292, 2001.
- [41] Z. Song, H. Hofmann, J. Li, X. Han, X. Zhang, and M. Ouyang, "A Comparison Study of Different Semi-active Hybrid Energy Storage System Topologies for Electric Vehicles," *Journal of Power Sources*, vol. 274, pp. 400 – 411, 2015.
- [42] Y. Wang, W. Wang, Y. Zhao, L. Yang, and W. Chen, "A Fuzzy-Logic Power Management Strategy Based on Markov Random Prediction for Hybrid Energy Storage Systems," *Energies*, vol. 9, p. 25, 2016.
- [43] W. Li, G. Joós, and J. Bélanger, "Real-time simulation of a wind turbine generator coupled with a battery supercapacitor energy storage system," *IEEE Transactions on Industrial Electronics*, vol. 57, no. 4, pp. 1137–1145, 2009.
- [44] Lijun Gao, R. A. Dougal, and Shengyi Liu, "Power Enhancement of an Actively Controlled Battery/Ultracapacitor Hybrid," *IEEE Transactions on Power Electronics*, vol. 20, no. 1, pp. 236–243, 2005.
- [45] A. Khaligh and Z. Li, "Battery, Ultracapacitor, Fuel Cell, and Hybrid Energy Storage Systems for Electric, Hybrid Electric, Fuel Cell, and Plug-In Hybrid Electric Vehicles: State of the Art," *IEEE Transactions on Vehicular Technology*, vol. 59, no. 6, pp. 2806–2814, 2010.
- [46] A. Kuperman, I. Aharon, S. Malki, and A. Kara, "Design of a Semiactive Battery-Ultracapacitor Hybrid Energy Source," *IEEE Transactions on Power Electronics*, vol. 28, no. 2, pp. 806–815, 2013.

- [47] E. Jamshidpour, S. Saadate, and P. Poure, “Energy Management and Control of a Stand-alone Photovoltaic/Ultra Capacitor/Battery Microgrid,” in *2015 IEEE Jordan Conference on Applied Electrical Engineering and Computing Technologies (AEECT)*, 2015, pp. 1–6.
- [48] S. M. Lukic, S. G. Wirasingha, F. Rodriguez, J. Cao, and A. Emadi, “Power Management of an Ultracapacitor/Battery Hybrid Energy Storage System in an HEV,” in *2006 IEEE Vehicle Power and Propulsion Conference*, 2006, pp. 1–6.
- [49] J. Cao and A. Emadi, “A New Battery/UltraCapacitor Hybrid Energy Storage System for Electric, Hybrid, and Plug-In Hybrid Electric Vehicles,” *IEEE Transactions on Power Electronics*, vol. 27, no. 1, pp. 122–132, 2012.
- [50] J. J. Soon and K.-S. Low, “Optimizing photovoltaic model for different cell technologies using a generalized multidimension diode model,” *IEEE Transactions on Industrial Electronics*, vol. 62, no. 10, pp. 6371–6380, 2015.
- [51] M. C. Cavalcanti, F. Bradaschia, A. J. do Nascimento, G. M. Azevedo, and E. J. Barbosa, “Hybrid maximum power point tracking technique for PV modules based on a double-diode model,” *IEEE Transactions on Industrial Electronics*, vol. 68, no. 9, pp. 8169–8181, 2020.
- [52] H. Patel and V. Agarwal, “Maximum power point tracking scheme for PV systems operating under partially shaded conditions,” *IEEE transactions on industrial electronics*, vol. 55, no. 4, pp. 1689–1698, 2008.
- [53] F. Jahanbani Ardakani, G. Riahy, and M. Abedi, “Design of an Optimum Hybrid Renewable Energy System Considering Reliability Indices,” in *2010 18<sup>th</sup> Iranian Conference on Electrical Engineering*, May 2010, pp. 842–847.
- [54] M. Yousefi, A. Hajizadeh, and M. N. Soltani, “A comparison study on stochastic modeling methods for home energy management systems,” *IEEE Transactions on Industrial Informatics*, vol. 15, no. 8, pp. 4799–4808, 2019.
- [55] A. M. Muzathik, “Photovoltaic Modules Operating Temperature Estimation Using a Simple Correlation,” in *International Journal of Energy Engineering*, vol. 4, Aug. 2014, pp. 151–158.
- [56] J. A. Kratochvil, W. E. Boyson, and D. L. King, “Photovoltaic array performance model.” Sandia National Laboratories, Tech. Rep., 2004.
- [57] P. Gilman, A. Dobos, N. DiOrio, J. Freeman, S. Janzou, and D. Ryberg, “Sam photovoltaic model technical reference update,” *NREL: Golden, CO, USA*, 2018.
- [58] C. Bueno and J. Carta, “Technical–Economic Analysis of Wind-Powered Pumped Hydrostorage Systems. Part I: Model Development,” *Solar Energy*, vol. 78, no. 3, pp. 382 – 395, 2005.

- [59] F. O. Hocaoglu, Ömer N. Gerek, and M. Kurban, “A Novel Hybrid (Wind–Photovoltaic) System Sizing Procedure,” *Solar Energy*, vol. 83, no. 11, pp. 2019–2028, 2009.
- [60] B. Singh, G. Bhuvaneswari *et al.*, “Sensorless SynRG based variable speed wind generator and single-stage solar pv array integrated grid system with maximum power extraction capability,” *IEEE Transactions on Industrial Electronics*, vol. 67, no. 9, pp. 7529–7539, 2019.
- [61] S. H. Alalwan and J. W. Kimball, “Optimal Sizing of a Wind/Solar/Battery Hybrid Microgrid System Using the Forever Power Method,” in *2015 Seventh Annual IEEE Green Technologies Conference*, April 2015, pp. 29–35.
- [62] B. Ould Bilal, V. Sambou, P. A. Ndiaye, C. M. F. Kébé, and M. Ndongo, “Multi-objective Design of PV-Wind-Batteries Hybrid Systems by Minimizing the Annualized Cost System and the Loss of Power Supply Probability (LPSP),” in *2013 IEEE International Conference on Industrial Technology (ICIT)*, Feb 2013, pp. 861–868.
- [63] G. Ofualagba and E. U. Ubeku, “Wind Energy Conversion System- Wind Turbine Modeling,” in *2008 IEEE Power and Energy Society General Meeting - Conversion and Delivery of Electrical Energy in the 21<sup>st</sup> Century*, July 2008, pp. 1–8.
- [64] C. N. Bhende, S. Mishra, and S. G. Malla, “Permanent Magnet Synchronous Generator-Based Standalone Wind Energy Supply System,” *IEEE Transactions on Sustainable Energy*, vol. 2, no. 4, pp. 361–373, Oct 2011.
- [65] D. Verma, S. Nema, A. Shandilya, and S. K. Dash, “Maximum power point tracking (mppt) techniques: Recapitulation in solar photovoltaic systems,” *Renewable and Sustainable Energy Reviews*, vol. 54, pp. 1018–1034, 2016.
- [66] M. A. Ramli, S. Twaha, K. Ishaque, and Y. A. Al-Turki, “A review on maximum power point tracking for photovoltaic systems with and without shading conditions,” *Renewable and Sustainable Energy Reviews*, vol. 67, pp. 144–159, 2017.
- [67] B. Subudhi and R. Pradhan, “A comparative study on maximum power point tracking techniques for photovoltaic power systems,” *IEEE Transactions on Sustainable Energy*, vol. 4, no. 1, pp. 89–98, 2013.
- [68] A. R. Jordehi, “Maximum power point tracking in photovoltaic (PV) systems: A review of different approaches,” *Renewable and Sustainable Energy Reviews*, vol. 65, pp. 1127–1138, 2016.
- [69] A. R. Reisi, M. H. Moradi, and S. Jamasb, “Classification and comparison of maximum power point tracking techniques for photovoltaic system: A review,” *Renewable and sustainable energy reviews*, vol. 19, pp. 433–443, 2013.

- [70] D.-Y. Li, Y.-D. Song, Z.-X. Gan, and W.-C. Cai, "Fault-tolerant optimal tip-speed-ratio tracking control of wind turbines subject to actuation failures," *IEEE transactions on industrial electronics*, vol. 62, no. 12, pp. 7513–7523, 2015.
- [71] K.-H. Kim, T. L. Van, D.-C. Lee, S.-H. Song, and E.-H. Kim, "Maximum output power tracking control in variable-speed wind turbine systems considering rotor inertial power," *IEEE transactions on industrial electronics*, vol. 60, no. 8, pp. 3207–3217, 2012.
- [72] S. M. R. Kazmi, H. Goto, H.-J. Guo, and O. Ichinokura, "A novel algorithm for fast and efficient speed-sensorless maximum power point tracking in wind energy conversion systems," *IEEE transactions on industrial electronics*, vol. 58, no. 1, pp. 29–36, 2010.
- [73] S. Musunuri and H. Ginn, "Comprehensive review of wind energy maximum power extraction algorithms," in *2011 IEEE power and energy society general meeting*. IEEE, 2011, pp. 1–8.
- [74] M. A. Abdullah, A. Yatim, C. W. Tan, and R. Saidur, "A review of maximum power point tracking algorithms for wind energy systems," *Renewable and sustainable energy reviews*, vol. 16, no. 5, pp. 3220–3227, 2012.
- [75] A. A. Al-Shamma'a and K. E. Addoweesh, "Optimum Sizing of Hybrid PV/Wind/Battery/Diesel System Considering Wind Turbine Parameters using Genetic Algorithm," in *2012 IEEE International Conference on Power and Energy (PECon)*, 2012, pp. 121–126.
- [76] T. Kovaltchouk, H. Ben Ahmed, B. Multon, J. Aubry, and P. Venet, "An Aging-Aware Life Cycle Cost Comparison between Supercapacitors and Li-ion Batteries to Smooth Direct Wave Energy Converter Production," in *2015 IEEE Eindhoven PowerTech*, 2015, pp. 1–6.
- [77] J.-K. Eom, S.-R. Lee, E.-J. Ha, B.-Y. Choi, and C.-Y. Won, "Economic Dispatch Algorithm Considering Battery Degradation Characteristic of Energy Storage System with PV System," in *2014 17<sup>th</sup> International Conference on Electrical Machines and Systems (ICEMS)*, 2014, pp. 849–854.
- [78] T. Kovaltchouk, B. Multon, H. Ben Ahmed, J. Aubry, and P. Venet, "Enhanced Aging Model for Supercapacitors taking into account Power Cycling: Application to the Sizing of an Energy Storage System in a Direct Wave Energy Converter," *IEEE Transactions on Industry Applications*, vol. 51, no. 3, pp. 2405 – 2414, May 2015.
- [79] X. Liu, P. C. Loh, P. Wang, and F. Blaabjerg, "A Direct Power Conversion Topology for Grid Integration of Hybrid AC/DC Energy Resources," *IEEE Transactions on Industrial Electronics*, vol. 60, no. 12, pp. 5696–5707, 2013.

- [80] F. Dincer and M. Meral, “Critical Factors that Affecting Efficiency of Solar Cells,” *Smart Grid and Renewable Energy*, vol. 1, no. 1, pp. 47–50, 2010.
- [81] K. Krishnamurthy, S. Padmanaban, F. Blaabjerg, R. B. Neelakandan, and K. R. Prabhu, “Power Electronic Converter Configurations Integration with Hybrid Energy Sources – A Comprehensive Review for State-of-the-Art in Research,” *Electric Power Components and Systems*, vol. 47, no. 18, pp. 1623–1650, 2019.
- [82] X. Li, D. Hui, and X. Lai, “Battery Energy Storage Station (BESS)-Based Smoothing Control of Photovoltaic (PV) and Wind Power Generation Fluctuations,” *IEEE Transactions on Sustainable Energy*, vol. 4, no. 2, pp. 464–473, 2013.
- [83] S. Kim, B. Kang, S. Bae, and J. Park, “Application of SMES and Grid Code Compliance to Wind/Photovoltaic Generation System,” *IEEE Transactions on Applied Superconductivity*, vol. 23, no. 3, 2013.
- [84] M. Kalantar and S. Mousavi G., “Dynamic Behavior of a Stand-alone Hybrid Power Generation System of Wind Turbine, Microturbine, Solar Array and Battery Storage,” *Applied Energy*, vol. 87, no. 10, pp. 3051 – 3064, 2010.
- [85] D. Wu, F. Tang, T. Dragicevic, J. C. Vasquez, and J. M. Guerrero, “A Control Architecture to Coordinate Renewable Energy Sources and Energy Storage Systems in Islanded Microgrids,” *IEEE Transactions on Smart Grid*, vol. 6, no. 3, pp. 1156–1166, 2015.
- [86] E. Kabalci, “Design and Analysis of a Hybrid Renewable Energy Plant with Solar and Wind Power,” *Energy Conversion and Management*, vol. 72, pp. 51–59, 2013.
- [87] S. Kim, J. Jeon, C. Cho, J. Ahn, and S. Kwon, “Dynamic Modeling and Control of a Grid-Connected Hybrid Generation System With Versatile Power Transfer,” *IEEE Transactions on Industrial Electronics*, vol. 55, no. 4, pp. 1677–1688, 2008.
- [88] L. Xu, X. Ruan, C. Mao, B. Zhang, and Y. Luo, “An improved optimal sizing method for wind-solar-battery hybrid power system,” *IEEE Transactions on Sustainable Energy*, vol. 4, no. 3, pp. 774–785, 2013.
- [89] H. Ghoddami, M. B. Delghavi, and A. Yazdani, “An Integrated Wind-Photovoltaic-Battery System with Reduced Power-Electronic Interface and Fast Control for Grid-tied and Off-grid Applications,” *Renewable Energy*, vol. 45, pp. 128 – 137, 2012.
- [90] P. Roy and J. He, “Grid-Connected Hybrid Wind-Solar Farm Hourly Dispatching with Battery and Supercapacitor Energy Storage,” in *IECON 2020 The 46<sup>th</sup> Annual Conference of the IEEE Industrial Electronics Society*, 2020, pp. 1831–1836.

- [91] J. Hui, A. Bakhshai, and P. K. Jain, “A Hybrid Wind-Solar Energy System: A New Rectifier Stage Topology,” in *2010 Twenty-Fifth Annual IEEE Applied Power Electronics Conference and Exposition (APEC)*, 2010, pp. 155–161.
- [92] W. Jiang and B. Fahimi, “Multiport Power Electronic Interface—Concept, Modeling, and Design,” *IEEE Transactions on Power Electronics*, vol. 26, no. 7, pp. 1890–1900, 2011.
- [93] W. Jiang and B. Fahimi, “Multi-port Power Electric Interface for Renewable Energy Sources,” in *2009 Twenty-Fourth Annual IEEE Applied Power Electronics Conference and Exposition*, 2009, pp. 347–352.
- [94] J. Zeng, W. Qiao, L. Qu, and Y. Jiao, “An Isolated Multiport DC–DC Converter for Simultaneous Power Management of Multiple Different Renewable Energy Sources,” *IEEE Journal of Emerging and Selected Topics in Power Electronics*, vol. 2, no. 1, pp. 70–78, 2014.
- [95] Z. Qian, O. Abdel-Rahman, and I. Batarseh, “An Integrated Four-Port DC/DC Converter for Renewable Energy Applications,” *IEEE Transactions on Power Electronics*, vol. 25, no. 7, pp. 1877–1887, 2010.
- [96] C. Chen, C. Liao, K. Chen, and Y. Chen, “Modeling and Controller Design of a Semiisolated Multiinput Converter for a Hybrid PV/Wind Power Charger System,” *IEEE Transactions on Power Electronics*, vol. 30, no. 9, pp. 4843–4853, 2015.
- [97] Z. Qian, O. Abdel-Rahman, H. Hu, and I. Batarseh, “A Zero-voltage Switching Four-port Integrated DC/DC Converter,” in *Intelec 2010*, 2010, pp. 1–8.
- [98] S. H. Hosseini, S. K. Haghghian, S. Danyali, and H. Aghazadeh, “Multi-input DC Boost Converter Supplied by a Hybrid PV/Wind Turbine Power Systems for Street Lighting Application Connected to the Grid,” in *2012 47<sup>th</sup> International Universities Power Engineering Conference (UPEC)*, 2012, pp. 1–6.
- [99] B. Mangu, S. Akshatha, D. Suryanarayana, and B. G. Fernandes, “Grid-Connected PV-Wind-Battery-Based Multi-Input Transformer-Coupled Bidirectional DC-DC Converter for Household Applications,” *IEEE Journal of Emerging and Selected Topics in Power Electronics*, vol. 4, no. 3, pp. 1086–1095, 2016.
- [100] N. K. Reddi, M. R. Ramteke, H. M. Suryawanshi, K. Kothapalli, and S. P. Gawande, “An Isolated Multi-Input ZCS DC–DC Front-End-Converter Based Multilevel Inverter for the Integration of Renewable Energy Sources,” *IEEE Transactions on Industry Applications*, vol. 54, no. 1, pp. 494–504, 2018.
- [101] T. Ishikawa, “Grid-connected Photovoltaic Power Systems: Survey of Inverter and Related Protection Equipments,” *International Energy Agency (IEA)*, 2002.



- [102] M. Calais and V. G. Agelidis, “Multilevel Converters for Single-phase Grid Connected Photovoltaic Systems-an Overview,” in *IEEE International Symposium on Industrial Electronics. Proceedings. ISIE’98 (Cat. No.98TH8357)*, vol. 1, 1998, pp. 224–229.
- [103] K. Zeb, W. Uddin, M. A. Khan, Z. Ali, M. U. Ali, N. Christofides, and H. Kim, “A Comprehensive Review on Inverter Topologies and Control Strategies for Grid Connected Photovoltaic System,” *Renewable and Sustainable Energy Reviews*, vol. 94, pp. 1120 – 1141, 2018.
- [104] B. K. Santhoshi, K. M. Sundaram, S. Padmanaban, J. B. Holm-Nielsen, and K. k. Prabhakaran, “Critical Review of PV Grid-Tied Inverters,” in *Energies*, vol. 12 (10), 2019, p. 1921.
- [105] M. Schweizer et. al, “Design and Implementation of a Highly Efficient Three-Level T-Type Converter for Low-Voltage Applications,” *IEEE Transactions on Power Electronics*, vol. 28, no. 2, pp. 899–907, 2013.
- [106] P. Kala and S. Arora, “A comprehensive study of classical and hybrid multilevel inverter topologies for renewable energy applications,” *Renewable and Sustainable Energy Reviews*, vol. 76, pp. 905–931, 2017.
- [107] M. Kurtoğlu, F. Eroğlu, A. O. Arslan, and A. M. Vural, “Recent contributions and future prospects of the modular multilevel converters: A comprehensive review,” *International Transactions on Electrical Energy Systems*, vol. 29, no. 3, p. e2763, 2019.
- [108] J. He, Q. Yang, and Z. Wang, “On-line fault diagnosis and fault-tolerant operation of modular multilevel converters—a comprehensive review,” *CES Transactions on Electrical Machines and Systems*, vol. 4, no. 4, pp. 360–372, 2020.
- [109] N. S. Hasan, N. Rosmin, D. A. A. Osman, A. H. Musta’amal *et al.*, “Reviews on multilevel converter and modulation techniques,” *Renewable and Sustainable Energy Reviews*, vol. 80, pp. 163–174, 2017.
- [110] M. Vijeh, M. Rezanejad, E. Samadaei, and K. Bertilsson, “A general review of multilevel inverters based on main submodules: Structural point of view,” *IEEE Transactions on Power Electronics*, vol. 34, no. 10, pp. 9479–9502, 2019.
- [111] M. Malinowski, K. Gopakumar, J. Rodriguez, and M. A. Perez, “A survey on cascaded multilevel inverters,” *IEEE Transactions on industrial electronics*, vol. 57, no. 7, pp. 2197–2206, 2009.
- [112] S. Debnath, “Control of modular multilevel converters for grid integration of full-scale wind energy conversion systems,” Ph.D. dissertation, Purdue University, 2015.

- [113] J. Wang, R. Burgos, and D. Boroyevich, “A survey on the modular multilevel converters—modeling, modulation and controls,” in *2013 IEEE Energy Conversion Congress and Exposition*. IEEE, 2013, pp. 3984–3991.
- [114] A. Rockhill, M. Liserre, R. Teodorescu, and P. Rodriguez, “Grid-filter design for a multimegawatt medium-voltage voltage-source inverter,” *IEEE Transactions on Industrial Electronics*, vol. 58, no. 4, pp. 1205–1217, 2010.
- [115] Y. Tang, P. C. Loh, P. Wang, F. H. Choo, F. Gao, and F. Blaabjerg, “Generalized design of high performance shunt active power filter with output LCL filter,” *IEEE Transactions on Industrial Electronics*, vol. 59, no. 3, pp. 1443–1452, 2011.
- [116] J. Bauer, “Single Phase Voltage Source Inverter Photovoltaic Application.” in *Acta Polytechnica*, vol. 50, no. 4, 2010, pp. 7–11.
- [117] P. Channegowda and V. John, “Filter optimization for grid interactive voltage source inverters,” *IEEE Transactions on Industrial Electronics*, vol. 57, no. 12, pp. 4106–4114, 2010.
- [118] P. Roy and J. He, “Hourly Dispatching Utility-Scale Solar PV Power with Megawatt Multilevel Grid Inverter,” in *2021 IEEE Kansas Power and Energy Conference (KPEC)*, 2021, pp. 1–6.
- [119] N. Tutkun, N. Çelebi, and N. Bozok, “Optimum Unit Sizing of Wind-PV-Battery System Components in a Typical Residential Home,” in *2016 International Renewable and Sustainable Energy Conference (IRSEC)*, 2016, pp. 432–436.
- [120] R. Siddaiah and R. Saini, “A Review on Planning, Configurations, Modeling and Optimization Techniques of Hybrid Renewable Energy Systems for Off Grid Applications,” *Renewable and Sustainable Energy Reviews*, vol. 58, pp. 376–396, 2016.
- [121] B. Zhao, X. Zhang, J. Chen, C. Wang, and L. Guo, “Operation Optimization of Standalone Microgrids Considering Lifetime Characteristics of Battery Energy Storage System,” *IEEE Transactions on Sustainable Energy*, vol. 4, no. 4, pp. 934–943, 2013.
- [122] L. Wang and C. Singh, “Multicriteria Design of Hybrid Power Generation Systems Based on a Modified Particle Swarm Optimization Algorithm,” *IEEE Transactions on Energy Conversion*, vol. 24, no. 1, pp. 163–172, 2009.
- [123] S. Sinha and S. Chandel, “Review of Recent Trends in Optimization Techniques for Solar Photovoltaic–Wind Based Hybrid Energy Systems,” *Renewable and Sustainable Energy Reviews*, vol. 50, pp. 755–769, 2015.

- [124] H. Yang, W. Zhou, L. Lu, and Z. Fang, "Optimal Sizing Method for Stand-alone Hybrid Solar–Wind System with LPSP Technology by using Genetic Algorithm," *Solar Energy*, vol. 82, no. 4, pp. 354 – 367, 2008.
- [125] B. Ould Bilal, V. Sambou, P. Ndiaye, C. Kébé, and M. Ndongo, "Optimal Design of a Hybrid Solar–Wind–Battery System Using the Minimization of the Annualized Cost System and the Minimization of the Loss of Power Supply Probability (LPSP)," *Renewable Energy*, vol. 35, no. 10, pp. 2388 – 2390, 2010.
- [126] Y. Cheng, M. Chuang, Y. Liu, S. Wang, and Z. Yang, "A Particle Swarm Optimization based Power Dispatch Algorithm with Roulette Wheel Re-distribution Mechanism for Equality Constraint," *Renewable Energy*, vol. 88, pp. 58 – 72, 2016.
- [127] P. Paliwal, N. Patidar, and R. Nema, "Determination of Reliability Constrained Optimal Resource Mix for an Autonomous Hybrid Power System using Particle Swarm Optimization," *Renewable Energy*, vol. 63, pp. 194 – 204, 2014.
- [128] H. Borhanazad, S. Mekhilef, V. Gounder Ganapathy, M. Modiri-Delshad, and A. Mirtaheeri, "Optimization of Micro-grid System using MOPSO," *Renewable Energy*, vol. 71, pp. 295 – 306, 2014.
- [129] A. R. Prasad and E. Natarajan, "Optimization of Integrated Photovoltaic–Wind Power Generation Systems with Battery Storage," *Energy*, vol. 31, no. 12, pp. 1943 – 1954, 2006.
- [130] U. Boonbumroong, N. Pratinthong, S. Thepa, C. Jivacate, and W. Pridasawas, "Particle Swarm Optimization for AC-coupling Stand alone Hybrid Power Systems," *Solar Energy*, vol. 85, no. 3, pp. 560 – 569, 2011.
- [131] B. Y. Ekren and O. Ekren, "Simulation Based Size Optimization of a PV/Wind Hybrid Energy Conversion System with Battery Storage Under Various Load and Auxiliary Energy Conditions," *Applied Energy*, vol. 86, no. 9, pp. 1387 – 1394, 2009.
- [132] H. Yang, Z. Wei, and L. Chengzhi, "Optimal Design and Techno-economic Analysis of a Hybrid Solar–Wind Power Generation System," *Applied Energy*, vol. 86, no. 2, pp. 163 – 169, 2009.
- [133] D. P. Clarke, Y. M. Al-Abdeli, and G. Kothapalli, "Multi-objective Optimisation of Renewable Hybrid Energy Systems with Desalination," *Energy*, vol. 88, pp. 457 – 468, 2015.
- [134] M. B. Shadmand and R. S. Balog, "Multi-Objective Optimization and Design of Photovoltaic-Wind Hybrid System for Community Smart DC Microgrid," *IEEE Transactions on Smart Grid*, vol. 5, no. 5, pp. 2635–2643, 2014.

- [135] F. Giraud and Z. M. Salameh, "Steady-state Performance of a Grid-connected Rooftop Hybrid Wind-Photovoltaic Power System with Battery Storage," *IEEE Transactions on Energy Conversion*, vol. 16, no. 1, pp. 1–7, 2001.
- [136] R. Hosseinalizadeh, H. Shakouri G, M. S. Amalnick, and P. Taghipour, "Economic Sizing of a Hybrid (PV–WT–FC) Renewable Energy System (HRES) for Stand-alone Usages by an Optimization-simulation Model: Case Study of Iran," *Renewable and Sustainable Energy Reviews*, vol. 54, pp. 139 – 150, 2016.
- [137] A. Kaabeche, M. Belhamel, and R. Ibtiouen, "Sizing Optimization of Grid-independent Hybrid Photovoltaic/Wind Power Generation System," *Energy*, vol. 36, no. 2, pp. 1214 – 1222, 2011.
- [138] A. Hassan, M. Kandil, M. Saadawi, and M. Saeed, "Modified Particle Swarm Optimisation Technique for Optimal Design of Small Renewable Energy System Supplying a Specific Load at Mansoura University," in *IET Renewable Power Generation*, vol. 9, no. 5, 2015, pp. 474–483.
- [139] A. Maleki, M. Ameri, and F. Keynia, "Scrutiny of Multifarious Particle Swarm Optimization for Finding the Optimal Size of a PV/Wind/Battery Hybrid System," *Renewable Energy*, vol. 80, pp. 552 – 563, 2015.
- [140] H. Baghaee, M. Mirsalim, G. Gharehpetian, and H. Talebi, "Reliability/cost-based Multi-objective Pareto Optimal Design of Stand-alone Wind/PV/FC Generation Microgrid System," *Energy*, vol. 115, pp. 1022 – 1041, 2016.
- [141] A. Askarzadeh and L. dos Santos Coelho, "A Novel Framework for Optimization of a Grid Independent Hybrid Renewable Energy System: A Case Study of Iran," *Solar Energy*, vol. 112, pp. 383 – 396, 2015.
- [142] B. Zhao, X. Zhang, P. Li, K. Wang, M. Xue, and C. Wang, "Optimal Sizing, Operating Strategy and Operational Experience of a Stand-alone Microgrid on Dongfushan Island," *Applied Energy*, vol. 113, pp. 1656 – 1666, 2014.
- [143] A. Ogunjuyigbe, T. Ayodele, and O. Akinola, "Optimal Allocation and Sizing of PV/Wind/Split-Diesel/Battery Hybrid Energy System for Minimizing Life Cycle Cost, Carbon Emission and Dump Energy of Remote Residential Building," *Applied Energy*, vol. 171, pp. 153 – 171, 2016.
- [144] J. Zeng, M. Li, J. F. Liu, J. Wu, and H. W. Ngan, "Operational Optimization of a Stand-alone Hybrid Renewable Energy Generation System Based on an Improved Genetic Algorithm," in *IEEE PES General Meeting*, 2010, pp. 1–6.
- [145] A. Maleki and A. Askarzadeh, "Artificial Bee Swarm Optimization for Optimum Sizing of a Stand-alone PV/WT/FC Hybrid System Considering LPSP Concept," *Solar Energy*, vol. 107, pp. 227 – 235, 2014.

- [146] S. Tito, T. Lie, and T. Anderson, “Optimal Sizing of a Wind-Photovoltaic-Battery Hybrid Renewable Energy System Considering Socio-demographic Factors,” *Solar Energy*, vol. 136, pp. 525 – 532, 2016.
- [147] P. Roy, J. He, and Y. Liao, “Cost Minimization of Battery-Supercapacitor Hybrid Energy Storage for Hourly Dispatching Wind-Solar Hybrid Power System,” *IEEE Access*, vol. 8, pp. 210 099–210 115, 2020.
- [148] T. Khatib, A. Mohamed, and K. Sopian, “Optimization of a pv/wind micro-grid for rural housing electrification using a hybrid iterative/genetic algorithm: Case study of kuala terengganu, malaysia,” *Energy and Buildings*, vol. 47, pp. 321–331, 2012.
- [149] M. Guezgouz, J. Jurasz, B. Bekkouche, T. Ma, M. S. Javed, and A. Kies, “Optimal hybrid pumped hydro-battery storage scheme for off-grid renewable energy systems,” *Energy Conversion and Management*, vol. 199, p. 112046, 2019.
- [150] C. Loutan, V. Gevorgian, P. Klauer, S. Chowdhury, S. Hall, M. Morjaria, V. Chadliev, N. Milam, and C. Milan, “Using renewables to operate a low carbon grid: Demonstration of advanced reliability services from a utility-scale solar pv plant,” *California ISO, NREL, First Solar*, 2016.
- [151] M. Glavin, P. K. Chan, S. Armstrong, and W. Hurley, “A stand-alone photovoltaic supercapacitor battery hybrid energy storage system,” in *2008 13th International power electronics and motion control conference*. IEEE, 2008, pp. 1688–1695.
- [152] D. Jager and A. Andreas, “Nrel national wind technology center (nwtc): M2 tower; boulder, colorado (data),” National Renewable Energy Lab.(NREL), Golden, CO (United States), Tech. Rep., 1996.
- [153] S. Teleke, M. E. Baran, S. Bhattacharya, and A. Q. Huang, “Rule-based control of battery energy storage for dispatching intermittent renewable sources,” *IEEE Transactions on Sustainable Energy*, vol. 1, no. 3, pp. 117–124, 2010.
- [154] S. Teleke, M. E. Baran, A. Q. Huang, S. Bhattacharya, and L. Anderson, “Control strategies for battery energy storage for wind farm dispatching,” *IEEE transactions on energy conversion*, vol. 24, no. 3, pp. 725–732, 2009.
- [155] M. Z. Daud, A. Mohamed, and M. Hannan, “An improved control method of battery energy storage system for hourly dispatch of photovoltaic power sources,” *Energy Conversion and Management*, vol. 73, pp. 256–270, 2013.
- [156] X. Wang, D. M. Vilathgamuwa, and S. Choi, “Determination of battery storage capacity in energy buffer for wind farm,” *IEEE Transactions on Energy Conversion*, vol. 23, no. 3, pp. 868–878, 2008.

- [157] Q. Li, S. S. Choi, Y. Yuan, and D. Yao, "On the determination of battery energy storage capacity and short-term power dispatch of a wind farm," *IEEE Transactions on Sustainable Energy*, vol. 2, no. 2, pp. 148–158, 2010.
- [158] C.-L. Nguyen, H.-H. Lee, and T.-W. Chun, "Cost-optimized battery capacity and short-term power dispatch control for wind farm," *IEEE Transactions on Industry Applications*, vol. 51, no. 1, pp. 595–606, 2014.
- [159] D. Yao, S. S. Choi, K.-J. Tseng, and T. T. Lie, "Determination of short-term power dispatch schedule for a wind farm incorporated with dual-battery energy storage scheme," *IEEE Transactions on Sustainable Energy*, vol. 3, no. 1, pp. 74–84, 2011.
- [160] D. Yao, S. Choi, K. Tseng, and T. Lie, "A statistical approach to the design of a dispatchable wind power-battery energy storage system," *IEEE Transactions on Energy Conversion*, vol. 24, no. 4, pp. 916–925, 2009.
- [161] K. Wee, S. S. Choi, and D. M. Vilathgamuwa, "Design of a least-cost battery-supercapacitor energy storage system for realizing dispatchable wind power," *IEEE Transactions on sustainable energy*, vol. 4, no. 3, pp. 786–796, 2013.
- [162] J. Chaires, H. B. Karayaka, Y. Yan, and P. Gardner, "Solar farm hourly dispatching using super-capacitor and battery system," in *2016 Clemson University Power Systems Conference (PSC)*. IEEE, 2016, pp. 1–7.
- [163] P. K. S. Roy, H. B. Karayaka, Y. Yan, and Y. Alqudah, "Size optimization of battery-supercapacitor hybrid energy storage system for 1mw grid connected pv array," in *2017 North American Power Symposium (NAPS)*. IEEE, 2017, pp. 1–6.
- [164] P. K. Singha Roy, H. B. Karayaka, Y. Yan, and Y. Alqudah, "Evaluation of reference generation algorithms for dispatching solar pv power," in *SoutheastCon 2018*, 2018, pp. 1–7.
- [165] P. K. S. Roy, H. B. Karayaka, Y. Yan, and Y. Alqudah, "Investigations into best cost battery-supercapacitor hybrid energy storage system for a utility scale pv array," *Journal of Energy Storage*, vol. 22, pp. 50–59, 2019.
- [166] H. Zheng, S. Li, C. Zang, and W. Zheng, "Coordinated control for grid integration of pv array, battery storage, and supercapacitor," in *2013 IEEE Power & Energy Society General Meeting*. IEEE, 2013, pp. 1–5.
- [167] A. M. Atallah, A. Abdelaziz, and R. S. Jumaah, "Implementation of perturb and observe mppt of pv system with direct control method using buck and buck - boost converters," 2014.
- [168] J. Chaires, H. B. Karayaka, Yanjun Yan, and P. Gardner, "Solar farm hourly dispatching using super-capacitor and battery system," in *2016 Clemson University Power Systems Conference (PSC)*, 2016, pp. 1–7.

- [169] H. Cai, W. Du, X. Yu, S. Gao, T. Littler, and H. Wang, “Day-ahead optimal charging/discharging scheduling for electric vehicles in micro-grids,” 2013.
- [170] D. B. Murray and J. G. Hayes, “Cycle testing of supercapacitors for long-life robust applications,” *IEEE Transactions on Power Electronics*, vol. 30, no. 5, pp. 2505–2516, 2015.
- [171] “Energy storage technology and cost characterization report,” *HydroWires: U.S. Department of Energy*, [Online]. Available: <https://www.energy.gov> [Accessed: Jan 20, 2020].
- [172] “Standard for interconnecting distributed resources with electric power systems,” *IEEE 1547*, 2003.
- [173] H. Ye, J. Wang, Y. Ge, J. Li, and Z. Li, “Robust integration of high-level dispatchable renewables in power system operation,” *IEEE Transactions on Sustainable Energy*, vol. 8, no. 2, pp. 826–835, 2016.
- [174] M. Amirabadi, H. A. Toliyat, and W. C. Alexander, “A Multiport AC link PV Inverter with Reduced Size and Weight for Stand-alone Application,” *IEEE Transactions on Industry Applications*, vol. 49, no. 5, 2013.
- [175] J. Zeng, W. Qiao, L. Qu, and Y. Jiao, “An Isolated Multiport DC–DC Converter for Simultaneous Power Management of Multiple Different Renewable Energy Sources,” *IEEE journal of emerging and selected topics in power electronics*, vol. 2, no. 1, pp. 70–78, 2013.
- [176] V. Nair R. et al., “Large Scale Grid Integration of Photovoltaic and Energy Storage Systems Using Triple Port Dual Active Bridge Converter Modules,” in *2018 IEEE PESGM*, 2018, pp. 1–5.
- [177] V. Nair R. et. al, “Integrating Photovoltaics and Battery Energy Storage to Grid Using Triple Active Bridge and Voltage Source Converters,” in *IECON 2020*, pp. 3691–3696.
- [178] C. Maxey et. al, “Oak Ridge National Laboratory (ORNL); rotating shadow-band radiometer (RSR); Oak Ridge, Tennessee (Data);,” NREL Report No. DA-5500-56512.
- [179] T. Givler and P. Lilienthal, “Using HOMER software, NREL’s micropower optimization model, to explore the role of gen-sets in small solar power systems; case study: Sri lanka,” National Renewable Energy Lab., Golden, CO (US), Tech. Rep., 2005.
- [180] K. Mongird, “Energy Storage Technology and Cost Characterization Report,” *HydroWires: U.S. Department of Energy*, July 2019, [Online]. Available: <https://www.energy.gov>.

- [181] M. Moonem and H. Krishnaswami, "Analysis and Control of Multi-level Dual Active Bridge DC-DC Converter," in *2012 IEEE Energy Conversion Congress and Exposition (ECCE)*. IEEE, 2012, pp. 1556–1561.
- [182] R. Liu, L. Xu, Y. Kang, Y. Hui, and Y. Li, "Decoupled TAB Converter with Energy Storage System for HVDC Power System of more Electric Aircraft," *The Journal of Engineering*, vol. 2018, no. 13, pp. 593–602, 2018.
- [183] J. Rabkowski, D. Peftitsis, and H.-P. Nee, "Silicon Carbide Power Transistors: A New Era in Power Electronics is Initiated," *IEEE Industrial Electronics Magazine*, vol. 6, no. 2, pp. 17–26, 2012.
- [184] ABB, "IGBT Module Data Sheet," [Online]. Available: [www.search.abb.com](http://www.search.abb.com) [Accessed: 20-March-2021].
- [185] Infineon, "IGBT Module Data Sheet," [Online]. Available: [www.mouser.com](http://www.mouser.com) [Accessed: 20-March-2021].
- [186] Hitachi, "SiC Module Data Sheet," [Online]. Available: [www.hitachi-power-semiconductor-device.com](http://www.hitachi-power-semiconductor-device.com) [Accessed: 20-March-2021].
- [187] Infineon, "Diode Data Sheet," [Online]. Available: [www.mouser.com](http://www.mouser.com) [Accessed: 20-March-2021].
- [188] H. J. Khasawneh, M. B. Mustafa, A. Al-Salaymeh, and M. Saidan, "Techno-economic evaluation of on-grid battery energy storage system in Jordan using HOMER Pro," in *2019 AEIT International Annual Conference (AEIT)*. IEEE, 2019, pp. 1–6.
- [189] Y. Zhou, L. Zhao, and W.-J. Lee, "Robustness analysis of dynamic equivalent model of dfig wind farm for stability study," *IEEE Transactions on Industry Applications*, vol. 54, no. 6, pp. 5682–5690, 2018.
- [190] K. Ni, Y. Hu, G. Chen, C. Gan, and X. Li, "Fault-tolerant operation of dfig-wt with four-switch three-phase grid-side converter by using simplified svpwm technique and compensation schemes," *IEEE Transactions on Industry Applications*, vol. 55, no. 1, pp. 659–669, 2018.
- [191] P. Roy and J. He, "Economic analysis for hourly dispatching wind energy power using battery and supercapacitor hybrid energy storage system," in *2021 IEEE Energy Conversion Congress and Exposition (ECCE)*, 2021, pp. 30–36.
- [192] H. B. Azad, S. Mekhilef, and V. G. Ganapathy, "Long-term wind speed forecasting and general pattern recognition using neural networks," *IEEE Transactions on Sustainable Energy*, vol. 5, no. 2, pp. 546–553, 2014.
- [193] M. De Giorgi, A. Ficarella, and M. Russo, "Short-term wind forecasting using artificial neural networks (anns)," *WIT Transactions on Ecology and the Environment*, vol. 121, 2009.



- [194] K. Parsopoulos et al., *Particle swarm optimization and intelligence: advances and applications: advances and applications*. IGI global, 2010.
- [195] R. Poli, J. Kennedy, and T. Blackwell, “Particle swarm optimization,” *Swarm intelligence*, vol. 1, no. 1, pp. 33–57, 2007.
- [196] G. M. Masters, *Renewable and efficient electric power systems*. John Wiley & Sons, 2013.
- [197] T. Stehly et al., “2019 Cost of Wind Energy Review,” *National Renewable Energy Laboratory; NREL Report No. NREL/TP-5000-78471*, 2020, [Online]. Available: <https://www.nrel.gov/docs>.
- [198] RTDS, “RTDS Manuals and Documentation,” *RTDS Technologies, Winnipeg, MB*, 2022.
- [199] M. M. Z. Moustafa, O. Nzimako, and A. Dekhordi, “Real time simulation of a wind turbine driven doubly fed induction generator,” in *2017 19th European Conference on Power Electronics and Applications (EPE'17 ECCE Europe)*. IEEE, 2017, pp. P–1.
- [200] M. Chen and G. A. Rincon-Mora, “Accurate electrical battery model capable of predicting runtime and iv performance,” *IEEE transactions on energy conversion*, vol. 21, no. 2, pp. 504–511, 2006.
- [201] S. Ibrahim, A. Cramer, X. Liu, and Y. Liao, “Pv inverter reactive power control for chance-constrained distribution system performance optimisation,” *IET Generation, Transmission & Distribution*, vol. 12, no. 5, pp. 1089–1098, 2018.

## Vita

**Pranoy Roy**, PhD Candidate

Department of Electrical and Computer Engineering, University of Kentucky

Pranoy Roy is a Ph.D. candidate in electrical engineering at the University of Kentucky, USA, focusing on high-performance renewable energy and power electronic systems. Pranoy also worked as a summer intern in the Eaton Research Labs, where he contributed to the development of a high power density bi-directional DC-DC converter. He obtained his M.Sc. degree in engineering technology from Western Carolina University in the USA and his B.Sc. degree in electrical and electronics engineering from Rajshahi University of Engineering & Technology, Bangladesh. To date, his research has yielded over 10 peer-reviewed conference and journal papers.